

**SISSA**

Scuola  
Internazionale  
Superiore di  
Studi Avanzati

Physics Area – PhD course in  
Theory and Numerical Simulation of Condensed Matter

Advanced Perspectives  
in Non-Equilibrium  
Quantum Dynamics

Candidate:

Alessandro Santini

Advisor:

Mario Collura

Giuseppe E. Santoro

Academic Year 2023-2024





## ABSTRACT

---

The study of non-equilibrium dynamics in quantum many-body systems is a rapidly evolving field at the intersection of condensed matter physics, quantum information theory, and statistical mechanics. These systems, which are far from thermal equilibrium, display rich and often counterintuitive behavior, driven by phenomena such as quantum coherence, entanglement, and criticality. Understanding the complex dynamics of these systems is not only of fundamental interest, but also essential for the development of next-generation quantum technologies, including quantum computation and simulation. This thesis aims to contribute to this growing body of knowledge by exploring advanced topics in the non-equilibrium dynamics of quantum systems. The work is divided into key sections, each addressing different aspects of quantum dynamics using a range of analytical and numerical techniques.

First, we present standard numerical and analytical techniques for simulating the dynamics of many-body quantum systems employing tensor network methods and Gaussian states to provide efficient descriptions of complex wave functions.

In the second part of the thesis, by employing tensor-network methods, we present a study on discrete-time crystals within two-dimensional Floquet systems, revealing the emergence of a long-range order and periodicity in driven quantum states. Then, we present some results to improve the tensor-network methods. In particular, we develop hybrid approaches that combine stabilizer circuits with tensor-network techniques, offering insights into the disentangling properties of Clifford unitaries contrasting the spread of entanglement in the evolution of these systems.

Finally, going beyond the unitary dynamics of quantum systems, we examine the effects of monitoring onto system dynamics, highlighting measurement induced phase transitions and the physics beyond the Lindblad dynamics in open quantum systems. In particular, we focus on the full counting statistics of the expectation values of observables in the ensemble of quantum trajectories. We examine different unravelings of the Lindblad equation in different setups.



## LIST OF PUBLICATIONS

---

The following is a list of publications that were completed during the Ph.D. studies.

### *Publications Included in This Thesis*

1. Alessandro Santini, Giuseppe E. Santoro, and Mario Collura. «Clean two-dimensional Floquet time crystal.» In: *Phys. Rev. B* 106 (13 Oct. 2022), p. 134301. DOI: [10.1103/PhysRevB.106.134301](https://doi.org/10.1103/PhysRevB.106.134301)
2. Antonio Francesco Mello, Alessandro Santini, and Mario Collura. «Hybrid Stabilizer Matrix Product Operator.» In: *Phys. Rev. Lett.* 133 (15 2024), p. 150604. DOI: [10.1103/PhysRevLett.133.150604](https://doi.org/10.1103/PhysRevLett.133.150604)
3. Antonio Francesco Mello et al. «Clifford Dressed Time-Dependent Variational Principle.» In: *arXiv* (2024). DOI: <https://arxiv.org/abs/2407.01692>
4. Emanuele Tirrito et al. «Full counting statistics as probe of measurement-induced transitions in the quantum Ising chain.» In: *SciPost Phys.* 15 (2023), p. 096. DOI: [10.21468/SciPostPhys.15.3.096](https://doi.org/10.21468/SciPostPhys.15.3.096)
5. Guglielmo Lami, Alessandro Santini, and Mario Collura. «Continuously monitored quantum systems beyond Lindblad dynamics.» In: *New Journal of Physics* 26.2 (Feb. 2024), p. 023041. DOI: [10.1088/1367-2630/ad1f0a](https://doi.org/10.1088/1367-2630/ad1f0a)
6. Alessandro Santini et al. «Semiclassical Quantum Trajectories in the Monitored Lipkin-Meshkov-Glick Model.» In: *arXiv* (2024). DOI: <https://arxiv.org/abs/2407.20314>

### *Other Publications by the same author*

1. Nishan Ranabhat et al. «Dynamical deconfinement transition driven by density of excitations.» In: *arXiv preprint arXiv:2310.02320* (2023). DOI: <https://doi.org/10.48550/arXiv.2310.02320>
2. Alessandro Santini et al. «Work statistics, quantum signatures, and enhanced work extraction in quadratic fermionic models.» In: *Phys. Rev. B* 108 (10 Sept. 2023), p. 104308. DOI: [10.1103/PhysRevB.108.104308](https://doi.org/10.1103/PhysRevB.108.104308)
3. Luca Capizzi et al. «Spreading of a local excitation in a quantum hierarchical model.» In: *Phys. Rev. B* 106.13 (13 Oct. 2022), p. 134210. DOI: [10.1103/PhysRevB.106.134210](https://doi.org/10.1103/PhysRevB.106.134210)
4. Alessandro Santini and Vittorio Vitale. «Experimental violations of Leggett-Garg inequalities on a quantum computer.» In: *Phys. Rev. A* 105 (3 Mar. 2022), p. 032610. DOI: [10.1103/PhysRevA.105.032610](https://doi.org/10.1103/PhysRevA.105.032610)
5. Alessandro Santini et al. «Observation of partial and infinite-temperature thermalization induced by repeated measurements on a quantum hardware.» In: *Journal of Physics Communications* 7.6 (2023), p. 065007. DOI: [10.1088/2399-6528/acdd4f](https://doi.org/10.1088/2399-6528/acdd4f)
6. Andrea Solfanelli, Alessandro Santini, and Michele Campisi. «Quantum thermodynamic methods to purify a qubit on a quantum processing unit.» In: *AVS Quantum Science* 4.2 (June 2022), p. 026802. ISSN: 2639-0213. DOI: [10.1116/5.0091121](https://doi.org/10.1116/5.0091121)
7. Alessandro Santini, Guido Giachetti, and Lapo Casetti. «Violent relaxation in the Hamiltonian mean field model: II. Non-equilibrium phase diagrams.» In: *Journal of Statistical Mechanics: Theory and Experiment* 2022.1 (2022), p. 013210. DOI: [10.1088/1742-5468/ac4516](https://doi.org/10.1088/1742-5468/ac4516)
8. Andrea Solfanelli, Alessandro Santini, and Michele Campisi. «Experimental Verification of Fluctuation Relations with a Quantum Computer.» In: *PRX Quantum* 2 (3 Sept. 2021), p. 030353. DOI: [10.1103/PRXQuantum.2.030353](https://doi.org/10.1103/PRXQuantum.2.030353)



*“Noi don Magnifico,  
duca e barone  
dell’antichissimo  
Montefiascone,  
grand’intendente,  
gran presidente,  
con gli altri titoli,  
con venti et cetera,  
in splenditudine  
d’autorità,  
riceva l’ordine  
chi leggerà.  
Di più non mescere  
per anni quindici  
nel vino amabile  
d’acqua una gocciola,  
alias capietur  
et stranguletur.”*

— G. Rossini,  
*La Cenerentola.*

## ACKNOWLEDGEMENTS

---

I would like to first thank my supervisor, who made this PhD possible in such a fantastic environment. I am also deeply grateful to all the people I have met over the past four years, even though, perhaps, I should say six, since SISSA had already welcomed me into its corridors long before the pandemic. I won't mention names, as I fear leaving someone out, but I truly appreciate everyone who has been part of this experience. Finally, I want to express my deepest gratitude to my partner, whose support has meant everything to me and without whom I might never have had the chance to embark on this adventure in Trieste.







# CONTENTS

---

<b>I</b>	<b>NONEQUILIBRIUM DYNAMICS OF QUANTUM SYSTEMS</b>	<b>3</b>
1	DYNAMICS OF MANY-BODY QUANTUM SYSTEMS	5
1.1	Quantum State and Observables . . . . .	5
1.2	Time Evolution . . . . .	6
1.3	Many-body quantum systems . . . . .	6
1.4	Fermionic gaussian systems . . . . .	7
1.4.1	Transverse Field Ising Chain . . . . .	9
1.5	Tensor Network methods . . . . .	10
1.5.1	Tensor Network . . . . .	10
1.5.2	Schmidt Decomposition . . . . .	11
1.5.3	Matrix Product States (MPS) . . . . .	13
1.5.4	Time-Evolving Block Decimation (TEBD) Algorithm .	16
1.5.5	Matrix Product Operators (MPO) . . . . .	19
1.5.6	Time-Dependent Variational (TDVP) Principle Algo- rithm . . . . .	24
<b>II</b>	<b>MANY-BODY QUANTUM SYSTEMS</b>	<b>31</b>
2	CLEAR DISCRETE FLOQUET 2D TIME CRYSTAL	33
2.1	Discrete Time Crystals . . . . .	33
2.2	Kicked Clean Ising Model . . . . .	33
2.3	Clean one-dimensional kicked Ising Chain . . . . .	34
2.4	Clean two-dimensional kicked Ising Chain . . . . .	36
2.5	Numerical results . . . . .	36
2.5.1	Exact diagonalization . . . . .	36
2.5.2	Tensor network time evolution . . . . .	37
2.5.3	Dynamical transition in the relaxation dynamics . . .	40
2.6	High-frequency limit . . . . .	41
2.7	Conclusions and outlooks . . . . .	44
3	HYBRID STABILIZER AND TENSOR-NETWORK METHODS	45
3.1	The Pauli Group . . . . .	45
3.2	Stabilizer States and the Clifford Group . . . . .	46
3.3	Hybrid Stabilizer Matrix Product Operators . . . . .	48
3.3.1	Transformation of local gate under Clifford Operations	49
3.3.2	Stabilizer Matrix Product Operator . . . . .	50
3.3.3	Random Clifford T-doped circuit . . . . .	52
3.3.4	Random Clifford Floquet Dynamics . . . . .	53
3.4	Clifford Dressed TDVP . . . . .	55
3.4.1	Clifford disentangled $\tau$ -TDVP . . . . .	57
3.4.2	Clifford Dressed $\tau$ -TDVP Numerical Experiments . . .	59
3.5	Conclusion & Outlook . . . . .	62
<b>III</b>	<b>MONITORED QUANTUM SYSTEMS</b>	<b>65</b>
4	MONITORED QUANTUM SYSTEMS	67
4.1	Measurement protocols . . . . .	68
4.1.1	Quantum Jumps . . . . .	68
4.1.2	Weak-measurements . . . . .	68
4.1.3	Continuous limit . . . . .	69
4.1.4	Lindblad Dynamics Average State . . . . .	70
4.2	Local Measurements have a non-local effect on entangled states	71
4.3	Measurement Induced Phase Transition . . . . .	72
4.4	Mean state and quantum trajectories . . . . .	72

5	FULL COUNTING STATISTICS IN THE MONITORED QUANTUM ISING CHAIN	75
5.1	Model . . . . .	75
5.2	Protocol . . . . .	77
5.3	Lindbladian dynamics of the averaged state . . . . .	78
5.4	Numerical Results . . . . .	80
5.4.1	Paramagnetic Magnetization . . . . .	81
5.4.2	Ferromagnetic Magnetization . . . . .	83
5.5	Conclusion . . . . .	86
6	UNRAVELING OF LINDBLAD EQUATION AND FULL COUNTING STATISTICS	89
6.1	Protocol . . . . .	89
6.2	Two-level system . . . . .	92
6.3	Hopping particle . . . . .	95
6.4	Appendices . . . . .	99
6.4.1	Appendix A: Lindblad equation solution for the two level system . . . . .	99
6.4.2	Appendix B: Lindblad equation solution for the hopping particle . . . . .	100
7	SEMICLASSICAL QUANTUM TRAJECTORIES IN THE MONITORED LMG MODEL	103
7.1	Monitoring and quantum trajectories . . . . .	103
7.1.1	Ensemble averages and full counting statistics . . . . .	104
7.2	Monitored LMG Model . . . . .	105
7.3	Semiclassical limit . . . . .	106
7.3.1	Unitary Evolution . . . . .	106
7.3.2	Monitored Evolution . . . . .	108
7.3.3	Non-commutativity of the limits . . . . .	109
7.4	Stationary probability distribution . . . . .	110
7.5	Conclusion & Outlook . . . . .	111
7.6	Appendices . . . . .	113
7.6.1	Appendix A: Coherent spin states . . . . .	113
7.6.2	Appendix B: Derivation of Eq. (380) . . . . .	114
7.6.3	Appendix C: Semiclassic limit and ensemble averages . . . . .	116
7.6.4	Appendix D: Hamiltonian dynamics close to the separatrix . . . . .	116
7.6.5	Appendix E: Large $\gamma$ limit . . . . .	117
	BIBLIOGRAPHY	120





## Part I

# NONEQUILIBRIUM DYNAMICS OF QUANTUM SYSTEMS

In the first part, we discuss the dynamics of many-body quantum systems. The content will cover numerical techniques, in particular focusing on exact methods and tensor-network states. This introduction aims to provide a foundational understanding of the numerical methods used to analyze complex quantum systems.





Quantum mechanics represents a fundamental breakthrough in our understanding of the universe. This field, despite its vast scope and impressive precision, is founded on a handful of core principles. In the following, we will briefly outline these fundamental concepts. Then we will discuss free-fermionic and tensor network ansatz methods for the dynamics of many-body wave functions.

### 1.1 QUANTUM STATE AND OBSERVABLES

In quantum mechanics, the concept of a quantum state is fundamental to describe a physical system. Any quantum system is associated with a Hilbert space  $\mathcal{H}$ . Elements of  $\mathcal{H}$ , usually denoted using ket notation  $|\psi\rangle$ , represent possible states of the system.

It is convenient to decompose a state  $|\psi\rangle$  with respect to an orthonormal basis of the Hilbert space  $|j\rangle$ , where  $j = 1, \dots, \dim(\mathcal{H})$ . This decomposition is expressed as

$$|\psi\rangle = \sum_j \psi_j |j\rangle, \quad (1)$$

where  $\psi_j \in \mathbb{C}$  are complex coefficients given by  $\langle j|\psi\rangle = \psi_j$ . For a physical state, the norm must be unity, which implies that  $|\langle\psi|\psi\rangle|^2 = 1$ . Consequently, we have

$$\sum_j |\psi_j|^2 = 1. \quad (2)$$

By choosing a particular basis, we can describe all the states in the Hilbert space through their respective components  $\psi_j$ . This effectively creates a correspondence between  $\mathcal{H}$  and  $\mathbb{C}^D$ . This approach is highly beneficial for practical purposes, as it allows for straightforward numerical computations by working with numerical values directly.

Observables are physical quantities that can be measured, such as position, momentum, and energy. These observables are represented by operators acting on  $\mathcal{H}$ . An observable  $O$  is typically a Hermitian operator, meaning that  $O = O^\dagger$ , where  $O^\dagger$  is the adjoint (or Hermitian conjugate) of  $O$ . This property ensures that the eigenvalues of  $O$ , which correspond to the possible measurement outcomes, are real numbers. Again, it is convenient to decompose an observable  $O : \mathcal{H} \rightarrow \mathcal{H}$  with respect to an orthonormal basis of  $\mathcal{H}$ . This decomposition can be represented as

$$O = \sum_{ij} O_{ij} |i\rangle\langle j|, \quad (3)$$

where  $O_{ij} = \langle i|O|j\rangle$ . Moreover, the expectation value of an observable  $O$  in a quantum state  $|\psi\rangle$  is given by

$$\langle O \rangle = \langle \psi|O|\psi \rangle. \quad (4)$$

This quantity represents the average outcome of many measurements of  $O$  on a system prepared in the state  $|\psi\rangle$ . It is important to stress that the act of measuring an observable in quantum mechanics is inherently probabilistic. In the case of what we will call *strong projective measurements*, when an

*Strong projective  
measurements  
probability*

observable  $O$  is measured in a state  $|\psi\rangle$ , the probability  $P(\lambda_j)$  of obtaining a particular eigenvalue  $\lambda_j$  of  $O$  is given by

$$P(\lambda_j) = |\langle \phi_j | \psi \rangle|^2, \quad (5)$$

where  $|\phi_j\rangle$  is the eigenstate of  $O$  corresponding to the eigenvalue  $\lambda_j$ . The state of the system after the measurement collapses to the eigenstate  $|\phi_j\rangle$  associated with the measured eigenvalue  $\lambda_j$ .

### 1.2 TIME EVOLUTION

*Time-dependent  
Schrödinger equation*

The time evolution of a quantum state is governed by the Schrödinger equation, a fundamental deterministic equation in quantum mechanics that describes how the quantum state of a physical system changes over time. For a system with a time-dependent Hamiltonian  $H(t)$ , the Schrödinger equation is given by

$$i\hbar \frac{\partial}{\partial t} |\psi(t)\rangle = H(t) |\psi(t)\rangle, \quad (6)$$

where  $\hbar$  is the reduced Planck constant,<sup>1</sup>  $|\psi(t)\rangle$  is the state of the system at time  $t$ , and  $H$  is the Hamiltonian operator representing the total energy of the system.

To solve this differential equation, we can express the state at any time  $t$  as

$$|\psi(t)\rangle = \mathcal{T}e^{-i \int_0^t H(t') dt'} |\psi(0)\rangle, \quad (7)$$

where  $|\psi(0)\rangle$  is the state of the system at the initial time  $t = 0$ . The unitary operator  $\mathcal{T}e^{-i \int_0^t H(t') dt'}$ , that is, the time-ordered exponential of the Hamiltonian  $H$ , also known as the time evolution operator, acts on the initial state to transform the state at any later time. Therefore, with this formalism, we can predict the future behavior of a quantum system based on its initial state and its Hamiltonian.

Finally, it is important to remark that the Schrödinger equation describes the evolution of isolated quantum systems. However, in reality, many quantum systems interact with their external environment, leading to open quantum systems. The dynamics of open quantum systems are more complex due to decoherence and dissipation effects. To account for these interactions, the evolution is often described by the Lindblad master equation or other non-unitary frameworks.

### 1.3 MANY-BODY QUANTUM SYSTEMS

The simplest non-trivial quantum system is a two-level system, where the Hilbert space is spanned by the states  $|0\rangle$  and  $|1\rangle$ . This system is known as a qubit, with  $|0\rangle$  and  $|1\rangle$  forming the computational basis.

Any operator acting on this Hilbert space can be constructed using the identity operator  $\mathbb{I}$  and the three Pauli operators  $X$ ,  $Y$ , and  $Z$ . The computational basis states are chosen to be the eigenstates of  $Z$ , such that  $Z|\sigma\rangle = (-1)^\sigma |\sigma\rangle$  for  $\sigma = 0, 1$ . The matrix representations of the Pauli operators are given by

*Pauli basis matrix  
representation*

$$\mathbb{I} = \begin{pmatrix} 1 & 0 \\ 0 & 1 \end{pmatrix}, X = \begin{pmatrix} 0 & 1 \\ 1 & 0 \end{pmatrix}, Y = \begin{pmatrix} 0 & -i \\ i & 0 \end{pmatrix}, Z = \begin{pmatrix} 1 & 0 \\ 0 & -1 \end{pmatrix}. \quad (8)$$

<sup>1</sup> In the following we will always consider  $\hbar = 1$ .

The state of a many-body system composed of multiple subsystems is described by the tensor product of the states of the individual subsystems. In particular, the wave-function of a N-qubit state is written as

$$|\Psi\rangle = \sum_{\sigma_1, \dots, \sigma_N} \psi_{\sigma_1, \dots, \sigma_N} |\sigma_1, \dots, \sigma_N\rangle. \quad (9)$$

We notice that  $\psi_{\sigma_1, \dots, \sigma_N}$  is a rank N tensor which contains  $2^N$  complex numbers. This exponential growth in the number of complex coefficients with the size of the system poses significant challenges for memory and computational resources. When  $N \gtrsim 30$ , the memory required to store the wavefunction becomes prohibitive, exceeding the capacity of conventional computing systems. Nevertheless, there are ways of taming this complexity. We start by reviewing some techniques to solve exactly the dynamics. Specifically, we will provide a brief overview of non-interacting systems characterized by fermionic Gaussian wave functions and Hamiltonians. Next, we will introduce tensor-network techniques to approximate the wave function and manage the exponential complexity present in interacting quantum systems.

#### 1.4 FERMIONIC GAUSSIAN SYSTEMS

In this section, we present some techniques for solving the dynamics of certain spin and fermionic systems, where the Hamiltonians and quantum states are quadratic in fermionic variables.

Consider a set of N Dirac fermionic creation and annihilation operators such that  $\{c_i, c_j^\dagger\} = \delta_{ij}$  and  $\{c_i, c_j\} = 0$  with the number operator  $n_i = c_i^\dagger c_i$ . The most general form of a quadratic gaussian Hamiltonian is expressed as

$$H = \sum_{ij} A_{ij} c_i c_j^\dagger - B_{ij}^* c_i^\dagger c_j^\dagger + B_{ij} c_i c_j - A_{ij}^* c_i^\dagger c_j \quad (10)$$

*Quadratic fermionic  
hamiltonian*

Since H is hermitean A has to be hermitean and B skew-symmetric. Introducing the vector of operators defined by

$$\Psi = (c_1^\dagger, \dots, c_N^\dagger, c_1, \dots, c_N)^T, \quad (11)$$

we can write the hamiltonian as

$$H = \Psi^\dagger \mathbb{H} \Psi \quad (12)$$

where  $\mathbb{H}$  is a  $2N \times 2N$  matrix and takes the following block form

$$\mathbb{H} = \begin{pmatrix} A & B \\ -B^* & -A^* \end{pmatrix}. \quad (13)$$

It is always possible to find a set of Dirac operators

$$\Phi = (b_1^\dagger, \dots, b_N^\dagger, b_1, \dots, b_N)^T = \mathbb{U} \Psi \quad (14)$$

where  $\mathbb{U}$  is the unitary transformation that diagonalize the hamiltonian

$$H = \Phi^\dagger \mathbb{H}_D \Phi \quad (15)$$

with

$$\mathbb{H}_D = \mathbb{U}^\dagger \mathbb{H} \mathbb{U} = \text{diag}(-\epsilon_1, \dots, -\epsilon_N, \epsilon_1, \dots, \epsilon_N) \quad (16)$$

notice that the eigenvalues  $\{\epsilon_j, -\epsilon_j\}$  appear in pairs due to the symplectic nature of  $\mathbb{H}$ .

Gaussian quantum state

We can focus now on the quantum states. We say that a quantum state is a Gaussian state if we can represent it as

$$\rho = \frac{e^{-\Psi^\dagger W \Psi}}{Z}, \quad (17)$$

where  $W = \Psi^\dagger W \Psi$  is referred to as the parent Hamiltonian of  $\rho$  and has the same structure of a quadratic Gaussian Hamiltonian. Observe the similarity between  $\rho$  and a canonical thermal state. Similar to the diagonalization of the Hamiltonian  $H$ , we can diagonalize the density matrix  $\rho$  by transforming  $W$ , with an appropriate unitary transformation  $\tilde{U}$ , into  $W_D = \tilde{U}^\dagger W \tilde{U}$ , with eigenvalues  $\{w_j, -w_j\}$ , and introducing a new set of fermionic variables  $\Phi = \tilde{U} \Psi$  such that

$$\rho = \prod_{n=1}^N \frac{e^{-w_n (b_n^\dagger b_n - b_n b_n^\dagger)}}{2 \cosh w_n}, \quad (18)$$

it is apparent that  $Z = \text{Tr}\{\rho\} = \prod_n 2 \cosh w_n$ . Gaussian quantum states are particularly important since they are completely determined by the correlation matrix

Correlation matrix

$$\mathbf{G} = \langle \Psi \Psi^\dagger \rangle = \begin{pmatrix} G_{c^\dagger c} & G_{c^\dagger c^\dagger} \\ G_{cc} & G_{cc^\dagger} \end{pmatrix}. \quad (19)$$

In fact, the correlation matrix and the parent Hamiltonian are connected through the formula

$$\mathbf{G} = \frac{1}{1 + e^{2W}} \quad (20)$$

Indeed

$$\begin{aligned} (\mathbf{G})_{ij} &= \text{Tr}\{\rho \Psi_i \Psi_j^\dagger\} = \sum_{kn} U_{ik} U_{jn}^\dagger \text{Tr}\left\{\frac{e^{\Phi^\dagger W_D \Phi}}{Z} \Phi_k \Phi_n^\dagger\right\} \\ &= \sum_{n=1}^L \frac{U_{in} U_{jn}^\dagger}{2 \cosh w_n} \text{Tr}\{e^{w_n (b_n^\dagger b_n - b_n b_n^\dagger)} b_n^\dagger b_n\} \\ &\quad + \sum_{n=1}^L \frac{U_{i,n+L} U_{j,n+L}^\dagger}{2 \cosh w_n} \text{Tr}\{e^{w_n (b_n^\dagger b_n - b_n b_n^\dagger)} b_n b_n^\dagger\} \\ &= \sum_{n=1}^L U_{in} U_{jn}^\dagger \frac{1}{1 + e^{-2w_n}} + \\ &\quad + \sum_{n=1}^L U_{i,n+L} U_{j,n+L}^\dagger \frac{1}{1 + e^{2w_n}} \\ &= \sum_{n=1}^{2L} U_{in} \left[ \frac{1}{1 + e^{2W_D}} \right]_{nn} U_{jn}^\dagger = \left[ \frac{1}{1 + e^{2W}} \right]_{ij}. \end{aligned} \quad (21)$$

TIME EVOLUTION — Let us now focus on the dynamics of quadratic fermionic systems. Consider the hamiltonian in its diagonal form

$$H = \Phi^\dagger H_D \Phi \quad (22)$$

from the Heisenberg picture we have that

$$\frac{db_n}{dt} = i[H, b_n] = -2i\epsilon_n b_n \quad (23)$$

which leads to the following

$$\Phi(t) = e^{-2iH_D t} \Phi(0) \quad (24)$$

going back to the  $\Psi$  fermions we obtain

$$\Psi(t) = e^{-2iHt}\Psi(0). \quad (25)$$

Thus, the evolution of the correlation matrix is given by

$$G(t) = e^{-2iHt}G(0)e^{2iHt} \quad (26)$$

Observe that, since the state  $\rho$  is gaussian, Wick's theorem holds. As such, evaluating the expectation values of products of Dirac fermion reduces to compute a suitable determinant.

#### 1.4.1 Transverse Field Ising Chain

The quantum transverse Ising chain is a fundamental model in quantum mechanics and statistical physics, used to study phase transitions and quantum criticality. It consists of a one-dimensional array of spins with interactions between neighboring spins and an external magnetic field applied perpendicular to the spin direction (the transverse field). The competition between the spin-spin interaction, which favors alignment, and the transverse magnetic field, which favors flipping the spins, leads to a quantum phase transition. We will examine this model repeatedly throughout this thesis. Here, we demonstrate how to solve its dynamics. The Hamiltonian of the transverse field quantum Ising model with periodic boundary conditions is the following

$$H_t = -\sum_{j=1}^L X_j X_{j+1} + h(t) \sum_{j=1}^L Z_j, \quad (27)$$

where  $X_j, Y_j$  and  $Z_j$  are the local Pauli matrices, with  $j = 1, \dots, N$ . To map the spin degrees of freedom into fermionic variables, we employ the so-called Jordan-Wigner transformation. Specifically, the mapping expresses fermionic creation and annihilation operators in terms of tensor products of Pauli matrices and identity matrices. In particular, we have

$$X_k = \prod_{j=1}^{k-1} Z_j (c_k^\dagger + c_k), \quad Y_k = i \prod_{j=1}^{k-1} Z_j (c_k^\dagger - c_k), \quad Z_k = 1 - 2n_k, \quad (28)$$

where  $\{c_i, c_j^\dagger\} = \delta_{ij}$  and  $n_j = c_j^\dagger c_j$ . Through the use of this transformation the transverse field Ising chain Hamiltonian can be represented as a quadratic fermionic problem

$$H_t = -\sum_{j=1}^L (c_j^\dagger c_{j+1} + c_j^\dagger c_{j+1}^\dagger + \text{h.c.}) - h(t) \sum_{j=1}^L (2c_j^\dagger c_j - 1). \quad (29)$$

Moreover, since the model is translationally invariant, the Hamiltonian  $H_t$  can be diagonalized by means of the discrete Fourier transform

$$c_j = \frac{e^{-i\pi/4}}{\sqrt{L}} \sum_p e^{ipj} \tilde{c}_p, \quad \tilde{c}_p = \frac{e^{i\pi/4}}{\sqrt{L}} \sum_{j=1}^L e^{-ipj} c_j \quad (30)$$

with  $p = 2\pi m/L$  and  $m = -L/2 + 1, \dots, L/2$ . Additionally, the invariance under the inversion symmetry  $p \rightarrow -p$  lets us to restrict the computations to positive momenta by defining  $\Psi_p = (\tilde{c}_p, \tilde{c}_{-p}^\dagger)^\top$ . Therefore,

$$H_t = \sum_{p>0} \Psi_p^\dagger \mathbb{H}_p(t) \Psi_p \quad (31)$$

*Transverse field Ising model*

*Jordan-Wigner transformation*

*Mapping to fermions transverse field Ising model*

where

$$\mathbb{H}_p(t) = \begin{pmatrix} -2 \cos p + 2h(t) & -2 \sin p \\ -2 \sin p & 2 \cos p - 2h(t) \end{pmatrix}. \quad (32)$$

The  $R_y(\phi_p(t)) = \exp(i\phi_p \sigma^y/2)$  rotation applied to the new fermions  $\Gamma_p(t) = (\gamma_p, \gamma_{-p}^\dagger)^\top$  diagonalizes the problem. Formally, one has

$$\Psi_p = \exp\left(i \frac{\phi_p(t)}{2} \sigma^y\right) \Gamma_p(t) \equiv R_y(\phi_p(t)) \Gamma_p(t), \quad (33)$$

where the eigenvectors of the rotation are given by

$$v_{+,p} = \begin{pmatrix} \cos \phi_p(t)/2 \\ \sin \phi_p(t)/2 \end{pmatrix} \quad \text{and} \quad v_{-,p} = \begin{pmatrix} -\sin \phi_p(t)/2 \\ \cos \phi_p(t)/2 \end{pmatrix}. \quad (34)$$

The rotation angles  $\phi_p$  are implicitly defined by the conditions  $\cos \phi_p(t) = 2(h(t) - \cos p)/\omega_p(t)$  and  $\sin \phi_p(t) = 2 \sin p/\omega_p(t)$ ; note that  $\phi_p(t) = -\phi_{-p}(t)$ . The Hamiltonian, written in terms of the new fermionic operators, then reads

$$H_t = \sum_{p>0} \Gamma_p^\dagger(t) \mathbb{D}_p(t) \Gamma_p(t) = \sum_{p>0} \Psi_p^\dagger R_y^\dagger(\phi_p(t)) \omega_p(t) \sigma^z R_y(\phi_p(t)) \Psi_p \quad (35)$$

where  $\mathbb{D}_p(t) = \omega_p(t) \sigma^z$  and the energies of each mode are given by  $\omega_p(t) = 2\sqrt{(\cos p - h(t))^2 + \sin^2 p}$ , with  $\omega_p(t) = \omega_{-p}(t)$ .

Observe that the transverse field Ising model serves as an excellent benchmark for numerical methods since it is exactly solvable.

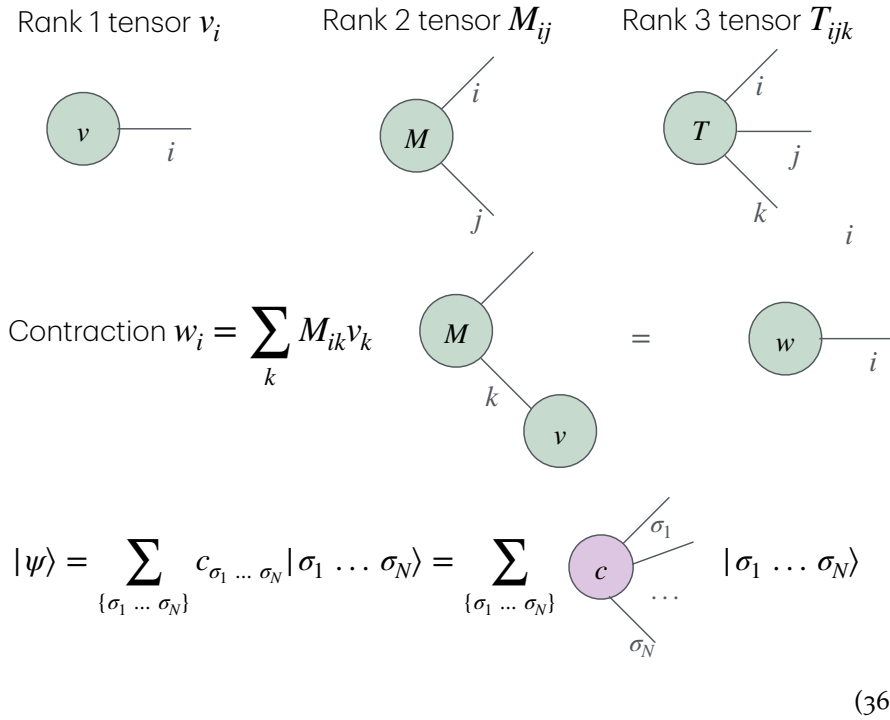
## 1.5 TENSOR NETWORK METHODS

In general, apart from a few integrable models, which can be solved using techniques similar to those discussed in the previous section, the dynamics of quantum systems cannot be solved exactly. Therefore, we must rely on numerical methods. One of the most powerful techniques for solving the dynamics of interacting quantum systems is tensor network methods, which aim to reduce the complexity of the wavefunction using an approximating ansatz.

### 1.5.1 Tensor Network

Tensor networks are mathematical structures. They consist of tensors, which are multi-dimensional arrays of numbers, connected by edges that represent the contraction (or summation) of indices between tensors. A graphical representation simplifies the handling of large amounts of data, such as a

quantum wave-function, reducing computational complexity. In particular, it works as shown in the following diagrams



Before presenting tensor network methods to decompose the wave-function, represent operators and present algorithms for the dynamics of quantum systems [15, 16], it is essential to review an important decomposition in many-body quantum systems, as it forms the foundation for understanding these methods.

### 1.5.2 Schmidt Decomposition

The Schmidt decomposition is a fundamental concept in linear algebra particularly valuable in quantum mechanics that provides a way to express the state of a bipartite quantum system in a particularly useful form.

Consider a quantum system divided into two subsystems, A and B. Any pure state  $|\psi\rangle$  of the combined system can be written as

$$|\psi\rangle = \sum_{i,j} \psi_{ij} |a_i\rangle \otimes |b_j\rangle, \tag{37}$$

where  $|a_i\rangle$  and  $|b_j\rangle$ , with  $i = 1, \dots, n$  and  $j = 1, \dots, m$ , are orthonormal bases for subsystems A and B, respectively, and  $\psi_{ij}$  are the coefficients of the state in this product basis. The Schmidt decomposition theorem states that there exist orthonormal bases  $\{|a'_k\rangle\}$  for subsystem A and  $\{|b'_k\rangle\}$  for subsystem B such that  $|\psi\rangle$  can be written in the form

$$|\psi\rangle = \sum_k \lambda_k |a'_k\rangle \otimes |b'_k\rangle, \tag{38}$$

where  $\lambda_k \geq 0$  are the Schmidt coefficients.

In order to give an operative way to find the Schmidt decomposition, we introduce a linear algebra decomposition called singular value decomposition (SVD). The singular value decomposition of an  $n \times m$  matrix  $M$  is a factorization that expresses  $M$  as a product of three matrices. Specifically,  $M$  can be written as

*Schmidt decomposition*

*Singular value decomposition*

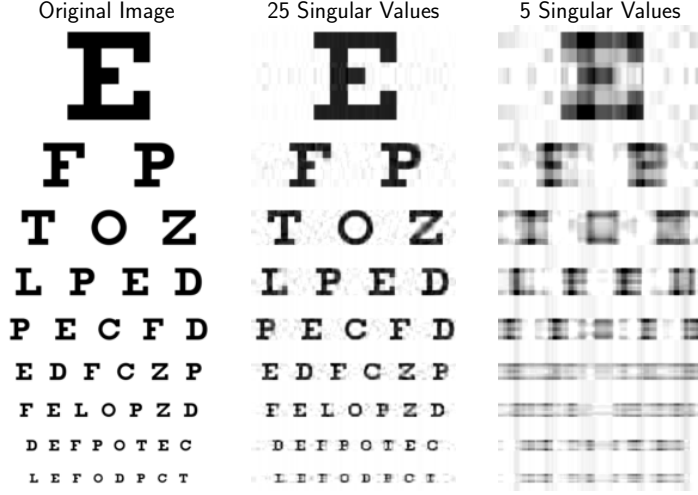


Figure 1: We examine an 800 by 350 pixels gray-scale image. By truncating the singular value spectrum at a specific threshold, a low-rank approximation of the image can be carried out. Observe that this approximation eliminates finer details while preserving the key features.

$$M = U\Lambda V^\dagger, \quad (39)$$

where  $U$  is an  $n \times \min(n, m)$  matrix and has orthonormal columns  $U^\dagger U = \mathbb{I}$ ,  $\Lambda$  is an  $\min(n, m) \times \min(n, m)$  diagonal matrix with non-negative real numbers on the diagonal, and  $V^\dagger$  is an  $\min(n, m) \times m$  matrix and has orthonormal rows  $V^\dagger V = \mathbb{I}$ . The diagonal entries of  $\Lambda$  are known as the singular values of  $M$  and are generally arranged in descending order.

The singular value decomposition provides us with a low-rank representation of the matrix  $M$  by minimizing the Frobenius norm between  $M$  and  $\tilde{M}$

*Frobenius norm*

$$\|M - \tilde{M}\| = \sqrt{\sum_{ij} (M_{ij} - \tilde{M}_{ij})^2}, \quad (40)$$

under the constraint that  $\text{rank}(\tilde{M}) = \chi < \text{rank}(M)$ . In fact, to do so, it is sufficient to set zero  $\lambda_k$  for  $k = \chi + 1, \dots, \min(n, m)$ . As an example of this compression, see Fig. 1 for the result of a low-rank approximation in showing a black and white image. Let us now consider the expression in Eq. (37) and perform a SVD of the matrix  $\psi_{ij}$

$$|\psi\rangle = \sum_{ij} \psi_{ij} |a_i b_j\rangle = \sum_{ijk} U_{ik} \Lambda_k V_{kj}^\dagger |a_i b_j\rangle = \sum_k \Lambda_k |a'_k b'_k\rangle, \quad (41)$$

where  $|a'_k\rangle = \sum_i U_{ik} |a_i\rangle$  and  $|b'_k\rangle = \sum_j V_{kj}^\dagger |b_j\rangle$  are orthonormal bases. The normalization constraint implies that  $\sum_k \Lambda_k^2 = 1$ .

Notice how, given the Schmidt decomposition, it is easy to trace out half of the system. Indeed, since  $|b'_n\rangle$  is an orthonormal base of  $B$ , we can describe the subsystem  $A$  considering the following mixed reduced density matrix

$$\rho_A = \sum_k \langle b'_k | |\psi\rangle\langle\psi| |b'_k\rangle = \sum_k \Lambda_k^2 |a'_k\rangle\langle a'_k|. \quad (42)$$

Using the Schmidt decomposition, one can easily calculate the bipartite von Neumann entanglement entropy, which quantifies the extent of quantum entanglement between two subsystems, as given by

*Bipartite entanglement entropy*

$$S_A = -\text{Tr}\{\rho_A \log \rho_A\} = -\sum_k \Lambda_k^2 \log \Lambda_k^2 = -\text{Tr}\{\rho_B \log \rho_B\} = S_B. \quad (43)$$



This is why the squared singular values of the bipartition are referred to as the entanglement spectrum. The low-rank approximation of  $\psi$  therefore represents an approximation of the level of entanglement between A and B in the wave function  $\tilde{\psi}$ .

In the following section, we will leverage on the low-rank approximation provided by the Schmidt decomposition to discuss the role of entanglement entropy in assessing complexity and present the tensor network approach for representing wave functions.

### 1.5.3 Matrix Product States (MPS)

Given the exponential growth of the state space in many-body quantum systems, efficient representations of quantum states are essential. One such powerful representation is the Matrix Product State (MPS), which provides a compact and scalable way to describe quantum states. Instead of directly storing  $2^N$  coefficients, an MPS expresses the wave function of an N-qubit system as a product of rank 3 tensors, each associated with a single qubit, significantly reducing the complexity.

First, let us construct the MPS representation of the many-body wave function in Eq. (9). The idea is to decompose the wave function from the high-dimensional rank N tensor  $\psi_{\sigma_1, \dots, \sigma_N}$  into a product of lower-dimensional tensors. Let us remind the graphical notation for tensors

Graphical notation

$$\begin{aligned} \psi_{\sigma_1, \dots, \sigma_N} &= \text{Diagram of a rank-N tensor } \psi \text{ with legs } \sigma_1, \sigma_2, \dots, \sigma_N, \\ \sum_{\sigma'_N} \psi_{\sigma_1, \dots, \sigma'_N} O_{\sigma'_N \sigma_N} &= \text{Diagram of a rank-N tensor } \psi \text{ with legs } \sigma_1, \sigma_2, \dots, \sigma_N \text{ and a contraction } O_{\sigma'_N \sigma_N}. \end{aligned} \quad (44)$$

We represent tensors of rank N with colored shapes, where the legs attached to these shapes represent indices. When we combine the legs of different tensors, we perform tensor contractions, summing over the shared indices.

**LEFT CANONICAL MPS** — We start our decomposition by performing an SVD on the reshaped tensor  $\psi_{\sigma_1, (\sigma_2, \dots, \sigma_N)}$ , with dimensions  $(2 \times 2^{N-1})$ , obtaining the following

$$\psi_{\sigma_1, (\sigma_2, \dots, \sigma_N)} = \sum_{k_1} A_{\sigma_1, k_1} \Lambda_{k_1} V_{k_1, (\sigma_2, \dots, \sigma_N)}^\dagger. \quad (45)$$

We can define  $\psi_{(k_1, \sigma_2), (\sigma_3, \dots, \sigma_N)} \equiv \Lambda_{k_1} V_{k_1, (\sigma_2, \dots, \sigma_N)}^\dagger$ , this decomposition, in graphical notation, is represented as

$$\text{Diagram of } \psi_{\sigma_1, (\sigma_2, \dots, \sigma_N)} = \text{Diagram of } A_{\sigma_1, k_1} \Lambda_{k_1} V_{k_1, (\sigma_2, \dots, \sigma_N)}^\dagger = \text{Diagram of } A_{\sigma_1, k_1} \psi_{(k_1, \sigma_2), (\sigma_3, \dots, \sigma_N)}. \quad (46)$$

Following this, we apply the reshape and SVD procedure again to  $\psi_{(k_1, \sigma_2), (\sigma_3, \dots, \sigma_N)}$ , resulting in

$$\psi_{(k_1, \sigma_2), (\sigma_3, \dots, \sigma_N)} = \sum_{k_2} A_{(k_1, \sigma_2), k_2}^{[2]} \Lambda_{k_2} V_{k_2, (\sigma_3, \dots, \sigma_N)}^\dagger, \quad (47)$$

Continuing in this manner, the general step using graphical notation is depicted as follows

$$\dots \xrightarrow{k_{j-1}} \begin{array}{c} \triangleleft A \\ \sigma_j \end{array} \xrightarrow{k_j} \begin{array}{c} \text{---} \psi \text{---} \\ \sigma_{j+1} \dots \sigma_N \end{array} = \dots \xrightarrow{k_{j-1}} \begin{array}{c} \triangleleft A \\ \sigma_j \end{array} \xrightarrow{k_j} \begin{array}{c} \triangleleft A \\ \sigma_{j+1} \end{array} \xrightarrow{k_{j+1}} \begin{array}{c} \diamond \Lambda \\ \sigma_{j+2}, \dots, \sigma_N \end{array} \quad (48)$$

We finally obtain (without explicitly writing the sums over the virtual bond indices  $k_1, \dots, k_{N-1}$  to keep the notation simple) the following MPS

$$\psi_{\sigma_1, \dots, \sigma_N} = \begin{array}{c} \triangleleft A \\ \sigma_1 \end{array} \xrightarrow{k_1} \begin{array}{c} \triangleleft A \\ \sigma_2 \end{array} \xrightarrow{k_2} \dots \xrightarrow{k_{N-2}} \begin{array}{c} \triangleleft A \\ \sigma_{N-1} \end{array} \xrightarrow{k_{N-1}} \begin{array}{c} \triangleleft A \\ \sigma_N \end{array} = A_{\sigma_1}^{[1]} A_{\sigma_2}^{[2]} \dots A_{\sigma_{N-1}}^{[N-1]} A_{\sigma_N}^{[N]} \quad (49)$$

referred to as the left canonical form of the MPS. In fact, each  $A_{\sigma_j}^{[j]}$  is a left orthogonal tensor that

$$\sum_{k_{j-1}, \sigma_j} \left( A_{\sigma_j}^{[j]} \right)_{k_{j-1}, k_j} \left( \bar{A}_{\sigma_j}^{[j]} \right)_{k_{j-1}, k'_j} = \delta_{k_j, k'_j} \rightarrow \begin{array}{c} \triangleleft A \\ \triangleleft \bar{A} \end{array} = \left( \quad \right), \quad (50)$$

where  $\bar{A}$  is the complex conjugate of  $A$ .

**RIGHT CANONICAL MPS** — Analogously, we can start from the rightmost bond and proceed from right to left. We start by reshaping the wave function as  $\psi_{(\sigma_1, \dots, \sigma_{N-1}), \sigma_N}$ , then perform an SVD

$$\psi_{(\sigma_1, \dots, \sigma_{N-1}), \sigma_N} = \sum_{k_{N-1}} u_{(\sigma_1, \dots, \sigma_{N-1}), k_{N-1}} \Lambda_{k_{N-1}} B_{k_{N-1}, \sigma_N}^{[N]}, \quad (51)$$

in graphical notation

$$\begin{array}{c} \text{---} \psi \text{---} \\ \sigma_1 \sigma_2 \dots \sigma_N \end{array} = \begin{array}{c} \triangleleft U \\ \sigma_1, \dots, \sigma_{N-1} \end{array} \xrightarrow{k_{N-1}} \begin{array}{c} \diamond \Lambda \\ \sigma_N \end{array} \xrightarrow{k_{N-1}} \begin{array}{c} \triangleleft B \\ \sigma_N \end{array} = \begin{array}{c} \text{---} \psi \text{---} \\ \sigma_2 \sigma_3 \dots \sigma_N \end{array} \xrightarrow{k_{N-1}} \begin{array}{c} \triangleleft B \\ \sigma_N \end{array}. \quad (52)$$

Then sweeping up to the first bond

$$\begin{array}{c} \text{---} \psi \text{---} \\ \sigma_1 \sigma_2 \dots \sigma_{j-1} \end{array} \xrightarrow{k_j} \begin{array}{c} \triangleleft B \\ \sigma_j \end{array} \dots = \begin{array}{c} \triangleleft U \\ \sigma_1, \dots, \sigma_{j-2} \end{array} \xrightarrow{k_{j-1}} \begin{array}{c} \diamond \Lambda \\ \sigma_{j-1} \end{array} \xrightarrow{k_{j-1}} \begin{array}{c} \triangleleft B \\ \sigma_{j-1} \end{array} \xrightarrow{k_j} \begin{array}{c} \triangleleft B \\ \sigma_j \end{array} \dots \quad (53)$$

finally obtaining the right canonical form of the MPS

$$\psi_{\sigma_1, \dots, \sigma_N} = B_{\sigma_1}^{[1]} B_{\sigma_2}^{[2]} \dots B_{\sigma_{N-1}}^{[N-1]} B_{\sigma_N}^{[N]}, \quad (54)$$

again, we avoid explicitly writing the sums over the virtual bond indices  $k_1, \dots, k_{N-1}$  to keep the notation simple. We call this decomposition right canonical since each  $B_{\sigma_j}^{[j]}$  is a right orthogonal tensor.

**MIXED CANONICAL MPS** — With the MPS formalism it is easy to obtain the Schmidt decomposition between the subsystems  $[1, j]$  and  $[j+1, N]$  by mixing up the two canonical forms, that is

$$\begin{array}{c} \triangleleft A \\ \sigma_1 \end{array} \xrightarrow{k_1} \begin{array}{c} \triangleleft A \\ \sigma_2 \end{array} \xrightarrow{k_2} \dots \xrightarrow{k_j} \begin{array}{c} \triangleleft A \\ \sigma_j \end{array} \xrightarrow{k_j} \begin{array}{c} \diamond \Lambda \\ \sigma_{j+1} \end{array} \xrightarrow{k_j} \begin{array}{c} \triangleleft B \\ \sigma_{j+1} \end{array} \dots \xrightarrow{k_{N-2}} \begin{array}{c} \triangleleft B \\ \sigma_{N-1} \end{array} \xrightarrow{k_{N-1}} \begin{array}{c} \triangleleft B \\ \sigma_N \end{array} \quad (55)$$

where  $\Lambda^2$  is the entanglement spectrum of the partition. In fact, we have that

$$|\psi\rangle = \sum_{\{\sigma\}} A_{\sigma_1}^{[1]} \dots A_{\sigma_j}^{[j]} \Lambda B_{\sigma_{j+1}}^{[j+1]} \dots B_{\sigma_N}^{[N]} |\sigma_1 \dots \sigma_N\rangle \quad (56)$$

where we can identify the orthonormal basis

$$|\phi_{L,k_j}^{[1,j]}\rangle = A_{\sigma_1}^{[1]} \dots A_{\sigma_j}^{[j]} |\sigma_1, \dots, \sigma_j\rangle \quad (57)$$

$$|\phi_{R,k_{j+1}}^{[j+1,N]}\rangle = B_{\sigma_{j+1}}^{[j+1]} \dots B_{\sigma_N}^{[N]} |\sigma_{j+1}, \dots, \sigma_N\rangle. \quad (58)$$

such that

$$|\psi\rangle = \sum_{k_j} \Lambda_{k_j} |\phi_{L,k_j}^{[1,j]}\rangle |\phi_{R,k_{j+1}}^{[j+1,N]}\rangle. \quad (59)$$

The size of the virtual index  $k_j$  (in contrast to the physical index,  $\sigma_j$ ) called the bond dimension express the complexity of the MPS representation. Therefore, a low-rank approximation of the MPS in the mixed-canonical representation corresponds to a truncation of the entanglement spectrum (also said truncation of the bond dimension). Notice that, to preserve the normalization of the wave function, when truncating the singular values

$$\Lambda = (\lambda_1, \dots, \lambda_\chi) \rightarrow \tilde{\Lambda} = (\lambda_1, \dots, \lambda_{\tilde{\chi}}, 0, \dots, 0) \quad (60)$$

it is important to normalize  $\tilde{\Lambda}$ , that is

$$\tilde{\Lambda} \rightarrow \frac{\tilde{\Lambda}}{\sqrt{\sum_{j=1}^{\tilde{\chi}} \lambda_j^2}}. \quad (61)$$

**RELEVANT MPS** — Here we present some low-entangled states which admits an exact MPS representation

1. The most basic MPS is a product state, which has the smallest bond dimension  $\chi = 1$ . For an  $N$  qubit system, the most general expression of a product state is given by

$$A_{\sigma_j=0}^{[j]} = (\alpha), \quad A_{\sigma_j=1}^{[j]} = (\beta), \quad (62)$$

with  $\sqrt{|\alpha|^2 + |\beta|^2} = 1$  to ensure the normalization of the state. Therefore we have

$$|\psi\rangle = \sum_{\{\sigma\}} \prod_{j=1}^N \left( A_{\sigma_j}^{[j]} |\sigma_j\rangle \right) = \sum_{\{\sigma\}} \langle A | \langle A | \langle A | \langle A | \langle A | |\sigma_1, \dots, \sigma_N\rangle \quad (63)$$

2. In the field of quantum information theory, a Greenberger Horne Zeilinger (GHZ) state represents a unique type of entangled quantum state encompassing at least three qubits [17]. These states may exhibit highly non-classical properties; however, it turns out that for an arbitrary number of qubits, they admit a very simple MPS (and thus, in a sense, "classical") representation.

Indeed, the standard MPS of the GHZ state for  $n$  qubits is given as

$$|\text{GHZ}\rangle = \frac{1}{\sqrt{2}} \begin{pmatrix} 1 & 1 \end{pmatrix} \begin{pmatrix} |0\rangle & 0 \\ 0 & |1\rangle \end{pmatrix}^n \begin{pmatrix} 1 \\ 1 \end{pmatrix} \quad (64)$$

$$= \frac{1}{\sqrt{2}} (|00 \dots 0\rangle + |11 \dots 1\rangle) \quad (65)$$

which is an exact representation with bond dimension  $\chi = 2$ . Notice that we expressed the GHZ state as a product of state-valued matrices. This notation is useful for representing the three-legged tensors  $A_j^{\sigma_j}$ .

3. The  $W$  state is an entangled quantum state of three qubits, represented in bra-ket notation as follows:

$$|W\rangle = \frac{1}{\sqrt{3}} (|001\rangle + |010\rangle + |100\rangle)$$

This state is remarkable for representing a specific type of multipartite entanglement and appears in several applications in quantum information theory. Particles prepared in this state exhibit the properties described by Bell's theorem, which asserts that no classical theory of local hidden variables can reproduce the predictions of quantum mechanics.

The  $W$  state exemplifies one of the two classes of three-qubit states that cannot be separated into independent subsystems. The other class is exemplified by the 3-qubit GHZ state. These two states,  $|W\rangle$  and  $|\text{GHZ}\rangle$ , cannot be transformed into each other, even probabilistically, via LOCC (local operations and classical communication). Therefore, they represent fundamentally different types of tripartite entanglement.

The concept of the  $W$  state has been extended to  $n$  qubits, referring to a quantum superposition where each term has equal coefficients, and exactly one qubit is in the state  $|1\rangle$  while the rest are in the  $|0\rangle$  state; it can be easily written as an MPS

$$\begin{aligned} |W_n\rangle &= \frac{1}{\sqrt{n}} \begin{pmatrix} 0 & 1 \end{pmatrix} \begin{pmatrix} |0\rangle & 0 \\ |1\rangle & |0\rangle \end{pmatrix}^n \begin{pmatrix} 1 \\ 0 \end{pmatrix} \\ &= \frac{1}{\sqrt{n}} (|100\dots 0\rangle + |010\dots 0\rangle + |001\dots 0\rangle + \dots + |000\dots 1\rangle) \end{aligned} \quad (66)$$

We can now start to illustrate some standard algorithm to solve the quantum dynamics. In particular, we want to solve the Schroedinger equation to solve the unitary quantum dynamics.

#### 1.5.4 Time-Evolving Block Decimation (TEBD) Algorithm

In this section, we present a way of evolving quantum states in the MPS ansatz through the Lie-Trotter formula [18]. In particular, we will deal with nearest-neighbor Hamiltonians, that is

$$H = \sum_j h_{j,j+1}, \quad (67)$$

we can approximate the exact evolution operator

$$U(t) = e^{-iHt} \quad (68)$$

by splitting the nearest neighbor hamiltonian in two terms

$$H_{\text{even}} = \sum_{j \in \text{even}} h_{j,j+1}, \quad H_{\text{odd}} = \sum_{j \in \text{odd}} h_{j,j+1}, \quad (69)$$

now, we can use the Baker–Campbell–Hausdorff (BCH) formula in order to approximate

$$\begin{aligned} U(dt) &\approx e^{-iH_{\text{even}}dt} e^{-iH_{\text{odd}}dt} e^{-i[H_{\text{even}}, H_{\text{odd}}]dt^2} \\ &\approx e^{-iH_{\text{even}}dt} e^{-iH_{\text{odd}}dt} + O(dt^2). \end{aligned} \quad (70)$$

We therefore have the following approximate evolution up to time  $t = kdt$

$$|\psi(kdt)\rangle \approx \prod_{j=1}^k e^{-iH_{\text{Even}} dt} e^{-iH_{\text{Odd}} dt} |\psi(0)\rangle. \quad (71)$$

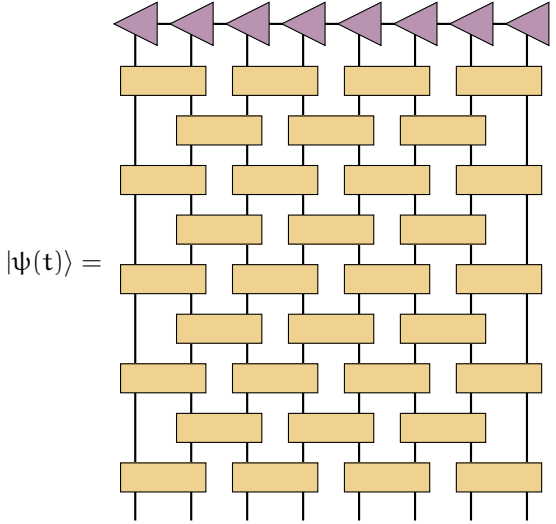
*First order Trotter decomposition*

We can now present the Time-Evolving Block Decimation (TEBD) method, whose fundamental block is the following two-site unitary gate

$$\begin{aligned} \mathcal{U}_{j,j+1}(dt) &= e^{ih_{j,j+1} dt} \\ &= \sum_{\substack{\sigma_j, \sigma'_j \\ \sigma_{j+1}, \sigma'_{j+1}}} \langle \sigma'_j, \sigma'_j + 1 | e^{ih_{j,j+1} dt} | \sigma_j, \sigma_j + 1 \rangle | \sigma'_j, \sigma'_j + 1 \rangle \langle \sigma_j, \sigma_j + 1 | \\ &= \sum_{\substack{\sigma_j, \sigma'_j \\ \sigma_{j+1}, \sigma'_{j+1}}} \mathcal{U}_{\sigma'_j, \sigma'_j + 1}^{\sigma_j, \sigma_j + 1} | \sigma'_j, \sigma'_j + 1 \rangle \langle \sigma_j, \sigma_j + 1 | \\ &= \sum_{\substack{\sigma_j, \sigma'_j \\ \sigma_{j+1}, \sigma'_{j+1}}} \begin{array}{c} \sigma'_j \quad \sigma'_{j+1} \\ \boxed{\phantom{\text{TEBD brick wall}}} \\ \sigma_j \quad \sigma_{j+1} \end{array} | \sigma'_j, \sigma'_j + 1 \rangle \langle \sigma_j, \sigma_j + 1 |. \end{aligned} \quad (72)$$

In graphical notation, in order to evolve the quantum state we have to contract the following network

*TEBD brick wall circuit*



$$|\psi(t)\rangle = \text{[Diagram of TEBD brick wall circuit]}, \quad (73)$$

which is a brick-wall quantum circuit contracted to an MPS.

First, let us express the wavefunction in the following local two-sites mixed canonical form

$$|\psi\rangle = \sum_{\substack{\sigma_j, \sigma_{j+1} \\ k_{j-1}, k_{j+1}}} \Theta_{k_j, k_{j+1}}^{\sigma_j, \sigma_{j+1}} |\phi_{L, k_{j-1}}^{[1, j-1]}\rangle |\sigma_j, \sigma_{j+1}\rangle |\phi_{R, k_j}^{[j+2, N]}\rangle \quad (74)$$

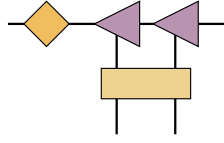
It is straightforward to obtain  $\Theta$  from the Schmidt decomposition. Since

$$\begin{aligned} |\psi\rangle &= \sum_{k_j} \Lambda_{k_{j-1}} |\phi_{L, k_{j-1}}^{[1, j-1]}\rangle |\phi_{R, k_{j+1}}^{[j, N]}\rangle \\ &= \sum_{k_j} \Lambda_{k_{j-1}} B_{\sigma_j}^{[j]} B_{\sigma_{j+1}}^{[j+1]} |\phi_{L, k_j}^{[1, j-1]}\rangle |\sigma_j, \sigma_{j+1}\rangle |\phi_{R, k_j}^{[j+2, N]}\rangle \end{aligned}$$

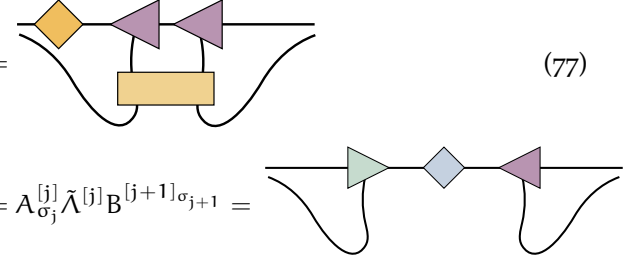
therefore we have

$$\Theta_{k_j, k_{j+1}}^{\sigma_j, \sigma_{j+1}} = \Lambda_{k_{j-1}} B_{\sigma_j}^{[j]} B_{\sigma_{j+1}}^{[j+1]} = \text{[Diagram of MPS contraction: a yellow diamond connected to two purple triangles]} \quad (75)$$

It is now easy to apply the two-site unitary gate  $U_{j,j+1}(dt)$  which transforms

$$\tilde{\Theta}_{k_j, k_{j+1}}^{\sigma_j, \sigma_{j+1}} = \sum_{\sigma'_j, \sigma'_{j+1}} U_{\sigma'_j, \sigma'_{j+1}}^{\sigma_j, \sigma_{j+1}} \Theta_{k_j, k_{j+1}}^{\sigma'_j, \sigma'_{j+1}} = \text{Diagram} \quad (76)$$


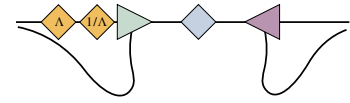
we can now reshape the tensor and perform an SVD

$$\begin{aligned} \tilde{\Theta}_{(\sigma_j, k_j), (\sigma_{j+1}, k_{j+1})} &= \text{Diagram} \\ &= \Lambda_{\sigma_j}^{[j]} \tilde{\Lambda}^{[j]} B^{[j+1]}_{\sigma_{j+1}} = \text{Diagram} \end{aligned} \quad (77)$$


Notice that the new wavefunction  $|\tilde{\psi}\rangle$  is in a mixed canonical form

$$\begin{aligned} |\tilde{\psi}\rangle &= \sum_{\substack{\sigma_j, \sigma_{j+1} \\ k_{j-1}, k_{j+1}}} \tilde{\Lambda}_{\sigma_j}^{[j]} \tilde{\Lambda}_{\sigma_{j+1}}^{[j+1]} |\phi_{L, k_{j-1}}^{[1, j-1]}\rangle |\sigma_j, \sigma_{j+1}\rangle |\phi_{R, k_j}^{[j+2, N]}\rangle \\ &= \sum_{k_j} \tilde{\Lambda}_{k_j} |\phi_{L, k_j}^{[1, j]}\rangle |\phi_{R, k_j}^{[j+1, N]}\rangle \end{aligned} \quad (78)$$

which means that we can perform a low-rank approximation of  $|\tilde{\psi}\rangle$  by truncating the SVD in  $\tilde{\Lambda}$ . In order to get back the initial canonical form one has to multiply  $\Lambda^{[j]}$  by  $\Lambda_{k_{j-1}}^{-1}$

$$|\tilde{\psi}\rangle = \sum_{\substack{\sigma_j, \sigma_{j+1} \\ k_{j-1}, k_{j+1}}} \text{Diagram} |\phi_{L, k_{j-1}}^{[1, j-1]}\rangle |\sigma_j, \sigma_{j+1}\rangle |\phi_{R, k_j}^{[j+2, N]}\rangle \quad (79)$$


therefore we have that

$$\tilde{B}_{\sigma_j}^{[j]} = \Lambda_{k_{j-1}}^{-1} \tilde{\Lambda}_{\sigma_j}^{[j]} \tilde{\Lambda}_{k_j} \quad (80)$$

**ERRORS** — The TEBD algorithm experiences two types of errors, both of which are manageable and can be estimated with relative ease. The first error is associated with the time step and is of order  $O(\delta^2)$  per time step for first-order TEBD and  $O(\delta^3)$  for second-order TEBD. When the total time interval  $T$  is divided into  $N = T/\delta$  steps, the cumulative error over the entire interval becomes  $O(\delta)$  and  $O(\delta^2)$  for first-order and second-order TEBD, respectively. This inherent time-step error does not compromise the unitarity of real-time evolution, as each operator  $e^{-i\delta H_\alpha}$  is unitary. However, if the time-step error is significant, it may lead to variations in conserved quantities such as energy. To mitigate this discretization error, one can opt for a smaller time-step size  $\delta$  or utilize a higher-order decomposition like TEBD4. The second error is the truncation error which arises from approximating the quantum state of a many-body system using MPS with limited bond dimensions. As the system evolves, the bond dimensions of the matrices grow, increasing computational demands. To maintain efficiency, TEBD truncates these matrices by performing the usual SVD and retaining only the most significant singular values.

## 1.5.5 Matrix Product Operators (MPO)

Matrix Product Operators basically constitute the operator analogue of MPS. Any linear operator  $O$  in the Hilbert space of  $N$  qubits is an object that maps  $\mathcal{H} \rightarrow \mathcal{H}$  therefore belongs to the tensor product  $\mathcal{H}^* \otimes \mathcal{H}$ , that is,

$$O = \sum_{\{\sigma\}, \{\sigma'\}} O_{\sigma_1, \dots, \sigma_N}^{\sigma'_1, \dots, \sigma'_N} |\sigma'_1, \dots, \sigma'_N\rangle \langle \sigma_1, \dots, \sigma_N|. \quad (81)$$

in graphical notation we have

$$O = \sum_{\{\sigma\}, \{\sigma'\}} \begin{array}{c} \sigma'_1 \quad \dots \quad \sigma'_N \\ \boxed{O} \\ \sigma_1 \quad \dots \quad \sigma_N \end{array} |\sigma'_1, \dots, \sigma'_N\rangle \langle \sigma_1, \dots, \sigma_N|. \quad (82)$$

It is apparent that by fusing the indices  $(\sigma_j, \sigma'_j)$  we can apply the same tensor decomposition of the MPS in order to obtain

$$O_{\sigma_1, \dots, \sigma_N}^{\sigma'_1, \dots, \sigma'_N} = \sum_{k_1, \dots, k_{N-1}} = O^{[1]}_{k_1}^{\sigma_1 \sigma'_1} O^{[2]}_{k_2 k_3}^{\sigma_2 \sigma'_2} \dots O^{[N]}_{k_{N-1}}^{\sigma_N \sigma'_N} \quad (83)$$

where we explicitly wrote the contraction on the virtual bonds  $k_j$ , resulting, in graphical notation, in

$$O_{\sigma_1, \dots, \sigma_N}^{\sigma'_1, \dots, \sigma'_N} = \sum_{\{\sigma\}, \{\sigma'\}} \begin{array}{c} \sigma'_1 \\ \boxed{O_1} \\ \sigma_1 \end{array} \begin{array}{c} \sigma'_2 \\ \boxed{O_2} \\ \sigma_2 \end{array} \dots \begin{array}{c} \sigma'_N \\ \boxed{O_N} \\ \sigma_N \end{array} |\sigma'_1, \dots, \sigma'_N\rangle \langle \sigma_1, \dots, \sigma_N|. \quad (84)$$

where we reshuffled back each fused index, so that  $O_j^{\sigma_j \sigma'_j}$  are matrices like the  $A_j^{\sigma_j}$  entering in the MPS, with the key distinction staying in the fact that, as representations of operators, they require both outgoing and incoming physical indices. Notice that, in general, a systematic procedure based on iterative SVD from a many-body representation of the operator itself requires an exponentially large amount of resources and is unlikely to be feasible in practical scenarios.

Conversely, there are instances where an MPO representation of an operator can be constructed operationally. First of all, let us examine the analogous of a product state. In the realm of the operators they are tensor product of local operators, which have the straightforward representation

$$O_{\sigma_1, \dots, \sigma_N}^{\sigma'_1, \dots, \sigma'_N} = \sum_{\{\sigma\}, \{\sigma'\}} \begin{array}{c} \sigma'_1 \\ \boxed{O_1} \\ \sigma_1 \end{array} \begin{array}{c} \sigma'_2 \\ \boxed{O_2} \\ \sigma_2 \end{array} \dots \begin{array}{c} \sigma'_N \\ \boxed{O_N} \\ \sigma_N \end{array} |\sigma'_1, \dots, \sigma'_N\rangle \langle \sigma_1, \dots, \sigma_N|. \quad (85)$$

with local bond dimension equal to one. As a further example, an highly non-local operator whose MPO representation can be written straightforwardly is the projector to a MPS state

$$|\psi\rangle \langle \psi| = \sum_{\{\sigma\}, \{\sigma'\}} \begin{array}{c} \text{---} \triangleleft \triangleleft \triangleleft \triangleleft \diamond \triangleright \triangleright \triangleright \text{---} \\ \text{---} \triangleleft \triangleleft \triangleleft \triangleleft \diamond \triangleright \triangleright \triangleright \text{---} \end{array} |\sigma'_1, \dots, \sigma'_N\rangle \langle \sigma_1, \dots, \sigma_N|. \quad (86)$$

where now by fusing the two auxiliary spaces, we can identify the local MPO matrices  $O_j^{\sigma_j \sigma'_j} = A_j^{\sigma_j} \otimes (A_j^*)^{\sigma'_j}$  ( and  $O_j^{\sigma_j \sigma'_j} = B_j^{\sigma_j} \otimes (B_j^*)^{\sigma'_j}$  ) with bond dimension given by the square of the MPS bond dimension.

MPO representation

MPO projector on  
MPS

MULTIPLY MPO TO MPO OR MPS — Suppose that we have the following MPS and MPO:

$$\begin{aligned}
 |\psi\rangle &= \begin{array}{c} \triangleleft A \triangleleft A \triangleleft A \triangleleft A \triangleleft A \triangleleft A \triangleleft A \triangleleft A \\ | \sigma_1 \dots \sigma_N \rangle \end{array} \\
 O &= \begin{array}{c} \square W \square W \square W \square W \square W \square W \square W \square W \\ | \sigma_1 \dots \sigma_N \rangle \langle \sigma'_1 \dots \sigma'_N | \end{array}
 \end{aligned} \tag{87}$$

with  $\dim(A_j^{\sigma_j}) = \chi_{j-1} \times \chi_j$  and  $\dim(W_j^{\sigma_j \sigma'_j}) = D_{j-1} \times D_j$ , and where we use the implicit summation convention for repeated indices. Applying the operator  $O$  to the state  $|\psi\rangle$  actually results in the following contraction

$$O|\psi\rangle = \begin{array}{c} \triangleleft A \triangleleft A \triangleleft A \triangleleft A \triangleleft A \triangleleft A \triangleleft A \triangleleft A \\ \square W \square W \square W \square W \square W \square W \square W \square W \\ | \sigma_1 \dots \sigma_N \rangle \end{array} \tag{88}$$

which is a new MPS state with matrices  $M_j^{\sigma_j}$

$$\begin{array}{c} \triangleleft A \triangleleft \\ \square W \square \end{array} = \begin{array}{c} \circ M \circ \\ \square \end{array} \tag{89}$$

whose auxiliary dimensions are  $\dim(M_j^{\sigma_j}) = D_{j-1}\chi_{j-1} \times D_j\chi_j$ . Notice that, a very similar procedure applies for the contraction of two operators  $O$  and  $V$  both having an MPO representation:

$$OO' = \begin{array}{c} \square W \square W \square W \square W \square W \square W \square W \square W \\ \square W' \square W' \square W' \square W' \square W' \square W' \square W' \square W' \\ | \sigma_1 \dots \sigma_N \rangle \langle \sigma'_1 \dots \sigma'_N | \end{array}$$

where the order of the physical indices contraction is relevant since in general  $[O, O'] \neq 0$ .

RELEVANT FINITE-DIMENSIONAL MPO — Constructing an exact compact MPO representation for certain physically relevant operators might initially seem daunting. However, analogously to the case of low-entangled states that admit an exact MPS representation, whenever "local" operators are involved (such as Hamiltonians with short-range interactions), an exact finite-dimensional MPO representation exists. Similarly to what we already did for MPS, we can rearrange a matrix product operator in terms of operator-value matrices, as follows

$$O = \begin{array}{c} \square W \square W \square W \square W \square W \square W \square W \square W \\ \square W \square \end{array} = \sum_{\sigma_j \sigma'_j} O^{\sigma_j \sigma'_j} |\sigma_j\rangle \langle \sigma'_j| \tag{90}$$



This representation is very useful to understand how to systematically construct exact MPO of relevant operators. In fact when considering the addition of two operators,  $O$  and  $O'$ , with both MPO representations, the resulting MPO is formed by the direct sum of the local operator-value matrices for all sites  $1 < j < n$ , with the exception of the boundary sites where we add row and column vectors. Essentially, we get

$$\begin{aligned}
 O + O' &= \begin{array}{c} \begin{array}{cccccccc} \boxed{W} & \boxed{W} & \boxed{W} & \boxed{W} & \boxed{W} & \boxed{W} & \boxed{W} & \boxed{W} \\ | & | & | & | & | & | & | & | \\ \hline \boxed{W'} & \boxed{W'} & \boxed{W'} & \boxed{W'} & \boxed{W'} & \boxed{W'} & \boxed{W'} & \boxed{W'} \\ | & | & | & | & | & | & | & | \end{array} \\ + \\ \begin{array}{c} \begin{array}{cccccccc} \boxed{W} & \boxed{W} & \boxed{W} & \boxed{W} & \boxed{W} & \boxed{W} & \boxed{W} & \boxed{W} \\ | & | & | & | & | & | & | & | \\ \hline \boxed{W'} & \boxed{W'} & \boxed{W'} & \boxed{W'} & \boxed{W'} & \boxed{W'} & \boxed{W'} & \boxed{W'} \\ | & | & | & | & | & | & | & | \end{array} \end{array} \\ = \\ \begin{array}{c} \begin{array}{cccc} \boxed{\begin{array}{cc} W & \\ \hline & W' \end{array}} & \boxed{\begin{array}{cc} W & \\ \hline & W' \end{array}} & \dots & \boxed{\begin{array}{cc} W & \\ \hline & W' \end{array}} \\ | & | & & | \end{array} \end{array} \quad |\sigma_1 \dots \sigma_N\rangle \langle \sigma'_1 \dots \sigma'_N|
 \end{aligned} \tag{91}$$

where basically we are using block diagonal matrices to take into account the independent effects of both operators. However, for *local* operators, the previous representation is sub-optimal, and we can systematically construct much better representations.

In the following, we present a list of example of operators which admit an exact MPO representation.

1. Let us start from a simplest example of a local Hamiltonian acting on  $n$  qubits

*Local Hamiltonian*

$$H = \sum_{j=1}^n h_j Z_j \tag{92}$$

This compact form of Hamiltonian can be written in a more general tensor product notation,

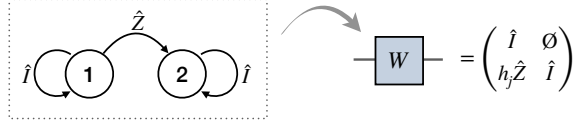
$$H = \sum_{j=1}^n I_1 \otimes \dots \otimes I_{j-1} \otimes h_j Z_j \otimes I_{j+1} \otimes \dots \otimes I_n \tag{93}$$

In this notation, it is evident that the size of the matrix corresponding to the operator  $H$  is  $d^n \times d^n$ , where each term in the sum is an exact product operator, i.e., an MPO with auxiliary dimension equal to one. Clearly, a suitable MPO representation of the Hamiltonian (92) requires an auxiliary space with dimension  $D > 1$ . The question then becomes: what is the minimal extra resource needed to store all the information in a suitable operator-valued matrix product form  $O_1 O_2 \dots O_n$ .

If we temporarily set aside the boundary vectors  $O_1$  and  $O_n$  and focus on the bulk matrices, we can ask ourselves what these matrices need to accomplish and remember:

- Insert the identity operator regardless of the lattice site.
- Insert the operator  $Z$  and remember having done so.
- After the previous step, insert only the identity operator.

Actually, we can accomplish, and visualise the effect of the operator-value matrices, via the following *auxiliary-state diagram*



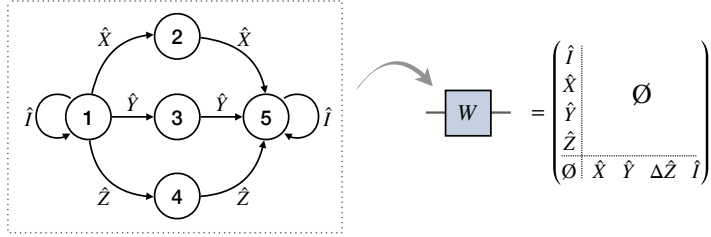
Finally, the boundary vectors can be easily obtained from the bulk matrix, by just picking up the last row and the first column, namely having  $O_1 = \begin{pmatrix} h_1 Z & 1 \end{pmatrix}$  and  $(O_n)^t = \begin{pmatrix} 1 & h_n Z \end{pmatrix}$ .

XXZ model MPO

- Let us consider now an interacting Hamiltonian like the Heisenberg one with anisotropy (i.e. the XXZ Hamiltonian)

$$H = \sum_{j=1}^{n-1} X_j X_{j+1} + Y_j Y_{j+1} + \Delta Z_j Z_{j+1}, \quad (94)$$

where for simplicity we are considering the anisotropy  $\Delta$  uniform along the chain. To find the MPO representation, let's focus on a generic neighboring interaction term  $\sum_j S_j S_{j+1}$ . Practically, as before, we need to insert the identity operator. Then, if the bulk matrix inserts the operator  $S$ , immediately after we have to insert the same operator again. After this step, we complete the operator chain with the identity. This needs to be done for each of the interaction terms. Using the auxiliary-state diagram, we get



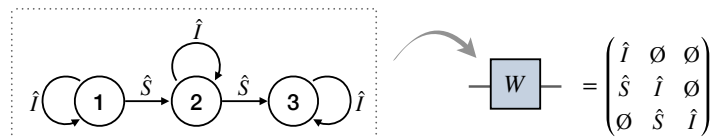
and similar considerations as before applies for the boundary vectors.

Long-range  
Hamiltonian MPO

- Next, we want to address arbitrary long-range interacting Hamiltonian. Let us start with the preliminary example of a fully connected spin system, such that

$$H = \sum_{j>i}^n S_i S_j, \quad (95)$$

and  $S$  here stays for a generic local operator. A generic operator entering in that sum can be written explicitly as  $\dots I \otimes I \otimes S \otimes I^{|j-i|} \otimes S \otimes I \otimes I \dots$  for any possible distance  $|j-i| \in \{1, \dots, n-1\}$ . The only difference between a simple neighboring site interaction  $S_j S_{j+1}$  is that, after inserting the operator  $S$  at any lattice site  $j$ , our MPO must allow for the insertion of an arbitrary number of identity operators until the second insertion of the operator  $S$  occurs. Thereafter, we complete our chain with the remaining identities. In terms of auxiliary-state diagram this reads



Now it is clear that, if we have exponentially decaying interactions such that

$$H = \sum_{j>i}^n e^{-|j-i|/\xi} S_i S_j = \sum_{j>i}^n \lambda^{|j-i|} S_i S_j \quad (96)$$

with  $\lambda \equiv \exp(-1/\xi)$ , we can slightly modify the state diagram of the fully connected Hamiltonian by introducing an additional numerical coefficient  $\lambda$  for each identity operator inserted by the auxiliary state 2, and another  $\lambda$  when transitioning from state 2 to state 3. This modification leads to the intriguing result that exponentially decaying interactions can be exactly encoded into an MPO with an auxiliary dimension of  $D = 3$ :

$$O_j = \begin{pmatrix} I & \emptyset & \emptyset \\ S & \lambda I & \emptyset \\ \emptyset & \lambda S & I \end{pmatrix}. \quad (97)$$

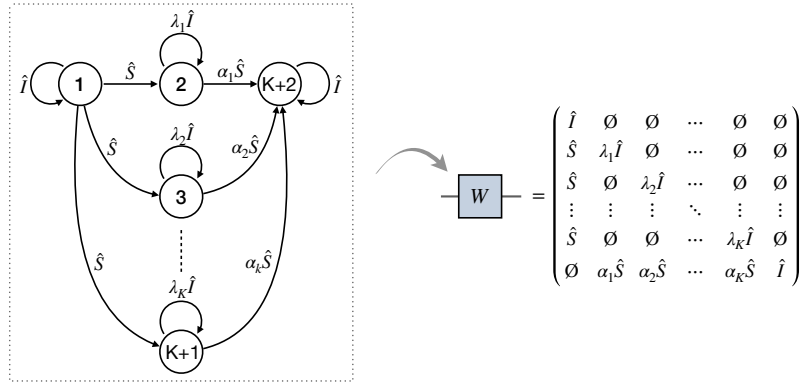
This results is extremely useful, because it allows to efficiently represent generic interacting Hamiltonians on a finite chain

$$H = \sum_{j>i}^n J(j-i-1) S_i S_j. \quad (98)$$

In fact, once we approximate the interactions as a sum of  $K$  different exponential  $J(r) \simeq \sum_{k=1}^K \alpha_k \lambda_k^r$ , we can rewrite the generic Hamiltonian as

$$H = \sum_{k=1}^K \sum_{j>i}^n \alpha_k \lambda_k^{j-i-1} S_i S_j, \quad (99)$$

and using the previous argument we can easily draw the following auxiliary-state diagram

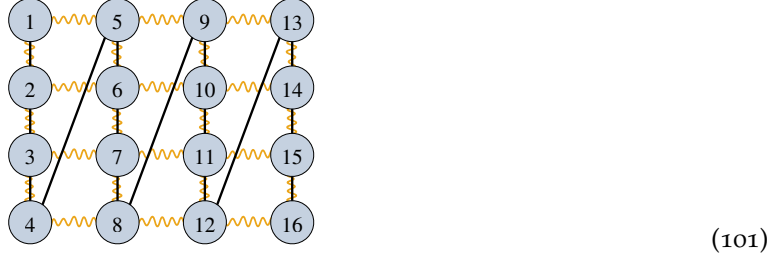


which results in a MPO with auxiliary dimension  $D = 2 + K$ .

4. In conclusion, it is worth mentioning that the sites of a 2D system can be reordered into a 1D snake-like structure to apply MPS techniques for simulating 2D systems. Let us consider the following classical Ising hamiltonian on a square  $N = L \times L$  lattice

$$H = - \sum_{\langle i,j \rangle} Z_i Z_j \longrightarrow H = - \sum_{i,j} J_{ij} Z_i Z_j. \quad (100)$$

where  $J_{ij} = 1$  if the sites are neighbors in the 2D lattice. As an example for the following snake



we will have that

$$\begin{cases} J_{j,j+1} = 1 & \text{if } j \bmod L \neq 0 \\ J_{j,j+L} = 1 \end{cases} \quad (102)$$

resulting in a MPO with auxiliary dimension  $D = 2 + L$ .

### 1.5.6 Time-Dependent Variational (TDVP) Principle Algorithm

The time-dependent variational principle (TDVP) gives an alternative to the Lie-Trotter formula for the approximation of the time evolution of wave functions. First of all, let us consider the general Schroedinger equation

$$i\dot{\psi}(t) = H\psi(t), \quad (103)$$

where  $\psi(t)$  is the wave function in the Hilbert space  $\mathcal{H}$ . Suppose  $\mathcal{M}$  is a submanifold within the Hilbert space  $\mathcal{H}$ , where we aim to find an approximate solution  $u(t)$  given that

$$\psi(0) = u(0) \in \mathcal{M}. \quad (104)$$

The Dirac-Frenkel variational principle seeks a variational solution  $u(t)$  in the tangent space  $\mathcal{T}_{u(t)}\mathcal{M}$  by imposing

$$\langle v | i\partial_t - H | u(t) \rangle = 0 \quad \forall v \in \mathcal{T}_{u(t)}\mathcal{M}, \quad (105)$$

with  $\dot{u}(t)$  lying in the tangent space. Equivalently, one may rephrase the orthogonality condition in terms of the orthogonal projection  $P_{u(t)} : \mathcal{H} \rightarrow \mathcal{T}_{u(t)}\mathcal{M}$  to the tangent space at  $u(t)$  and state the Dirac-Frenkel principle as the non-linear evolution equation

$$i\dot{u}(t) = P_{u(t)} H u(t), \quad (106)$$

in which we project back  $Hu(t)$  into the tangent space.

Let us now apply this formalism to variational manifolds constructed using the MPS ansatz. The idea is to construct the MPS manifold  $\mathcal{M}_{\text{MPS}}$  such that we can write the variational principle for the wave function

$$|\psi(M)\rangle = M_{\sigma_1}^{[1]} \dots M_{\sigma_N}^{[N]} |\sigma_1 \dots \sigma_N\rangle, \quad (107)$$

by projecting in the tangent space the Schroedinger equation

$$\frac{d}{dt} |\psi(M)\rangle = -i P_{|\psi(M)\rangle} H |\psi(M)\rangle. \quad (108)$$

We refer to [19, 20] for the construction of tangent space to  $|\psi(M)\rangle$ . The tangent space projector can be decomposed as

$$P_{|\psi(M)\rangle} = \sum_{n=1}^N P_L^{[1:(n-1)]} \otimes \mathbb{I}_n \otimes P_R^{[(n+1):N]} - \sum_{n=1}^{N-1} P_L^{[1:n]} \otimes P_R^{[(n+1):N]}, \quad (109)$$

where

$$P_L^{[1:n]} = \sum_{\alpha} \left| \phi_{L,\alpha}^{[1:n]} \right\rangle \left\langle \phi_{L,\alpha}^{[1:n]} \right|, \quad \left| \phi_{L,\alpha}^{[1:n]} \right\rangle = A_{\sigma_1}^{[1]} \dots A_{\sigma_n}^{[n]} |\sigma_1 \dots \sigma_n\rangle, \quad (110)$$

$$P_R^{[n:N]} = \sum_{\beta} \left| \phi_{L,\beta}^{[n:N]} \right\rangle \left\langle \phi_{L,\beta}^{[n:N]} \right|, \quad \left| \phi_{L,\beta}^{[n:N]} \right\rangle = B_{\sigma_n}^{[n]} \dots B_{\sigma_N}^{[N]} |\sigma_n \dots \sigma_N\rangle. \quad (111)$$

We can represent the projector using graphical notation as

$$P_{|\psi(M)\rangle} = \sum_{n=1}^N \left( \text{Diagram 1} \right) - \sum_{n=1}^{N-1} \left( \text{Diagram 2} \right) \quad (112)$$

If  $M_{\sigma_n}^{[n]}$  is the one-site center tensor, then  $\left| \phi_{L,\alpha}^{[1,n-1]} \right\rangle$  and  $\left| \phi_{R,\beta}^{[n+1,N]} \right\rangle$  are the orthonormal basis of the left and right block of the lattice respectively. Such that

$$|\psi\rangle = \sum_{\alpha,\beta} M_{\sigma_n}^{[n]} \left| \phi_{L,\alpha}^{[1,n-1]} \right\rangle |\sigma_n\rangle \left| \phi_{R,\beta}^{[n+1,N]} \right\rangle, \quad (113)$$

we can move the orthogonality center from the site  $n$  with an SVD we can write  $M_{\sigma_n}^{[n]} = A_{\sigma_n}^{[n]} \Lambda^{[n+1]} = \Lambda^{[n]} B_{\sigma_n}^{[n]}$ , where we denoted  $\Lambda^{[n]} = \Lambda_{k_n}$  in fact

$$k_n \text{---} M \text{---} k_{n+1} = \frac{k_n}{\sigma_n} \text{---} A \text{---} k_{n+1} \text{---} \Lambda \text{---} k_{n+1} = k_n \text{---} \Lambda \text{---} k_n \text{---} B \text{---} \frac{k_{n+1}}{\sigma_n} \quad (114)$$

by contracting  $\Lambda^{[n]}$  ( $\Lambda^{[n+1]}$ ) with  $A^{[n-1]}$  ( $B^{[n+1]}$ ) we shift the center by one site to the left (right).

By projecting the MPS from Eq. (113), we obtain the following expression, where the Hamiltonian is represented in its MPO form

$$\begin{aligned} \frac{d}{dt} |\psi(t)\rangle &= -i \sum_{n=1}^N P_L^{[1:(n-1)]} \otimes \mathbb{I}_n \otimes P_R^{[(n+1):N]} H |\psi\rangle \\ &\quad + i \sum_{n=1}^{N-1} P_L^{[1:n]} \otimes P_R^{[(n+1):N]} H |\psi\rangle \end{aligned} \quad (115)$$

It is not possible to solve the equation in a single step; instead, we need to solve  $N$  sequentially forward-evolving equations simultaneously

$$\frac{d}{dt} |\psi\rangle = -i P_L^{[1:(n-1)]} \otimes \mathbb{I}_n \otimes P_R^{[(n+1):N]} H |\psi\rangle, \quad (116)$$

with the corresponding  $N-1$  backward-evolving equations

$$\frac{d}{dt} |\psi\rangle = -i P_L^{[1:(n)]} \otimes P_R^{[(n+1):N]} H |\psi\rangle. \quad (117)$$

Next, to derive the evolution of the one-site center tensors  $M_{\sigma_n}^{[n]}$ , we project these single-site Schrödinger equations by multiplying with the orthonormal bases  $\left\langle \phi_{L,\alpha}^{[1:(n-1)]} \right| \left\langle \phi_{R,\beta}^{[(n+1):N]} \right|$ , that is

$$\frac{d}{dt} M_{\sigma_n}^{[n]} = -i H_{\text{eff}} M_{\sigma_n}^{[n]} \longrightarrow M_{\sigma_n}^{[n]}(t + dt) = e^{-i H_{\text{eff}} dt} M_{\sigma_n}^{[n]}(t), \quad (118)$$

where we have that

$$H_{\text{eff}} M_{\sigma_n}^{[n]} = \quad (119)$$

and, analogously for the singular values

$$\frac{d}{dt} \Lambda^{[n+1]} = +iK_{\text{eff}} \Lambda^{[n+1]} \longrightarrow \Lambda^{[n+1]}(t + dt) = e^{iK_{\text{eff}} dt} \Lambda^{[n+1]}(t), \quad (120)$$

where again in graphical notation

$$K_{\text{eff}} \Lambda^{[n+1]} = \quad (121)$$

Notice that, in order to solve the time-dependent Schroedinger equation it is sufficient to know the action of  $H_{\text{eff}}$  and  $K_{\text{eff}}$  on the state to exponentiate the operator with Krylov subspace techniques such as Lanczos or Davidson methods. We call this method the 1-TDVP in which no truncation of the bond dimension has to occur after the projection of the Hamiltonian into the MPS manifold. This implies that the norm of the state and the energy of the system are exactly conserved.

An easy extension of this single-site algorithm, known as 2-TDVP, involves projecting onto the local tensor  $M_{(n,n+1)} = M_{\sigma_n}^{[n]} M_{\sigma_{n+1}}^{[n+1]}$  after the evolution step. Following this,  $M_{(n,n+1)}$  must be truncated, which results in the MPS no longer staying in the tangent manifold. As a consequence, the norm and the average of  $H$  are not preserved. However, this approach allows for the bond dimension to be adjusted during the evolution process.

Here, we outline the 2-TDVP algorithm. The projected Schrödinger equation is the following

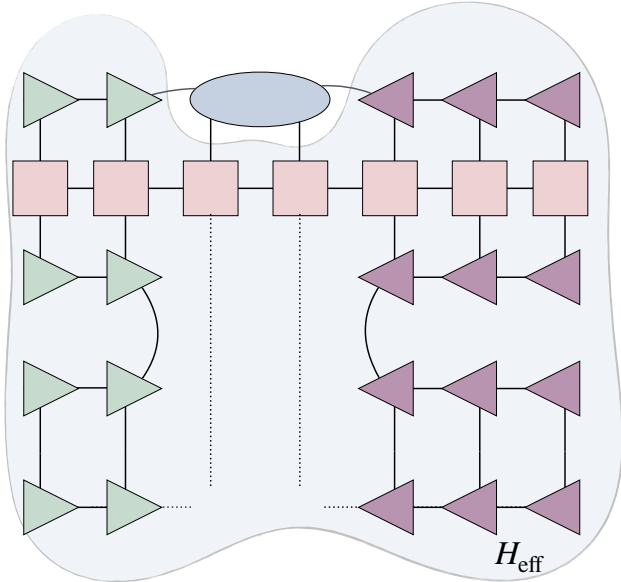
$$\begin{aligned} \frac{d}{dt} |\psi(t)\rangle = & -i \sum_{n=1}^N P_L^{[1:(n-1)]} \otimes \mathbb{I}_n \otimes \mathbb{I}_{n+1} \otimes P_R^{[(n+2):N]} H |\psi\rangle \\ & + i \sum_{n=1}^{N-1} P_L^{[1:(n-1)]} \otimes \mathbb{I}_n \otimes P_R^{[(n+1):N]} H |\psi\rangle \end{aligned} \quad (122)$$

which implies the solution of the following forward and backward equations

$$\frac{d}{dt} (M_{\sigma_n}^{[n]} M_{\sigma_{n+1}}^{[n+1]}) = -i H_{\text{eff}} (M_{\sigma_n}^{[n]} M_{\sigma_{n+1}}^{[n+1]}), \quad (123)$$

$$\frac{d}{dt} (M_{\sigma_{n+1}}^{[n+1]}) = +i K_{\text{eff}} (M_{\sigma_{n+1}}^{[n+1]}). \quad (124)$$

In graphical notation, the forward evolution reads



$H_{\text{eff}}$

(125)

Then, the two-site evolved tensor needs to be truncated

$$(M_{\sigma_n}^{[n]} M_{\sigma_{n+1}}^{[n+1]})(t) = A_{\sigma_n}^{[n]} (\Lambda^{[n+1]} V_{\sigma_n}^{[n+1]}) = A_{\sigma_n}^{[n]} M_{\sigma_n}^{[n+1]}. \quad (126)$$

Subsequently, the backward evolution evolves the new  $M_{\sigma_{n+1}}^{[n+1]}$  with

$$K_{\text{eff}} M_{\sigma_{n+1}}^{[n+1]} = \text{Diagram} \quad (127)$$

We stress again that to solve the Schrödinger equation, it is enough to know how  $H_{\text{meff}}$  and  $K_{\text{eff}}$  acts on the state in order to exponentiate the operator using Krylov subspace techniques.

**ERROR** — The TDVP algorithm encounters four main types of errors. The first is the projection error, which arises from projecting the full time-dependent Schrödinger equation onto the MPS manifold with fixed bond dimension. This error is minimized when the bond dimension is large and is exactly zero for maximal bond dimensions. It does not violate energy conservation or alter the norm of the state during evolution. The second error is the finite time-step error, which occurs because the algorithm sequentially solves coupled time-dependent Schrödinger equations for each site tensor. This error is of order  $O(\delta^3)$  per time step and  $O(\delta^2)$  per unit time, and its magnitude is influenced by the bond dimension of the input state. The third error, truncation error, results from the singular value decomposition (SVD) needed to split two-site tensors into separate ones. This error must be carefully analyzed, as it is significant unless the MPS has maximal bond dimensions. Finally, the fourth error stems from the inexact solution of local equations, which can be minimized by using sufficiently many Krylov vectors. Importantly, altering the time-step size  $\delta$  affects these errors differently. Smaller  $\delta$  reduces the time-step error but increases projection and truncation errors. Therefore, careful selection of truncation thresholds and time-step size is essential to balance these errors. In  $1\text{TDVP}$ , the energy and norm are exactly conserved, whereas, in  $2\text{TDVP}$ , they are only influenced by the truncation error.







## Part II

### MANY-BODY QUANTUM SYSTEMS

In the second part, we turn our attention to the dynamics of closed quantum systems. The first chapter focuses on periodic dynamics within a two-dimensional framework, specifically examining the kicked quantum Ising chain. We utilize tensor network simulations to assess the robustness and viability of a two-dimensional discrete time-crystal. In the subsequent chapter, after a review of the stabilizer formalism, we discuss enhancements to tensor network simulations through the integration of Clifford operations. This methodological advancement aims to refine simulation accuracy and efficiency, providing deeper insights into the dynamics of complex quantum systems.



In this chapter, we make use of the TDVP algorithm to analyze the dynamics of a 2D kicked Ising model. We examine the system's response to the periodic evolution and explore the impact of dimensionality comparing the 1D analytical results to the 2D numerical simulations.

## 2.1 DISCRETE TIME CRYSTALS

In a seminal work [21], Wilczek introduced the intriguing concept of a “time crystal”, a new phase of matter characterized by the breaking of continuous time symmetry. Although initial theories suggesting the existence of such phases were later disproved [22, 23], the idea of breaking “discrete” time symmetry to create discrete time crystals (DTC) persisted.

Simply put, DTCs are systems driven by periodic interactions that exhibit stable responses at submultiples of the driving frequency. For these systems to avoid heating up to an infinite temperature, which disrupts order, their response to the driving force needs to be synchronized, thus stabilizing the phase of matter. Importantly, this response should be robust against generic perturbations and persist in the thermodynamic limit.

Floquet DTCs, which typically involve lattice spin models subjected to quick and periodic pulses, have become a standard model for studying these phenomena [24–27]. Many-body localization (MBL) [28, 29], where disorder helps prevent the system from reaching thermal equilibrium, is often used to freeze the local excitation caused by the driving, thereby stabilizing discrete time-crystals [30].

However, MBL is not the only player in the game. Various mechanisms have been explored to create stable DTC phases or at least transient signatures of DTCs in a range of systems, both theoretically and experimentally. These include pre-thermalization [31–37], emergent Floquet integrability with specific symmetries [38–40], quantum many-body scarring [41–43], and confinement of excitations [44]. There has been significant interest in identifying clean DTCs, which operate without the need for disorder. The simplest strategy for achieving a stable DTC involves systems that exhibit long-range order in a Gibbs ensemble at finite temperatures [45].

Guided by this idea, we extend our investigation of the kicked quantum Ising model from the *one-dimensional* setting to *two dimensions*. After reviewing results in one dimension, we present some numerical findings in two dimensions, paralleling advances in higher-dimensional classical systems [46, 47].

## 2.2 KICKED CLEAN ISING MODEL

We consider a  $d$ -dimensional nearest-neighbor quantum Ising model on a hyper-cubic lattice subjected to delta-periodic pulses of the transverse magnetic field. The time-dependent Hamiltonian operator of the system reads

$$H(t) = -J \sum_{\langle jj' \rangle} X_j X_{j'} - \left( \frac{\pi}{2} + \epsilon \right) \sum_{n=1}^{\infty} \delta(t - n\tau) \sum_j Z_j, \quad (128)$$

where  $J > 0$  is the ferromagnetic coupling between nearest-neighbor spins and  $\epsilon > 0$  is the transverse magnetic field, and  $X_j, Y_j$  and  $Z_j$  for  $j = 1, \dots, N$ ,

*Kicked  
d-dimensional Ising  
model*

with  $N = L^d$ ,  $L$  being the size of the hyper-cube, are the standard Pauli matrices. Here  $\langle jj' \rangle$  denotes the sum over nearest-neighbors.

The unitary dynamics generated by the time-dependent Hamiltonian in Eq. (128) can be understood as a Floquet dynamics governed by the Ising Hamiltonian evolution operator

$$V = e^{iJ\tau \sum_{\langle jj' \rangle} X_j X_{j'}} , \quad (129)$$

intertwined by sudden imperfect single-spin kicks along the  $z$ -axis

$$K_{\pi/2+\epsilon} = e^{i(\pi/2+\epsilon) \sum_j Z_j} , \quad (130)$$

at times  $t_n = n\tau = \tau, 2\tau, \dots$ , which are integer multiples of the period  $\tau$ . The resulting single-period Floquet operator thus reads  $U = K_{\pi/2+\epsilon} V$ .

To see the cleanest realization of DTC order, the system is initially prepared in the fully polarized state with positive magnetization along the  $x$  direction, i.e.  $|+\rangle = |\uparrow_x \dots \uparrow_x\rangle$ , where  $|\uparrow_x\rangle$  ( $|\downarrow_x\rangle$ ) is the eigenvector of the Pauli matrix  $X$  with eigenvalue  $+1$  ( $-1$ ). The system experiences a stroboscopic dynamics, and the state after  $n$  periods is given by

$$|\psi_n\rangle = U^n |+\rangle = (K_{\pi/2+\epsilon} V)^n |+\rangle . \quad (131)$$

Since  $K_{\pi/2+\epsilon} = K_{\pi/2} K_\epsilon$ , and  $K_{\pi/2} = i^N P$  with  $P = \prod_j Z_j$  being the global spin flip operator, such that  $[P, V] = 0$ , we can factor out from the evolution the product of all perfect spin flips, thus obtaining

$$|\psi_n\rangle = (K_\epsilon V)^n K_{\pi/2}^n |+\rangle = (i)^n (K_\epsilon V)^n |(-)^n\rangle . \quad (132)$$

This can be interpreted as a stroboscopic change of reference frame, which results in a non-trivial evolution only due to  $(K_\epsilon V)^n$ , on top of perfect alternating jumps between  $|+\rangle$  and  $|-\rangle = |\downarrow_x \dots \downarrow_x\rangle$ .

The  $x$ -magnetization after every kick provides information about the persistence of the ferromagnetic order during the stroboscopic dynamics, and it is given by

$$m(n) = \frac{(-1)^n}{N} \sum_{j=1}^N \langle + | (V^\dagger K_\epsilon^\dagger)^n X_j (K_\epsilon V)^n |+\rangle . \quad (133)$$

Setting  $\epsilon = 0$  results in a trivial dynamics in which the system periodically jumps between the two product states  $|+\rangle$  and  $|-\rangle$ , with magnetization being equal to  $m(n) = (-1)^n$ , thus exhibiting a perfect time-crystal behavior. As a matter of fact, one might say that  $m(n)$  shows a ‘‘period-doubling’’ since  $m(n) = m(n+2)$  whereas  $H(n) = H(n+1)$ . Nonetheless, we stress that, in order to realize a stable non-equilibrium DTC phase, the long-range ferromagnetic order has to be robust against arbitrary (sufficiently weak) perturbations in the thermodynamic limit  $L \rightarrow \infty$ .

### 2.3 CLEAN ONE-DIMENSIONAL KICKED ISING CHAIN

In order to highlight the emergent stability of such phase in two-dimensions, here we recap some recent results for the one-dimensional case [44].

The time-dependent Hamiltonian operator in the 1D setting, factoring out the perfect spin flips, reads

$$H(t) = -J \sum_j X_j X_{j+1} - \epsilon \sum_{n=1}^{\infty} \delta(t - n\tau) \sum_j Z_j . \quad (134)$$

Since both  $K_\epsilon = e^{i\epsilon \sum_j Z_j}$  and  $V = e^{iJ\tau \sum_j X_j X_{j+1}}$  are Gaussian operators in terms of Jordan-Wigner fermions, then, we can solve analytically

*Change of reference  
frame*

the dynamics induced by the Floquet operator. Indeed, the Jordan-Wigner transformation

$$X_j = \prod_{i=1}^{j-1} Z_i (c_j^\dagger + c_j), \quad Y_j = i \prod_{i=1}^{j-1} Z_i (c_j^\dagger - c_j), \quad Z_j = 1 - 2c_j^\dagger c_j, \quad (135)$$

where  $\{c_i, c_j^\dagger\} = \delta_{ij}$  and  $\{c_i, c_j\} = 0$ , transforms the evolution operators to

$$K_\epsilon = e^{i\epsilon \sum_j (c_j c_j^\dagger - c_j^\dagger c_j)}, \quad V = e^{iJ\tau \sum_j (c_j^\dagger - c_j)(c_{j+1}^\dagger + c_{j+1})}. \quad (136)$$

We can further simplify the problem by means of the discrete Fourier transform

$$c_j = \frac{1}{\sqrt{L}} \sum_p e^{-ipj} c_p, \quad (137)$$

where  $p = 2\pi n/L$  with  $n = -L/2, \dots, L/2 - 1$ . Notice that we enforced the symmetry sector  $P = 1$  of the spin-flip operator  $P = \prod_{j=1}^N Z_j$ . In this way we obtain

$$K_\epsilon = e^{i\epsilon \sum_p \psi_p^\dagger K \psi_p}, \quad V = e^{iJ \sum_p \psi_p^\dagger V \psi_p}, \quad (138)$$

where we defined the vector  $\psi_p = (c_p, c_{-p}^\dagger)^\top$  and the matrices

$$K = -2i\sigma^z \quad V = 2iJ\tau [\sigma^z \cos p - \sin p \sigma^y], \quad (139)$$

where  $\sigma^\alpha$ , are the Pauli matrices, for  $\alpha = x, y, z$ . For each  $p > 0$  we compose the two Gaussian operators by using the identity

$$e^{\mathbb{H}} = e^K e^V \quad (140)$$

where  $\mathbb{H} = i\phi_p r_p \cdot \sigma$  with

$$\cos \phi_p = \cos(2J\tau) \cos(2\epsilon) + \sin(2J\tau) \sin(2\epsilon) \cos(p), \quad (141)$$

and

$$r_p = \frac{1}{\sin \phi_p} \begin{pmatrix} \sin(2J\tau) \sin(2\epsilon) \sin(p) \\ -\sin(2J\tau) \cos(2\epsilon) \sin p \\ \sin(2J\tau) \cos(2\epsilon) \cos(p) - \cos(2J\tau) \sin(2\epsilon) \end{pmatrix}. \quad (142)$$

We can then perform a Bogoliubov transformation, i.e.,  $\psi_p = \mathbb{U}_p \xi_p$ , to diagonalize the Floquet operator

$$K_\epsilon V = e^{i\phi_p} \xi_p^\dagger \sigma_z \xi_p. \quad (143)$$

where we have  $\mathbb{U}_p = e^{-i\epsilon \sigma_z} e^{-i\theta_p \sigma_x / 2}$  with

$$\sin \theta_p = \frac{\sin(2J\tau) \sin p}{\sin \phi_p}, \quad (144)$$

$$\cos \theta_p = \frac{\sin(2J\tau) \cos(2\epsilon) \cos p - \cos(2J\tau) \sin(2\epsilon)}{\sin \phi_p}. \quad (145)$$

This allows us to compute the time evolution of the two-point function  $\langle X_0(n) X_\ell(n) \rangle$ . The idea is first to connect the initial state

$$|\psi_0\rangle = (|+\rangle + |-\rangle) / \sqrt{2}, \quad (146)$$

i.e., the vacuum of  $\xi_p^{[0]}$  fermions to the Jordan-Wigner fermions  $\psi_p$ , namely,  $\xi_p^{[0]} = \mathbb{U}_p^{[0]} \psi_p$ . We can then transform  $\psi_p$  to the post-quench diagonal fermions  $\xi_p$  obtaining

$$\xi_p^{[0]} = \mathbb{U}_p^{[0]} \mathbb{U}_p \xi_p. \quad (147)$$

These rotations identify a single Bogoliubov angle  $\Delta_p$  such that

$$\cos(\Delta_p) = \cos(\theta_p) \cos(p) + \sin(\theta_p) \cos(2\epsilon) \sin(p), \quad (148)$$

therefore the magnetization decays as

$$|\langle X_j \rangle| \propto e^{-\gamma n}, \quad (149)$$

as outlined in [48], the rate of decay is

$$\gamma = - \int_0^\pi \frac{dp}{2\pi} \partial_p \phi_p \ln |\cos \Delta_p|. \quad (150)$$

When taking the limit  $\epsilon \rightarrow 0$ , we observe that  $\gamma \propto \epsilon^3$ . Consequently, the magnetization will decay to zero as long as  $(\epsilon \bmod \pi) \neq 0$ .

## 2.4 CLEAN TWO-DIMENSIONAL KICKED ISING CHAIN

In the next section, we investigate the robustness against the parameter  $\epsilon$  of the DTC response in the two-dimensional kicked Ising model, via state-of-the-art numerical techniques, and try to infer its thermodynamic behavior.

## 2.5 NUMERICAL RESULTS

### 2.5.1 Exact diagonalization

We start our analysis by considering small system sizes whose dynamics have been computed via exact diagonalization (ED) techniques [49]. In Fig. 2 we show a color density plot of the stroboscopic evolution of the magnetization and its Fourier transform, for  $\epsilon$  ranging in  $[0, 0.6]$  and fixed energy scale  $J\tau = 1$ . The system consists of  $N = 16$  lattice sites, arranged in a chain in the 1D case, and in a  $4 \times 4$  square lattice for the 2D geometry.

The one-dimensional setting is in agreement with the results of [50] in which it is shown that finite-size kicked spin chains can sustain a time-crystalline response. However, this behavior is a finite-size effect and does not hold in the thermodynamic limit as shown in [44, 51]. Similarly to the 1D case, a very preliminary analysis confirms that in two dimensions does exist a region in the  $\epsilon - n$  plane wherein stable oscillations of the order parameter are present, at least up to  $n = 500$  unit periods, and for small system sizes (see Fig. 2(b)). For these values of the parameters, the system synchronizes to the driving and behaves in a time-crystalline way. Both in one and two dimensions, by increasing the value of  $\epsilon$  we disrupt the spatio-temporal order by letting excitations proliferate in the system thus breaking the DTC response. Interestingly, from the stroboscopic density plots, it seems that the meta-stable ferromagnetic dynamical region extends up to  $\epsilon \simeq 0.4$  in the 1D case, while in the 2D case the order starts disappearing at  $\epsilon \simeq 0.15$ . However, while in the 1D setup the system exhibits a smooth transition from one dynamical behavior to the other, in the 2D geometry the transition is remarkably sharper. This is confirmed by a thorough analysis of the excitation spectrum via discrete Fourier transform (DFT).

In order to explore the excitation spectrum of the system we plot in Fig. 2(c-d) the modulus of the discrete Fourier transform  $m(\omega)$  of  $m(n)$ . When  $\epsilon = 0$  there is only the time-crystal characteristic frequency  $\omega = \pi$ , which corresponds to the period-doubling of the magnetization. By increasing the value of the kick perturbation  $\epsilon$ , we generate more and more excitations in the system at different frequencies, which will eventually break the order. Let us stress that in the 1D case, due to integrability, the excitations that proliferate in the chain result in an extensive set of prominent



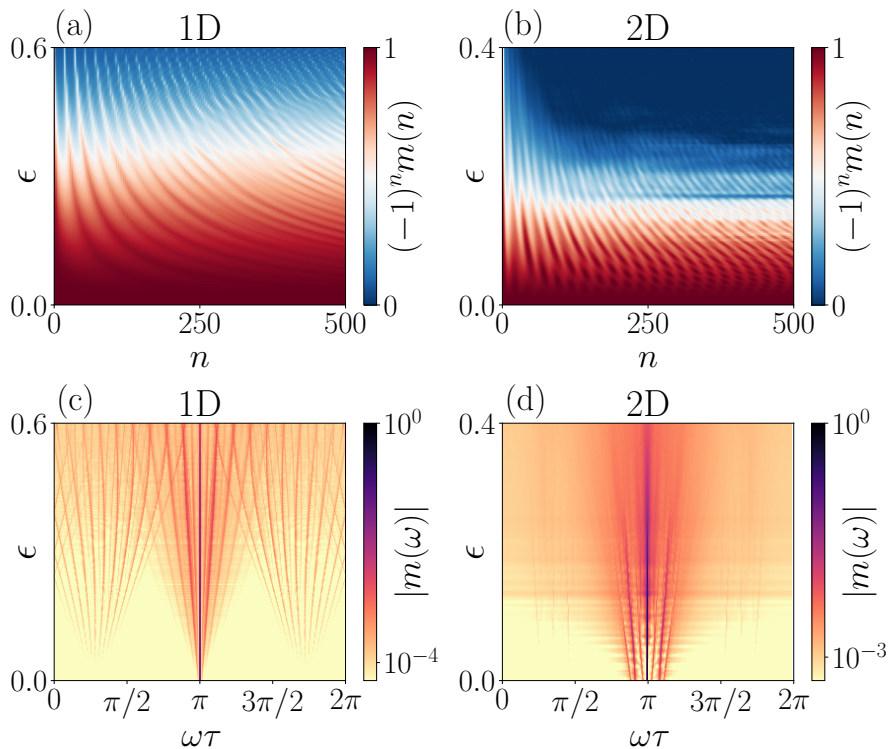


Figure 2: Floquet dynamics of the kicked Ising model with  $N = 16$  lattice sites and  $J\tau = 1$ . (a-b) Stroboscopic evolution of the magnetization in 1D and 2D. (c-d) Absolute value of the discrete Fourier Transform of the corresponding magnetization.

frequencies (delta-peak in the spectrum) which are present already from  $\epsilon = 0^+$ ; they correspond to stable quasi-particle traveling across the system and leading to the melt-down of the DTC behavior at large time. Quite interesting, in the 2D geometry, the Fourier spectrum is dominated by only a few peaks for small kick perturbations; as far as the number of such quasi-particle remains finite, we do expect the DTC response to be robust for a finite but long-lasting time in the thermodynamic limit.

Only for  $\epsilon \gtrsim 0.15$  they sharply melt into a continuum of excitations, thus leading to a transition without DTC order.

### 2.5.2 Tensor network time evolution

The results shown in the previous section are based on the analysis of small systems. In order to confirm the fact that in the 2D geometry the kicked Ising model may sustain a DTC phase, we need to rule out whether the evidence we found are artifacts due to finite-size effects.

In particular, we aim at understanding how the recurrences in the order parameter (see Fig. 2) are possibly caused by finite-size effects rather than being a genuine DTC signature. In order to do so, we explored the dynamics for larger lattice sizes using Tensor Network (TN) based techniques. Both for 1D and 2D geometries, we used a suitable matrix product state (MPS) representation of the many-body wave function, joined with the correspondent matrix product operator (MPO) representation of the Hamiltonian. The non-equilibrium Floquet dynamics has been computed via the time-dependent variational principle (TDVP) algorithm [16, 19, 20].

We start with the one-dimensional case, where we expect that by increasing the system size, the space-time order should disappear. Indeed, in Figs. 3(a-b) we show the evolution of the magnetization, with fixed  $J\tau = 1$ ,

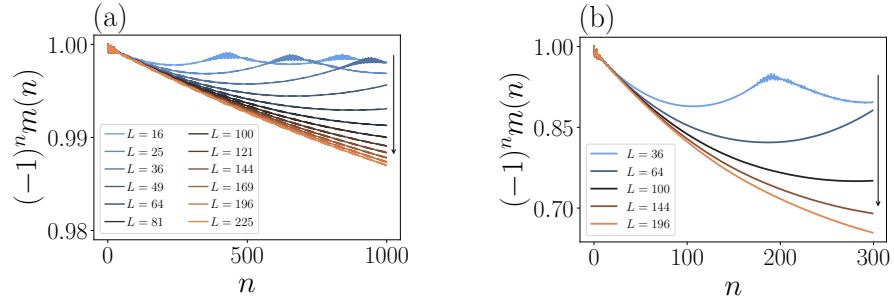


Figure 3: Stroboscopic evolution of the magnetization for the 1D kicked Ising model, with  $J\tau = 1$  and (a)  $\epsilon = 0.02$ , (b)  $\epsilon = 0.1$ . The arrows mark the trend of the stroboscopic magnetization with increasing the system size  $L$ .

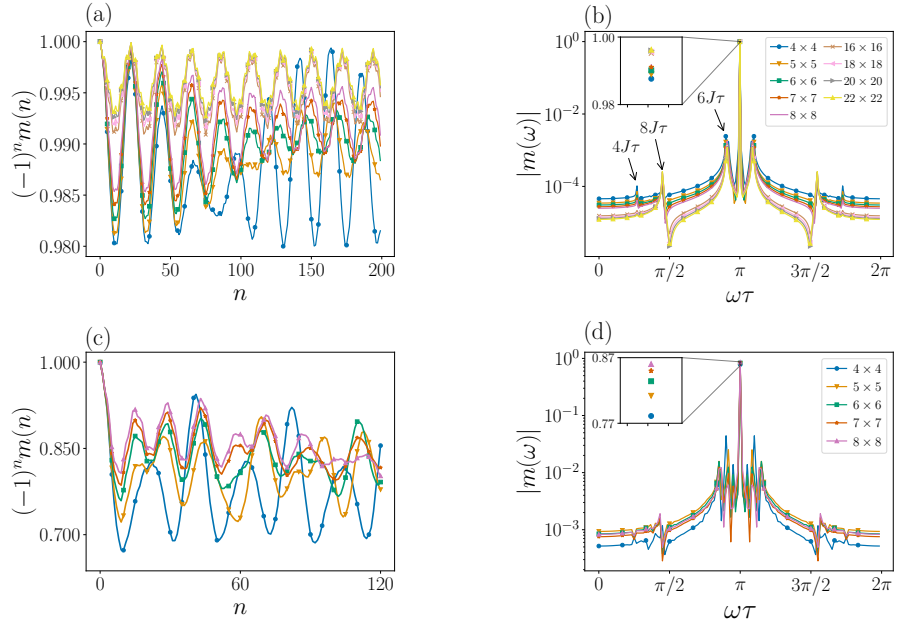


Figure 4: (a,c) Same as in Fig. 3 for the 2D case, with  $\epsilon = 0.02$  in panel (a) and  $\epsilon = 0.1$  in (c). (b,d) Absolute value of the discrete Fourier transform of the corresponding stroboscopic magnetization. The insets are close-up of the period-doubling peak at  $\omega\tau = \pi$ . The color code and markers in the legends apply also for the (a,c) panels, respectively.

and  $\epsilon = 0.02, 0.1$ , respectively. We observe that the smaller the system the sooner recurrences appear in the evolution of the magnetization. As a matter of fact, with increasing  $L$ , the curves are approaching the exponentially decaying thermodynamic line. As expected, the long-time oscillations are thus finite-size effects whereas in the thermodynamic limit the magnetization does decay to zero. This will give us a well-grounded numerical reference to compare the forthcoming novel 2D results with.

In Figs. 4(a-c) we show the same Floquet dynamics for the two-dimensional geometry. Remarkably, we find a completely different picture: as the system size is getting larger, the DTC response becomes more robust. In particular, in Fig. 4(a) where  $\epsilon$  is kept small, the many-body wave function remains low entangled, and we are able to simulate fairly large systems, up to  $N = 22 \times 22 = 484$  lattice sites, for a relatively large number of kicks. This allows us to safely exclude the possibility that finite-size effects may mimic the presence of a stable DTC. Indeed, what is crucial here is that, as opposed to the 1D case, passing from the smaller lattice ( $4 \times 4$ ) to the larger

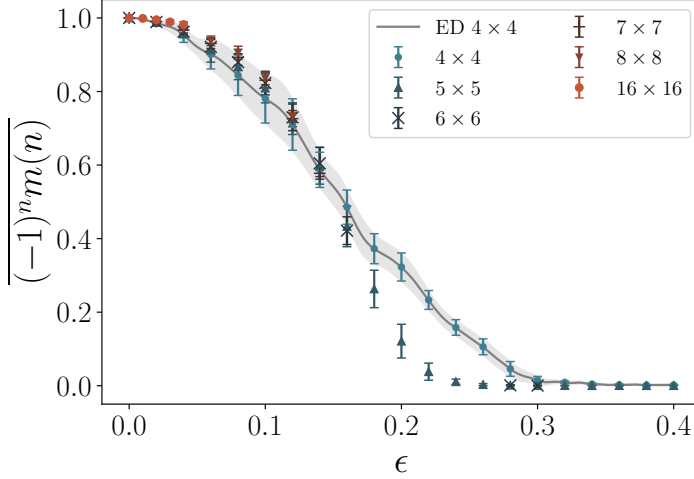


Figure 5: Time-average magnetization vs  $\epsilon$  for different system size and  $J\tau = 1$ . The averages have been taken over the time interval  $[75\tau, 120\tau]$ . The solid line represents ED results with shaded region representing the standard deviation. Symbols with error bars are TDVP results.

one ( $22 \times 22$ ), we observe an enhancement of the average stroboscopic magnetization, from  $\sim 0.985$  to  $\sim 0.995$ .

When we consider larger values of  $\epsilon$ , as in Fig. 4(c), the entanglement that the MPS should encode grows much faster, thus preventing us to consider system sizes bigger than  $N = 64$  without a sensible numerical error. Nonetheless, the qualitative pattern we found is the same as the one illustrated before: increasing the system size stabilizes the space-time order. Furthermore, by comparing the 1D case with the 2D case, namely, Fig. 3(b) vs Fig. 4(c), we observe that, initially, all system sizes manifest the same behavior during the first few kicks. However, in 1D, this initial “transient” is getting longer by increasing the system size, suggesting that it is not representing a transient at all, but instead the thermodynamic behavior. On the contrary, in 2D, the departure from the transient decay starts sooner as the system size is getting larger, showing almost immediately a stable oscillating magnetization. As a matter of fact, this suggests that the role of two-dimensional spin-spin interaction is non-trivial and stabilizes the dynamics, as in the case of long-range one-dimensional interactions [44]. We thus expect that the two-dimensional space-time order should persist in the thermodynamic limit, provided a sufficiently small value of the kick perturbation  $\epsilon$  is used.

We further analyze the numerical data by inspecting the power spectrum of the magnetization. In Fig. 4(b) we plot the absolute value of the discrete Fourier transform of the magnetization shown in Fig. 4(a). We marked the peaks of the power spectrum corresponding to the following frequencies

$$\omega\tau = \pi \pm \tau\Delta E_J \pmod{2\pi}, \quad (151)$$

where  $\Delta E_J$  measures the energy cost of a single spin-flip on top of the fully polarised state.

In particular,  $\Delta E_J = 8J$  corresponds to flipping a spin in the bulk of the system,  $\Delta E_J = 6J$  to flipping a spin in one of the borders of the square lattice, and  $\Delta E_J = 4J$ , finally, to flipping one of the corner spins. When the driving perturbation  $\epsilon$  is weak, single spin-flip excitations represent the lower excited states of the system, and we may expect them to play a dominant role in the dynamics. In a  $L \times L$  square lattice with OBC we have 4 excited states with energy gap  $\Delta E_J = 4J$  (obtained by a single spin-flip at the corners),  $4L$  excited states with gap equal to  $\Delta E_J = 6J$  — the  $4(L - 2)$  states obtained

by a single spin-flip on the 4 sides, plus 8 states obtained by flipping two adjacent spins at the corners — and finally  $(L - 2)^2$  states with  $\Delta E_J = 8J$ , obtained via a single spin-flip in the bulk.

The role of these single-flip excitations in the dynamics reflects in the power spectrum of the magnetization. Apart from the peak at  $\omega\tau = \pi$ , due to the period-doubling of the magnetization induced by the perfect driving, the next higher contribution comes at  $\omega\tau = \pi \pm 6J\tau \bmod 2\pi$ , for small  $\epsilon$ : here the dynamics of the system is mostly confined on lattice boundaries. Notice that the energetically most favorable transitions toward the corner spin-flip states (the  $4J\tau$  peak), get suppressed with the system size since their number is not extensive.

Similarly, in Fig. 4(d) we plot the power spectrum corresponding to the magnetisation reported in Fig. 4(c). Since here  $\epsilon = 0.1$  is larger, we are approaching the continuum of the spectrum, and the picture outlined above is going to break down; in practice, the isolated quasi-particle excitations cannot be exactly identified in single spin flips. Nonetheless, the peak at  $\omega\tau = \pi$ , indicating the presence of DTC order, is getting higher for larger system sizes, meaning that the time-crystalline response is getting more robust.

So far, the numerical finite-size analysis gives evidence of a stable DTC response for finite values of the kick perturbation  $\epsilon$ . Of course, increasing  $\epsilon$  we expect the DTC response to break down, eventually. In the following, we characterize, at least qualitatively, such transition. In order to do so, we analyzed the long time average of the stroboscopic magnetization  $\overline{(-1)^n m(n)}$  as a function of  $\epsilon$  for different system sizes, see Fig. 5. Even though we are far from the thermodynamic limit, we expect a ferromagnetic to paramagnetic dynamical phase transition with  $\epsilon_c \in [0.1, 0.2]$ . Indeed, for  $\epsilon \lesssim 0.15$ , the average magnetization data manifest a global increasing trend with the lattice size dimension  $L$ ; on the contrary, when  $\epsilon \gtrsim 0.15$ , the average magnetization is going to zero as  $L$  grows larger.

Notice that, for weak perturbation,  $\epsilon < 0.05$ , we are able to simulate big systems with hundreds of lattice sites since the auxiliary dimension of the MPS remains relatively small. Increasing the strength of the perturbation greatly reduces the system sizes we can handle, down to  $N \approx 36$ . For this reason, we cannot quantitatively describe the exact nature of such transition.

### 2.5.3 Dynamical transition in the relaxation dynamics

To complement the analysis of the dynamical phase transition outlined in the previous section, we further look at the evolution of the stroboscopic magnetization and we study the initial decay of the order parameter before reaching the asymptotic equilibrium. As stated before, in the case of a one-dimensional kicked Ising model it has been proved that in the thermodynamic limit the order parameter decays to zero as  $|m(n)| \sim e^{-\gamma n}$  with  $\gamma \propto |\epsilon|^3$ ; thus here we inspect whether a similar relation occurs also in the two-dimensional case.

In 2D the situation is more delicate, due to the presence of a reasonable stable DTC response for  $\epsilon \lesssim 0.15$ . In this sense, the extrapolated decay only represents a transient toward a stationary value which can be zero or different from zero depending on the non-equilibrium dynamical phase the system ends up.

In order to obtain an estimate of  $\gamma$ , we fitted the absolute value of the magnetization with the function  $Ae^{-\gamma n}$ , using only the first kicks (whose number depends on how fast the magnetization decays and on the number of kicks we are able to numerically evolve), for the different system sizes. In Fig. 6(a) we show a representative example of the time evolution of the order

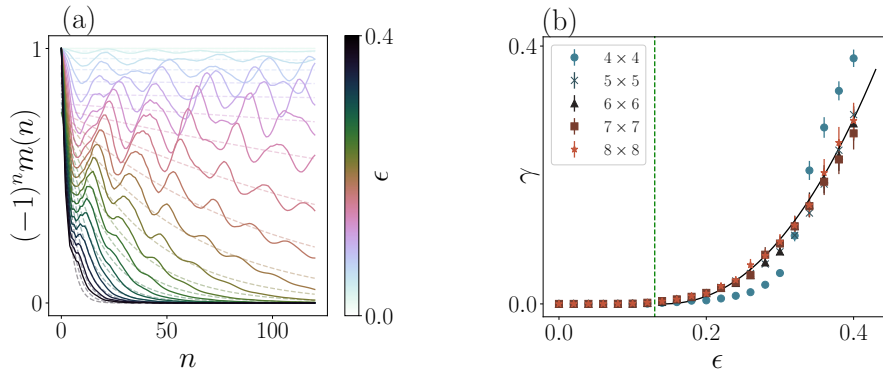


Figure 6: (a) Solid lines: evolution of the magnetization for a  $5 \times 5$  system, dashed lines: exponential decay  $Ae^{-n\gamma}$  for fitted values of  $\gamma$  and  $A$ . (b) Decay rates  $\gamma$  against  $\epsilon$  for different system sizes. In the thermodynamic limit, we expect that the  $\gamma$  before the vertical dashed line is identically vanishing.

parameter for a  $5 \times 5$  lattice for different values of  $\epsilon$  and their relative best-fit initial transient  $|m(n)| \sim e^{-\gamma n}$ . We then repeated the procedure for larger system sizes. Once again, we stress that for large systems and high values of  $\epsilon$  we are able to time evolve the many-body state just for a few kicks, which are not enough in order to determine the stationary magnetization, but they turn out to be sufficient to evaluate the decay rate. Our analysis suggest that  $\gamma$ , in the region where the order parameter is expected to decay toward zero (no-DTC response), increases as a power law  $\gamma \sim |\epsilon|^\alpha$  with  $\alpha \approx 4$ . In practice, by increasing the dimensionality of the problem, the decaying rate of the magnetization is not just quantitatively increased, but rather “non-perturbatively” modified, passing from  $\gamma \sim |\epsilon|^3$ , in 1D, to  $\gamma \sim |\epsilon|^\alpha$ , in 2D.

This is somehow related to the presence of long-lived domain-wall excitations, which slow down the decay of the fully polarized initial state. In practice, when  $|\epsilon| \ll J\tau$ , the length of the interface between different magnetic domains becomes a quasi-conserved “charge”.

## 2.6 HIGH-FREQUENCY LIMIT

The picture emerging from the previous analysis is compatible with a dynamical phase transition driven by the strength  $\epsilon$  of the kick perturbation. Besides the evidence of a dynamical transition in the way, the order parameter is decaying — discussed at the end of the previous section —, the two phases are also characterized by a change in the stationary properties of the system, which undergoes a transition from a long-lasting long-range ordered ferromagnetic phase to a paramagnetic (disordered) phase. It is possible to understand the nature of this transition by studying the expected stationary behavior of the system induced by the periodic kicks. As a matter of fact, the system under investigation is non-integrable, thus its stationary properties are expected to be captured by a canonical Gibbs ensemble, at least in an intermediate “pre-thermal” regime [45], before a final infinite temperature state is possibly attained. In order to do so, let us introduce the Floquet Hamiltonian  $H_{\text{eff}}$  as follow

$$U = K_\epsilon V \equiv e^{-i\tau H_{\text{eff}}} . \quad (152)$$

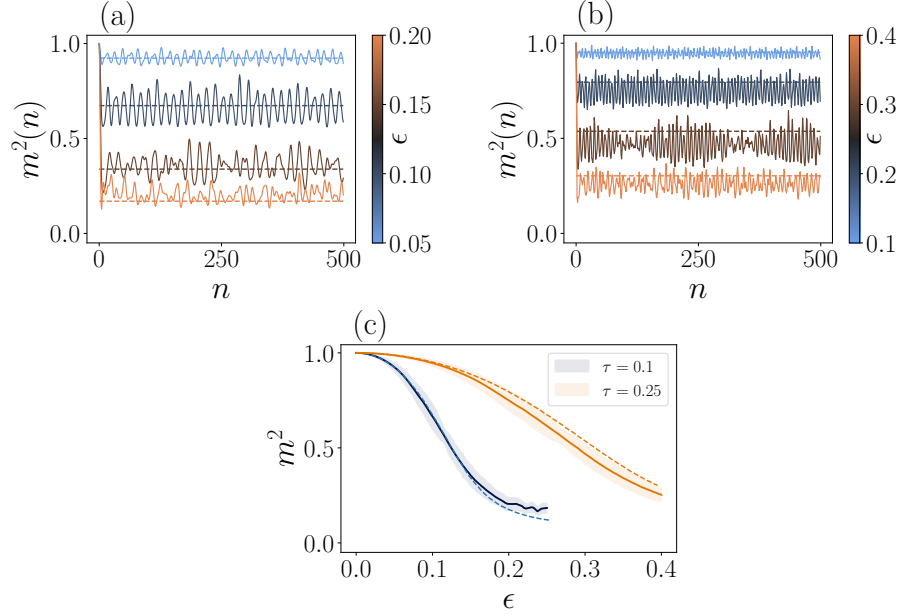


Figure 7: (a-b) Stroboscopic evolution of the second moment of the magnetization with  $J = 1$  and  $\tau = 0.1$ (a),  $\tau = 0.25$ (b). The dashed lines are the relative thermal average computed in the 2D quantum Ising thermal state at late times. (c) Comparison between time averages (solid lines) and thermal averages (dashed lines) as a function of the kick perturbation  $\epsilon$ . The shaded area represents the standard deviation.

If we define  $K_\epsilon = e^A$  and  $V = e^B$ , hence  $A = i\epsilon \sum_j Z_j$  and  $B = iJ\tau \sum_{\langle jj' \rangle} X_j X_{j'}$ , the Floquet Hamiltonian can be formally computed from the Baker Campbell Hausdorff (BCH) series

$$\begin{aligned} -i\tau H_{\text{eff}} &= A + B + \frac{1}{2}[A, B] \\ &+ \frac{1}{12}([A, [A, B]] - [B, [A, B]]) + \dots \end{aligned} \quad (153)$$

The evolution of the system after  $n$  periods, therefore, reads

$$|\psi_n\rangle = e^{-in\tau H_{\text{eff}}} |+\rangle, \quad (154)$$

meaning that the evolution is effectively described as the quench dynamics under  $H_{\text{eff}}$  of the generally excited initial state  $|\uparrow \dots \uparrow\rangle$ .

Since our system is not integrable which implies that Eigenstate Thermalization Hypothesis [52, 53] is generically expected to hold [54, 55], we do expect that, after the initial transient, the time averages of local observables should relax toward thermal averages computed in the Gibbs ensemble [54, 56]

$$\rho = \frac{e^{-\beta H_{\text{eff}}}}{\mathcal{Z}}, \quad (155)$$

where the partition function is  $\mathcal{Z} = \text{Tr}(e^{-\beta H_{\text{eff}}})$ , and the inverse temperature  $\beta$  has been fixed by the equivalence between micro-canonical and canonical ensemble, namely

$$\langle +|H_{\text{eff}}|+\rangle = \text{Tr}(\rho H_{\text{eff}}), \quad (156)$$



which is nothing more than the conservation of the effective Hamiltonian expectation value. These considerations allow us to compute the thermal average of the order parameter

$$\langle m \rangle_\beta = \frac{1}{N} \sum_j \text{Tr}(\rho X_j), \quad (157)$$

at an effective inverse temperature  $\beta$  given by the specific quench protocol, and thus effectively making a bridge between the time-dependent Floquet problem and the finite-temperature behaviour of a system with a very complicated effective Hamiltonian  $H_{\text{eff}}$ .

Notice that, this picture holds if and only if the formal series in Eq. (153) is convergent. Indeed, the natural guess on the Floquet dynamics is that, since the driving breaks the energy conservation (where here energy refers to the expectation value of the Ising Hamiltonian), and we are dealing with an ergodic system, we expect to eventually heat the system towards the infinite-temperature state, i.e., the maximally entropic state. On the other hand, it has been proven that, in the high-frequency driving limit, a quasi-conserved Hamiltonian is expected to constraint the dynamics up to a time  $\tau^*$  which scales exponentially with the driving frequency; this emergent conservation law prevents the system from heating up and lets it evolve towards a meta-stable long-lived prethermal state [45].

Since we cannot explore exponentially large times with our numerics, we cannot infer if the plateaux we found in the previous section are actually meta-stable or infinitely lived. Nonetheless, for the non-interacting 1D case, the quadratic Floquet Hamiltonian  $H_{\text{eff}}$  can be computed exactly in the thermodynamics limit, thus implying that the BCH expansion is convergent, and the long-time limit of the Floquet dynamics has to match with the Generalised Gibbs Ensemble constructed with post-quench Bogoliubov fermions [44]. In the 2D case, the system is no longer integrable, and the effective Hamiltonian  $H_{\text{eff}}$  is much harder to compute and control: if it is a local Hamiltonian sustaining long-range magnetic order, then a clean DTC response is expected to survive, at least for a suitably large time, after which the effect of possible small non-local terms might appear [45].

Again, since the Floquet operator in Eq. (152) is  $\mathbb{Z}_2$ -symmetric, the time-crystal response we observed in the previous section should be related to the ferromagnetic to paramagnetic finite-temperature phase-transition of an effective quantum spin model in two-dimensions. If universality holds, for a sufficiently small perturbation, we may expect that, in the meta-stable regime, all the critical properties of our model can be extracted by those of the two-dimensional transverse field quantum Ising model, whose phase diagram is known since 80s [57]. The absence of a genuine time-crystal for short-range Hamiltonians in 1D, and its existence in 2D is indeed a consequence of the Peierls argument [58]. Indeed, since in a short-range quantum Ising model there is no long-range order at finite temperature in 1D, we expect that in a short-range kicked quantum Ising model there is no DTC order for  $\epsilon \neq 0$  in 1D. Analogous considerations hold for the stochastic dynamics of a 2D classical kicked Ising model in which the non-equilibrium stationary state is in the Ising universality class [59].

We are going to show that this thermodynamic picture holds in a simple case in which we are able to approximate  $H_{\text{eff}}$ . Indeed, in the high-frequency regime when  $J\tau, \epsilon \ll 1$  at the lowest order in  $J\tau\epsilon$  we may neglect all the commutators of  $A$  and  $B$  in the BCH expansion and approximate

$$H_{\text{eff}} = -J \sum_{\langle jj' \rangle} X_j X_{j'} - h \sum_j Z_j + O(J^2 \tau \epsilon^2), \quad (158)$$

where  $h = \epsilon/\tau$  plays the role of an effective transverse field. Because of the  $\mathbb{Z}_2$ -symmetry, the thermal average  $\langle m \rangle_\beta$  is identically vanishing. In order

to study the finite-temperature spontaneous symmetry-breaking we need to evaluate the second moment of the magnetization, namely

$$\langle m^2 \rangle_\beta = \frac{1}{N^2} \sum_{jj'}^N \text{Tr}(\rho X_j X_{j'}), \quad (159)$$

and compare it with the time evolution under the Floquet dynamics

$$m^2(n) = \frac{1}{N^2} \sum_{jj'}^N \langle \psi_n | X_j X_{j'} | \psi_n \rangle. \quad (160)$$

In Fig. 7(a-b) we compare the asymptotic thermal averages with the stroboscopic dynamics of the magnetisation fluctuations in a  $4 \times 4$  system, for two different choices of the period  $\tau$ . Thermal averages have been computed with a generalization of the TDVP algorithm after a Wick rotation in imaginary time [16]. In particular, we observe that the time-evolved  $m^2(n)$  is kept oscillating around the corresponding thermal averages; as expected, by increasing  $\epsilon$  the agreement is getting worse, due to the error in the truncation of the BCH expansion. Finally, in Fig. 7(c) we compare the thermal equilibrium data of the second moment of the magnetisation with the asymptotic time averages, for two choices of  $\tau$ . We find a good agreement among the two curves for small enough values of  $\epsilon$  and  $\tau$ , where deviations are typically  $O(\max((J\tau)^2, \epsilon^2))$ . As a matter of fact, this analysis suggests that the stationary properties of the system are well described by the effective 2D Ising Hamiltonian, for a characteristic time which scales as  $\sim 1/(\tau)^2 \epsilon^2$ .

## 2.7 CONCLUSIONS AND OUTLOOKS

We studied the evolution of a clean two-dimensional quantum Ising model periodically kicked with imperfect global spin flips. We compared the stroboscopic evolution of the magnetization with the one obtained in the one-dimensional kicked Ising model, and by a size-scaling analysis exploiting TDVP calculations, we showed the possibility of realizing a DTC with a two-dimensional clean system. Moreover, in the high-frequency limit, we studied a metastable regime wherein local time averages are in perfect agreement with thermal averages computed over an effective Floquet Hamiltonian. We pointed out that this quasi-stable time-crystalline response is closely related to the existence of a long-range ordered phase at *finite* temperature, which may survive for exponentially long times.

Let us remark that the non-equilibrium protocol we have studied can be implemented on currently available quantum platforms, such as trapped ions or superconducting qubits [60–63]. In principle, quantum hardware with long coherence times and a small gate noise could outperform the results obtained by means of tensor-network techniques.

Finally, it is worth to further investigate the connection between stable time-crystalline response and finite-temperature long-range order. In this respect, it would be interesting to study periodically-driven dynamics of other different interacting models and lattice topologies, with and without frustration, which may or may not sustain long-range order at finite temperature.



Due to their unique characteristics and wide-ranging applications, the Clifford group and stabilizer states play a crucial role in quantum information theory. Specifically, in the context of quantum error correction and quantum computation, the Clifford group, comprising a subset of unitary operators, and stabilizer states, a specialized class of quantum states, together establish a robust foundation which makes managing and understanding quantum systems simpler.

One of the most striking features of stabilizer states is that, despite their high potential for entanglement, they can be described and manipulated using classical computational resources. This classical tractability is attributed to the fact that operations within the Clifford group, when applied to stabilizer states, do not increase the computational complexity beyond classical limits.

In this chapter, we present methods to improve and enhance tensor network algorithms by leveraging the stabilizer formalism.

### 3.1 THE PAULI GROUP

In the next sections, we introduce some fundamental concepts of the stabilizer formalism, beginning with the Pauli group, which comprises the identity operator  $\mathbb{I}$  and the three Pauli operators represented as follows

*Pauli operators*

$$\begin{aligned}\hat{X} &= \sum_{i,j} \begin{array}{c} j \\ \textcircled{X} \\ i \end{array} |i\rangle\langle j| = |0\rangle\langle 1| + |1\rangle\langle 0| \\ \hat{Y} &= \sum_{i,j} \begin{array}{c} j \\ \textcircled{Y} \\ i \end{array} |i\rangle\langle j| = -i|0\rangle\langle 1| + i|1\rangle\langle 0| \\ \hat{Z} &= \sum_{i,j} \begin{array}{c} j \\ \textcircled{Z} \\ i \end{array} |i\rangle\langle j| = |0\rangle\langle 0| - |1\rangle\langle 1|\end{aligned}\quad (161)$$

where the tensors are given by the usual expressions

$$\begin{pmatrix} 0 & 1 \\ 1 & 0 \end{pmatrix} = \begin{array}{c} \textcircled{X} \\ | \\ | \end{array} \quad \begin{pmatrix} 0 & -i \\ i & 0 \end{pmatrix} = \begin{array}{c} \textcircled{Y} \\ | \\ | \end{array} \quad \begin{pmatrix} 1 & 0 \\ 0 & -1 \end{pmatrix} = \begin{array}{c} \textcircled{Z} \\ | \\ | \end{array}\quad (162)$$

The complete set of these operators forms the Pauli group for a single qubit, denoted as  $\mathcal{P} = \{\sigma^\mu\}_{\mu=0}^3$ , where  $\sigma^0 = \mathbb{I}$ ,  $\sigma^1 = X$ ,  $\sigma^2 = Y$ , and  $\sigma^3 = Z$ . These operators satisfy the orthogonality relation given by

$$\text{Tr}(\sigma^\mu \sigma^\nu) = 2\delta_{\mu\nu}. \quad (163)$$

Consider a system with  $N$  qubits and identify the local computational basis  $\{|0\rangle, |1\rangle\}$  with the eigenstates of the  $\sigma^3$  Pauli matrix, such that  $\sigma^3 |s\rangle =$

$(-1)^s |s\rangle$ . Any operator acting on a single qubit can be decomposed in terms of the Pauli matrices and the identity matrix. Using this local basis, using a boldface apex  $\mu$  to identify the set  $\{\mu_1, \dots, \mu_N\}$ , we can construct a generic Pauli string (or Pauli Product) as

$$\Sigma^\mu = \sigma_1^{\mu_1} \sigma_2^{\mu_2} \dots \sigma_N^{\mu_N}, \quad (164)$$

where  $\Sigma^\mu$  is an element of the tensor product of the N-qubit Pauli group  $\mathcal{P}_N = \mathcal{P}^{\otimes N}$  and has the following diagrammatic representation

$$\sigma_1 \sigma_2 \dots \sigma_N = \begin{array}{c} | \\ \bullet \\ | \end{array} \begin{array}{c} | \\ \bullet \\ | \end{array} \dots \begin{array}{c} | \\ \bullet \\ | \end{array} | \sigma'_1 \dots \sigma'_N \rangle \langle \sigma_1 \dots \sigma_N | \quad (165)$$

In subsequent discussions, whenever the subscript denoting the qubit is unnecessary, it will be omitted for the sake of notation simplicity.

The Pauli strings are therefore a complete basis for any operator  $O$  acting on the many-body Hilbert space  $\mathcal{H} = \{|0\rangle, |1\rangle\}^{\otimes N}$ , namely

$$O = \sum_{\mu} O_{\mu} \Sigma^{\mu} \quad (166)$$

where the coefficients are given by

$$O_{\mu} = \text{Tr}(O \Sigma^{\mu}) / 2^N, \quad (167)$$

and we used the orthogonality condition  $\text{Tr}(\Sigma^{\mu} \Sigma^{\nu}) = 2^N \delta_{\mu\nu}$ . When associated with the local operator  $\sigma^{\mu_j}$ , we may construct the operator-valued matrix  $O_j = \sum_{\mu} O_j^{\mu} \sigma^{\mu_j}$ , such that we get the compact notation for the original operator itself  $O = O_1 O_2 \dots O_N$ . It is worth noting that the most straightforward example of an operator with an exact Pauli-based MPO representation (with a bond dimension of one) is a general Pauli string  $\Sigma^{\mu}$ . Another useful example which admits an MPO representation with bond dimension one is a projector on a computational basis state  $|s_1, s_2, \dots, s_N\rangle$ , since  $|s\rangle\langle s| = (\sigma^0 + (-1)^s \sigma^3) / 2$ .

### 3.2 STABILIZER STATES AND THE CLIFFORD GROUP

Given a pure quantum state  $|\psi\rangle$ , a unitary matrix  $U$  is said to stabilize  $|\psi\rangle$  if  $|\psi\rangle$  is an eigenstate of  $U$  corresponding to the eigenvalue 1, i.e.,

$$U |\psi\rangle = |\psi\rangle \quad (168)$$

We do not ignore the global phase. The collection of unitary matrices that stabilize a state forms a group, denoted by  $\text{stab}(|\psi\rangle)$ . Specifically:

- If both  $U$  and  $V$  stabilize  $|\psi\rangle$ , then their product  $UV$  also stabilizes  $|\psi\rangle$ .
- If  $U$  stabilizes  $|\psi\rangle$ , then its inverse  $U^{-1}$  also stabilizes  $|\psi\rangle$ .
- The identity matrix  $I$  stabilizes all states  $|\psi\rangle$ .

Generally, to identify the generators of the stabilizer group of a quantum state it is required an exponential number of parameters. However, a particular class of quantum states can be characterized by a significantly smaller group, namely, the intersection of the stabilizer group with the Pauli group, represented as  $S(|\psi\rangle) \equiv \text{stab}(|\psi\rangle) \cap \mathcal{P}^N$ . Indeed, according to a theorem by Gottesman and Aaronson [64], for an N-qubit state  $|\psi\rangle$ , the following statements are equivalent:

- $|\psi\rangle$  can be constructed from  $|0\rangle^{\otimes N}$  using only CNOT, H, and S gates.
- $|\psi\rangle$  can be constructed from  $|0\rangle^{\otimes N}$  using only CNOT, H, S gates, and measurement gates in the computational basis.
- $|\psi\rangle$  is stabilized by precisely  $2^N$  Pauli operators.
- $|\psi\rangle$  is uniquely determined by  $S(|\psi\rangle)$ .

Since we are constructing circuits utilizing only CNOT, H, S, and measurement gates (i.e., a *stabilizer circuit*), we define any state generated by applying the stabilizer circuit to  $|0\rangle^{\otimes N}$  as a *stabilizer state*.

A Clifford operation is a special unitary quantum operation. Indeed, we can decompose it into a stabilizer circuit containing the minimal set of H (Hadamard), S (phase gate), and CNOT (control-not) gates, whose matrix form in the computational basis are given by

*Clifford unitaries*

$$\begin{aligned} \frac{1}{\sqrt{2}} \begin{pmatrix} 1 & 1 \\ 1 & -1 \end{pmatrix} &= \boxed{\text{H}} & \begin{pmatrix} 1 & 0 \\ 0 & e^{i\pi/2} \end{pmatrix} &= \boxed{\text{S}} \\ \begin{pmatrix} 1 & 0 & 0 & 0 \\ 0 & 1 & 0 & 0 \\ 0 & 0 & 0 & 1 \\ 0 & 0 & 1 & 0 \end{pmatrix} &= \text{CNOT} & & \end{aligned} \tag{169}$$

Formally, an operator  $C$  is a Clifford operation if, for any Pauli string  $P$ , the conjugated operator  $C^\dagger P C$  is also a Pauli product. This property allows Clifford operations to be characterized, up to a global phase, by their action on Pauli strings. The *Gottesman-Knill theorem* leverages this property to state that stabilizer circuits can be perfectly simulated in polynomial time on a probabilistic classical computer. The efficiency arises precisely on the fact that Clifford gates map Pauli strings to other Pauli strings, allowing the state of the quantum system to be tracked using a polynomial number of classical operations. This implies that while stabilizer circuits can create highly entangled states, they do not offer a computational speedup over classical algorithms.

*Stabilizer tableaux*

A stabilizer tableau is a representation of a Clifford operation that directly encodes how the operation conjugates each generator of the Pauli group. The generators  $X_q$  and  $Z_q$  are used for each qubit  $q$  affected by the operation; note that  $Y_q = iX_q Z_q$  is fully determined by the transformations of  $X_q$  and  $Z_q$ . For example, consider the stabilizer tableau for the composition of the Controlled-Z and Controlled-X gates ( $C \equiv C_X C_Z$ ):

$$\text{tableau}(C) = \begin{array}{c|cc|cc} & X_1 & Z_1 & X_2 & Z_2 \\ \hline \pm & - & + & + & + \\ 1 & Y & Z & Z & Z \\ 2 & Y & I & X & Z \end{array} \tag{170}$$

Each column in the tableau specifies how  $C$  conjugates one of the four generators of the two-qubit Pauli group. For instance, the column labeled  $X_1$  indicates that  $C$  conjugates  $X_1$  into  $-Y_1 Y_2$ , meaning that  $C^\dagger X_1 C = -Y_1 Y_2$ . Let us see how to use the tableau for a Pauli string

$$C^\dagger X_1 Y_2 C = iC^\dagger X_1 C C^\dagger X_2 C C^\dagger Z_2 C = -iY_1 Y_2 Z_1 X_2 Z_1 Z_2 = -Y_1 \tag{171}$$

Any qubit not mentioned in the tableau remains unaffected by the operation. For example, if  $X_q$  does not appear in the tableau, it is implied that the operation conjugates  $X_q$  into  $X_q$ .

For a stabilizer tableau to be valid and accurately represent a Clifford operation, it must preserve the commutation and anticommutation relationships among the Pauli products. The Pauli products in the tableau's columns must commute or anticommute in the same manner as their corresponding generators. Specifically, the column for  $X_a$  must commute with the columns for  $X_b$  and  $Z_b$ , but, it must anticommute with the column for  $Z_a$ . Additionally, a valid tableau cannot have missing columns. If a row for qubit  $q$  is present, there must be columns for the generators  $X_q$  and  $Z_q$ .

Despite their strength and utility, the Clifford gates do not form a universal set of quantum gates. Some gates outside the Clifford group cannot be arbitrarily approximated with a finite set of Clifford operations. An example is the T gate

*Magic T-gate*

$$\begin{pmatrix} 1 & 0 \\ 0 & e^{i\pi/4} \end{pmatrix} = \begin{array}{c} | \\ \boxed{\text{T}} \\ | \end{array} \quad (172)$$

Indeed, the following shows that the T gate does not map a Pauli string to another Pauli string

$$\begin{aligned} T^\dagger \Sigma T &= (\mathbb{I} \cos \pi/8 - iZ \sin \pi/8) \Sigma (\mathbb{I} \cos \pi/8 + iZ \sin \pi/8) \\ &= \Sigma \cos^2 \pi/8 + Z \Sigma Z \sin^2 \pi/8 - \frac{i}{2} (Z \Sigma - \Sigma Z) \sin \pi/4, \end{aligned} \quad (173)$$

i.e., if  $\Sigma = X$  we get  $T^\dagger X T = X \cos \pi/4 - Y \sin \pi/4$ . Despite this limitation, the Clifford group, when supplemented with the T gate, forms a set of universal quantum gates for quantum computation. This means that any quantum operation can be approximated to arbitrary precision using a combination of Clifford gates and the T gate.

**QUANTUM MAGIC** — Non-stabilizerness acts as a measure to evaluate the resource known as *quantum magic*, indicating how far a quantum state is from being a stabilizer state. Similarly, it may reflect the number of magic gates within a quantum circuit to prepare a state  $\rho$ . Several measures have been suggested to quantify magic as a resource. Among the most common is the Stabilizer Rényi Entropy (SRE), defined for a quantum state  $\rho$  as

$$M_n(\rho) = \frac{1}{1-n} \log \sum_{\Sigma^\mu \in \mathcal{P}_N} \frac{1}{2^N} \text{Tr}(\rho \Sigma^\mu)^{2n}. \quad (174)$$

where we are summing over all the  $N$ -qubit Pauli strings  $\Sigma^\mu = \sigma_1^{\mu_1} \dots \sigma_N^{\mu_N}$

### 3.3 HYBRID STABILIZER MATRIX PRODUCT OPERATORS

We can leverage upon the stabilizer formalism to deal with one of the most challenging tasks in quantum physics, the simulation of the unitary dynamics of a many-body system. The significance of this investigation is twofold. Firstly, it propels scientific advancements in fields such as condensed matter physics and quantum chemistry, where large, error-corrected quantum devices are still under development [65]. Secondly, it enables a critical assessment of the quantum advantage claims by state-of-the-art devices [66, 67].

This unitary evolution, which involves numerous qubits and a vast array of unitary gate operations, requires a high degree of entanglement to encode the wave function. Such a requirement poses a substantial challenge to current classical numerical methods, particularly those based on tensor network [15, 16, 68]. While tensor network based techniques efficiently manage

*relevant* entanglement by controlling the auxiliary space dimensions  $\chi$  of the ansatz, they face inherent limitations. For instance, in the one-dimensional MPS framework, the computational complexity is held at  $O(N\chi^3)$ , limiting the maximum entanglement that can be effectively encoded into the wave function. Unfortunately, it is well-known that generic unitary evolution introduces correlations across the system, propagating linearly with time, which leads to a linear increase in entanglement. As a result, the MPS bond dimension grows exponentially, ultimately causing the breakdown of the classical simulation [69–71].

Often, in physics, the primary interest lies not on the full evolution of the many-body wave function, but rather on the expectation values of local observables; and, as expected, this remains one of the most challenging, yet fundamental, problem in many-body physics, i.e., the calculation of  $\langle \psi | U^\dagger O U | \psi \rangle$ , for a generic unitary evolution  $U$  and local observable  $O$ , starting from a state with relatively short-range correlations [72, 73].

As previously demonstrated, when the unitary evolution is governed by a Clifford operator, the computational complexity of evaluating the expectation values of local observables reduces from exponential to polynomial in the number  $N$  of qubits [74–78]. Significantly, the quantum complexity of such tasks depends not only on entanglement but also on a critical quantum resource known as non-stabilizerness (or Magic). The interplay between these two factors can deeply influence computational feasibility [79–92]. Developing sophisticated classical algorithms that can effectively manage both entanglement and non-stabilizerness is crucial.

Here, first of all, we detail our development of a hybrid stabilizer and tensor network scheme aimed at disentangling MPS. This method enables the precise computation of expectation values over longer circuits depths using a fixed amount of resources, denoted by  $\chi$ .

Specifically, we model the evolution into a tensor network evolution coupled with a Clifford operations. Using the stabilizer formalism, we apply the Clifford operator to the local observable, continue the state’s evolution using tensor network techniques, and then calculate the expectation value of the conjugated observable. Then, in a second part, we will explore techniques to enhance the Time-Dependent Variational Principle (TDVP) algorithm by incorporating the stabilizer formalism, further broadening the scope and efficiency of our computational methods.

### 3.3.1 Transformation of local gate under Clifford Operations

Let us consider the unitary group, composed of all unitary matrices acting on  $N$  qubits, generated by the elementary gates: Hadamard (H), phase (S), Magic (T), and the entangling controlled-NOT gate (CNOT). The latter, essential for building up correlations, acts on two qubits. Using these gates, one can implement any quantum circuit [93–95]. Focusing on the subset H, S, CNOT, these generate the Clifford group, which maps any Pauli string to another, modulo a  $\pm 1$  phase [74]. Despite the potential for significant entanglement, operations within the Clifford Group preserve the low computational complexity characteristic of Pauli strings.

The key interplay in our discussion is between a generic Clifford unitary and the non-stabilizer generator, specifically the Magic gate  $T = e^{i\pi(\sigma^0 - \sigma^3)/8}$ . For broader applicability, we consider a generic rotation  $R^\mu(\theta) = e^{-i(\theta/2)\sigma^\mu}$  as a method to inject non-stabilizerness into the many-body wave function, noting that  $T \propto R^3(\pi/4)$ . Utilizing the Pauli-based MPO formalism, we can easily manage any Clifford transformation combined with a Magic gate or a local rotation.

Local rotation  
conjugation

We want to model, with tensor network, an arbitrarily complex Clifford operation  $C$  on  $N$  qubits and a local rotation gate  $R_l^\mu(\theta)$  acting on qubit  $l$ . This gives rise to the following Pauli-based MPO decomposition

$$C^\dagger R_l^\mu(\theta) C = \mathbb{I} \cos \theta/2 \mp i \Sigma^\gamma \sin \theta/2 = \mathbb{T}_1 \mathbb{T}_2 \cdots \mathbb{T}_N, \quad (175)$$

where the transformation relies on the property  $C^\dagger \sigma_l^\mu C = \pm \Sigma^\gamma$ , with indices  $\gamma = \gamma_1, \dots, \gamma_N$  depending on the Clifford transformation and the local rotation.

The operator-valued MPO, diagonal in the auxiliary basis, has a maximum bond dimension of two, taking the form of a controlled-Pauli gate. We denote the coefficients  $c \equiv \cos(\theta/2)$  and  $s \equiv \sin(\theta/2)$  as  $\phi = \{\phi_0, \phi_1\} = \{c^{1/N}, (\mp i s)^{1/N}\}$ . Indeed, we have that

$$\mathbb{T}_k = \begin{pmatrix} \phi_0 \mathbb{I}_k & 0 \\ 0 & \phi_1 \sigma_k^{\gamma_k} \end{pmatrix}, \quad (176)$$

for  $k = 2, \dots, N-1$ , and the boundary vectors

$$\mathbb{T}_1 = \begin{pmatrix} \phi_0 \mathbb{I}_1 & \phi_1 \sigma_1^{\gamma_1} \end{pmatrix}, \quad \mathbb{T}_N = \begin{pmatrix} \phi_0 \mathbb{I}_N \\ \phi_1 \sigma_N^{\gamma_N} \end{pmatrix}. \quad (177)$$

Therefore, it is apparent that it takes the following form in terms of a controlled Pauli matrix gate (where we omitted the subscript)

$$\hat{\mathbb{T}} = \begin{pmatrix} \phi_0 \hat{\sigma}^0 & 0 \\ 0 & \phi_1 \hat{\sigma}^{\gamma_n} \end{pmatrix} \rightarrow \langle i | \hat{\mathbb{T}}_{\alpha\beta} | j \rangle = \alpha \begin{array}{c} \begin{array}{c} j \\ \sigma^{\gamma_n} \end{array} \\ \text{---} \\ \begin{array}{c} \phi \\ \text{---} \\ i \end{array} \end{array} \quad (178)$$

where the indices  $\{\alpha, \beta\}$  span the two-dimensional auxiliary space.

The entire tensor network layer for the Clifford-transformed rotation gate is thus represented

$$\langle i_1, \dots, i_N | \hat{C}^\dagger \hat{R}_l^\mu(\theta) \hat{C} | j_1, \dots, j_N \rangle = \begin{array}{c} \begin{array}{c} j_1 \\ \sigma^{\gamma_1} \end{array} \\ \text{---} \\ \begin{array}{c} \phi \\ \text{---} \\ i_1 \end{array} \end{array} \begin{array}{c} \begin{array}{c} j_2 \\ \sigma^{\gamma_2} \end{array} \\ \text{---} \\ \begin{array}{c} \phi \\ \text{---} \\ i_2 \end{array} \end{array} \cdots \begin{array}{c} \begin{array}{c} j_N \\ \sigma^{\gamma_N} \end{array} \\ \text{---} \\ \begin{array}{c} \phi \\ \text{---} \\ i_N \end{array} \end{array} \quad (179)$$

This representation highlights that when  $\gamma_n = 0$  for some  $n$ , the physical and auxiliary spaces become locally disconnected, simplifying the network's complexity.

Importantly, the auxiliary space associated with each magic layer functions similarly to an additional qubit, forming a two-dimensional tensor network as depicted in Fig. 8. In this configuration, all local coefficients  $\phi$  are inserted into a single auxiliary qubit state  $|\theta\rangle = c|0\rangle \mp is|1\rangle$ , which accounts for the phase rotation.

### 3.3.2 Stabilizer Matrix Product Operator

As outlined earlier, our aim is to develop an efficient algorithm for computing the non-equilibrium dynamics of the expectation value of local operators, particularly Pauli strings. Specifically, we focus on calculating the expectation value as expressed below:

$$\langle \psi | U^\dagger \Sigma^\mu U | \psi \rangle, \quad (180)$$

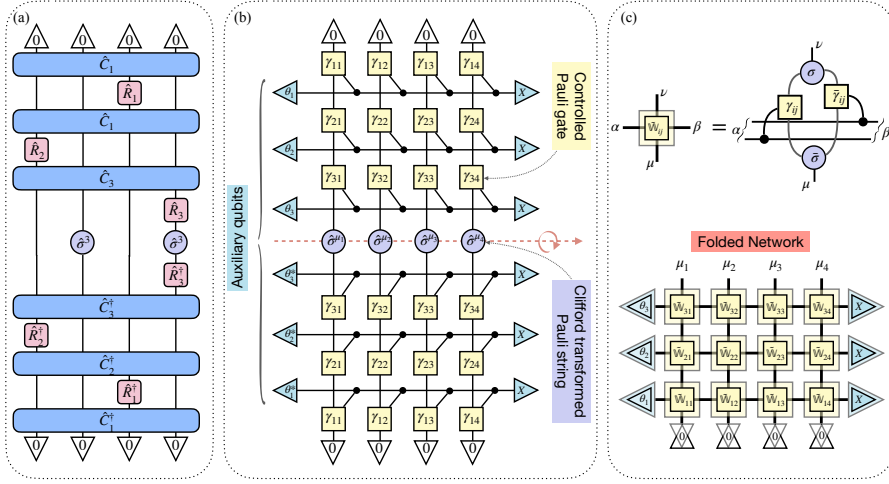


Figure 8: Tensor network contraction in the stabilizer MPO formalism. (a) Example of 3 layers of Clifford and Magic operations acting on 4 qubits initialised in  $|0000\rangle$ ; the network is contracted with its complex conjugate to compute the expectation value of a two-point function. (b) The transformed network, in the stabilizer MPO formalism, exhibits a bi-dimensional grid comprising Pauli gates  $\sigma^{\gamma_{ij}}$  (as depicted with subscripts only in the figure), controlled by auxiliary qubits  $|\theta_i\rangle \equiv \cos(\theta_i/2)|0\rangle \mp i \sin(\theta_i/2)|1\rangle$  (and  $|\theta_i^*\rangle$ ), which serve to induce slight entanglement between each individual row and all columns, i.e. the physical qubits. The majority of the entanglement is in fact effectively accounted for through a straightforward transformation of the original Pauli string. Finally each row of the entire network is contracted to the not normalised state  $|X\rangle \equiv |0\rangle + |1\rangle$ . (c) Folded tensor network in the Pauli basis as a bi-dimensional grid of  $\tilde{W}_{ij}$  4-order tensors, whose entries coincides with those of the  $W$  (see main text) after discarding the coefficient  $\phi_0$  and  $\phi_1$  which here are absorbed in the definition of the  $|\theta_i\rangle$  boundary vectors.

where  $|\psi\rangle$  denotes a state with short-range correlations. Despite the complexity, any unitary matrix can be broken down into a sequence (arbitrarily deep) of local Magic gates interspersed with Clifford circuits [93]. Consequently, we model our unitary as

$$U = R_{j_M} C_M \cdots R_{j_2} C_2 R_{j_1} C_1, \quad (181)$$

with  $M$  representing the total number of single-qubit Magic gates in the decomposition, and  $j_m$  indicating all the parameters of the local rotation  $R_{j_m}$ .

This decomposition generally leads to exponential computational complexity due to the unbounded amount of entanglement introduced by each Clifford layer. By strategically disentangling from the rightmost layer inserting  $C_1 C_1^\dagger$  as a disentangler for  $R_{j_1} C_1 |\psi\rangle$ ,

$$C_1 C_1^\dagger R_{j_1} C_1 |\psi\rangle = C_1 \mathbb{T}_{1,1} \mathbb{T}_{1,2} \cdots \mathbb{T}_{1,N} |\psi\rangle, \quad (182)$$

we progressively simplify the computation. Repeating this approach through all layers, we construct a *stabilizer MPO* as follows

$$U = \mathcal{C} \mathcal{T}_M \cdots \mathcal{T}_2 \mathcal{T}_1, \quad (183)$$

where each layer  $\mathcal{T}_m$  is defined as:

$$\mathcal{T}_m = C_1^\dagger \cdots C_m^\dagger R_{j_m} C_m \cdots C_1 = \mathbb{T}_{m,1} \mathbb{T}_{m,2} \cdots \mathbb{T}_{m,N}, \quad (184)$$



for  $m \in 1, 2, \dots, M$ , with the Clifford unitary  $\mathcal{C} = C_M \cdots C_1$ , and  $\mathcal{T}_m$  MPO of bond dimension 2. Consequently, the expectation value simplifies to:

$$\langle \psi | \mathcal{T}_1^\dagger \cdots \mathcal{T}_M^\dagger \Sigma^\nu \mathcal{T}_M \cdots \mathcal{T}_1 | \psi \rangle, \quad (185)$$

where  $\Sigma^\nu = \pm \mathcal{C}^\dagger \Sigma^\mu \mathcal{C}$ . This stabilizer MPO configuration significantly reduces the entanglement in comparison to the original unitary process. Additionally, horizontal contraction of the network during computation, as illustrated in Fig. 8, may mitigate the growth of temporal entanglement [96–98] relative to vertical contraction, potentially leading to a zero state due to the matrix elements vanishing.

*Folded tensor network*

Let us finally mention that this technique can be exploited in conjunction with the folding scheme where basically Eq. (185) can be evaluated as

$$\text{Tr}(\Sigma^\nu \mathcal{T}_M \cdots \mathcal{T}_1 | \psi \rangle \langle \psi | \mathcal{T}_1^\dagger \cdots \mathcal{T}_M^\dagger). \quad (186)$$

We can indeed represent the folded TN as

$$\sum_{\mu} \Upsilon_1^{\mu_1} \cdots \Upsilon_N^{\mu_N} \sigma^{\mu_1} \cdots \sigma^{\mu_N}. \quad (187)$$

Applying a new layer of the network induces a transformation of each local tensor according to (here we omit the subscripts to simplify the notation)

$$\Upsilon^\mu \rightarrow \sum_{\nu} \mathbb{W}^{\mu\nu} \Upsilon^\nu \quad (188)$$

where  $\mathbb{W}^{\mu\nu}$ , is a diagonal matrix acting on a four dimensional auxiliary space, whose entries are

$$\begin{aligned} \mathbb{W}^{\mu\nu} &= \frac{1}{2} \text{Tr}[\sigma^\mu \mathbb{T} \sigma^\nu \mathbb{T}^\dagger] \\ &= \text{diag}(|\phi_0|^2 \delta_{\mu\nu}, \phi_0 \phi_1^* \Gamma_{\mu\nu}, \phi_0^* \phi_1 \Gamma_{\nu\mu}, |\phi_1|^2 S_\mu \delta_{\mu\nu}), \end{aligned} \quad (189)$$

where

$$\Gamma_{\mu\nu} = \Gamma_{\nu\mu}^* = \text{Tr}(\sigma^\mu \sigma^\nu \sigma^\gamma) / 2 = i^{\varepsilon_{0\mu\nu\gamma}} \delta_{\mu \oplus \nu \gamma}, \quad (190)$$

and

$$S_\mu = \text{Tr}(\sigma^\mu \sigma^\gamma \sigma^\mu \sigma^\gamma) / 2 = -(-1)^{\delta_{\mu\gamma} + \delta_{\mu 0} + \delta_{\gamma 0}} \quad (191)$$

and  $\gamma$  accounts for the Pauli matrix appearing in  $\mathbb{T}$ . In the previous definitions,  $\varepsilon_{0\mu\nu\gamma}$  is the Levi-Civita symbol,  $\mu \oplus \nu$  is indicating the bit-wise xor between the indices (see Fig. 8(c) for a graphical representation of the folded network).

The strategy outlined in this section can be applied in various scenarios.

### 3.3.3 Random Clifford T-doped circuit

Our initial investigation focuses on random Clifford T-doped circuits. These circuits are made up of  $m$  brick-wall shaped random Clifford layers of depth  $D$ , each followed by a  $T_j$  gate targeting a randomly selected qubit  $j$ , as depicted in the left panel of Fig. 9.

We apply this approach to a system of  $N = 40$  qubits initialized in the state  $|0\rangle^{\otimes N}$ , subjected to  $M = 20$  intertwined brick-wall Clifford and local T-gate layers. The entanglement entropy for the half-chain, averaged across 50 realizations and shown in the right panels of Fig. 9, demonstrates this setup's efficacy for both  $D = 1$  and  $D = 6$  depths. Notably, our protocol, by effectively disentangling the state with a fixed resource allocation  $\chi$ , extends



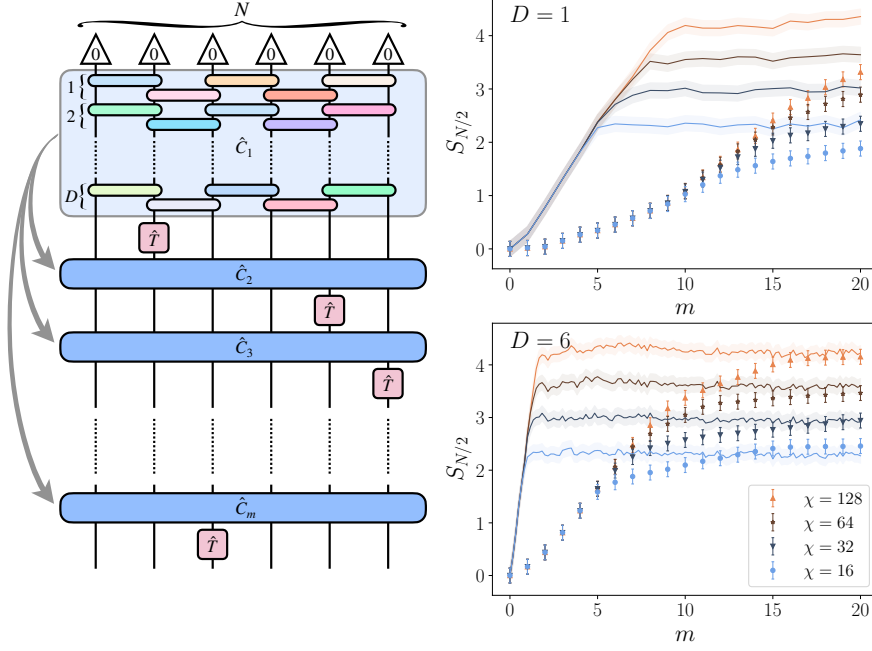


Figure 9: Random Clifford T-doped circuit. *Left panel*: sketch of the evolution. *Right panels*: evolution of the half-chain entanglement entropy of the state evolved according to the stabilizer-MPO formalism (dots) vs the standard full state entanglement entropy (solid lines). The system size is  $N = 40$ .

the feasible simulation depth compared to the traditional sequential gate application (indicated by solid lines). Notice that, multiple  $T$  gates acting simultaneously on the system can be addressed within the same setup.

Moreover, as illustrated in Fig. 10, we track the evolution of the averaged temporal-entanglement entropy  $\overline{\mathcal{S}}_{n,m}$  associated with the observable  $O = \sigma_{N/2}^3$ . For each random configuration,  $O$  is transformed through successive Clifford layers tailored to the specific  $m$  setting. Specifically, following the process outlined in Fig. 8(b), for each fixed evolution depth  $m$ , the left boundary auxiliary vector is systematically extended horizontally, progressively adding physical layers from  $n = 1$  to  $n = N$ . At each step, the symmetric bi-partited entanglement entropy is computed. Although in this setup the horizontal contraction does not lead to a significant advantage in terms of the employed resources, it paves the way for further studies in more specific settings.

### 3.3.4 Random Clifford Floquet Dynamics

In this section, we investigate Floquet dynamics induced by the repeated application of a single period evolution operator on the initial state  $|0\rangle^{\otimes N}$ :

$$U_m = \left( \prod_{j=1}^N R_j^1(\pi + 2\epsilon) \right) C_m \quad (192)$$

where  $m$  represents the step, and  $C_m$  are random  $U(1)$ -symmetric Clifford gates acting on  $N$  qubits. In particular, these gates commute with the operator  $M = \sum_j \sigma_j^3 / N$ , simulating typical Floquet behavior within a random Clifford framework [1, 21, 44, 63, 99]. The only deviation from perfect magnetization oscillation arises from a finite  $\epsilon$ .

Random  
 $U(1)$ -symmetric  
 Clifford kicked  
 Floquet dynamics

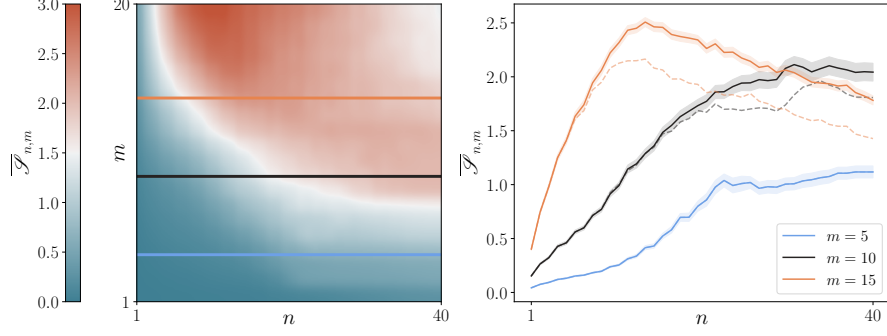


Figure 10: Random Clifford T-doped circuit. *Left panel*: evolution of the average half-chain temporal entanglement entropy  $\overline{\mathcal{F}}_{n,m}$ , for the observable  $O = \sigma_{N/2}^3$ , against the number of sites  $n$  and time  $m$ ; parameters  $D = 1$ , bond dimension  $\chi = 64$ . *Right panel*: line plot extracted from left panel for some values of  $m$ : dashed-line  $\chi = 32$ , solid line  $\chi = 64$ .

A general operator of the  $U(1)$ -symmetric Clifford group is constructed as follows [100]:

$$e^{i\phi} \left( \prod_{1 \leq i < j \leq N} CZ_{ij}^{\nu_{ij}} \right) \left( \prod_{j=1}^N S_j^{\mu_j} \right) P_n \quad (193)$$

where  $\mu_j \in \{0, 1, 2, 3\}$ ,  $\nu_{ij} \in \{0, 1\}$ ,  $\phi \in [-\pi, \pi]$ , and  $P_n$  is a permutation operator on  $n$  qubits, potentially using up to  $N(N-1)/2$  swap operations. Additionally,  $S = \text{diag}(1, i)$  is the single-qubit phase gate, and  $CZ = \text{diag}(1, 1, 1, -1)$  is the Controlled-Z gate. For our analysis, the global phase factor is irrelevant; thus, we set  $\phi = 0$ .

It is important to note that the highly non-local nature of the Clifford unitary layers  $C_m$  makes this setup challenging for standard Time Evolving Block Decimation (TEBD) algorithms [68], yet it is well-suited for our stabilizer MPO approach.

Here, we derive an analytical expression for the decay of magnetization throughout the evolution in a random Clifford Floquet setup. Henceforth, we denote by  $C$  a random Clifford operator from the  $U(1)$ -symmetric Clifford unitaries, which preserves magnetization. Let  $M_z = \sum_{i=1}^N Z_i/N$  be the magnetization operator. We aim to evaluate

$$\begin{aligned} \overline{Z_j}(m) &= \overline{\langle 0 \dots 0 | C_1^\dagger R^\dagger \dots C_m^\dagger R^\dagger Z_j R C_m \dots R C_1 | 0 \dots 0 \rangle} \\ &= \overline{\text{Tr} \left( Z_j R C_m \dots R C_1 | 0 \dots 0 \rangle \langle 0 \dots 0 | C_1^\dagger R^\dagger \dots C_m^\dagger R^\dagger \right)} \\ &= \overline{\langle Z_j | (R \otimes R^*) (C_m \otimes C_m^*) \dots (R \otimes R^*) (C_1 \otimes C_1^*) | 0 \dots 0, 0 \dots 0 \rangle} \end{aligned} \quad (194)$$

with  $R = \prod_{j=1}^N R_j^1(\pi + 2\epsilon)$ . Rewriting the discrete parametrization for the generic Clifford as  $C = CZ^{\vec{\nu}} S^{\vec{\mu}} P$ , we can graphically represent the quantity we are averaging as shown in Fig. 11.

The average in the three terms, i.e., permutations  $P$ ,  $S$  gates, and controlled-Z gates, appearing in the decomposition of  $C$  can be performed independently. Everything becomes immediately simpler by noticing that the average of the local  $S$  gates reads

$$S = \frac{1}{4} \sum_{\mu=0}^3 S^\mu \otimes S^{\mu*} = |00\rangle\langle 00| + |11\rangle\langle 11|. \quad (195)$$

The correlated action of  $CZ$  in two replicas of the system is thus trivial no matter the qubits on which it acts. Specifically, labeling with  $c$  ( $c'$ ) the

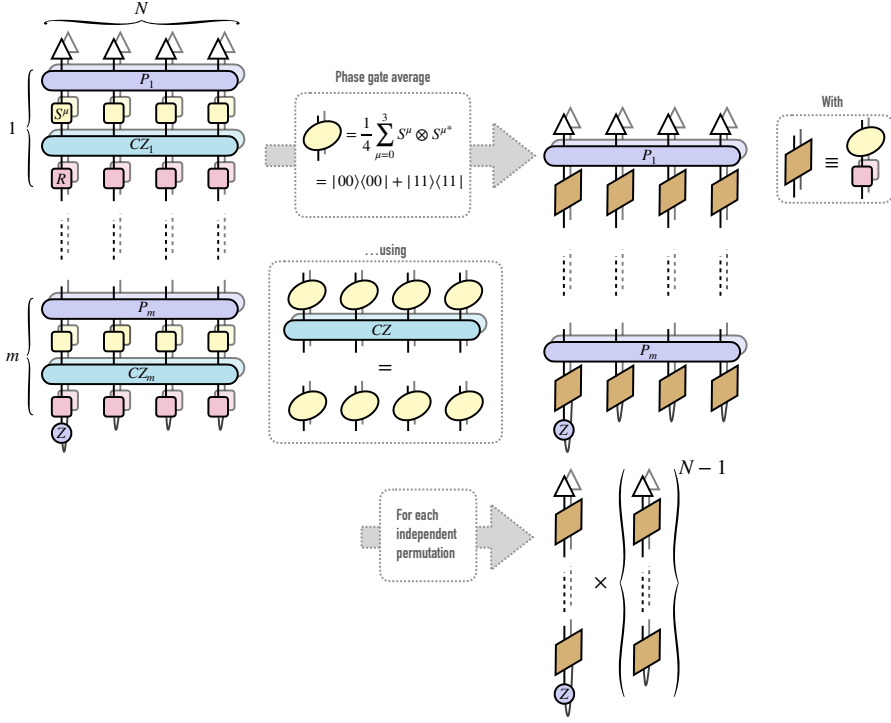


Figure 11: Sketch of the average over the U(1)-symmetric Clifford group, see the text for additional details.

control qubit of the system (replica), and with  $t$  ( $t'$ ) the target qubit of the system (replica), we have:

$$\begin{aligned} CZ_{ct} \otimes CZ_{c't'} (|00\rangle\langle 00| + |11\rangle\langle 11|)_{cc'} \otimes (|00\rangle\langle 00| + |11\rangle\langle 11|)_{tt'} &= \\ &= (|00\rangle\langle 00| + |11\rangle\langle 11|)_{cc'} \otimes (|00\rangle\langle 00| + |11\rangle\langle 11|)_{tt'}. \end{aligned} \quad (196)$$

Additionally, each permutation acts identically on the state and its replica. Apart from the application of the  $Z_j$  gate, the system is permutation invariant, hence any permutation contributes equally to the average.

We thus define the operator  $[R^1(\pi + 2\epsilon) \otimes R^{1*}(\pi + 2\epsilon)]S$  (brown boxes in Fig. 11) for which the states  $|00\rangle \pm |11\rangle$  are eigenstates with eigenvalues 1 and  $-\cos(2\epsilon)$  respectively. Consequently, all  $N - 1$  qubits where  $Z_j$  does not appear will contribute with  $(-1)^m$  for a  $m$ -layer evolution to the average in Eq. (194), and the only nontrivial contribution comes from the single qubit on which  $Z_j$  acts, yielding  $\bar{Z}_j(m) = (-1)^m [\cos(2\epsilon)]^m$ .

Fig. 12 displays the stabilizer MPO evolution of the averaged magnetization and entanglement entropy across various random realizations and for two distinct bond dimensions. We compare these numerical results with the exact analytical expression for average magnetization:

$$\overline{M_z/N}(m) = (-1)^m (\cos 2\epsilon)^m. \quad (197)$$

We observe a strong correspondence between the analytical predictions and the numerical simulations for small  $\epsilon$  values, a result unattainable with conventional tensor network methods.

### 3.4 CLIFFORD DRESSED TDVP

Simulating non-equilibrium dynamics in quantum many-body systems is challenging due to the exponential growth of Hilbert space and complex entanglement, often addressed by MPS which efficiently represent one-dimensional quantum states [15, 16, 68, 101–106].

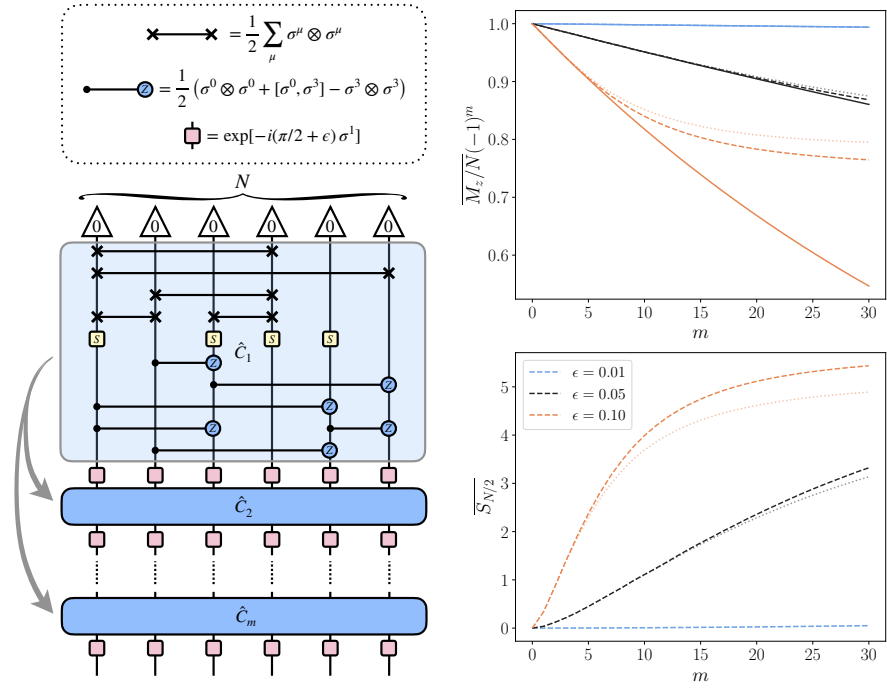


Figure 12: Random Clifford Floquet Dynamics. *Left panel*: sketch of the evolution. *Top right panel*: evolution of the kicked magnetization for some values of the kick strength  $\epsilon$  and  $N = 40$ . *Bottom right panel*: evolution of the half chain entanglement entropy. Solid lines, analytical prediction; dashed lines, bond dimension  $\chi = 512$ ; dotted lines, bond dimension  $\chi = 256$ .

A common method for simulating the non-equilibrium dynamics of a MPS wave function is to use Trotterization on the evolution operator. This process converts continuous Hamiltonian dynamics into a sequence of discrete, localized unitary gates acting on neighboring qubits, forming the core of the Time-Evolving Block Decimation (TEBD) scheme [68]. TEBD effectively manages real-time evolution by breaking down the complex, global evolution into simpler, local interactions.

On the other hand, the Time-Dependent Variational Principle (TDVP) method updates the MPS parameters directly within its specific variational framework [19, 20]. TDVP keeps the quantum state as an optimal MPS approximation throughout its evolution, offering a more precise representation of the system's dynamics. This is particularly useful for extended simulations and in situations with rapid entanglement increase. TDVP is crucial for investigating quantum dynamics such as quantum quenches [107], transport phenomena [108], and entanglement dynamics [109, 110], where conventional methods may not suffice due to the exponential growth of the Hilbert space.

Regardless of the method used, a quantum system in a non-equilibrium state undergoes quantum information scrambling, seen as entanglement spreading across the system [69, 70]. In the MPS framework, it manifests as an uncontrolled increase in the bond dimension. Consequently, after a certain time, this exponential growth in complexity results in a decline in the accuracy of the wave function's approximation because the MPS can no longer effectively encapsulate the system's entanglement.

As discussed in earlier sections, integrating the MPS framework with the stabilizer formalism presents notable challenges [64, 111, 112]. Indeed, strategically manipulating the wave function to manage quantum correlations can significantly enhance classical algorithms simulating quantum dynamics. Notably, circuits using only Clifford gates remain tractable on classi-

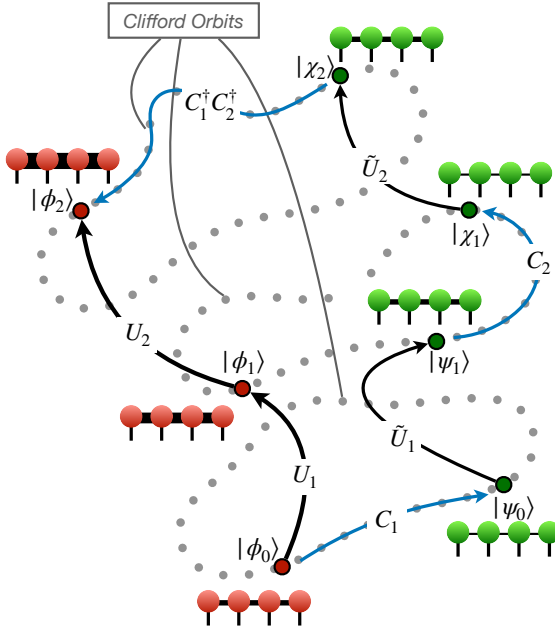


Figure 13: Clifford orbits. The evolution of the state  $|\phi_0\rangle$ , driven by the successive application of  $U_1$  and  $U_2$ , is transformed according to a modified evolution path  $\tilde{U}_2\tilde{U}_1$ . In this new trajectory, each intermediate state is strategically adjusted within its respective Clifford orbit to significantly reduce the entanglement in its MPS representation. This approach ensures that the MPS wave-function maintains a lower entanglement throughout the evolution, enhancing the efficiency and accuracy of the simulation.

cal systems, which allows high entanglement yet efficient classical simulation through the tableaux algorithm [64, 74–77]. This suggests that entanglement alone does not necessarily complicate classical simulations of quantum states.

Recent advancements have been made in this area, highlighted by the development of an efficient algorithm for identifying the stabilizer Pauli strings in an MPS [89, 113]. Further progress includes the creation of the stabilizer tensor network ansatz [114] and the introduction of Clifford enhanced MPS (cMPS) [115], which are quantum states formed by applying a Clifford unitary to an MPS. These innovations represent significant steps forward in the practical application of MPS within quantum computational frameworks.

An optimization algorithm for these states, specifically aimed at ground state searches, has effectively augmented the Density Matrix Renormalization Group (DMRG) with Clifford circuits, as proposed in Ref.[116]. Additionally, hybrid Clifford tensor network algorithms have been introduced in Refs.[2] and [117]. Building on these developments, the subsequent sections will explore a novel approach that integrates a Clifford-based disentanglement scheme with the TDVP algorithm, aiming to reduce the complexity of simulating out-of-equilibrium quantum systems.

### 3.4.1 Clifford disentangled 1-TDVP

The common scenario we explore involves the dynamics generated by the Hamiltonian  $H_0$ , starting with the system in a short-range correlated initial state (e.g., a product state) at time  $t = 0$ . The subscript zero in  $H_0$  indicates that the Hamiltonian is in its "bare" form, unaltered by any Clifford disentanglers.

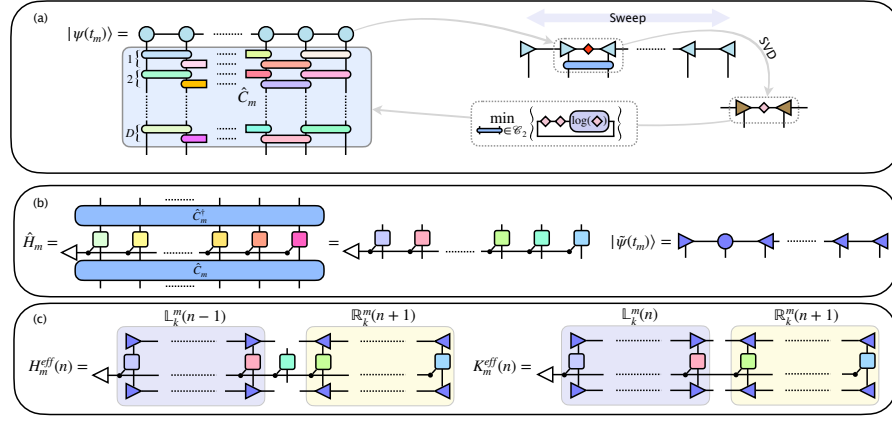


Figure 14: Clifford dressed evolution. (a) Clifford dressed TDVP steps, the disentangling routine optimally selects local Clifford two-qubit gates by minimizing the bipartite entanglement entropy, then sweeps along the chain up to a number of Clifford bi-layers of depth  $D$ . (b) At the end of the disentangling procedure, we obtain the Clifford dressed state  $|\tilde{\psi}(t_m)\rangle$ . The optimal Clifford transformation  $C_m$  is encoded using the stabilizer tableau and applied to the diagonal MPO Hamiltonian  $H_{m-1}$ , preserving its diagonal structure. (c) The effective operators for the next TDVP step are iteratively constructed from the MPS of the Clifford dressed state in mixed canonical form, and the MPO of the Clifford dressed Hamiltonian.

Our main focus is on evolving the state and monitoring local observables that are important for experiments. This includes calculating the expectation value of Pauli strings

$$\langle \psi(0) | e^{iH_0 t} \Sigma^\mu e^{-iH_0 t} | \psi(0) \rangle. \quad (198)$$

Typically, the time evolution of the state is implemented by dividing time into small intervals,  $dt$ . The state, approximated as an MPS with a set bond dimension  $\chi$ , is evolved using the single-site 1-TDVP scheme [20].

However, the entanglement entropy typically grows unboundedly, making the MPS representation inadequate as a wave function ansatz beyond a certain short time threshold. This is where Clifford-inspired disentangling strategies become relevant.

At each time step  $m \in \{1, \dots\}$ , corresponding to time  $t_m = m dt$ , a suitable Clifford transformation  $C_m$  is applied to the state  $|\psi(t_m)\rangle$  to reduce the entanglement in the new state

$$|\tilde{\psi}(t_m)\rangle = C_m |\psi(t_m)\rangle. \quad (199)$$

The disentangling routine, known as "entanglement cooling" [115, 118–121], modifies the Hamiltonian as follows

$$H_m = C_m H_{m-1} C_m^\dagger. \quad (200)$$

This transformation can be efficiently executed using the stabilizer tableau formalism [122].

Practically, we can rewrite the original discrete evolution

$$\prod_{m=0}^{\lfloor t/dt \rfloor - 1} e^{-iH_0 dt} |\psi(0)\rangle \quad (201)$$

Clifford dressed evolution

as a Clifford dressed evolution (see Fig. 14(a)):

$$\prod_{m=0}^{\lfloor t/dt \rfloor - 1} e^{-iH_m dt} C_m |\psi(0)\rangle, \quad (202)$$

where  $C_0 = \mathbb{I}$  is the identity operator, and the product is understood to be in reverse order. The Clifford dressed evolution iteratively constructs the final CMPS resulting in [115]

$$C_{\lfloor t/dt \rfloor - 1} \cdots C_1 e^{-iH_0 t} |\psi(0)\rangle. \quad (203)$$

Additionally, at each time step  $t_m$ , any Pauli string of interest for measurement is transformed as

$$C_m \cdots C_1 \Sigma^\mu C_1^\dagger \cdots C_m^\dagger. \quad (204)$$

Note that we assume the application of a Clifford disentangler at each time step in the TDVP integrator. However, this is not strictly necessary. The entanglement cooling routine could be applied less frequently, for instance, every  $k$  time steps, to reduce computational overhead while still controlling entanglement growth.

The disentangling routine constructs the optimal Clifford operator iteratively by sweeping over two-qubit Clifford unitaries that connect neighboring sites in a checkerboard pattern [115, 118], with the number of bi-layers denoted by  $D$  (see Fig. 14(b)). The optimal two-qubit Clifford gate is selected by searching through a subset of 720 Clifford tableaux with positive sign [122] and choosing one at random that minimizes the von Neumann entanglement entropy. While the sign of the tableau does not affect the local Singular Value Decomposition (SVD) of the MPS tensors, it may influence subsequent minimizations, prompting us to reintroduce a random sign from the  $2^4$  possible configurations. This process is repeated, sweeping sequentially back and forth across the entire chain.

We employ the 1-TDVP scheme, a symplectic integrator, to evolve the state from  $t_m$  to  $t_{m+1}$ , projecting the dressed Hamiltonian  $H_m$  using the MPS tensors of the Clifford-enhanced state

$$|\tilde{\psi}(t_m)\rangle = \mathbb{A}_L^{s_1} \cdots \mathbb{A}_L^{s_{n-1}} \mathbb{A}_C^{s_n} \mathbb{A}_R^{s_{n+1}} \cdots \mathbb{A}_R^{s_N} |s_1, \dots, s_N\rangle, \quad (205)$$

which is in mixed canonical form with respect to the central site  $n$ . This setup allows us to define the effective Hamiltonian (see Fig. 14(c))

$$H_m^{\text{eff}}(n) = \sum_k^{O(N)} J_k \mathbb{L}_k^m(n-1) \otimes \sigma_n^{\mu_k} \otimes \mathbb{R}_k^m(n+1), \quad (206)$$

remaining diagonal in the operator auxiliary dimension, as  $H_m$  is kept diagonal in the Pauli basis. The couplings  $J_k$  are associated with each Pauli string. A similar transformation is applied for  $K_m^{\text{eff}}(n)$ , with further details on the TDVP algorithm in the context of MPS provided in Ref. [20].

### 3.4.2 Clifford Dressed 1-TDVP Numerical Experiments

We benchmark our algorithm on the following bare Hamiltonian

*Benchmark  
hamiltonian*

$$\begin{aligned} H_0 = & J_1^x \sum_{j=0}^{N-2} \sigma_j^1 \sigma_{j+1}^1 + J_1^y \sum_{j=0}^{N-2} \sigma_j^2 \sigma_{j+1}^2 + \\ & + J_2^x \sum_{j=0}^{N-3} \sigma_j^1 \sigma_{j+2}^1 + h \sum_{j=0}^{N-1} \sigma_j^3. \end{aligned} \quad (207)$$

Specifically, after fixing the MPS bond dimension  $\chi$ , that is the amount of employable resources, we compare the standard 1-TDVP with our novel strategy where the Clifford disentangler routine is invoked every  $k$  time steps (for various values of  $k$ ).



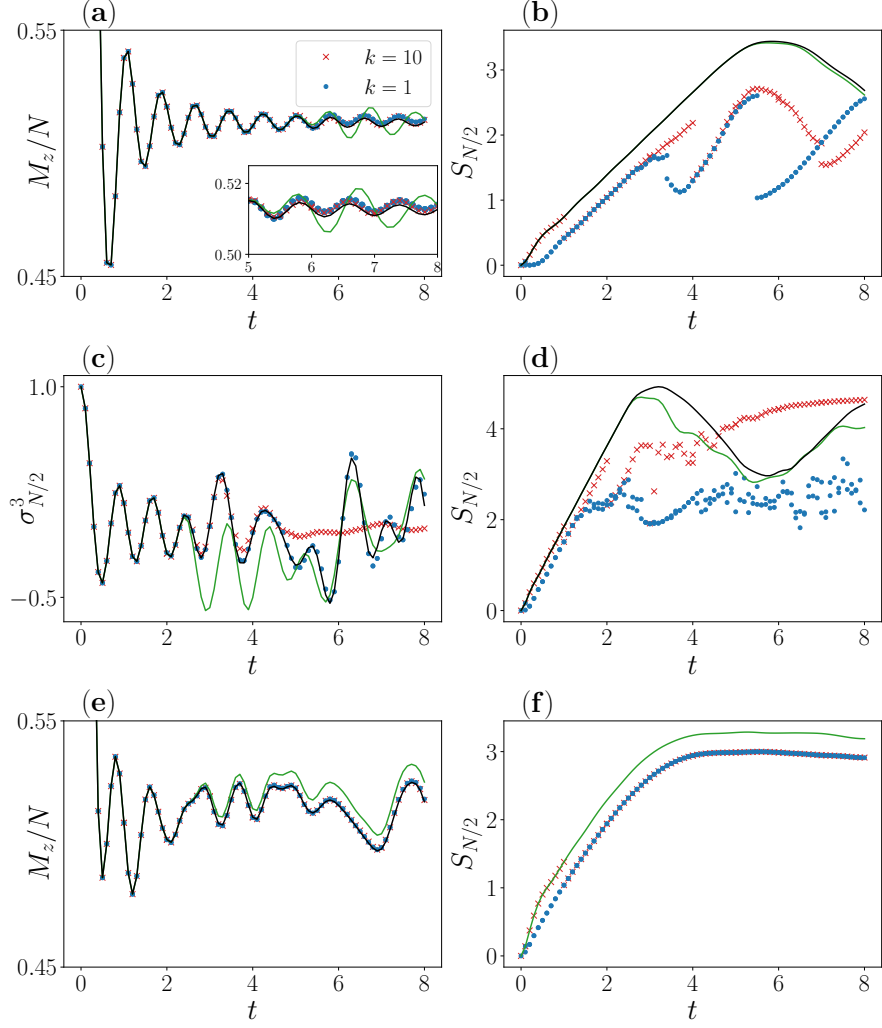


Figure 15: (a) Average magnetization and (b) half-chain entanglement entropy for the critical transverse field Ising model. (c) Half-chain magnetization and (d) half-chain entanglement entropy for the XX model. (e) Average magnetization and (f) half-chain entanglement entropy for the next-to-nearest-neighbors Ising chain. Black lines represent free-fermions (upper and central panels) or ED results (lower panel). Solid green lines are TDVP data. Markers indicate the Clifford disentangler, applied every  $k$  time steps (see legend in the upper panel). In all panels we set  $N = 20$ ,  $\chi = 128$ .

Firstly, we consider two integrable cases by setting  $J_2^x = 0$  in Eq. (207). Specifically, the critical quantum Ising chain  $J_1^y = 0$ ,  $J_1^x = -h = 1$  prepared in the fully polarized state  $|00\dots 0\rangle$  along the  $z$  direction, and, the XX model with  $J_1^x = J_1^y = 1$  and  $h = 0$  prepared in the Néel state  $|0101\dots 01\rangle$ . Finally, we consider the non-integrable next-to-nearest-neighbors Ising model by setting  $J_2^x = J_1^x = -h = 1$  and  $J_1^y = 0$  prepared in  $|00\dots 0\rangle$ .

During the time evolution, we monitor the dynamics of the bipartite entanglement entropy at the midpoint of the chain, noting discontinuities each time a Clifford disentangler is applied.

To assess the algorithm's ability to accurately reproduce the expectation values of local observables (which may become non-local post-Clifford dressing), we measure the half-chain magnetization  $\sigma_{N/2}^3$  in the XX model. This model possesses a  $U(1)$  symmetry, ensuring conservation of total magnetization. Conversely, in the Ising model, we compute the average magnetization  $M_z/N = \sum_{j=0}^{N-1} \sigma_j^z/N$ . These quantities, which are not conserved, undergo



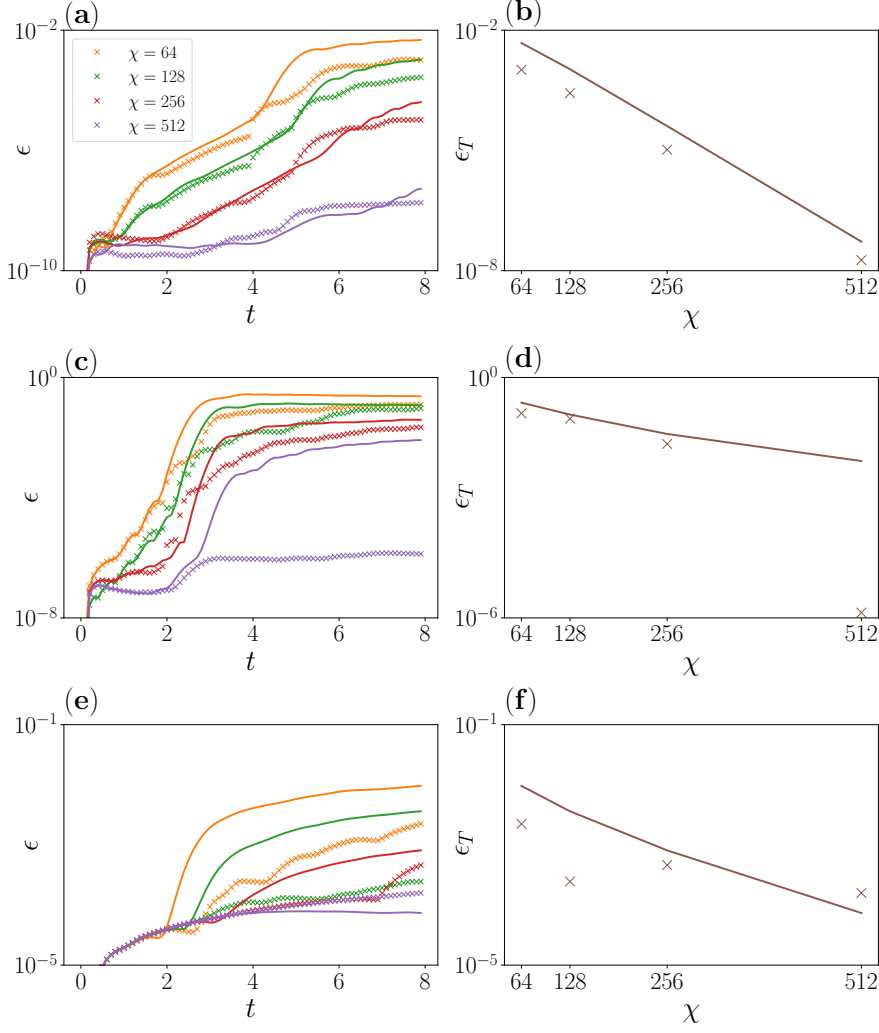


Figure 16: Error on expectation value of observables (same observables as in Fig. 15). (a)(c)(e) Integrated error  $\epsilon(t)$ , and (b)(d)(f) integrated error at final time  $\epsilon_T$  ( $T = 8$ ). (a)(b) Critical transverse field Ising model. (c)(d) XX model. (e)(f) Next-to-nearest-neighbors Ising chain. Solid lines are TDVP data. Markers indicate the Clifford disentangler, applied every  $k = 10$  time steps. We set  $N = 20$  and explore different bond dimensions  $\chi$  (see legend in the upper panel).

nontrivial evolution. The XX model and the critical nearest-neighbors Ising model are exactly solvable, allowing us to validate our numerical results against exact solutions derived from free-fermion techniques. For the next-to-nearest-neighbors Ising model, we rely on comparisons with exact diagonalization (ED) calculations.

We define a measure of the error up to time  $t$  as the integrated distance between the exact expectation value of an observable  $O(t)$  and the corresponding value obtained with either TDVP or Clifford enhanced TDVP denoted as  $\tilde{O}_\chi(t)$  (for fixed  $\chi$ ), i.e.

$$\epsilon(t) = \frac{1}{t} \int_0^t |\tilde{O}_\chi(t') - O(t')| dt'. \quad (208)$$

We also define the integrated error at final time as  $\epsilon_T = \epsilon(T)$ . As mentioned, in our case  $O$  corresponds to either the average magnetization or the on site half-chain magnetization.

Fig. 15 displays the results for the observable evolution and the half-chain entanglement entropy in all analyzed models for a fixed bond dimension

*Integrated error*

$\chi = 128$  and system size  $N = 20$ . The corresponding panels in Fig. 16 illustrate the evolution of the error  $\epsilon(t)$  for  $k = 10$ .

For the critical Ising chain, as shown in Figs. 15(a) and 15(b), our approach effectively limits the growth of entanglement entropy and enables us to achieve higher precision in magnetization dynamics compared to the standard 1-TDVP, which becomes ineffective around  $t \approx 5$  due to the entanglement exceeding the bond dimension  $\chi$ .

Remarkable results are observed for the XX model in Figs. 15(c) and 15(d), where the 1-TDVP simulation breaks down around  $t \approx 2$ . The Clifford dressed evolution closely matches the exact solution for significantly longer times, demonstrating several orders of magnitude improvement in precision using the same resources.

Finally, Figs. 15(e) and 15(f) pertain to the non-integrable setup, where disentangling the evolved state poses greater challenges than in the previous scenarios. Nonetheless, the evolution of the Clifford dressed observable appears to align with the results provided by exact diagonalization (ED) for  $\chi \leq 128$ . The integrated error, unlike in other case studies, does not indicate a significant advantage.

### 3.5 CONCLUSION & OUTLOOK

In this Chapter, we have introduced two complementary strategies aimed at enhancing the simulation of quantum many-body dynamics. First, we developed a hybrid method that incorporates the stabilizer formalism with tensor network techniques, specifically through our stabilizer MPO approach, which efficiently leverages Clifford transformations to disentangle quantum states. This method significantly reduces the complexity of unitary evolution, facilitating the computation of expectation values of Pauli strings and enabling extended simulation depths beyond standard techniques. Furthermore, we have enhanced the standard single-site 1-TDVP algorithm by integrating optimized Clifford disentanglers to manage entanglement growth effectively.

The potential for future research is vast. Immediate directions include optimizing Clifford disentanglers more effectively, potentially by introducing finite temperature strategies or optimizing multiple local gates simultaneously to avoid sub-optimal local minima. An extension to the two-site TDVP (2-TDVP) is also envisioned, which would involve applying a two-qubit Clifford disentangler to disentangle the state prior to SVD, thereby maintaining locality while managing entanglement efficiently. Additionally, there is significant potential for utilizing our methods in benchmarking quantum devices by facilitating precise comparisons between classical simulations and quantum hardware performance.

Moreover, a crucial theoretical question remains unanswered: how to quantitatively assess the effectiveness of our ansatz and distinguish between quantum states that can be significantly Clifford disentangled and those for which it is infeasible. Investigating the entanglement spectrum statistics may provide insights into the irreversibility of entanglement and help elucidate the full scope of our methods' benefits and limitations [120, 121].





## Part III

### MONITORED QUANTUM SYSTEMS

In the third part, we explore the dynamics of open quantum systems, with a particular emphasis on monitored quantum systems and measurement-induced phase transitions. We focus on unraveling the Lindblad equation, which describes the evolution of the density matrix in open quantum systems subject to non-Hamiltonian dynamics. We explore various unraveling techniques and their implications for system dynamics, highlighting the interplay between system-environment interactions and measurement processes.



Quantum systems at zero temperature, described by a Hamiltonian  $H = H_1 + gH_2$  with non-commuting parts  $[H_1, H_2] \neq 0$ , can exhibit different phases depending on the parameter  $g$ . By adjusting  $g$ , quantum fluctuations may induce a transition in the many-body ground state, known as a quantum phase transition [123, 124]. This interplay between non-commuting operators is fundamental in quantum mechanics, influencing correlations and frustration in many-body systems.

In reality, quantum systems are not perfectly isolated and interact with external environments. Studying open systems is essential for accurately describing quantum evolution observed in experiments. Isolated systems evolve unitarily according to the Schrödinger equation, but external interactions introduce non-unitary and stochastic dynamics [125, 126]. This interaction causes phenomena such as decoherence and dissipation, offering insights into the link between quantum and classical dynamics [127], and is vital for developing quantum technologies [128].

Recently, the study of monitored systems, where measurement apparatuses act as environments, has gained attention. Quantum measurements affect system dynamics through stochastic back-action. Any potential stochastic evolution is called a quantum trajectory [129–132]. The average state results from averaging over these trajectories and, under typical assumptions, evolves according to the Lindblad equation, which erases the details of the measurement protocols [125]. Conversely, quantum trajectories can be derived by unraveling the Lindblad equation [133–137], with different protocols leading to diverse noisy dynamics such as quantum jumps or diffusion [138–140].

By focusing on the properties of the ensemble of quantum trajectories, we identify a series of non-equilibrium phase transitions known as measurement-induced phase transitions (MIPT). This effect is similar to transitions driven by the non-commutativity between generators of unitary dynamics and measured operators, leading to distinct stationary states. In fact, analyzing full-counting statistics of quantum trajectories reveals phenomena not typically visible in ensemble averages [141–144], such as measurement-induced entanglement phase transitions (MIPT) [4, 145–172], quantum error correction and information scrambling, [173, 174], and dynamical purification [175–177]. This has been investigated in quantum circuits [14, 145, 149–151, 168, 178–189], quantum spin systems [154, 190–201], trapped atoms [202], and trapped ions [203–205].

Specifically, regarding the growth of entanglement, we observe a shift from the expected bipartite entanglement entropy growth over time in a closed system, as described by the Cardy-Calabrese quasiparticle model. [69, 109, 206, 207], where the system thermalizes (in a generalized Gibbs sense), characterized by highly entangled eigenstates that scale extensively with volume [208–210]. In contrast, projective quantum measurements inhibit entanglement growth, illustrated by the quantum Zeno effect [211–215], where continuous measurements interfere with the system dynamics. However, the average entanglement entropy can still transition between logarithmic and area law phases at critical measurement strength, or display purely logarithmic scaling depending on the stochastic protocol [156]. A logarithmic growth of entanglement entropy is intriguing, as the average state is expected to be effectively thermal, hinting at a critical, conformally-invariant phase. Similar findings exist for free-fermion random circuits with

temporal randomness [216], recently extended to higher dimensions [217], and for Majorana random circuits [218, 219]. The persistence of logarithmic entanglement entropy in the thermodynamic limit remains debated, as different models and protocols yield varied conclusions. For instance, [164] demonstrates that stationary entanglement entropy averages show area-law behavior at any finite measurement rate in the thermodynamic limit. A logarithmic scaling remnant appears only for finite sub-system sizes, with a characteristic scaling law between sizes and measurement rate established.

In the next chapters, we will present results concerning the full counting statistics of monitored quantum systems. However, before that, we will revisit some notions related to monitored quantum systems.

#### 4.1 MEASUREMENT PROTOCOLS

Measurement in quantum mechanics is a fundamental aspect that significantly influences the state of a quantum system. The nature of quantum measurements can be broadly categorized into two types: projective (or strong) measurements, which are typically associated with quantum jumps, and weak measurements.

##### 4.1.1 Quantum Jumps

Consider a quantum many-body system, with the total Hilbert space  $\mathcal{H} = \bigotimes_j \mathcal{H}_j$  being the tensor product of single-particle Hilbert spaces  $\mathcal{H}_j$ . If the system is isolated from the environment, it evolves according to the Schrödinger equation

$$|\psi(t)\rangle = e^{-i\hat{H}t} |\psi(0)\rangle, \quad (209)$$

where  $\hat{H}$  is the full interacting Hamiltonian of the system and  $|\psi(0)\rangle$  is the initial state.

Assume that the unitary dynamics are sporadically disrupted by local measurements. Each local Hilbert space  $\mathcal{H}_j$  is briefly coupled to a measurement apparatus that measures a local observable  $\hat{O}_j = \sum_{k=1}^K o_k \Pi_j^{(k)}$ , where  $o_k$  are the possible outcomes and  $\Pi_j^{(k)}$  are the corresponding projection operators. These measurements occur at discrete time intervals  $dt$  with a characteristic rate  $\gamma$ . When a measurement occurs, the state  $|\psi\rangle$  is projected according to Born's rule

*Strong projective  
measurement*

$$|\psi\rangle \rightarrow \frac{\Pi_j^{(k)} |\psi\rangle}{\sqrt{P(k)}}, \quad (210)$$

with probability  $P(k) = \langle \psi | \Pi_j^{(k)} | \psi \rangle$ . According to this protocol, the evolution of the many-body state  $|\psi(t)\rangle$  depends on the series of measurement events and their results, featuring occasional quantum jumps that are sudden transitions in the quantum system. Notice that the quantum state is pure during the entire evolution.

##### 4.1.2 Weak-measurements

Here, we introduce the concept of weak-measurements and derive the stochastic Schrödinger equation (SSE) for continuously monitored quantum dynamics [131, 220].

A weak measurement is a measurement that extracts partial information from a quantum system. The traditional way of describing a quantum mea-



surement, referred to as von Neumann projective measurements, is to write the state of the system into the eigenstates of a given observable  $O$ , namely

$$|\psi\rangle = \sum_{\alpha} c_{\alpha} |\alpha\rangle, \quad O = \sum_{\alpha} o_{\alpha} |\alpha\rangle\langle\alpha|. \quad (211)$$

The probability  $P(\alpha)$  of measuring  $o_{\alpha}$  and thus projecting the state of the system into  $|\alpha\rangle$  is  $|c_{\alpha}|^2$ . The state of the system state therefore transforms as

$$\rho = |\psi\rangle\langle\psi| \longrightarrow \rho_f = |\alpha\rangle\langle\alpha| = \frac{\Pi_{\alpha}\rho\Pi_{\alpha}}{\text{Tr}\{\Pi_{\alpha}\rho\Pi_{\alpha}\}}, \quad (212)$$

with  $P(\alpha) = \text{Tr}\{\Pi_{\alpha}\rho\Pi_{\alpha}\} = |c_{\alpha}|^2$ . Such a measurement leaves completely projects  $\rho$  in an eigenstate of the observable, thus extracting maximal information.

Generalized measurements are described in terms of POVMs, i.e. positive operator-valued measures. Consider a set of operators  $L_{\alpha}$  such that  $\sum_{\alpha} L_{\alpha}^{\dagger}L_{\alpha} = \mathbb{I}$ . The measurement process can be described in a similar fashion by transforming

$$\rho \longrightarrow \rho_f = \frac{L_{\alpha}\rho L_{\alpha}^{\dagger}}{\text{Tr}\{L_{\alpha}\rho L_{\alpha}^{\dagger}\}} \quad (213)$$

with probability  $P(\alpha) = \text{Tr}\{L_{\alpha}\rho L_{\alpha}^{\dagger}\}$ .

The following simple model provides a clear illustration of a weak projective measurement. Consider a two-level ancilla, represented by the eigenstates  $\{|+\rangle, |-\rangle\}$  of the Pauli matrix  $\sigma_z$ , initially prepared in the state

$$|\alpha\rangle = \frac{|+\rangle + |-\rangle}{\sqrt{2}}. \quad (214)$$

The ancilla is coupled to the system of interest, represented by the state  $|\psi_t\rangle$ . Let both the ancilla and the system evolve over a time  $\Delta t$  under the unitary evolution operator,  $\hat{U}_{S+A}(\Delta t)$

$$\hat{U}_{S+A}(\Delta t) |\psi_t\rangle |\alpha\rangle = (L_+ |\psi_t\rangle) |+\rangle + (L_- |\psi_t\rangle) |-\rangle, \quad (215)$$

where  $L_{\pm} = \langle\pm|\hat{U}_{S+A}(\Delta t)|\alpha\rangle$  act exclusively on the system's Hilbert space. Following this evolution, a projective measurement acts on the ancilla along the  $z$ -axis, resulting in the outcome  $\alpha = \pm 1$ . As a result, the back-action of the measurement places the system in the state

$$|\psi_{t+\Delta t}\rangle = \frac{L_{\alpha} |\psi_t\rangle}{\sqrt{\langle\psi_t|L_{\alpha}^{\dagger}L_{\alpha}|\psi_t\rangle}}. \quad (216)$$

### 4.1.3 Continuous limit

Let us now consider the continuous limit  $\Delta t \rightarrow 0$ . We have to derive the explicit form of the operators  $L_{\pm}$ . If we want to measure the observable  $X$ , let us consider the coupling between a system  $S$  and an ancilla  $A$  of the form

$$H_{S+A} = H + \lambda X \sigma_y. \quad (217)$$

We now take the limit  $\Delta t \rightarrow 0$ , scaling lambda in such a way that  $\gamma = \lambda^2 \Delta t$  is kept constant. Expanding the propagator  $U$  we have

$$\begin{aligned} U_{S+A} &= e^{-i(\Delta t H + \sqrt{\gamma \Delta t} X \sigma_y)} \\ &= 1 - i\Delta t H - i\sqrt{\gamma \Delta t} X \sigma_y - \frac{1}{2}\gamma \Delta t O^2 + O(\Delta t^{3/2}) \end{aligned} \quad (218)$$

We thus obtain for the  $L_{\pm}$

$$L_{\pm} = \frac{1}{\sqrt{2}} \left( 1 - i\Delta t H \mp \sqrt{\gamma\Delta t} X - \frac{1}{2}\gamma\Delta t X^2 \right). \quad (219)$$

In order to compute the norm, we expand

$$L_a^\dagger L_a = \frac{1}{2} - \alpha\sqrt{\gamma\Delta t} X, \quad (220)$$

while the corresponding probabilities become

$$P(a) = \frac{1}{2} - \alpha\sqrt{\gamma\Delta t} \langle X \rangle. \quad (221)$$

It follows that

$$\begin{aligned} |\psi_{t+\Delta t}\rangle &= |\psi_t\rangle - iH\Delta t |\psi_t\rangle - \alpha\sqrt{\gamma\Delta t}(X - \langle X \rangle) |\psi_t\rangle \\ &\quad + \frac{3}{2}\gamma\Delta t \langle X \rangle^2 |\psi_t\rangle - \gamma\Delta t \langle X \rangle X |\psi_t\rangle - \frac{1}{2}\gamma\Delta t X^2 |\psi_t\rangle \end{aligned} \quad (222)$$

Finally, we have to put this in the form of a stochastic equation. To this aim we observe that the measurement outcome  $a$  is a random variable that satisfies

$$\bar{a} = -2\sqrt{\gamma\Delta t} \langle X \rangle, \quad \bar{a}^2 = 1. \quad (223)$$

Let us thus introduce  $Y_t = \sqrt{\Delta t} \sum_{t' \leq t} a$ : in the limit  $\Delta t \rightarrow 0$  this converges to a continuous stochastic variable such that

$$dY = -2\sqrt{\gamma} \langle X \rangle dt + d\xi, \quad (224)$$

where  $\xi_t$  is a real Wiener process (i.e.  $\overline{d\xi} = 0$  and  $\overline{d\xi^2} = dt$ ). Replacing  $a \rightarrow dY/\sqrt{\Delta t}$  and using (224) in the limit  $\Delta t \rightarrow 0$ , we recover

*Continuously  
monitored quantum  
system*

$$\begin{aligned} d|\psi\rangle &= -iHdt |\psi_t\rangle + \\ &\quad \left( \sqrt{\gamma}(X - \langle X \rangle)d\xi - \frac{\gamma}{2}(X - \langle X \rangle)^2 dt \right) |\psi_t\rangle \end{aligned} \quad (225)$$

#### 4.1.4 Lindblad Dynamics Average State

Here, we discuss the evolution of the mean quantum state  $\rho = \overline{|\psi\rangle\langle\psi|}$  by averaging across all the realization of the noise

$$d\rho = \overline{|\overline{d\psi}\rangle\langle\overline{\psi}| + |\overline{\psi}\rangle\langle\overline{d\psi}| + |\overline{d\psi}\rangle\langle\overline{d\psi}|}. \quad (226)$$

The time evolution of  $\rho$  can be described by

$$\frac{d\rho}{dt} = -i[H, \rho] - \frac{\gamma}{2}[X, [X, \rho]], \quad (227)$$

depicted in a master equation of the Lindblad form. The observable  $X$  functions as the jump operator, representing the interaction with the external environment. Given that the jump operator is Hermitian, for any finite dimension  $N$ , the Lindblad dynamics will evolve towards the maximally mixed state within any symmetry sector of the Hilbert space, thereby erasing all initial state information of  $\rho(0)$  except for invariant subspaces [131, 221]. In the absence of symmetry,  $\rho(t \rightarrow \infty) \propto \mathbb{I}$  across the entire Hilbert space. It is important to note that various measurement protocols yield the same average quantum state.

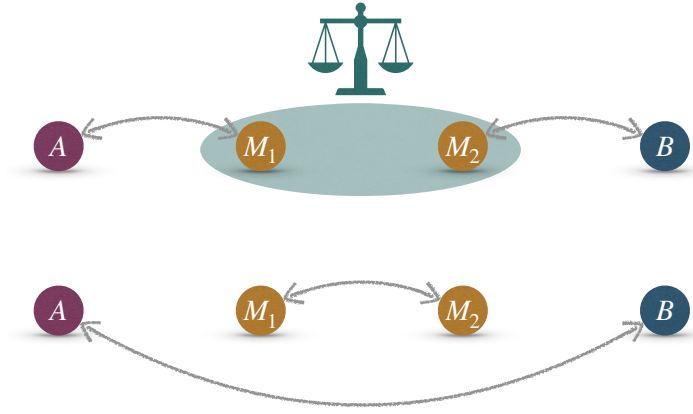


Figure 17: Entanglement Swapping: initially  $(A, M_1)$  and  $(M_2, B)$  are entangled. After measuring  $M = (M_1, M_2)$  in the Bell basis, we entangle  $(A, B)$ , establishing a quantum correlation previously absent.

#### 4.2 LOCAL MEASUREMENTS HAVE A NON-LOCAL EFFECT ON ENTANGLED STATES

Before analyzing the role that projective measurements play in many-body systems, as a warm-up let us start our analysis by exploring the phenomenon of measurement-induced entanglement swapping, demonstrating the non-local effects that local measurements can have on entangled states; see Fig. 17 for a scheme of the process.

To illustrate this concept, we consider a simple four-qubit system involving two distant components, Alice (denoted as qubit  $A$ ) and Bob (denoted as qubit  $B$ ), and a composite system  $M$  represented by qubits  $M_1$  and  $M_2$ , which will be measured.

Let us introduce the Bell basis  $\{|\Phi^\pm\rangle, |\Psi^\pm\rangle\}$  of a pair of qubits

$$|\Phi^\pm\rangle = \frac{1}{\sqrt{2}} (|00\rangle \pm |11\rangle), \quad (228)$$

$$|\Psi^\pm\rangle = \frac{1}{\sqrt{2}} (|01\rangle \pm |10\rangle). \quad (229)$$

We begin with an initial state where Alice and Bob share a Bell state with the composite system  $M$ , so that the global system state  $|\psi\rangle$  is given by

$$\begin{aligned} |\psi\rangle &= \left| \Phi_{AM_1}^+ \right\rangle \left| \Phi_{M_2B}^+ \right\rangle \\ &= \frac{1}{2} (|0_A 0_{M_1}\rangle + |1_A 1_{M_1}\rangle) (|0_{M_2} 0_B\rangle + |1_{M_2} 1_B\rangle). \end{aligned} \quad (230)$$

Next, we want to perform a projective measurement on the composite system  $M$  in the Bell basis. To this extent it is convenient to write the state  $|\psi\rangle$  in terms of the Bell pairs of  $M$

$$\begin{aligned} |\psi\rangle &= \frac{1}{2} \left[ |0_A 0_B\rangle \frac{|\Phi_M^+\rangle + |\Phi_M^-\rangle}{\sqrt{2}} + |1_A 1_B\rangle \frac{|\Phi_M^+\rangle - |\Phi_M^-\rangle}{\sqrt{2}} \right. \\ &\quad \left. + |0_A 1_B\rangle \frac{|\Psi_M^+\rangle + |\Psi_M^-\rangle}{\sqrt{2}} + |1_A 0_B\rangle \frac{|\Psi_M^+\rangle - |\Psi_M^-\rangle}{\sqrt{2}} \right]. \end{aligned} \quad (231)$$

The measurement results in the generation of one of the following entangled pairs between Alice and Bob, each occurring with equal probability

$$\begin{aligned} |\psi_1\rangle &= |\Phi_{AB}^+\rangle |\Phi_M^+\rangle, & |\psi_2\rangle &= |\Phi_{AB}^-\rangle |\Phi_M^-\rangle, \\ |\psi_3\rangle &= |\Psi_{AB}^+\rangle |\Psi_M^+\rangle, & |\psi_4\rangle &= |\Psi_{AB}^-\rangle |\Psi_M^-\rangle. \end{aligned} \quad (232)$$

*Entanglement swapping*

Our simplified model highlights the non-local characteristics of quantum systems, where local measurements performed on one segment of the system can instantaneously influence the entangled relationships among distant particles. Specifically, when measurements are conducted non-locally in the Bell basis—a fundamental set of states used to demonstrate quantum correlations—the system  $M$  establishes a quantum correlation between components  $A$  and  $B$  that was not previously present. This behavior underscores the intriguing aspect of quantum entanglement, where actions on one part of the system can affect other parts instantaneously, regardless of the distance separating them. This phenomenon, often described as *spooky action at a distance*, vividly illustrates one of the most profound and debated aspects of quantum theory, as discussed in foundational works such as J.S. Bell's paper on the EPR paradox and non-locality [222].

#### 4.3 MEASUREMENT INDUCED PHASE TRANSITION

As stated in the introduction to this chapter, there has been a considerable fascination with MIPT. Unlike traditional phase transitions driven by thermal fluctuations or external fields, MIPTs are driven purely by the effect of quantum measurements on the state of the system. This makes MIPT a purely non-equilibrium phenomenon, depending crucially on the dynamics introduced by the measurement process, including the rate, strength, and nature of the measurements.

Recently, there has been growing attention to the behavior of average entanglement entropy dynamics. Let us review the main results. Specifically, let  $p = \gamma dt$  denote the probability of a measurement occurring, with  $\gamma$  rate of measurement. We can identify a critical threshold  $p_c$  that separates two distinct phases. When  $p > p_c$  frequent measurements inhibit the propagation of correlations in a quantum system, obstructing the spread of information. In this phase, dubbed the quantum Zeno phase, the entanglement has an area-law scaling. Conversely, when measurements are sparse enough, that is  $p < p_c$ , the entanglement follows a volume-law scaling, allowing quantum correlations to propagate throughout the system. The results are summarized in Fig. 18.

Experimentally, MIPT have been observed in various platforms, such as superconducting qubits and trapped ions, where the controlled application of measurements is feasible. These experiments not only test the theoretical predictions, but also explore the practical consequences of MIPT, such as their impact on quantum coherence and the ability to maintain entangled states. Moreover, for quantum computing, understanding MIPT is important because it relates directly to how information is processed and maintained in a quantum system. This can be exploited for quantum error correction, where measurements are used to protect information against decoherence.

#### 4.4 MEAN STATE AND QUANTUM TRAJECTORIES

In the next chapters, we want to change back the point of view by restoring the usual connection to the well established way of characterizing quantum phase transitions: namely, by identifying a possible local-order parameter and by inspecting its full counting statistics.

In particular, since a monitored evolution is implemented by an unital dynamical quantum map, then the completely mixed state is a fixed point of the dynamics. We therefore expect the dynamics to bring the mean state (apart from symmetry protected sectors of the Hilbert space) toward the trivial infinite temperature one. Therefore, we say that averages computed with the mean state are known *a priori*.

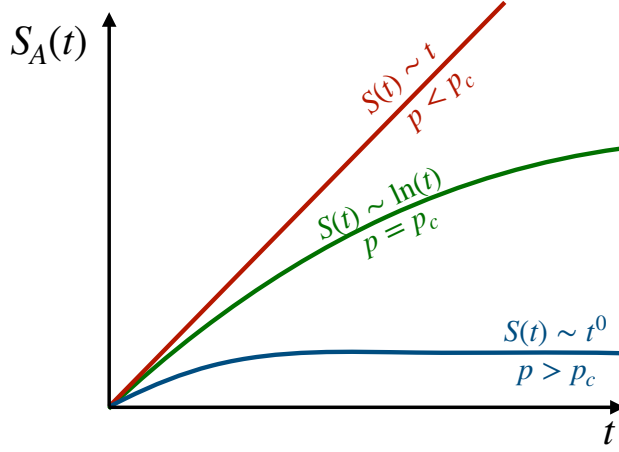


Figure 18: Entanglement growth: varying the probability of applying a measurements' operator  $p$  there are three different phases, for  $p > p_c$  we are in the *Quantum Zeno* phase in which there is no growth of entanglement, if  $p < p_c$  the measurements are too sparse and the entanglement as a volume-law growth, finally for  $p = p_c$  we are in the critical phase in which the entanglement grows logarithmically.

On the other hand, we may consider single quantum trajectories described by a set of not-averaged density matrices  $\rho_{t,\xi} = |\psi_{t,\xi}\rangle\langle\psi_{t,\xi}|$  where  $\xi$  represents a single realization of the stochastic protocol. We then consider averages of a functional of our state  $\mathcal{F}[\rho]$  over the set of quantum trajectories, it is apparent that

$$\mathcal{F}[\overline{\rho_t}] \neq \overline{\mathcal{F}[\rho_{t,\xi}]}, \quad (233)$$

as long as  $\mathcal{F}$  is *not a linear functional* of  $\rho_{t,\xi}$ . As a simple example we observe that the purity of our states  $\overline{\text{Tr}\{\rho_{t,\xi}^2\}} = 1$  for the set of quantum trajectories (since the state is always a product state), meanwhile since the mean state is generically mixed we have  $\text{Tr}\{\overline{\rho_t}^2\} < 1$ .

Let us now consider an operator  $A$  and a set of quantum trajectories  $\rho_{t,\xi}$ . Given a certain fixed realization of the measurement protocol  $\xi$  we can define a *quantum probability*

$$\mathcal{P}_{t,\xi}(a; A) = \text{Tr}\{\delta(A - a)\rho_{t,\xi}\} \quad (234)$$

of obtaining certain outcomes from the eigenvalues of  $A$ . Given that this distribution is linear in  $\rho_{t,\xi}$ , following the previous discussion, we have that the average of the distribution over the set of quantum trajectories

$$\mathcal{P}_t(a; A) = \overline{\mathcal{P}_{t,\xi}(a; A)} = \text{Tr}\{\delta(A - a)\overline{\rho_t}\}, \quad (235)$$

is a deterministic quantity known *a priori*, which is completely described by the dynamics of the mean state. Furthermore, all the moments of  $\mathcal{P}_{t,\xi}(a)$ , i.e.

$$\langle A_{t,\xi}^n \rangle = \text{Tr}\{A^n \rho_{t,\xi}\} \quad (236)$$

are linear functionals of  $\rho_{t,\xi}$  and therefore display a deterministic *a priori* dynamics. Despite this we can consider the cumulants of the distributions (234) over the set of quantum trajectories which result in *non-linear functional* of  $\rho_{t,\xi}$ . In particular, the  $n$ -th cumulants of the distribution is given by

$$K_{t,n}(A) = \left. \partial_\lambda^n \overline{\log [\text{Tr}\{e^{\lambda A} \rho_{t,\xi}\}]} \right|_{\lambda=0}. \quad (237)$$

Quantum statistics  
over each trajectory

As for instance, we may write the second cumulant

$$K_{t,2}(A) = \overline{\text{Tr}\{A^2\rho_{t,\xi}\}} - \overline{\text{Tr}\{A\rho_{t,\xi}\}}^2 = \text{Tr}\{A^2\overline{\rho_{t,\xi}}\} - \overline{\text{Tr}\{A\rho_{t,\xi}\}}^2, \quad (238)$$

which is clearly given by an average of a *non-linear* functional of  $\rho_{t,\xi}$ .

We are going now to construct a different probability distribution whose second moment is the very same non-linear contribution of the former cumulant  $\overline{\text{Tr}\{A\rho_{t,\xi}\}}^2$ . Indeed, we may consider a *classical probability* obtained by considering  $\mathcal{N}$  different trajectories and computing the average of the observable over each realization of the stochastic protocol  $\xi$

$$a_{t,\xi} = \text{Tr}\{A\rho_{t,\xi}\}, \quad (239)$$

in the limit of  $\mathcal{N} \rightarrow \infty$  the averages over this set will be distributed according to a probability distribution

Probability  
distribution  
expectation values

$$P_t(a; A) = \lim_{\mathcal{N} \rightarrow \infty} \frac{1}{\mathcal{N}} \sum_{\xi=1}^{\mathcal{N}} \delta(a_{t,\xi} - a) = \overline{\delta(\text{Tr}\{A\rho_{t,\xi}\} - a)} \quad (240)$$

not dependent on the particular realization  $\xi$  and *non-linear* in  $\rho_{t,\xi}$ . Then, we can consider the moments of the latter distribution

$$\mu_{t,n}(A) = \int P_t(a; A) a^n da, \quad (241)$$

which in this case are *non-linear* functionals of  $\rho_{t,\xi}$ . As a clarifying example, let us consider the second moment

$$\mu_{t,2}(A) = \int P_t(a; A) a^2 da = \lim_{\mathcal{N} \rightarrow \infty} \frac{1}{\mathcal{N}} \sum_{\xi=1}^{\mathcal{N}} [\text{Tr}\{A\rho_{t,\xi}\}]^2 = \overline{\text{Tr}\{A\rho_{t,\xi}\}}^2. \quad (242)$$

As it is apparent, there is a close connection among the cumulants of  $\mathcal{P}_{t,\xi}(a; A)$  and the moments of the distributions  $\{P_t(a; A^k)\}_{k \in \mathbb{N}}$ . This is due to the fact that it is possible to compute the  $n$ -th cumulant of  $\mathcal{P}_{t,\xi}(a; A)$  with a linear combination the moments of  $\{P_t(a; A^k)\}_{k \leq n}$ .

## FULL COUNTING STATISTICS IN THE MONITORED QUANTUM ISING CHAIN

In this chapter, we study the competition between the unitary dynamics and the random projective measurements in a quantum Ising chain coupled to an environment which continuously measures its transverse magnetization. For this particular model several works have discussed the relationship between measurements and entanglement transition. In particular in Refs [169, 196, 223], the authors considered the one-dimensional quantum Ising model coupled to an environment which continuously measures its transverse magnetization focusing in the quantum state diffusion protocol [139, 224] and in the quantum jump [225]. They found a sharp phase transition from a critical phase with logarithmic scaling of the entanglement to an area-law phase. Instead, the Ref. [194] presents the transverse Ising model with two non-commuting projective measurements and no unitary dynamics showing the entanglement transition between two distinct steady states that both exhibit area law entanglement.

In particular, we investigate how the stationary probability distribution of magnetizations and its momenta (and cumulant) are affected by the monitoring of local degrees of freedom. In particular, upon increasing the ratio  $\gamma$  between measurement rate and Hamiltonian coupling we find a transition from a correlated to a uncorrelated phase.

### 5.1 MODEL

The Ising Hamiltonian (with no transverse field) reads

$$H = -J \sum_{j=1}^{L-1} \sigma_j^x \sigma_{j+1}^x \quad (243)$$

where  $\sigma_j^\alpha$  are the local Pauli matrices, such that  $[\sigma_p^\alpha, \sigma_q^\beta] = 2i\delta_{pq}\epsilon^{\alpha\beta\gamma}\sigma_p^\gamma$ . Here we consider open boundary conditions (OBC). The Hamiltonian is invariant under the action of the global spin flip operator  $P = \prod_{j=1}^L \sigma_j^z$ . In the following we enforce such symmetry and work in the invariant sector with  $P = +1$ .

Using the Jordan-Wigner transformation

$$\sigma_\ell^x = \prod_{j=1}^{\ell-1} (1 - 2n_j)(c_\ell^\dagger + c_\ell), \quad \sigma_\ell^y = i \prod_{j=1}^{\ell-1} (1 - 2n_j)(c_\ell^\dagger - c_\ell), \quad \sigma_\ell^z = 1 - 2n_\ell, \quad (244)$$

where  $\{c_i, c_j^\dagger\} = \delta_{ij}$  and  $n_i \equiv c_i^\dagger c_i$ , the Hamiltonian takes the form

$$H = -J \sum_{j=1}^{L-1} (c_j^\dagger - c_j)(c_{j+1}^\dagger + c_{j+1}). \quad (245)$$

Within the approach we will be using in the next sections, it is convenient to replace the fermions  $c_j$  with the Majorana fermions (here we define two sets of operators through the apexes  $x$  and  $y$ )

$$a_j^x = (c_j^\dagger + c_j), \quad a_j^y = i(c_j^\dagger - c_j), \quad (246)$$

which are hermitian and satisfy the algebra  $\{a_i^\alpha, a_j^\beta\} = 2\delta_{ij}\delta_{\alpha\beta}$ , and such that one has

$$\sigma_j^x = \prod_{m=1}^{j-1} (ia_m^y a_m^x) a_j^x, \quad \sigma_j^y = \prod_{m=1}^{j-1} (ia_m^y a_m^x) a_j^y, \quad \sigma_j^z = ia_j^y a_j^x. \quad (247)$$

*Classical Ising  
Hamiltonian with  
Majorana fermions*

In terms of the Majorana fermions, the Hamiltonian reads

$$H = J \sum_{j=1}^{L-1} \left[ \frac{i}{2} a_j^y a_{j+1}^x - \frac{i}{2} a_{j+1}^x a_j^y \right] = \frac{J}{2} \mathbf{a}^\dagger \mathbb{T} \mathbf{a}, \quad (248)$$

where we defined the vector  $\mathbf{a}^\dagger = (a_1^x, \dots, a_L^x, a_1^y, \dots, a_L^y)$ , and identified the  $2L \times 2L$  couplings matrix

$$\mathbb{T} = \begin{bmatrix} 0 & \mathbb{H} \\ \mathbb{H}^\dagger & 0 \end{bmatrix} \quad (249)$$

with  $\mathbb{H}_{pq} = -i\delta_{p,q+1}$  for  $p, q$  in  $\{1, \dots, L\}$ . Introducing the unitary matrix  $\mathbb{V} = (v_1, \dots, v_{2L})$ , (i.e.  $\mathbb{V}^\dagger \mathbb{V} = \mathbb{I}_{2L \times 2L}$ ), whose column vectors are parametrised as

$$v_q = \frac{1}{\sqrt{2}} \begin{pmatrix} \phi_q \\ -i\psi_q \end{pmatrix}, \quad (250)$$

we get from the eigenvalue equation  $\mathbb{T}v_q = \epsilon_q v_q$  the following coupled equations

$$-i\mathbb{H}\psi_q = \epsilon_q \phi_q, \quad (251)$$

$$\mathbb{H}^\dagger \phi_q = -i\epsilon_q \psi_q. \quad (252)$$

We can notice here that these equations are invariant under the simultaneous change  $\epsilon_q \rightarrow -\epsilon_q$  and  $\psi_q \rightarrow -\psi_q$ . So, to each positive eigenvalue,  $\epsilon_q > 0$ , corresponds a negative eigenvalue  $\epsilon_{q'} = -\epsilon_q$  with the associated eigenvector  $v_{q'} = (\sigma^z \otimes \mathbb{I}_{L \times L})v_q$ . From these equations it is straightforward to obtain two decoupled eigenvalue equations  $\mathbb{H}\mathbb{H}^\dagger \phi_q = \epsilon_q^2 \phi_q$  and  $\mathbb{H}^\dagger \mathbb{H} \psi_q = \epsilon_q^2 \psi_q$ . Since  $\mathbb{H}\mathbb{H}^\dagger$  and  $\mathbb{H}^\dagger \mathbb{H}$  are real symmetric matrices, their eigenvectors can be chosen real and they satisfy completeness and orthogonality relations.

In the specific case of the Ising Hamiltonian in Eq. (248), those matrices are already diagonal (with one eigenvalue equals to zero, and  $L - 1$  eigenvalues equal to one), specifically  $(\mathbb{H}\mathbb{H}^\dagger)_{pq} = \delta_{pq} - \delta_{p1}\delta_{q1}$  and  $(\mathbb{H}^\dagger \mathbb{H})_{pq} = \delta_{pq} - \delta_{pL}\delta_{qL}$ . Choosing the coefficients  $\phi_{pq} = \delta_{pq}$  for  $p$  and  $q$  in  $\{1, \dots, L\}$ , leads to  $\psi_{pq} = -\delta_{p,q-1}$  for  $q$  in  $\{2, \dots, L\}$  and  $\psi_{p1} = -\delta_{pL}$ . This implies  $\mathbb{V}^\dagger \mathbb{T} \mathbb{V} = \sigma^z \otimes \mathbb{H}\mathbb{H}^\dagger$ . From the Majorana field we get the following diagonal Fermi operators corresponding to positive energies

$$\eta_q = \frac{1}{2} \sum_{p=1}^L [\phi_{pq} a_p^x + i\psi_{pq} a_p^y] = \frac{1}{2} [a_q^x - ia_{q-1}^y], \quad \text{for } q = 2, \dots, L \quad (253)$$

and  $\eta_1 = [a_1^x - ia_L^y]/2$ . They satisfy canonical anticommutation relations  $\{\eta_q, \eta_p^\dagger\} = \delta_{pq}$ . From those, the inverse relations reads

$$a_q^x = \eta_q + \eta_q^\dagger, \quad a_q^y = i[\eta_{q+1} - \eta_{q+1}^\dagger], \quad (254)$$

with  $a_L^y = i[\eta_1 - \eta_1^\dagger]$ , leading to the diagonal Hamiltonian

$$H = \sum_{q=1}^L \epsilon_q \eta_q^\dagger \eta_q - J(L-1), \quad (255)$$



with  $\epsilon_p = 2J(1 - \delta_{p1})$ . From the previous relations, the unitary time evolution of the Majorana operators can be easily worked out

$$a_p^x(t) = \cos(\epsilon_p t) a_p^x - \sin(\epsilon_p t) a_{p-1}^y, \quad (256)$$

$$a_p^y(t) = \sin(\epsilon_{p+1} t) a_{p+1}^x + \cos(\epsilon_{p+1} t) a_p^y, \quad (257)$$

where periodic boundary conditions in the indices are intended, namely  $0 \rightarrow L$  and  $L+1 \rightarrow 1$ .

For a Gaussian state all the information is encoded in the two-point correlation function of the Majorana operators, namely

$$\mathbb{A} = \langle \mathbf{a} \cdot \mathbf{a}^\dagger \rangle = \begin{pmatrix} \mathbb{A}^{xx} & \mathbb{A}^{xy} \\ \mathbb{A}^{yx} & \mathbb{A}^{yy} \end{pmatrix}, \quad (258)$$

*Correlation Matrix  
Majorana operators  
time evolution*

which under the classical Ising Hamiltonian evolve from time  $s$  to time  $s+t$  according to  $\mathbb{A}(s+t) = \mathbb{R}(t)\mathbb{A}(s)\mathbb{R}^\dagger(t)$ , with

$$\mathbb{R}(t) = \begin{pmatrix} \mathbb{R}^{xx}(t) & \mathbb{R}^{xy}(t) \\ \mathbb{R}^{yx}(t) & \mathbb{R}^{yy}(t) \end{pmatrix}, \quad (259)$$

whose matrix elements are

$$\mathbb{R}_{pq}^{xx}(t) = \cos(\epsilon_p t) \delta_{pq} \quad (260a)$$

$$\mathbb{R}_{pq}^{yy}(t) = \cos(\epsilon_{p+1} t) \delta_{pq} \quad (260b)$$

$$\mathbb{R}_{pq}^{yx}(t) = \sin(\epsilon_{p+1} t) \delta_{p,q-1} \quad (260c)$$

$$\mathbb{R}_{qp}^{xy}(t) = -\sin(\epsilon_p t) \delta_{p,q+1} \quad (260d)$$

## 5.2 PROTOCOL

We prepare the system in the symmetric ( $P = +1$ ) ground state of the Hamiltonian in Eq. (243), namely the GHZ state

$$|\psi_0\rangle = \frac{1}{\sqrt{2}} [|\cdots \uparrow \cdots\rangle + |\cdots \downarrow \cdots\rangle] \quad (261)$$

where here  $|\uparrow\rangle$  and  $|\downarrow\rangle$  represents the eigenstates of  $\sigma^x$  with eigenvalues respectively  $+1$  and  $-1$ . This initial state is described by a correlation matrix whose matrix elements are

$$\mathbb{A}_{pq}^{xx} = \mathbb{A}_{pq}^{yy} = \delta_{pq} \quad \mathbb{A}_{pq}^{xy} = -i\delta_{p,q+1} \quad \mathbb{A}_{pq}^{yx} = +i\delta_{p+1,q}, \quad (262)$$

where once again, PBC in the indices are intended, i.e.  $L+1 \rightarrow 1$ ; as expected, the initial correlation matrix would be unaffected by just the unitary evolution generated by the Ising Hamiltonian in Eq. (243). However, the system experiences random interactions with local measuring apparatus such that the full time-dependent protocol becomes highly non-trivial. In practice, with a characteristic rate  $\gamma$ , for each single lattice site  $k$ , the local magnetization along  $z$  is measured, i. e.  $\sigma_k^z = \sum_\sigma \sigma P_k^{(\sigma)}$ . Here  $\sigma = \pm 1$  are the possible outcomes of the measurements, and  $P_k^{(\sigma)} = (1 + \sigma \sigma_k^z)/2$  is the projector to the corresponding subspace.

Let us stress that both the unitary evolution and the local projective measurements keep the state Gaussian in terms of the Majorana fermions. While the former comes straightforwardly from the fact that  $\exp(-itH)$  is Gaussian; the latter may not be immediately visible from the simple structure of the projectors  $P_k^\sigma$ . However, it is easy to show that

$$P_k^{(\sigma)} = \lim_{x \rightarrow \infty} \frac{e^{x\sigma\sigma_k^z}}{\text{Tr}(e^{x\sigma\sigma_k^z})}, \quad (263)$$

thus also being a Gaussian operator in terms of Majorana fermions. Finally, let us mention that the protocol also preserves the spin-flip invariance, the state thus remaining always in the  $P = +1$  sector.

For the aforementioned reasons, during the entire dynamics, the full information of the state is completely encoded within the two-point functions  $\mathbb{A}_{pq}^{\alpha\beta} = \langle a_p^\alpha a_q^\beta \rangle$ , and all higher-order correlators split into sums of products of the two-point function only, according to the Wick theorem.

Since  $\sigma_k^z$  operators acting on different lattice sites commute, we can measure the local spins in any arbitrary order; specifically, if at time  $t$  the  $k$ -th site has been measured, following the Born rule, if the outcome is  $\sigma = \pm 1$ , then the state  $|\Psi(t)\rangle$  transforms into  $P_k^{(\sigma)}|\Psi(t)\rangle/\sqrt{\langle\Psi(t)|P_k^{(\sigma)}|\Psi(t)\rangle}$ . The resulting state remaining Gaussian, we can thus focus on the two-point function  $\mathbb{A}_{pq}^{\alpha\beta}(t)$  which completely characterises the entire system. The recipe is the following: for each time step  $dt$  and each site  $k$ , we extract a random number  $q_k \in (0, 1)$  and only if  $q_k \leq \gamma dt$  we take the measurement of  $\sigma_k^z$ . In such case, we extract another random number  $p_k \in (0, 1)$ , and the two-point function immediately after the projection to the  $\sigma_k^z$  local eigenstates becomes (in the following we omit the time dependence in order to simplify the notation)

Correlation matrix  
after strong  
projective  
measurement

$$\mathbb{A}_{pq}^{\alpha\beta|\sigma} = \frac{2}{1 + i\sigma\mathbb{A}_{kk}^{yx}} \left[ \frac{1}{4}\mathbb{A}_{pq}^{\alpha\beta} + \frac{i\sigma}{4}\langle\{a_p^\alpha a_q^\beta, a_k^y a_k^x\}\rangle - \frac{1}{4}\langle a_k^y a_k^x a_p^\alpha a_q^\beta a_k^y a_k^x \rangle \right] \quad (264)$$

where  $\sigma = +1$  if  $p_k \leq 1/2 + \langle\sigma_k^z\rangle/2$ , otherwise  $\sigma = -1$ .

The second term can be easily evaluated using the Wick theorem obtaining

$$\langle\{a_p^\alpha a_q^\beta, a_k^y a_k^x\}\rangle = 2\mathbb{A}_{kk}^{yx}\mathbb{A}_{pq}^{\alpha\beta} + (\mathbb{A}_{pk}^{\alpha x}\mathbb{A}_{qk}^{\beta y} + \mathbb{A}_{kp}^{x\alpha}\mathbb{A}_{kq}^{y\beta}) - (\mathbb{A}_{pk}^{\alpha y}\mathbb{A}_{qk}^{\beta x} + \mathbb{A}_{kp}^{y\alpha}\mathbb{A}_{kq}^{x\beta}). \quad (265)$$

Finally, using the fact that

$$\begin{aligned} a_p^\alpha a_q^\beta a_k^y a_k^x &= -4\delta_{pk}\delta_{qk}\delta^{\alpha y}\delta^{\beta x} + 2\delta_{qk}\delta^{\beta y}a_p^\alpha a_k^x + 2\delta_{pk}\delta^{\alpha y}a_k^x a_q^\beta \\ &+ 2\delta_{qk}\delta^{\beta x}a_k^y a_p^\alpha - 2\delta_{pk}\delta^{\alpha x}a_k^y a_q^\beta + a_k^y a_k^x a_p^\alpha a_q^\beta, \end{aligned} \quad (267)$$

after a bit of algebra, also the last term in Eq. (264) can be explicitly decomposed as follow

$$\begin{aligned} \langle a_k^y a_k^x a_p^\alpha a_q^\beta a_k^y a_k^x \rangle &= -\mathbb{A}_{pq}^{\alpha\beta} - 4\delta_{pk}\delta_{qk} \left( \delta^{\alpha y}\delta^{\beta x} - \delta^{\beta y}\delta^{\alpha x} \right) \mathbb{A}_{kk}^{yx} - 2\delta_{qk}\delta^{\beta y}\mathbb{A}_{kp}^{y\alpha} \\ &+ 2\delta_{pk}\delta^{\alpha y}\mathbb{A}_{kq}^{y\beta} - 2\delta_{qk}\delta^{\beta x}\mathbb{A}_{kp}^{x\alpha} + 2\delta_{pk}\delta^{\alpha x}\mathbb{A}_{kq}^{x\beta}. \end{aligned} \quad (268)$$

### 5.3 LINDBLADIAN DYNAMICS OF THE AVERAGED STATE

In this work, we study observables affected by the continuous monitoring of the system. Before doing so, it is important to stress the differences between quantum trajectories and mean states [153]. The mean state of our protocol is defined as the average of the density matrix over the measurements outcomes

$$\overline{\rho_t} = \overline{|\Psi_t\rangle\langle\Psi_t|} \quad (269)$$

where with  $\overline{(\dots)}$  we denote the average over the measurement protocol. The projective measurement protocol, relies on the fact that, at every single

measurement step, we know which lattice sites are measured, together with the outcomes of the measurements as well.

However, if we do not know whether the lattice site  $k$ -th is measured and no information about the measurement is retained, then a generic state  $\rho$  transforms accordingly to the quantum mechanic prescription as follow

$$\rho \rightarrow \mathcal{M}_k(\rho) = \left(1 - \frac{\gamma dt}{2}\right) \rho + \frac{\gamma dt}{2} \sigma_k^z \rho \sigma_k^z, \quad (270)$$

where  $\gamma dt$  is the probability that a single site is measured, after a discretization of the continuum time evolution has been applied. Therefore, after a time step  $dt$  the entire system with  $L$  lattice sites transform according to

$$\rho \rightarrow e^{-i dt H} [\mathcal{M}_L \circ \dots \circ \mathcal{M}_2 \circ \mathcal{M}_1(\rho)] e^{i dt H}. \quad (271)$$

The discrete protocol in the previous equation can be easily implemented in a tensor network algorithm, where each measurement operation  $\mathcal{M}_k$  is easily implemented as a transformation of the local tensor in the MPO representation of the mixed state  $\rho$ .

From an analytical point of view, if we are interested in the continuum limit of Eq. (271), where  $dt \rightarrow 0$  with fixed  $\gamma$ , we can keep the first order terms in the composition of the measurement string, obtaining

$$\mathcal{M}_L \circ \dots \circ \mathcal{M}_2 \circ \mathcal{M}_1(\rho) = \left(1 - L \frac{\gamma dt}{2}\right) \rho + \frac{\gamma dt}{2} \sum_k \sigma_k^z \rho \sigma_k^z + O(dt^2) \quad (272)$$

Combining the previous expansion with the unitary part in the evolution, we finally get the following Lindblad master equation

*Lindblad equation*

$$\partial_t \rho = -i[H, \rho] + \frac{\gamma}{2} \sum_{k=1}^L \left( \sigma_k^z \rho \sigma_k^z - \frac{1}{2} \{ \sigma_k^z \sigma_k^z, \rho \} \right), \quad (273)$$

where we used the fact that  $(\sigma_k^z)^\dagger = \sigma_k^z$  and  $(\sigma_k^z)^2 = 1$ .

**AVERAGE STATE FULL COUNTING STATISTICS** — In our protocol, the initial state  $|\psi_0\rangle\langle\psi_0|$  admits a MPO representation whose local tensors for each lattice site  $k$  are

$$\begin{aligned} \Gamma_k &= \begin{bmatrix} |\uparrow\rangle\langle\uparrow| & 0 & 0 & 0 \\ 0 & |\uparrow\rangle\langle\downarrow| & 0 & 0 \\ 0 & 0 & |\downarrow\rangle\langle\uparrow| & 0 \\ 0 & 0 & 0 & |\downarrow\rangle\langle\downarrow| \end{bmatrix} \\ &= \frac{1}{2} \begin{bmatrix} 1 + \sigma^x & 0 & 0 & 0 \\ 0 & \sigma^z - i\sigma^y & 0 & 0 \\ 0 & 0 & \sigma^z + i\sigma^y & 0 \\ 0 & 0 & 0 & 1 - \sigma^x \end{bmatrix}, \end{aligned} \quad (274)$$

and both left and right boundary vectors are given by  $\vec{l} = \vec{r} = (1, 1, 1, 1)/\sqrt{2}$ . Once again, here  $|\uparrow\rangle$  and  $|\downarrow\rangle$  represents the eigenstates of  $\sigma^x$  with eigenvalues respectively  $+1$  and  $-1$ . In particular, even under the action of the local transformation  $\mathcal{M}_k$  (which does not change the MPO auxiliary dimension), the averaged state remains always an eigenstate of the classical Ising Hamiltonian  $H_{xx}$ . In other words, the unitary part in Eq. (271) does not play any role, and the only contribution to the averaged state evolution comes from the nested application of  $\mathcal{M}_k$  on each lattice site. In addition, each single operator in the diagonal MPO  $\Gamma_k$ , transforms independently.

The local dynamics induced by the nested transformations of  $\mathcal{M}_k$  can be easily solved in the Pauli matrix representation of each local state. Indeed, discarding the index  $k$  for a sake of clarity, and expanding a generic local density matrix as  $\rho = \sum_{\mu} c_{\mu} \sigma^{\mu}$ , we easily get

$$c_{\mu}(t) = \sum_{\nu} \mathbb{M}(t)_{\mu\nu} c_{\nu}(0), \quad \text{with} \quad \mathbb{M}(t) = \begin{pmatrix} 1 & 0 & 0 & 0 \\ 0 & e^{-\gamma t} & 0 & 0 \\ 0 & 0 & e^{-\gamma t} & 0 \\ 0 & 0 & 0 & 1 \end{pmatrix}. \quad (275)$$

Using this last result with the initial condition in Eq. (274) we obtain

$$\Gamma_k(t) = \frac{1}{2} \begin{bmatrix} 1 & 0 & 0 & 0 \\ 0 & \sigma^z & 0 & 0 \\ 0 & 0 & \sigma^z & 0 \\ 0 & 0 & 0 & 1 \end{bmatrix} + \frac{e^{-\gamma t}}{2} \begin{bmatrix} \sigma^x & 0 & 0 & 0 \\ 0 & -i\sigma^y & 0 & 0 \\ 0 & 0 & i\sigma^y & 0 \\ 0 & 0 & 0 & -\sigma^x \end{bmatrix}. \quad (276)$$

The time evolved averaged state is therefore described by  $\bar{\rho}(t) = \vec{1} \cdot \prod_{k=1}^L \Gamma_k(t) \cdot \vec{r}$ , and it relaxes toward the infinite temperature state within the  $\mathbb{Z}_2$  symmetry sector with  $P = 1$ , namely  $\bar{\rho}(\infty) = (1 + P)/2^L$ .

In addition, the averaged generating function of the moments of  $M_{\ell}^x$  can be easily computed as follow

$$\text{Tr}\{e^{\lambda M_{\ell}^x} \bar{\rho}(t)\} = t \frac{1}{2} \left\{ [\cosh(\lambda/2) + e^{-\gamma t} \sinh(\lambda/2)]^{\ell} + [\cosh(\lambda/2) - e^{-\gamma t} \sinh(\lambda/2)]^{\ell} \right\}, \quad (277)$$

#### 5.4 NUMERICAL RESULTS

In order to examine the melting of the ferromagnetic order of the Ising chain under continuous projective paramagnetic measures, we will consider the following observables

$$M_{\ell}^z = \frac{1}{2} \sum_{j \in \ell} \sigma_j^z, \quad M_{\ell}^x = \frac{1}{2} \sum_{j \in \ell} \sigma_j^x, \quad M_{\ell}^{xx} = \frac{1}{4} \sum_{i \neq j \in \ell} \sigma_i^x \sigma_j^x, \quad (278)$$

and study the classical distribution  $P_t$  of the averages computed over a set quantum trajectories or, when this will not be possible, the cumulants of  $\mathcal{P}_{t,\xi}$ .

We recap here the numerical procedure that implements the continuous measurement protocol. We remark that, since we are working with an evolution that preserves the state Gaussian, the correlation matrix  $\mathbb{A}$  contains all the information of the system. The starting point of the dynamics is the GHZ state whose correlation matrix is given in Eq. (262). The system is then evolved unitarily by  $dt$  with Eqs. (260), then we apply the projective measurement step. To do so, sequentially projective measurements of the  $z$ -magnetization on each site are applied with probability  $p_{\text{meas}} = \gamma dt$ , thus transforming the system correlation matrix  $\mathbb{A}$  as pointed out in Eq. (264).

In our simulations, in order to set a time scale, we evolve our system up to a fixed time which depends on gamma, we chose  $t_f = \mathcal{T}/\gamma$ . This means that, on average, for each choice of  $\gamma$  the same number of projective measurements are executed. Indeed, we have  $t_f/dt$  time steps where with probability  $\gamma dt$  for each of the  $L$  sites a projective measurement is done. This implies an average number of measurements of

$$N_{\text{meas}} = \frac{t_f}{dt} L \gamma dt = \mathcal{T}L, \quad (279)$$

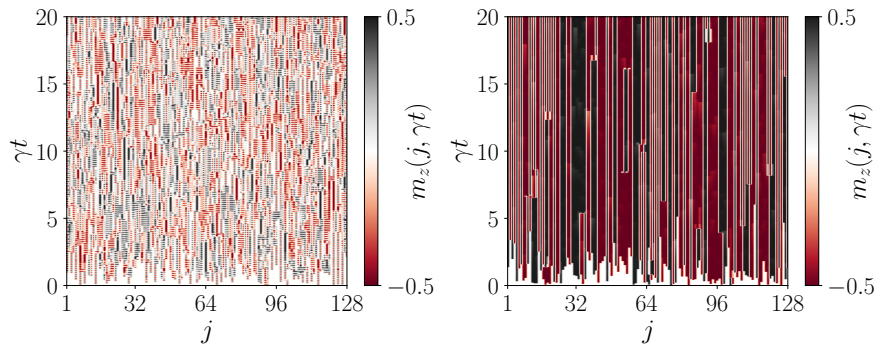


Figure 19: Local z-magnetization computed on single realization of a quantum trajectory. Left panel:  $\gamma = 0.1$ ; Right panel:  $\gamma = 10$ .

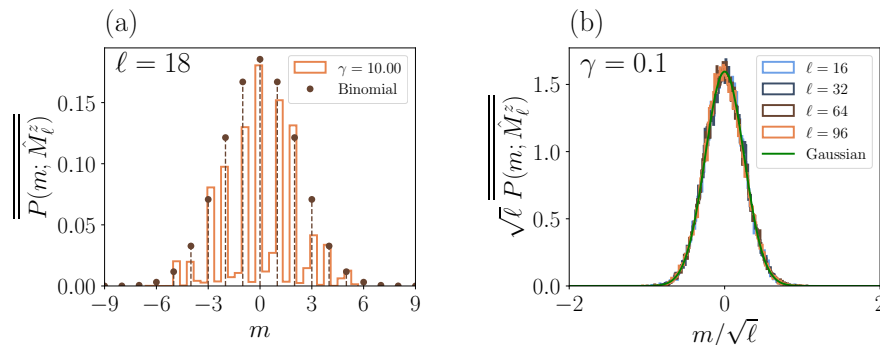


Figure 20: Stationary probabilities of the subsystem paramagnetic magnetization. (a) regime of fast measurements  $\gamma = 10$ , the numerically probability (obtained from an histogram) is compared to a binomial distribution. (b) sparse measurements regime  $\gamma = 0.1$  the numerically probability (obtained from an histogram) is compared to a Gaussian distribution. Details on the normalization of the two histograms are in the main text.

in our simulations  $\mathcal{T} = 20$ ,  $L = 128$  then, on average, each realization of the stochastic protocol consist of  $N_{\text{meas}} = 2560$  projective measurements. Furthermore, in the following, for each choice of the parameters, we chose a set of  $\mathcal{N} = 200$  quantum trajectories.

In the following paragraphs, we study how the initial ferromagnetic order melts under the influence of repeated measures.

#### 5.4.1 Paramagnetic Magnetization

First of all, we start by analyzing the dynamics of the paramagnetic magnetization, we will denote with  $|0\rangle$  and  $|1\rangle$  the two eigenstates of  $\sigma^z$  with eigenvalue 1 and  $-1$  respectively. In Fig. 19 we show the evolution of the local z-magnetization

$$m_z(j, \gamma t) = \frac{1}{2} \text{Tr} \left\{ \sigma_j^z \rho_{t, \varepsilon} \right\}, \quad (280)$$

for a single realization of the stochastic protocol and two different choices of the measurement rate  $\gamma$ . It is apparent that, due to the quantum Zeno effect [212, 213], increasing the measurement rate, local regions in which the magnetization is frozen appear. On the other hand, if measurements are sparse in time we expect a completely random evolution of the system.

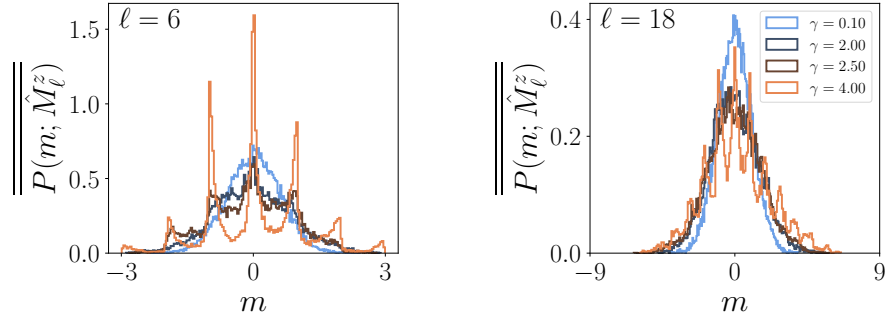


Figure 21: Distribution of the magnetization  $M_\ell^z$  on a sub-lattice of size  $\ell$  centered in the middle of the spin chain in the stationary state  $\gamma t \gg 1$ . The values of the distribution are extracted from an histogram.

To be more quantitative, we are going to analyze the behavior of  $P_t(m_\ell^z; M_\ell^z)$  in the stationary case for which  $\gamma t \gg 1$  by defining the distribution

$$\overline{\overline{P(m; M_\ell^z)}} = \frac{1}{t_f - t_0} \int_{t_0}^{t_f} P_t(m_\ell^z; M_\ell^z) dt, \quad (281)$$

where  $\overline{(\dots)}$  denotes the time average, in our simulations we chose  $t_0$  such that  $\gamma t_0 = 5$ , we will study the aforementioned limiting case of fast measurements  $\gamma \gg 1$  and rare  $\gamma \ll 1$ .

We start our analysis by the limit case in which  $\gamma \gg 1$  we are constantly monitoring all the sites of the system, the unitary evolution thus becomes negligible, and therefore we are effectively blocking the system in the product state outcome of first measurement. Since we are starting from the ferromagnetic GHZ ground state, the first measurement outcome with equal probability is one of the product states  $|\tau_1 \dots \tau_L\rangle$ , with  $\tau_j = 0, 1$  for  $j = 1, \dots, L$ . Since in this limit the state is blocked in the first measurement outcome we have that  $\overline{\overline{P(m_\ell^z; M_\ell^z)}}$  will be equivalent to the quantum probability  $\mathcal{P}(m_\ell^z; M_\ell^z)$  of obtaining from the state a certain eigenvalue of  $M_\ell^z$ . Thus  $\overline{\overline{P(m_\ell^z; M_\ell^z)}}$  will be the discrete binomial distribution

*Dense measurements*

$$\overline{\overline{P(m; M_\ell^z)}} = \frac{1}{2^\ell} \binom{\ell}{m_\ell^z + \frac{\ell}{2}} \quad m_\ell^z \in -\ell/2, \dots, \ell/2, \quad (282)$$

In Fig. 20(a), for  $\gamma = 10$ , we compare the numerical distribution obtained from an histogram to the theoretical prediction obtaining a good agreement. Since we want to compare this distribution to a discrete one, we normalized the histogram such that the sum over all the heights of the distribution in each bin is equal to one.

On the other hand, the case in which  $\gamma \ll 1$  means that measurements are diluted in time and that the information can propagate along the chain. We then have a dynamics dominated by the unitary evolution which may produce an entangled state by propagating the defects generated from the projective measurements. In first approximation, in the limit of  $\gamma \ll 1$ , we found from the numerics that the local magnetization  $m_z(j, \gamma t)$  is distributed in  $[-1/2, 1/2]$  with a variance  $\sigma^2 \approx 1/16$ . From the central limit theorem, we thus find that the subsystem magnetization is distributed as a Gaussian centered in zero with standard deviation  $\sigma\sqrt{\ell}$ , and thus its probability distribution is given by

*Sparse measurements*

$$\overline{\overline{P(m; M_\ell^z)}} = \sqrt{\frac{16}{2\pi\ell}} \exp\left[-\frac{16(m_\ell^z)^2}{2\ell}\right]. \quad (283)$$

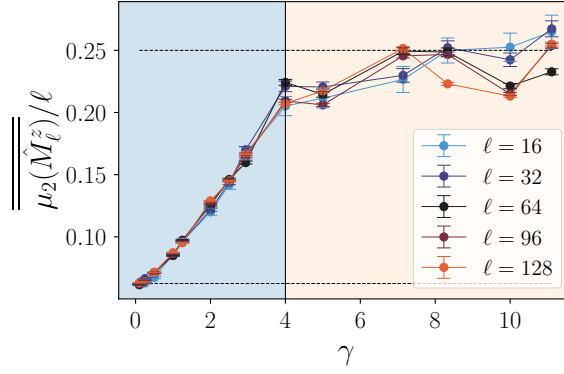


Figure 22: Second moment of the subsystem paramagnetic magnetization  $M_\ell^z$  rescaled with the size of the subsystem. If  $\gamma < 4$  there is a perfect matching between data, after the phase transition we witness a different behavior of the magnetization. Error bars are given by the error of the mean.

In Fig. 20(b), for  $\gamma = 0.1$ , we compare the numerical distribution obtained from an histogram, now normalized such that the integral over the bins is equal to one, to the Gaussian distribution obtaining a good agreement.

Finally, in Fig. 21, for  $\gamma = 0.1, 2, 2.5, 4$  and  $\ell = 6, 18$  we plot the distributions of the subsystem magnetizations. Qualitatively, as it is suggested by the plot, there is a crossover from a Gaussian distribution to the binomial one. Furthermore, for values of the measurement rate around the critical value of the measurement induced phase transition  $\gamma_c \simeq 4$ , the distribution starts to develop peaks in correspondence of  $m_\ell^z \in -\ell/2, \dots, \ell/2$  which are the values of the eigenvalues of  $M_\ell^z$ .

In order to study the latter behavior more deeply, in Fig. 22 we plot, for different subsystem sizes, the value of the second moment of the subsystem magnetization, rescaled with the subsystem size, against the measurement rate  $\gamma$

$$\mu_2(M_\ell^z) = \frac{1}{t_f - t_0} \int_{t_0}^{t_f} \overline{\text{Tr}\{M_\ell^z \rho_{t,\xi}\}^2} dt \quad (284)$$

where once again  $\gamma t_0 = 5$  and  $\gamma t_f = 20$ . When  $\gamma$  is less than 4, so that the dynamics is in the long-range correlated region of the phase diagram, there is a perfect match of the data points. Increasing the value of  $\gamma$  we witness spreading of the averages, meaning that we are in a different regime.

#### 5.4.2 Ferromagnetic Magnetization

We are now going to study the behavior of the ferromagnetic magnetization along  $x$  in the stationary state. We can not proceed as in the previous section. Indeed, due to the  $\mathbb{Z}_2$  symmetry of the protocol and of the initial state  $\langle \sigma_j^x \rangle = 0$  in any site and all the times. This result in a trivial distribution of the ferromagnetic magnetization

$$P_t(\mathbf{m}; M_\ell^x) = \delta(\mathbf{m}) \quad \forall t. \quad (285)$$

On the other hand, we can consider the quantum probability

$$\mathcal{P}_{t,\xi}(\mathbf{m}; M_\ell^x) = \text{Tr}\{\delta(M_\ell^x - \mathbf{m}) \rho_{t,\xi}\}, \quad (286)$$

and compute the generating function of the cumulants. In particular we studied the fourth cumulant. Despite it has a non trivial a priori evolution, it does not contain any relevant information on the measurement-induced phase transition, due to the fact that we could not have access to sufficiently large subsystems.



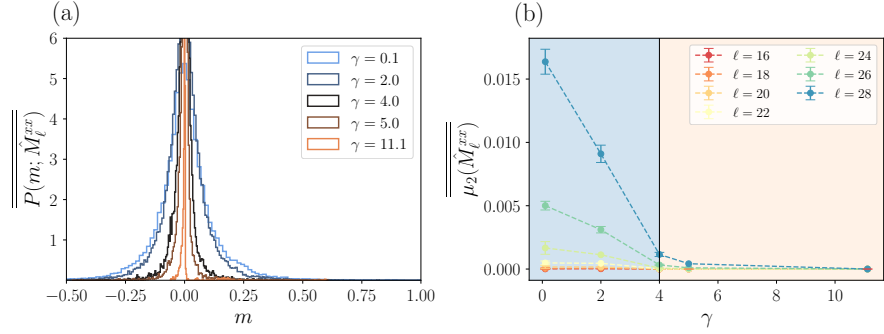


Figure 23: (a) Stationary probability distribution of  $M_\ell^{xx}$  for  $\ell = 28$  integrated for  $5 < \gamma t_0 < 20$ . (b) Variance of  $m_\ell^{xx}$  extracted from the probabilities distributions, the errorbar is given by its fluctuation.

#### 5.4.2.1 Probability of $M_\ell^{xx}$

In order to overcome the limitations described in the previous paragraph, we considered the full counting statistics over the trajectories of the following observable

$$M_\ell^{xx} = \frac{1}{4} \sum_{i \neq j \in \ell} \sigma_i^x \sigma_j^x. \quad (287)$$

To extract information on the spectrum of  $M_\ell^{xx}$ , we rewrite its expression as follow

$$M_\ell^{xx} = \frac{1}{4} \sum_{i, j \in \ell} \sigma_i^x \sigma_j^x - \frac{\ell}{4} = \frac{1}{4} \left( \sum_{i \in \ell} \sigma_i^x \right)^2 - \frac{\ell}{4} = \frac{(2M_\ell^x)^2 - \ell}{4}. \quad (288)$$

The maximum eigenvalue  $M_\ell^{xx}$  corresponds to  $\ell(\ell - 1)/8$  while the minimum is  $-\ell/8$ . Since we consider an evolution starting from the GHZ state we start from the maximum of value of  $\langle M_\ell^{xx} \rangle$  and evolve towards a stationary state. In Fig. 23(a) we show the stationary classical probability  $\overline{P(m; \hat{M}_\ell^{xx})}$  for a subsystem of size  $\ell = 28$ . In the case in which  $\gamma \gg 1$  the system is not far from an eigenstate of  $M_\ell^z$  thus the distribution is well described by a  $\delta(m)$ , we expect thus that all the moments of the distribution in this limit to be equal to zero. On the other hand, decreasing the value of  $\gamma$  the distribution transition towards a distribution centered in  $m_\ell^{xx} = 0$  with a width that increases decreasing the value of  $\gamma$ . Indeed, in Fig. 23(b) we plot the width of the aforementioned distribution for different values of the subsystem size, which decreases with the measurement rate  $\gamma$ . We see that  $(M_\ell^x)^2$  could witness the measurement induced phase transition since crossing the critical value  $\gamma \sim 4$  the width changes dramatically behavior with the subsystem size: in the Zeno-like regime (namely for  $\gamma > 4$ ), the fluctuations are basically suppressed; instead, for  $\gamma < 4$  they show a remarkable dependence with the  $\ell$ , already for relatively small sizes.

As a matter of fact, although this behavior seems not as clean as what we have found for the paramagnetic magnetization, the ferromagnetic fluctuations have the paramount advantage to keep the extensive (with the subsystem size) character only when entering the strongly correlated phase. In other words, while  $\mu_2(M_\ell^z)$  is expected to show a non-analytic behavior at  $\gamma \simeq 4$  in the thermodynamics limit;  $\mu_2(M_\ell^{xx})$  is not just non-analytic at the transition point, but in addition it clearly characterizes the entire correlated phase already looking at small subsystems.



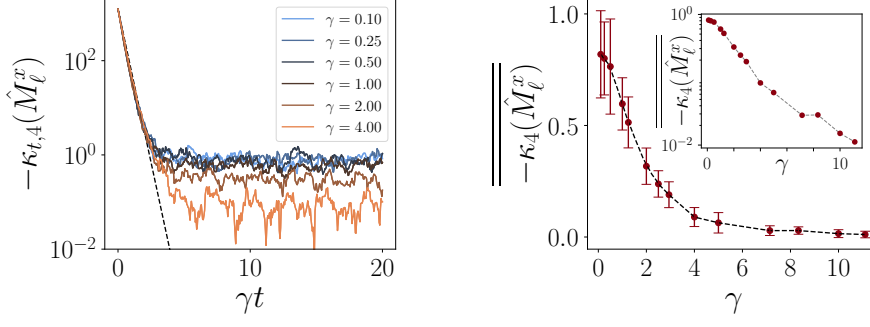


Figure 24: *Non a priori* contribution to the fourth cumulant. Left panel: evolution of the fourth cumulant towards the stationary state. Right panel: time averaged fourth cumulant in the stationary state (after  $\gamma t_0 = 5$ ), the error bars are estimated as the standard deviation of the time average, inset log-linear plot of the mean values. Subsystem size  $\ell = 10$ .

CUMULANTS FERROMAGNETIC MAGNETIZATION — Since we are interested in the statistics of the order parameter  $M_\ell^x = \frac{1}{2} \sum_{j=1}^{\ell} \sigma_j^x$ , in a subsystem of  $\ell$  contiguous lattice sites, we do identify  $F_\ell(\lambda)$  via

$$e^{F_\ell(\lambda)} \equiv \langle e^{\lambda M_\ell^x} \rangle, \quad \text{with} \quad K_\ell^n = \partial_\lambda^n F_\ell(\lambda)|_{\lambda=0}, \quad (289)$$

as the generating function of all cumulants  $K_\ell^n$  of the subsystem magnetization. From the large deviation theory we may expect  $F_\ell(\lambda) \sim \ell \tilde{F}(\lambda)$  for  $\ell \gg 1$ , where  $\tilde{F}(\lambda)$  is the large deviation function. However, this relies on the extensive behavior of the cumulants, which is violated in the initial GHZ state. For such reason, it is worth to investigate at the average over the quantum trajectory dynamics of the ratio  $\overline{F_\ell(\lambda)}/\ell = \overline{\log \langle e^{i\lambda M_\ell^x} \rangle}/\ell$ .

The computation of the subsystem generating function is a very hard task mainly because  $\sigma^x$  is a nonlocal operator in terms of Majorana fermions. By exploiting the  $\mathbb{Z}_2$  symmetry of the measurement protocol, we have

$$F_\ell(\lambda) \equiv G_\ell(\lambda) + \ell \log \cosh(\lambda/2), \quad (290)$$

with

$$G_\ell(\lambda) = \log \sum_{n=0}^{\lfloor \ell/2 \rfloor} \tanh(\lambda/2)^{2n} \sum_{j_1 < j_2 < \dots < j_{2n}} \langle \sigma_{j_1}^x \sigma_{j_2}^x \dots \sigma_{j_{2n}}^x \rangle, \quad (291)$$

where the ordered indexes  $\{j_1, \dots, j_{2n}\}$  are in the interval  $[1, \ell]$ . Here we decided to highlight the nontrivial part  $G_\ell(\lambda)$  of the generating function, whilst the second term in Eq. (290) simply gives the infinite temperature contribution. Indeed, we may define the *non a priori* contribution  $\kappa_n$  of the cumulants as

$$\partial_\lambda^n F_\ell(\lambda)|_{\lambda=0} = \kappa_n + \ell \partial_\lambda^n \log \cosh(\lambda/2)|_{\lambda=0}, \quad (292)$$

so that  $\kappa_n \equiv \partial_\lambda^n G_\ell(\lambda)|_{\lambda=0}$ . The evaluation of  $G_\ell(\lambda)$  reduces to the computation of the generic string  $\langle \sigma_{j_1}^x \sigma_{j_2}^x \dots \sigma_{j_{2n}}^x \rangle$ . Following Ref. [226], it can be evaluated as the Pfaffian of a skew-symmetric real matrix which explicitly depends on the particular choice of the indices:

$$\langle \sigma_{j_1}^x \sigma_{j_2}^x \dots \sigma_{j_{2n}}^x \rangle = (-1)^{\mathcal{L}_{j_n}(\mathcal{L}_{j_n-1})/2} \text{pf} \begin{bmatrix} \mathbb{F}_{j_n}^{yy} & \mathbb{G}_{j_n}^{yx} \\ \mathbb{G}_{j_n}^{xy} & \mathbb{F}_{j_n}^{xx} \end{bmatrix} \quad (293)$$

where we used the shorthand notation  $\mathbf{j}_n \equiv \{j_1, \dots, j_{2n}\}$  for the full set of indices, and  $\mathcal{L}_{j_n} = \sum_{k=1}^n (j_{2k} - j_{2k-1})$ . The real matrices  $\mathbb{F}_{j_n}$  and  $\mathbb{G}_{j_n}$  ( $\mathbb{F}_{j_n}$

being also skew-symmetric) have dimensions  $\mathcal{L}_{j_n} \times \mathcal{L}_{j_n}$  and entries given by [48]

$$(\mathbb{F}_{j_n}^{yy})_{m_p, n_q} = -i\langle a_p^y a_q^y \rangle + i\delta_{pq} = -i\mathbb{A}_{pq}^{yy} + i\delta_{pq} \quad (294)$$

$$(\mathbb{F}_{j_n}^{xx})_{m_p, n_q} = -i\langle a_{p+1}^x a_{q+1}^x \rangle + i\delta_{pq} = -i\mathbb{A}_{p+1, q+1}^{xx} + i\delta_{pq} \quad (295)$$

$$(\mathbb{G}_{j_n}^{yx})_{m_p, n_q} = -i\langle a_p^y a_{q+1}^x \rangle = -i\mathbb{A}_{p, q+1}^{yx} \quad (296)$$

$$(\mathbb{G}_{j_n}^{xy})_{m_p, n_q} = -i\langle a_{p+1}^x a_q^y \rangle = -i\mathbb{A}_{p+1, q}^{xy} \quad (297)$$

with  $\{p, q\} \in [j_1, j_2 - 1] \cup [j_3, j_4 - 1] \cup \dots \cup [j_{2n-1}, j_{2n} - 1]$  and where the indices  $m_p$  and  $n_q$  run in  $\{0, \dots, \mathcal{L}_{j_n} - 1\}$ , and have the function of shrinking all together the intervals. The knowledge of the Majorana correlation functions together with the representation (293) are the basic ingredients to compute the generating function in Eq. (291).

We note that, due to the  $\mathbb{Z}_2$  symmetry of our system, all the odds cumulants are null. Moreover, for the same reason the second cumulant has a trivial *a priori* evolution since

$$K_{t,2}(M_\ell^x) = \overline{\text{Tr}\{(M_\ell^x)^2 \rho_{t,\varepsilon}\}} - \overline{\text{Tr}\{M_\ell^x \rho_{t,\varepsilon}\}}^2 = \text{Tr}\{(M_\ell^x)^2 \overline{\rho_{t,\varepsilon}}\}, \quad (298)$$

since the non-linear contribution is equal to zero. The first non-trivial contribution is therefore the fourth cumulant, namely

$$K_{t,4}(M_\ell^x) = \text{Tr}\{(M_\ell^x)^4 \overline{\rho_{t,\varepsilon}}\} - 3 \overline{\text{Tr}\{(M_\ell^x)^2 \rho_{t,\varepsilon}\}}^2, \quad (299)$$

where the second term does give a non-linear contribution. In Fig. 24 we plot the time evolution of the *non a priori* part of the fourth cumulant, i.e.  $\kappa_{t,4}$ , and its time average in the stationary state

$$\overline{\kappa_4(M_\ell^x)} = \frac{1}{t_f - t_0} \int_{t_0}^{t_f} \overline{\kappa_{t,4}(M_\ell^x)} dt, \quad (300)$$

with  $\gamma t_0 = 5$  and for a subsystem of size  $\ell = 10$ , and where again  $\overline{(\dots)}$  denotes a time average in the stationary configuration. Increasing the value of the measurement rate  $\gamma$ , we find an exponential decay of the stationary value of the 4-th cumulant towards zero, namely the infinite temperature value. On the other hand, the non-trivial time-evolution does not contain any relevant information on the measurement-induced phase transition. This is probably due to the fact that we could not have access to sufficiently large subsystems. As a matter of fact, the numerical evaluation of the full counting statistics is a very involved procedure, which scales exponentially with the subsystem dimension, thus not allowing to reach thermodynamic relevant sizes.

## 5.5 CONCLUSION

The interplay of local measurements and unitary evolution can give rise to phase transitions, manifesting in, e.g., either delocalized, strongly entangled or localized, weakly entangled conditional states.

In this work, we investigated the quantum quench dynamics in a quantum Ising chain under local projective measurements of the paramagnetic magnetization  $S_z$ .

Very much like in a classical equilibrium situation, when non-commuting observables compete in driving a system across a quantum phase transition; here the unitary driving and the projective measurements compete in creating or destroying the local order.

In a genuinely statistical sense, different quantum trajectories naturally fluctuate under our dynamical map; this gives rise to non-equilibrium probability distributions of local quantities which contain signature of paramount yet elusive transitions, going much beyond the simple dynamics of the mean state.

In particular, during the time evolution, by computing the statistics of the expectation values of the system magnetisation in the  $z$  direction, we are able to distinguish different regimes, namely different phases. Starting from the strong measurement phase, increasing the imperfection rate, the distribution changes from a bimodal distribution into a Gaussian distribution, the transition point being located at measurements rate  $\gamma_c \simeq 4$ , in agreement with what have been observed for the entanglement entropy transition [196].

As a matter of fact, our approach, based on the observation of the statistics of local quantities, is naturally related to what is done in the nowadays experiments. However, especially for devising projective-measurement protocols in the real quantum world, the ultimate challenge, which need to be addressed yet, remains the *post-selection problem*: namely the possibility to experimentally reproduce the same trajectory  $\rho_{t,\xi}$  many many times, without being affected by the exponentially inefficient measurement-induced post-selection.



## UNRAVELING OF LINDBLAD EQUATION AND FULL COUNTING STATISTICS

In this chapter, we investigate quantum systems that are coupled to a measuring apparatus, analyzing their evolution based on unitary dynamics interrupted by projective measurements. We focus on the scenario where projective measurements occur at a fixed rate  $\gamma$ , which aligns naturally with Poissonian statistics for waiting times between successive measurements. In order to get analytical predictions the measurements are applied across the entire Hilbert space, thus projecting the system onto an eigenstate of the measured observable.

To demonstrate our method, we present results for two key examples: a single qubit measuring its magnetization and a free hopping particle measuring its position. Consequently, we provide an exact method for calculating the probability distribution of the expectation value of observables averaged over the set of quantum trajectories.

### 6.1 PROTOCOL

Let us consider an  $N$ -level quantum system described by a time-independent hamiltonian  $H$ , whose unitary evolution is governed by  $U(t) = e^{-iHt}$ . In addition, all along the evolution, we couple the system to a measuring apparatus that project, with a fixed measurement rate  $\gamma$ , the evolved state in to an eigenstate of the observable

$$A = \sum_{a=1}^N \nu_a |a\rangle\langle a|, \quad (301)$$

such that  $[A, H] \neq 0$ . At time  $t = 0$  the system has been prepared in a fixed state  $|\psi(0)\rangle$  corresponding to an eigenstate  $|a_0\rangle$  of  $A$ . We are interested in evaluating the probability distribution of the expectation value of a generic observable  $O = \sum_a o_a |a\rangle\langle a|$  commuting with  $A$ , i.e.

$$P_O(x;t) = \overline{\delta(\langle \psi_\xi(t) | O | \psi_\xi(t) \rangle - x)}, \quad (302)$$

*Probability  
distribution  
expectation values*

with  $t > 0$ . Here, the over-line is indicating the average over the quantum trajectories, where each trajectory comprises a sequence of unitary time evolutions interspersed with instantaneous projective measurements of  $A$  at random times, and is labelled by an integer  $\xi$ . A sketch of our dynamical protocol is shown in Figure 25. Considering this protocol, we can split this average by putting apart the contributions for different  $n$  clicks of the measuring apparatus. For each  $n$  the system is projected in one of the eigenstates of  $A$  at times  $\{s_j\}$ , with  $j = 1, \dots, n$  such that  $0 < s_1 < \dots < s_n < t$ . We define

$$P_O(x;t) = P_O^{(n>0)}(x;t) + P_O^{(0)}(x;t), \quad (303)$$

where  $P_O^{(0)}$ ,  $P_O^{(n>0)}$  are respectively the no-click ( $n = 0$ ) and click ( $n > 0$ ) contributions to the probability distribution of  $\langle \psi_\xi(t) | O | \psi_\xi(t) \rangle$ . Now we proceed with the rewriting of these two quantities, explicitly specifying for  $P_O^{(n>0)}$  the contribution coming from events with  $n$  measurements and summing over  $n = 1, 2, 3, \dots$  (see [138] for a similar approach). Moreover, we have

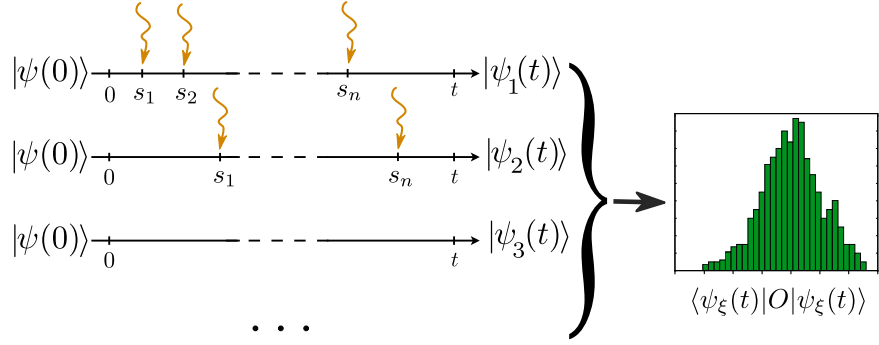


Figure 25: Scheme of the dynamical protocol. We consider a system prepared in a fixed initial state  $|\psi(0)\rangle = |a_0\rangle$ , undergoing random projective measurements of an observable  $A$  (see Eq. (301)). Measurements occur with a fixed rate  $\gamma$  at times  $s_1 < s_2 < \dots$ , whereas in the intervals  $(s_j, s_{j+1})$  the system follows an unitary time evolution. Different quantum trajectories are labelled by the integer  $\xi$ . The ensemble of states  $|\psi_\xi(t)\rangle$  defines the probability distribution function of  $\langle \psi_\xi(t) | O | \psi_\xi(t) \rangle$  (right).

to integrate over the possible measurement times  $s_j$  and summing over their possible outcomes  $a_j$ . We obtain

$$\begin{cases} P_O^{(0)}(x; t) &= e^{-\gamma t} \mathcal{D}(x, a_0, t) \\ P_O^{(n>0)}(x; t) &= \sum_{n=1}^{\infty} \gamma^n e^{-\gamma t} \times \\ &\times \sum_{a_1, \dots, a_n} \mathcal{T} \int_0^t ds_1 \dots ds_n p(x, t | s_n, a_n; \dots; s_1, a_1; 0, a_0), \end{cases} \quad (304)$$

where

$$\mathcal{D}(x, a, t) \equiv \delta \left( x - \langle a | U^\dagger(t) O U(t) | a \rangle \right) \quad (305)$$

and  $p(x, t | s_n, a_n; \dots; s_1, a_1; 0, a_0)$  is the conditional probability density of getting the average value  $x$  at the final time  $t$ , given that the system was found in the eigenstates  $\{|a_j\rangle\}$  of  $A$  at times  $\{s_j\}$ .  $\mathcal{T}$  denotes the time-ordered product. The term  $\gamma^n e^{-\gamma t}$  is the Poisson weight associated to the  $n$ -measurements events (the factor  $1/n!$  is removed since inside the time-ordered integral the events labelled by  $1, 2, \dots, n$  occurs at fixed times  $s_1 < s_2 < \dots < s_n$ ). Since the measurement process is Markovian, we have that

$$\begin{aligned} p(x, t | s_n, a_n; \dots; s_1, a_1; 0, a_0) &= \\ &= \mathcal{D}(x, a_n, t - s_n) p(s_n, a_n | s_{n-1}, a_{n-1}) \dots p(s_1, a_1 | 0, a_0), \end{aligned} \quad (306)$$

where the delta contribution can be rewritten as

$$\mathcal{D}(x, a, t) = \delta \left( x - \sum_{a'=1}^N o_{a'} p(t, a' | 0, a) \right), \quad (307)$$

and gives the contribution to the probability due to the last time-interval  $(s_n, t)$ . In addition, the transition probabilities between eigenstates of  $A$  read <sup>1</sup>

$$p(s', a' | s, a) \equiv \mathbb{T}_{a', a}(s' - s) = \left| \langle a' | U(s' - s) | a \rangle \right|^2. \quad (308)$$

<sup>1</sup> Transition probability matrices, such as  $\mathbb{T}$ , obtained by calculating the modulus square of each element of a unitary matrix, are frequently referred to as *unistochastic* matrices in the literature. These matrices form a subset of the bistochastic matrices. [227]

Let us assume that the transition matrix  $\mathbb{T}$  can be diagonalised, i.e.  $\mathbb{T}(s' - s) = \mathbb{V} \mathbb{D}(s' - s) \mathbb{V}^\dagger$  with eigenvalues  $\mathbb{D}_{\alpha, \beta}(t) = d_\alpha(t) \delta_{\alpha, \beta}$ , and time-independent unitary matrix  $\mathbb{V}$  whose columns are the orthonormal eigenvectors<sup>2</sup>. Notice that, since  $\mathbb{T}(t)$  is a bistochastic matrix,  $d_1(t) = 1$  is the largest eigenvalue for any time  $t$ , meanwhile as a consequence of the Perron–Frobenius theorem  $|d_\alpha(t)| \leq 1$  for  $\alpha = 2, \dots, N$ , where the equality holds in case of degeneracy [228, 229]. In addition, since  $\sum_a \mathbb{T}_{a, b} = \sum_b \mathbb{T}_{a, b} = 1$ , the eigenvector associated to largest eigenvalue is simply given by  $\mathbb{V}_{a, 1} = 1/\sqrt{N}$ . Now let us focus on the nontrivial  $P_O^{(n>0)}(x; t)$ . For each order  $n$  and fixed states  $\{a_0, a_n\}$ , the sum over all the possible intermediate outcomes can be rewritten as

$$\begin{aligned} & \sum_{a_1, \dots, a_{n-1}} \mathbb{T}_{a_n, a_{n-1}}(s_n - s_{n-1}) \cdots \mathbb{T}_{a_1, a_0}(s_1) = \\ & = \sum_{\alpha=1}^N \mathbb{V}_{a_n, \alpha} \prod_{j=1}^n d_\alpha(s_j - s_{j-1}) (\mathbb{V}^\dagger)_{\alpha, a_0}, \end{aligned} \quad (309)$$

with starting time  $s_0 = 0$ . We thus get

$$\begin{aligned} P_O^{(n>0)}(x; t) &= \\ &= e^{-\gamma t} \sum_{n=1}^{\infty} \left[ \int_0^t \gamma ds_n \sum_{a_n=1}^N \mathcal{D}(x, a_n, t - s_n) \sum_{\alpha=1}^N \mathbb{V}_{a_n, \alpha} I_{n, \alpha}(s_n) (\mathbb{V}^\dagger)_{\alpha, a_0} \right] \end{aligned} \quad (310)$$

where we defined the time-ordered integrals

$$I_{n, \alpha}(s_n) = \int_0^{s_n} \gamma ds_{n-1} d_\alpha(s_n - s_{n-1}) \cdots \int_0^{s_2} \gamma ds_1 d_\alpha(s_2 - s_1) d_\alpha(s_1), \quad (311)$$

which satisfy the following recursive relations

$$\begin{cases} I_{1, \alpha}(s_1) = d_\alpha(s_1), \\ I_{n, \alpha}(s_n) = \int_0^{s_n} \gamma ds_{n-1} d_\alpha(s_n - s_{n-1}) I_{n-1, \alpha}(s_{n-1}), \quad n > 1. \end{cases} \quad (312)$$

In Eq. (310) the sum over  $n$  can be safely taken, since  $s_n$  and  $a_n$  are dummies variables. Thus, we can introduce  $I_\alpha(s) = \sum_{n=1}^{\infty} I_{n, \alpha}(s)$  which satisfy the following linear Volterra integral equation of the second kind

$$I_\alpha(s) - d_\alpha(s) = \int_0^s \gamma ds' d_\alpha(s - s') I_\alpha(s'). \quad (313)$$

Exploiting the Laplace transform of the integral kernel, i.e.  $\mathcal{L}[d_\alpha](z) = \int_0^\infty e^{-zt} d_\alpha(t) dt$ , we can easily solve the previous equation obtaining

$$I_\alpha(s) = \mathcal{L}^{-1} \left[ \frac{\mathcal{L}[d_\alpha](z)}{1 - \gamma \mathcal{L}[d_\alpha](z)} \right] (s), \quad (314)$$

where  $\mathcal{L}^{-1}[\dots]$  is the inverse Laplace transform. As expected, it easy to show that

$$\mathcal{L}[I_\alpha](z) = \frac{\mathcal{L}[d_\alpha](z)}{1 - \gamma \mathcal{L}[d_\alpha](z)} = \sum_{n=1}^{\infty} \gamma^{n-1} \mathcal{L}[d_\alpha]^n(z) = \sum_{n=1}^{\infty} \mathcal{L}[I_{n, \alpha}](z), \quad (315)$$

<sup>2</sup> It is assumed here that the transition matrix is diagonalizable. Although, as far as we know, this property does not derive from the mathematical properties of  $\mathbb{T}$ , we are not aware of physical cases in which  $\mathbb{T}$  is not diagonalizable.

thus identifying  $\mathcal{L}[I_{n,\alpha}](z) = \gamma^{n-1} \mathcal{L}[d_\alpha]^n(z)$ . We can finally collect all those results, further simplify and finding the following general expression for the probability distribution

$$P_O^{(n>0)}(x;t) = e^{-\gamma t} \sum_{\alpha=1}^N \sum_{\alpha=1}^N \int_0^t \gamma ds \mathcal{D}(x, \alpha, t-s) \mathbb{V}_{\alpha,\alpha} I_\alpha(s) (\mathbb{V}^\dagger)_{\alpha,\alpha_0}. \quad (316)$$

Let us finally mention that using this expression we can easily compute the  $k$ -th moment of the distribution, defined as  $\langle x^k \rangle_{P_O} = \int dx x^k P_O(x;t) = \overline{\langle \psi_\xi(t) | O | \psi_\xi(t) \rangle^k}$ . The first moment ( $k = 1$ ) is particularly simple, since it does reduce to the expectation value of  $O$  over the averaged density matrix  $|\overline{\psi_\xi(t)}\rangle \langle \overline{\psi_\xi(t)}|$  whose dynamics is fully described by the Lindblad equation (see 6.4.2). In particular, using that  $\sum_b \mathbb{T}_{a,b}(t-s) \mathbb{V}_{b,\alpha} = d_\alpha(t-s) \mathbb{V}_{\alpha,\alpha}$ , we easily get

$$\begin{aligned} \langle x \rangle_{P_O} &= e^{-\gamma t} \sum_{\alpha=1}^N o_\alpha \mathbb{T}_{\alpha,\alpha_0}(t) + \\ &+ e^{-\gamma t} \sum_{\alpha=1}^N o_\alpha \sum_{\alpha=1}^N \mathbb{V}_{\alpha,\alpha} \left[ \int_0^t \gamma ds d_\alpha(t-s) I_\alpha(s) \right] (\mathbb{V}^\dagger)_{\alpha,\alpha_0}, \end{aligned} \quad (317)$$

which can be further simplified exploiting Eq. (313), finally obtaining

$$\langle x \rangle_{P_O} = e^{-\gamma t} \sum_{\alpha=1}^N o_\alpha \sum_{\alpha=1}^N \mathbb{V}_{\alpha,\alpha} I_\alpha(t) (\mathbb{V}^\dagger)_{\alpha,\alpha_0}. \quad (318)$$

Let us stress that the simplified expression in Eq. (318) applies only for averages of operators  $O$  which are diagonal in the eigenbasis of the monitored observable  $A$  (i.e. when  $[O, A] = 0$ ). Every time we are interested in higher moments or probability distribution of non-diagonal operators, the computation have to be carried out from scratch, basically starting from Eq. (316). Finally, due to the properties of the transfer matrix  $\mathbb{T}$ , the stationary limit  $t \rightarrow \infty$  of the previous average can be easily taken; in fact, only  $\alpha = 1$ , with  $I_1(t) = e^{\gamma t}$ , will contribute to the sum over  $\alpha$ , leading to  $\langle x \rangle_{P_O} \rightarrow \frac{1}{N} \sum_{\alpha=1}^N o_\alpha$ , where we used the fact that  $\mathbb{V}_{\alpha,1} = 1/\sqrt{N}$ . As expected from the Lindblad dynamics, it does correspond to the expectation value of the operator  $O$  over the infinite temperature state  $\frac{1}{N} \sum_{\alpha=1}^N |\alpha\rangle \langle \alpha|$ .

## 6.2 TWO-LEVEL SYSTEM

We start by considering a continuously monitored two-level system. Despite their simplicity, two-level systems are the fundamental building block of the most studied quantum many-body systems and therefore understanding their behavior is crucial. The system consists of a single spin-1/2, whose unitary evolution is governed by the following hamiltonian

$$H = -J\sigma^x, \quad (319)$$

where  $\sigma^\alpha$  are the Pauli matrices with  $\alpha = x, y, z$  and  $[\sigma^\alpha, \sigma^\beta] = 2i\epsilon_{\alpha\beta\gamma}\sigma^\gamma$ . The system is continuously monitored along  $z$  with a rate  $\gamma$  (therefore  $A = \sigma^z$ ). We will denote with  $|\sigma\rangle = |+1\rangle, |-1\rangle$  the eigenstates of  $\sigma^z$  with eigenvalue  $\sigma = \pm 1$  respectively. We consider a two-level spin which starts from  $|+1\rangle$  and we want to evaluate

$$P_{\sigma^z}(x;t) = \overline{\delta(\langle \psi_\xi(t) | \sigma^z | \psi_\xi(t) \rangle - x)} = P_{\sigma^z}^{(n>0)}(x;t) + P_{\sigma^z}^{(0)}(x;t), \quad (320)$$



i.e. the probability distribution of the expectation value of  $O = \sigma^z$ . It is easy to find that  $\mathbb{T}(t) = \cos(Jt)^2 \mathbb{I} + \sin(Jt)^2 \sigma^x$ , and  $\mathbb{V} = (\sigma^z + \sigma^x)/\sqrt{2}$  whose columns are the eigenvectors of  $\sigma^x$ . As expected  $d_1 = 1$  and  $d_2(t) = \cos(\Omega t)$ , where  $\Omega = 2J$  is the splitting between the energy eigenvalues of the system. Notice that, from these eigenvalues we can derive two recursion relations as in the integral equations (312), then, since  $d_1 = 1$  we immediately get  $I_1(s) = e^{\gamma s}$ . In the following, we will simplify the notation  $I_2(s) = I(s)$ . Finally, we notice that  $\mathcal{D}(x, \sigma_n, t - s_n) = \delta(x - \sigma_n \cos(\Omega(t - s_n)))$ , from which we can compute the no-click contribution

$$P_{\sigma^z}^{(0)}(x; t) = e^{-\gamma t} \delta(x - \cos(\Omega t)). \quad (321)$$

In order to find the full probability distribution, we can use equation (316) to write

$$P_{\sigma^z}^{(n>0)}(x; t) = \frac{e^{-\gamma t}}{2} \int_0^t \gamma ds \sum_{\sigma=\pm 1} \delta(x - \sigma \cos(\Omega(t - s))) [e^{\gamma s} + \sigma I(s)] \quad (322)$$

For a better understanding of the solution, we do not apply the Laplace method to solve the integral equation (313) for  $I(s)$ . Instead, we differentiate it twice with respect to  $s$ , which yields the following differential equation for  $I(s)$

$$\ddot{I} = \gamma \dot{I} - \Omega^2 I \quad (323)$$

with the initial conditions  $I(0) = 1$  and  $\dot{I}(0) = \gamma$ . This is the equation of motion of an ‘‘anti-damped’’ harmonic oscillator (since  $\gamma > 0$ ). The solution can be found easily using standard methods [230], obtaining

$$I(s) = e^{\gamma s/2} \left[ \cosh\left(\frac{\Gamma s}{2}\right) + \frac{\gamma}{\Gamma} \sinh\left(\frac{\Gamma s}{2}\right) \right], \quad (324)$$

where we defined the following characteristic frequency  $\Gamma = \sqrt{\gamma^2 - 4\Omega^2}$ . As expected, we find three different regimes depending on the sign of  $\gamma^2 - 4\Omega^2$ . Let us analyze the behavior of the function  $e^{-\gamma s/2} I(s)$ . When  $\gamma < 2\Omega$ , we have that  $\Gamma$  is an imaginary quantity. Therefore, we find a regime in which the function oscillates with a frequency of  $\Omega \sqrt{1 - \gamma^2/(4\Omega^2)}$ , which is lower than the natural frequency  $\Omega$ . When  $\gamma = 2\Omega$ , we get the critical regime for which the function  $e^{-\gamma s/2} I(s)$  becomes linear,  $(1 + \gamma s/2)$ . Finally, if  $\gamma > 2\Omega$ , it grows exponentially with a rate  $\gamma/2 \sqrt{1 - 4\Omega^2/\gamma^2}$  smaller than  $\gamma/2$ .

Let us finally consider the Dirac-delta function contribution. Solving for  $x - \sigma \cos(\Omega(t - s)) = 0$ , we easily get

$$\tilde{s}_k = t \pm \frac{1}{\Omega} \arccos(x\sigma) + \frac{2\pi k}{\Omega}, \quad k \in \mathbb{Z}. \quad (325)$$

Using the properties of the Dirac-delta distribution, we can rewrite it as

$$\delta(x - \sigma \cos(\Omega(t - s))) = \sum_{k \in \mathbb{Z}} \frac{\delta(s - \tilde{s}_k)}{\Omega \sqrt{1 - x^2}}. \quad (326)$$

Since in Eq. (322), the integral is taken over a finite interval  $[0, t]$ , we need to constraint the solutions  $\tilde{s}_k$  in Eq. (325) only to those falling in that region. However, we may relax that condition by explicitly introducing the Heaviside step function  $\theta(x)$ , such that Eq. (322) finally reads

$$P_{\sigma^z}^{(n>0)}(x; t) = \frac{\gamma e^{-\gamma t}}{2\Omega \sqrt{1 - x^2}} \sum_{\sigma=\pm 1} \sum_{k \in \mathbb{Z}} [e^{\gamma \tilde{s}_k} + \sigma I(\tilde{s}_k)] \theta(t - \tilde{s}_k) \theta(\tilde{s}_k), \quad (327)$$

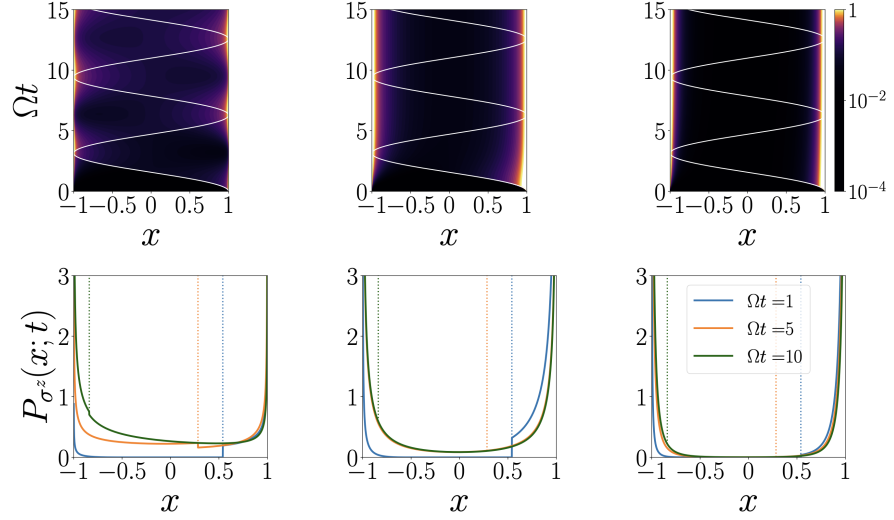


Figure 26: Upper panels: the time-dependent probability distribution  $P_{\sigma_z}(x; t)$  for a two-level system ( $\Omega = 1$ ). The white continuous line represents the no-click contribution  $P^{(0)}(x; t)$  in Eq. (321). We set  $\gamma = 0.2$  (left),  $\gamma = 2.0$  (center) and  $\gamma = 5.0$  (right). Lower panels: the distribution  $P_{\sigma_z}(x; t)$  for  $\Omega t = 1, 5, 10$  and the same values of  $\gamma$ . Dotted lines represent the delta peak corresponding to the no-click contribution  $P^{(0)}(x; t)$ .

where  $\tilde{s}_k$  implicitly depends on  $x$  and  $t$  as well. In Figure 26, we plot the entire distribution  $P_{\sigma_z}(x; t)$ . As expected, at early time the probability is highly asymmetric, having support only in the vicinity of  $x = 1$ . The no-click term is in fact localised at  $x = \cos(\Omega t)$  but its weight is exponentially suppressed in time. The click contribution is also showing a nontrivial asymmetric evolution and has a discontinuity corresponding to the value of the no-click delta peak (see lower panels). Its behavior strongly depends on  $\gamma$  indeed: in the oscillatory regime ( $\gamma < 2\Omega$ ), the probability distribution function bounces back and forth between the two extremes  $x = \pm 1$  of its domain; after many oscillations, the number depending on the value of  $\gamma$ , it is expected to relax toward a symmetric distribution, the typical relaxation time being  $\tau = 2/\gamma$ . For  $\gamma > 2\Omega$  the probability is not oscillating anymore and the relaxation time becomes  $\tau = 2/(\gamma - \Gamma)$ . Interestingly, as the measurement rate is getting higher, the time needs for the magnetisation statistics to reach the equilibrium becomes larger and larger, diverging as  $\tau \sim \gamma/\Omega^2$ .

The first moment of  $P_{\sigma_z}(x; t)$ , namely the magnetisation average  $\langle x \rangle_{P_{\sigma_z}} = e^{-\gamma t} I(t)$ , does coincide with the expectation value over the averaged state (see 6.4.1). Nevertheless, our approach allows to easily compute the fluctuations of the magnetization along the trajectories. Indeed, by means of Eqs. (321) and (322), we can easily get the second moment of the distribution

$$\langle x^2 \rangle_{P_{\sigma_z}} = e^{-\gamma t} \int_0^t \gamma ds \cos(\Omega(t-s))^2 e^{\gamma s} + e^{-\gamma t} \cos(\Omega t)^2, \quad (328)$$

which simplifies to

$$\langle x^2 \rangle_{P_{\sigma_z}} = \frac{\gamma^2 + 2\Omega^2}{\gamma^2 + 4\Omega^2} + \frac{e^{-\gamma t}}{2(\gamma^2 + 4\Omega^2)} \left[ 2\gamma\Omega \sin(2\Omega t) + \Omega^2 \cos(2\Omega t) \right], \quad (329)$$

and which cannot be computed using the a Lindblad approach since it corresponds to  $\overline{\langle \psi_\xi(t) | \sigma_z | \psi_\xi(t) \rangle^2}$ . In Figure 27, we represents  $\langle x \rangle_{P_{\sigma_z}}, \langle x^2 \rangle_{P_{\sigma_z}}$  as a function of time for different values of the measurement rate  $\gamma$ .

Finally, let us mention that one can easily obtain the asymptotic stationary distribution  $P_{\sigma_z}(x, t \rightarrow \infty)$ . Indeed, from a careful inspection of Eq. (322)

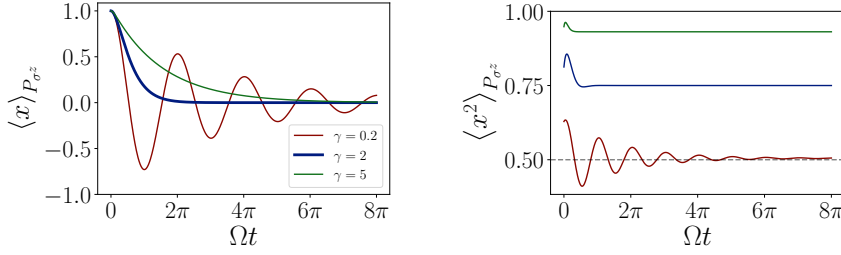


Figure 27: First (left) and second (right) moment of the probability distribution  $P_{\sigma^z}(x; t)$  for a two-level system ( $\Omega = 1$ ). Notice that the critical value of  $\gamma = 2$  leads to the fastest convergence to the equilibrium stationary value of the average magnetization.

one can argue that for large time the contribution coming from  $I(s)$  is bounded by  $e^{-\gamma t} \int_0^t ds |I(s)|$ , thus decaying exponentially for large time. The only term that survives and contributes to the asymptotic stationary distribution is the one depending on  $e^{\gamma s}$ . Therefore, for any finite  $\gamma$ , the stationary distribution can be exactly evaluated as

$$P_{\sigma^z}(x) = \frac{\gamma}{2} \sum_{\sigma=\pm 1} \int_0^\infty ds \delta(x - \sigma \cos(\Omega s)) e^{-\gamma s} \quad (330)$$

$$= \frac{\gamma \left[ e^{2\gamma \arcsin(x)/\Omega} + 1 \right] e^{\gamma \arccos(x)/\Omega}}{2\Omega (e^{\pi\gamma/\Omega} - 1) \sqrt{1-x^2}}, \quad (331)$$

which, as expected, is an even function of  $x$ . Interestingly, all (non-vanishing) stationary moments can be easily computed from the integral representation of the probability, namely

$$\begin{aligned} \langle x^{2n} \rangle_{P_{\sigma^z}} &= \int_0^\infty ds e^{-s} \cos^{2n}(s\Omega/\gamma) \\ &= \frac{{}_2F_1(-2n, -n - i\gamma/(2\Omega); 1 - n - i\gamma/(2\Omega); -1)}{2^{2n}(1 - 2i\Omega/\gamma)}, \end{aligned} \quad (332)$$

while the odd moments are identically vanishing. In particular, when  $\gamma \rightarrow \infty$ ,  $\langle x^{2n} \rangle_{P_{\sigma^z}} \rightarrow 1$  for all  $n$ , confirming the fact that the stationary distribution converges to  $[\delta(x-1) + \delta(x+1)]/2$ .

Observe that, having already taken the limit  $t \rightarrow \infty$  to derive the stationary distribution, the limit  $\gamma \rightarrow \infty$  does not result in the distribution linked to Zeno's effect, namely  $\delta(x-1)$ . To clarify, the order of limits matters, and to obtain the Zeno's effect distribution, one have to first take the limit  $\gamma \rightarrow \infty$ .

### 6.3 HOPPING PARTICLE

A free hopping quantum particle propagates in a lattice with a ballistic spreading. However, there are ways to prevent or slow down the propagation as, for instance, adding a disorder potential which induces Anderson localization [231, 232]. Here, we show that the quantum Zeno effect due to the coupling of the hopping particle to a measurement apparatus can also results into a slowdown of the particle propagation [233, 234]. Related protocols have been studied in the context of quantum stochastic resetting, in which the hopping particle is reset to the initial state with a certain probability [235].

We consider a simple hopping fermion on a 1D lattice, whose hamiltonian reads

$$H = -\Omega \sum_{j=1}^L \left( c_j^\dagger c_{j+1} + c_{j+1}^\dagger c_j \right) \quad (333)$$

with periodic boundary conditions (i.e.  $c_{j+L} = c_j$ ). Here the lattice dimension  $L$  (even) plays the role of an infrared cutoff. In the following we will take the limit  $L \rightarrow \infty$  whenever it will be unambiguous. The Fermionic operators satisfy the canonical anti-commutation relations  $\{c_i, c_j^\dagger\} = \delta_{ij}$ . We define the Fourier modes operators

$$\tilde{c}_k = \frac{1}{\sqrt{L}} \sum_j e^{ikj} c_j, \quad c_j = \frac{1}{\sqrt{L}} \sum_k e^{-ikj} \tilde{c}_k, \quad (334)$$

such that  $\{\tilde{c}_p, \tilde{c}_q^\dagger\} = \delta_{pq}$ , and  $k \in \{-\pi, -\pi + 2\pi/L, -\pi + 4\pi/L, \dots, \pi\}$ . The Hamiltonian become diagonal in the Fourier representation, i.e.

$$H = \sum_k \varepsilon(k) \tilde{c}_k^\dagger \tilde{c}_k, \quad (335)$$

where  $\varepsilon(k) = -2\Omega \cos k$ . We now restrict the problem to the single-particle sector of the hamiltonian, we can define the states  $|j\rangle = c_j^\dagger |\emptyset\rangle$  and  $|\tilde{k}\rangle = \tilde{c}_k^\dagger |\emptyset\rangle$ , which represents the particle in position  $j$  or with momentum  $k$  respectively. Notice that  $\langle j|\tilde{k}\rangle = \exp(-ikj)/\sqrt{L}$  is the normalised wave function. Since  $H$  commute with the total number of particles, the unitary dynamics can be restricted in such sector and it is governed by the following single-particle Hamiltonian

$$H = -\Omega \sum_{j=1}^L (|j\rangle\langle j+1| + |j+1\rangle\langle j|) = \sum_k \varepsilon(k) |\tilde{k}\rangle\langle \tilde{k}|. \quad (336)$$

We consider the particle initial localised at the origin  $j = 0$  of our lattice, namely  $|\psi_\xi(0)\rangle = |0\rangle$  for all trajectories  $\xi$ . We then suppose to continuously measure, with a rate  $\gamma$ , the position operator

$$q = \sum_j j |j\rangle\langle j|. \quad (337)$$

We are thus interested in the displacement of the particle along each single trajectory, however, for symmetry reasons, when no measurement occurs (i.e.  $\gamma = 0$ ) the probability function of the outcome of  $\langle q \rangle_t$  is time independent, namely  $\overline{\delta(x - \langle q \rangle_t)} = \delta(0)$ . This is not in contradiction with the expected ballistic spreading under the free evolution, which can be extracted when observing even power of  $q$  (see 6.4.2). Notice that, this is not true anymore when  $\gamma \neq 0$ . We are thus interested in the probability distribution function of the particle displacement itself, namely

$$P_q(x; t) = \overline{\delta(\langle \psi_\xi(t) | q | \psi_\xi(t) \rangle - x)} = P_q^{(n>0)}(x; t) + P_q^{(0)}(x; t), \quad (338)$$

where in this case the no-click contribution is trivially given by  $P_q^{(0)}(x; t) = e^{-\gamma t} \delta(x)$ , and we used the following results for the evolution amplitudes in the thermodynamic limit

$$\begin{aligned} \langle j | U(t) | l \rangle &= \sum_k \langle j | e^{-itH} | \tilde{k} \rangle \langle \tilde{k} | l \rangle \\ &= \int_{-\pi}^{\pi} \frac{dk}{2\pi} e^{i[k(j-l) - 2t\Omega \cos k]} \\ &= (-i)^{j-l} J_{j-l}(2\Omega t), \end{aligned} \quad (339)$$

with  $J_n(x)$  being the Bessel function of the first kind. Now the transition probability matrix reads  $\mathbb{T}_{i,j}(t) = J_{i-j}^2(2\Omega t)$ , which is a circulant matrix due

to translational invariance. Let us define the not normalised eigenvectors whose component are  $\mathbb{V}_{n,k} = e^{-ink}$ , such that

$$\begin{aligned} (\mathbb{T}(t)\mathbb{V})_{n,k} &= \sum_j J_{n-j}^2(2\Omega t) e^{-ijk} \\ &= e^{-ink} \sum_l J_l^2(2\Omega t) e^{ilk} \equiv \mathbb{V}_{n,k} d_k(t) \end{aligned} \quad (340)$$

where we identified the eigenvalues of the transfer matrix as

$$d_k(t) = \sum_l J_l^2(2\Omega t) e^{ikl} = J_0[\omega_k t], \quad (341)$$

with  $\omega_k = 4\Omega \sin(k/2)$ . Following Section 6.1, we can easily solve the integral equation (313) for  $I_k(s) = \sum_{n=1}^{\infty} I_{n,k}(s)$  with kernel  $J_0[\omega_k t]$ ; the Laplace transform reads

$$\mathcal{L}[I_k](z) = \frac{1}{\sqrt{z^2 + \omega_k^2} - \gamma} = \sum_{n=1}^{\infty} \frac{\gamma^{n-1}}{(z^2 + \omega_k^2)^{n/2}}, \quad (342)$$

and we can identify with  $\mathcal{L}[I_{n,k}](z)$  the terms of the series expansion, thus finally getting

$$I_{n,k}(s) = \sqrt{\pi} \gamma^{n-1} \left( \frac{s}{2|\omega_k|} \right)^{\frac{n-1}{2}} \frac{J_{\frac{n-1}{2}}(s|\omega_k|)}{\Gamma(n/2)}. \quad (343)$$

With a simple generalization of equation (310), we can write the click contribution to the probability distribution as

$$P_q^{(n>0)}(x;t) = e^{-\gamma t} \sum_j \int_0^t \gamma ds \int_{-\pi}^{\pi} \frac{dk}{2\pi} \mathcal{D}(x,j,t-s) e^{-ijk} I_k(s), \quad (344)$$

where, thanks to the properties of the Bessel functions, the delta contribution reduces to  $\mathcal{D}(x,j,t-s) = \delta(x-j)$ , which basically says that the probability has only support on  $x \in \mathbb{Z}$ . The entire probability distribution  $P_q(x;t)$  is represented in Figure 28 together with some representative quantum trajectories for different values of  $\gamma$ .

We have previously observed that the first moment of the probability distribution is identically vanishing due to the inversion symmetry. The second moment instead gets a nontrivial contribution from the  $P_q^{(n>0)}$  part, thus reading

$$\langle x^2 \rangle_{P_q} = e^{-\gamma t} \int_0^t \gamma ds \int_{-\pi}^{\pi} \frac{dk}{2\pi} \left[ \sum_j j^2 e^{-ijk} \right] I_k(s), \quad (345)$$

which can be further simplified using the identity  $\sum_j j^2 e^{-ijk} = -\sum_j \partial_k^2 e^{ijk} = -2\pi \delta''(k)$ , leading to

$$\langle x^2 \rangle_{P_q} = -e^{-\gamma t} \int_0^t \gamma ds [\partial_k^2 I_k(s)]|_{k=0} = \frac{4\Omega^2}{\gamma^2} [(\gamma t - 2) + e^{-\gamma t}(\gamma t + 2)]. \quad (346)$$

The second moment does behave differently depending on the time-scale, showing the following scaling behaviour

$$\langle x^2 \rangle_{P_q} \sim \begin{cases} \gamma \Omega^2 t^3 & \gamma t \ll 1 \\ \frac{4\Omega^2 t}{\gamma} & \gamma t \gg 1 \end{cases}. \quad (347)$$

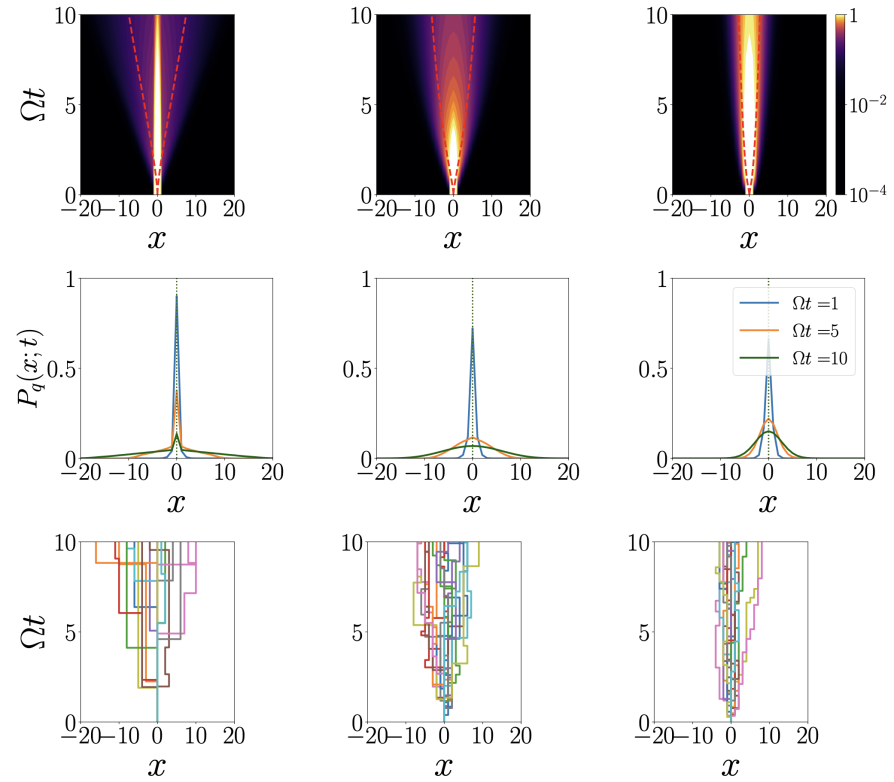


Figure 28: Upper panels: the time-dependent probability distribution  $P_q(x;t)$  for an hopping particle ( $\Omega = 1$ ). Red lines represents the standard deviation  $\pm \langle x^2 \rangle_{P_q}^{1/2}$  as in Eq. (346). We set  $\gamma = 0.25$  (left),  $\gamma = 1.0$  (center) and  $\gamma = 5.0$  (right). Middle panels: the distribution  $P_q(x;t)$  for  $\Omega t = 1, 5, 10$  and the same values of  $\gamma$ . Dotted lines represent the delta peak corresponding to the no-click contribution  $P^{(0)}(x;t)$ . Lower panels: the expectation value  $\langle \psi_\xi(t) | q | \psi_\xi(t) \rangle$  for 20 trajectories and the same values of  $\gamma$ .

Let us mention that the fluctuations of the  $P_q(x;t)$  distribution cannot give information about the ballistic behavior at  $\gamma = 0$ , due to the inversion symmetry. As a matter of fact, what Eq. (347) gives us is the leading term for  $\gamma \neq 0$ . In the asymptotic regime  $\gamma t \gg 1$ , it does coincide (as expected) with  $\langle x \rangle_{P_{q^2}}$  confirming the diffusive behavior for any finite measurement rate. However, in the  $\gamma t \ll 1$  regime, the  $O(\gamma^0)$  term is missing, and it is recovered in the expansion of  $\langle x \rangle_{P_{q^2}}$  (see 6.4.2).

## 6.4 APPENDICES

In this section, we provide two appendices related to the chapter.

### 6.4.1 Appendix A: Lindblad equation solution for the two level system

When we are interested in the dynamical map averaged over the quantum trajectories, the measurement protocol outlined in the main text can be reformulated in terms of a Lindblad equation for the averaged density matrix  $\rho(t) = |\psi_\xi(t)\rangle\langle\psi_\xi(t)|$ . In fact, averaging over different trajectories does correspond to relax both the information on whether the spin has been measured, and the result of the measurement itself. See [236] for some results of projective measurement-based dissipation descriptions of Lindblad equations for quantum spin systems.

In particular for a single spin undergoing projective measurements of  $\sigma^z$  (see Sec. 6.2), the average state  $\rho$  transforms accordingly to

$$\rho(t) \rightarrow \left(1 - \frac{\gamma dt}{2}\right) \rho(t) + \frac{\gamma dt}{2} \sigma^z \rho(t) \sigma^z, \quad (348)$$

where  $\gamma dt$  is the probability that the system is measured, after a discretization of the continuum time evolution has been applied.

Combining the previous expansion with the unitary part of the evolution, and taking the continuum limit  $dt \rightarrow 0$  with  $\gamma$  fixed, we finally get the following Lindblad master equation

$$\partial_t \rho = -i[H, \rho] + \frac{\gamma}{2} (\sigma^z \rho \sigma^z - \rho), \quad (349)$$

with  $H = -J\sigma^x$ . This equation can be easily solved by expanding the density operator in the basis of Pauli matrices

$$\rho(t) = \frac{1}{2}\mathbb{I} + \frac{1}{2} \sum_{\alpha=1}^3 m_\alpha(t) \sigma^\alpha, \quad (350)$$

where  $m_\alpha(t) = \text{Tr}[\sigma^\alpha \rho(t)]$  and  $\mathbb{I}$  is the  $2 \times 2$  identity matrix. The Lindblad equation becomes a linear differential equation for the three components of the magnetisation  $(m_x, m_y, m_z)^T$ , which reads

$$\partial_t \begin{pmatrix} m_x \\ m_y \\ m_z \end{pmatrix} = \begin{pmatrix} -\gamma & 0 & 0 \\ 0 & -\gamma & \Omega \\ 0 & -\Omega & 0 \end{pmatrix} \begin{pmatrix} m_x \\ m_y \\ m_z \end{pmatrix} \quad (351)$$

where  $\Omega = 2J$ . The  $z$  component evolves following the differential equation of a damped harmonic oscillator  $\partial_t^2 m_z = -\Omega^2 m_z - \gamma \partial_t m_z$ , with initial condition  $m_z(0) = 1$ ,  $\partial_t m_z(0) = 0$ . From the solution of such equation we easily recover the result of the main text, namely

$$m_z(t) = e^{-\gamma t/2} \left[ \cosh\left(\frac{\Gamma t}{2}\right) + \frac{\gamma}{\Gamma} \sinh\left(\frac{\Gamma t}{2}\right) \right] \equiv \langle x \rangle_{P_{\sigma^z}} \quad (352)$$

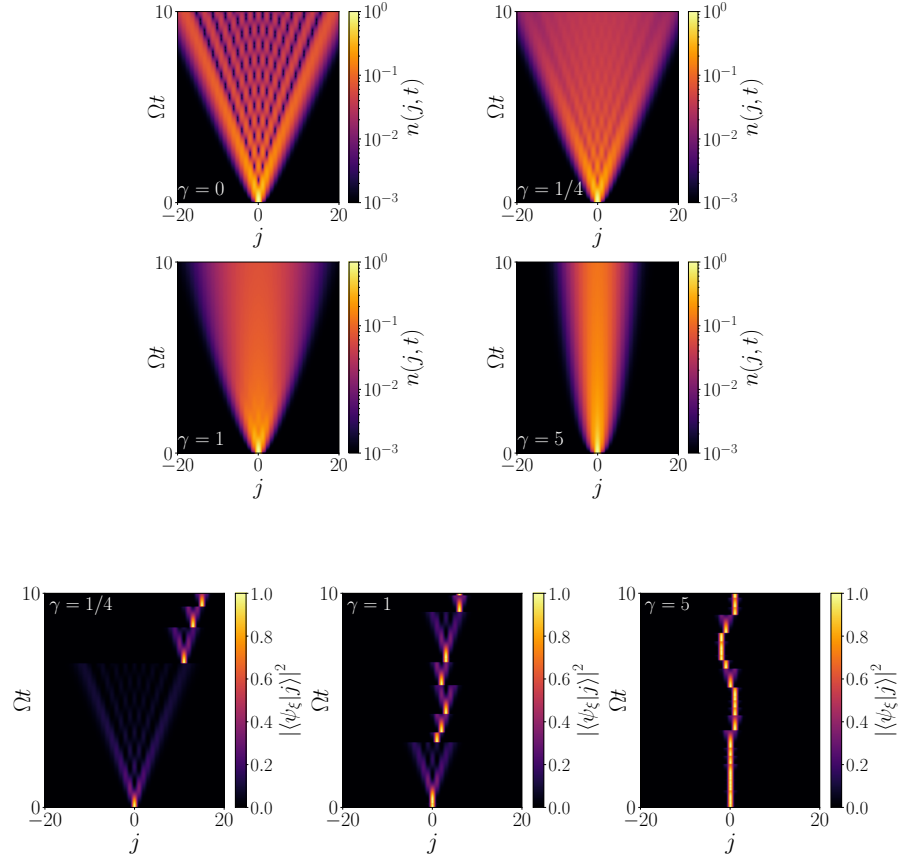


Figure 29: Upper four panels: average local particle density  $n(j, t)$  obtained from the average state given by Lindblad equation (Eq. 355). Different measurement rates are considered (i.e.  $\gamma = 0, 0.25, 1, 5$ ), showing a clear transition from ballistic to diffusive dynamics. Lower three panels: the local particle density  $|\langle\psi_\xi|j\rangle|^2$  obtained from quantum trajectories at different measurement rates ( $\gamma = 0.25, 1, 5$ ).

with  $\Gamma = \sqrt{\gamma^2 - 4\Omega^2}$ . In addition, we also gets

$$m_x(t) = 0, \quad m_y(t) = e^{-\gamma t/2} \frac{2\Omega}{\Gamma} \sinh\left(\frac{\Gamma t}{2}\right). \quad (353)$$

#### 6.4.2 Appendix B: Lindblad equation solution for the hopping particle

In the case of the hopping particle, to analyze the dynamical map averaged over quantum trajectories, we can again reframe the measurement procedure as a Lindblad equation for the averaged density matrix  $\rho(t)$ . When we perform projective measurements of the particle's position at a rate  $\gamma$ , the average state  $\rho$  undergoes the following transformation in accordance with the usual rules of quantum mechanics

$$\rho(t) \rightarrow (1 - \gamma dt) \rho(t) + \gamma dt \sum_j \pi_j \rho(t) \pi_j. \quad (354)$$

Here,  $\pi_j = |j\rangle\langle j|$  represents the projectors over the lattice sites. The Lindblad master equation can be obtained by taking the limit  $dt \rightarrow 0$  with a fixed value of  $\gamma$ , resulting in

$$\partial_t \rho = -i[H, \rho] + \gamma \left[ \sum_j \pi_j \rho \pi_j - \rho \right], \quad (355)$$



with  $H$  as in Eq. (336). In the case of a system with finite size, we can solve numerically the dynamical map

$$\rho(t + dt) = \rho(t) - idt (H\rho - \rho H) + \gamma dt \left[ \sum_j \pi_j \rho(t) \pi_j - \rho(t) \right], \quad (356)$$

and define the site densities  $n(j, t) = \text{Tr}\{\rho(t)\pi_j\}$  as depicted in the upper four panels in Fig. 29. In accordance to what have been discussed in the main text, the averages over the probability distribution coincides with the expectation values taken over the averaged state.

Now, we collect few results for the first moment of some relevant observables. In particular, from the probability distribution of a generic power  $q^m$ , by using the generic equation (318) we explicitly get

$$\langle x \rangle_{P_{q^m}} = \text{Tr}\{\rho(t)q^m\} = e^{-\gamma t} \int_{-\pi}^{\pi} \frac{dk}{2\pi} \sum_j j^m e^{-ijk} I_k(t). \quad (357)$$

By exploiting  $\sum_j j^m e^{-ijk} = i^m 2\pi \delta^{(m)}(k)$ , we obtain

$$\langle x \rangle_{P_{q^m}} = i^m e^{-\gamma t} \partial_k^m I_k(t)|_{k=0}. \quad (358)$$

As expected,  $\langle x \rangle_{P_q} = 0$ , while the first non-vanishing average occurs for  $m = 2$ , giving

$$\langle x \rangle_{P_{q^2}} = \frac{4\Omega^2 (\gamma t + e^{-\gamma t} - 1)}{\gamma^2} \sim \begin{cases} 2\Omega^2 t^2 & \gamma t \ll 1 \\ \frac{4\Omega^2 t}{\gamma} & \gamma t \gg 1 \end{cases} \quad (359)$$

thus, we recover the ballistic behavior at early time (or for  $\gamma = 0$ ), whilst a diffusive behavior for any  $\gamma \neq 0$  at large time, with a diffusion constant  $D_\gamma = 2\Omega^2/\gamma$  such that  $\langle x_{q^2} \rangle \sim 2D_\gamma t$ . This behavior has been observed in the many-body description of the model, in particular studying the particle current after quenching an initial domain wall configuration [153]. Due to its linear nature, this exact result can be compared with the solution of the Lindblad equation. Indeed, the average of  $q^2$  is also given by  $\langle x \rangle_{P_{q^2}} = \sum_j j^2 n(j, t)$ , where  $n(j, t) = \text{Tr}\{\rho(t)\pi_j\}$  can be evaluated numerically (see Fig. 29 upper panels), or analytically taking the average over the probability distribution associated to  $\pi_j$

$$P_{\pi_j}(x; t) = \overline{\langle \psi_\xi(t) | \pi_j | \psi_\xi(t) \rangle - x}. \quad (360)$$

Explicitly we get

$$\langle x \rangle_{P_{\pi_j}} = n(j, t) = e^{-\gamma t} \int_{-\pi}^{\pi} \frac{dk}{2\pi} e^{-ijk} I_k(t), \quad (361)$$

notice that, as expected,  $\sum_j n(j, t) = 1$ , since  $I_0(t) = e^{\gamma t}$ .



## SEMICLASSICAL QUANTUM TRAJECTORIES IN THE MONITORED LMG MODEL

An interesting playground for the investigation of MIPTs is given by long-range interacting systems, in which the interactions between their different components decay slowly (typically as a power-law function of the distance) or do not decay at all, as in fully-connected models. Long-range physics has recently attracted a lot of attention due its peculiar properties [237, 238] and to the possibility of engineering such systems in experimental setups within the context of atomic, molecular and optical (AMO) systems. Examples are Rydberg atoms [239–241], trapped ions [242, 243], and quantum gases in a cavity [244, 245], showing promising features for the development of quantum technologies.

In this Chapter, we focus of the so-called Lipkin-Meshkov-Glick (LMG) model, i.e. a ferromagnetic all-to-all interacting spin model with  $\mathbb{Z}_2$  symmetry. First introduced in the context of nuclear physics [246], the LMG model has become a paradigmatic example used to exemplify plenty of non-trivial dynamical behavior of long-range quantum systems [247–250], such as time-crystals [99, 251–253], anomalous entanglement growth [254, 255], dynamical phase transitions [255]. The interplay between long-range interactions and monitoring has also been investigated [177, 256, 257], finding that the range of the interaction can significantly alter even hinder MIPTs [160], as well as the effect of the global losses in AMO systems [258]. Moreover, the full-counting statics of the quantum trajectories in the open long-range spin systems and also in the LMG limit, has been also recently studied [144].

Here, we focus on a different class of observables. In particular, we analyse the stochastic dynamics of the expectation values of the global spin on the quantum trajectories in the thermodynamic limit, discovering that a phase transition is already present at the level of its ensemble average, a quantity which for finite size is known to converge trivially to its infinite temperature value. This signals a non-commutativity of the long-time and large-size limits, that can be traced back to the fact that, while individual quantum trajectories allow for a semiclassical description in the thermodynamic limit, this is no longer true if one consider the ensemble average of the quantum state. Let us notice that presence of a MIPT already at the presence of ensemble averages has a great interests as it allows to circumvent the post-selection issue, since these quantities are linear in the quantum state.

### 7.1 MONITORING AND QUANTUM TRAJECTORIES

The evolution of a quantum system continuously interacting with a monitoring environment is intrinsically stochastic due to the random nature of quantum measurements. As a consequence, its time evolution is described by a stochastic Schrödinger equation (SSE). Many detection protocols exist and here we focus on the case of weak Gaussian measurements [220], which can be experimentally reproduced with a homodyne detection scheme [131, 220]. Considering a pure state evolving under the action of a Hamiltonian  $H$  and continuous monitoring of observable  $X$  with strength  $\gamma$ , its SSE is given by (see 4.1.2 for details)

$$d|\psi_t\rangle = -iH|\psi_t\rangle dt + (|v\rangle \gamma dt + |u\rangle \sqrt{\gamma} d\xi), \quad (362)$$

*Stochastic  
Schrödinger  
evolution equation  
monitored quantum  
system*

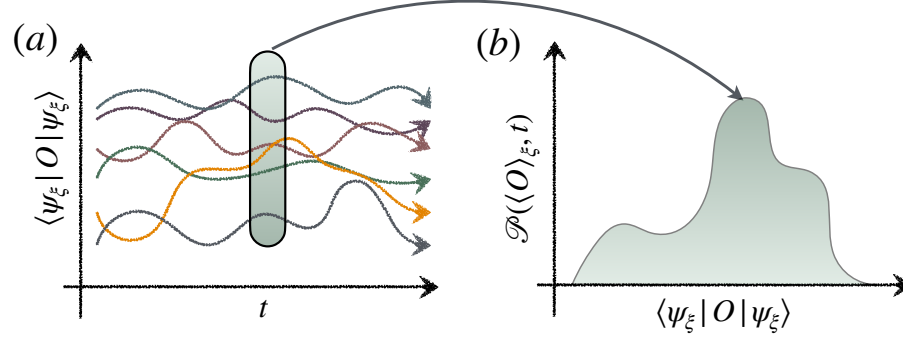


Figure 30: (a) Evolution of the expectation value of a set of quantum trajectories. (b) Probability distribution of the expectation values of the observable  $O$  over the ensemble of quantum trajectories.

where  $d\xi$  is a real Itô differential with  $\overline{d\xi^2} = dt$  and

$$|v\rangle = -\frac{1}{2}(X - \langle X \rangle)^2 |\psi_t\rangle, \quad |u\rangle = (X - \langle X \rangle) |\psi_t\rangle. \quad (363)$$

The SSE is solved by an ensemble of quantum trajectories  $\{|\psi(t)_\xi\rangle\}$  in the Hilbert space, each induced by a specific realization of the white noise  $d\xi$ . Correspondingly, the expectation values of an observable  $O$  evaluated along a trajectory evolve along a classical stochastic process. According to Itô calculus [229], we expand

$$d\langle O \rangle = \langle d\psi | O | \psi \rangle + \langle \psi | O | d\psi \rangle + \langle d\psi | O | d\psi \rangle, \quad (364)$$

where  $\langle O \rangle = \langle \psi | O | \psi \rangle$  and  $\langle d\psi | O | d\psi \rangle = \gamma dt \langle u | O | u \rangle$  as a consequence of  $d\xi^2 \approx dt$ . The stochastic differential equation satisfied by  $\langle O \rangle$  is then

$$d\langle O \rangle = idt \langle [H, O] \rangle + \langle [X - \langle X \rangle, O] \rangle \sqrt{\gamma} d\xi - \frac{\gamma}{2} dt \langle [X, [X, O]] \rangle. \quad (365)$$

Stochastic  
Heisenberg evolution  
equation monitored  
quantum system

### 7.1.1 Ensemble averages and full counting statistics

Let us introduce the average of the state of the system over all measurement outcomes, namely  $\rho = |\overline{\psi_\xi}\rangle\langle\overline{\psi_\xi}|$ , where  $\overline{\cdot}$  denotes the average over  $d\xi$ . From Eq. (362) it is immediate to find that the evolution over time of  $\rho$  is described by

Lindblad Equation

$$\frac{d\rho}{dt} = -i[H, \rho] - \frac{\gamma}{2}[X, [X, \rho]], \quad (366)$$

that is a master equation of the Lindblad form. The observable  $X$  is playing the role of the jump operator, which encode the interaction with the external environment. As the jump operator is Hermitian, for any finite dimension  $N$  the Lindblad dynamics will evolve towards the maximally mixed state in any of the symmetry sector of the Hilbert space, thus washing away all the information contained in the initial state  $\rho(0)$  except for the presence of invariant subspaces [131, 221]. If no symmetry is present then  $\rho(t \rightarrow \infty) \propto \mathbb{I}$  over the whole Hilbert space.

In the same way, the averages along trajectories of expectation values follow Lindblad dynamics since  $\langle O \rangle = \text{tr}[|\psi_\xi\rangle\langle\psi_\xi| O] = \text{tr}[\rho O] \equiv \langle O \rangle_\rho$ . Their evolution is generated by the adjoint Lindbladian

$$d\overline{\langle O \rangle} = idt \overline{\langle [H, O] \rangle} - \frac{\gamma}{2} dt \overline{\langle [X, [X, O]] \rangle}. \quad (367)$$

Analogously, for finite  $N$  we have that  $\overline{\langle O \rangle}$  will converge asymptotically to its infinite-temperature expectation values for large times.

Although linear averages only admit trivial long-time asymptotic values, it is important to note that important features of the ensemble of quantum trajectories are hidden in the higher moments of the distribution. A prominent example is the purity: starting from a pure state, while for any  $t > 0$   $\rho(t)$  will be a mixed state, asymptotically reaching the maximally mixed state, individual trajectories remain pure, so that

$$\text{Tr}\{\rho^2\} \leq \overline{\text{Tr}\{|\psi_\xi\rangle\langle\psi_\xi|^2\}} = 1. \quad (368)$$

In other words, the SSE carries more information than the Lindblad equation. Here, we want to go beyond the Lindblad approach and study statistical properties of the ensemble of weak monitoring quantum trajectories. As an example, as depicted in Fig. 30, we consider the characteristics of the probability distribution of the expectation values of operators [4, 5, 259, 260]

$$P(x, t) = \overline{\delta(x - \langle\psi_\xi|O|\psi_\xi\rangle)}. \quad (369)$$

## 7.2 MONITORED LMG MODEL

Given a set of  $N$  spin-1/2 particles, each located in a lattice site  $j$ , the LMG model is described by the following Hamiltonian

*LMG model*

$$H = -\frac{1}{2N} \sum_{ij} \sigma_i^x \sigma_j^x - h \sum_i \sigma_i^z, \quad (370)$$

where  $\sigma_j^\alpha$  are the Pauli operators for each site,  $h$  is a magnetic field and the  $1/N$  factor is the Kac scaling [261] that ensures the correct extensive scaling of the energy. We are working in units such that  $\hbar = 1$ . The above Hamiltonian can be seen as a quantum Ising model in transverse field, in presence of infinite-range ferromagnetic interactions. It is convenient to express it in terms of collective spin operators  $S_\alpha$  or, equivalently, of the reduced global magnetization  $m_\alpha$

$$S_\alpha = \frac{1}{2} \sum_j \sigma_j^\alpha, \quad m_\alpha = \frac{S_\alpha}{S} = \frac{1}{N} \sum_j \sigma_j^\alpha, \quad (371)$$

with  $\alpha = x, y, z$ ,  $S = N/2$ , so that

$$H = -\frac{1}{S} S_x^2 - 2h S_z = -\frac{N}{2} \left( m_x^2 + 2h m_z \right). \quad (372)$$

As  $H$  and  $S^2$  commute, the unitary dynamics takes place in subspaces with fixed  $S^2 = S(S+1)$ ,  $S = 1, \dots, N/2$ .

Let us now introduce a deformation of the the LMG model in which the global spin  $S_z$  undergoes a continuous weak monitoring. Due to the global nature of the monitored observables, the dynamics of the resulting SSE (362) will share the same symmetry of the unitary evolution, so that the monitored dynamics will also decompose into invariant subspaces with  $S^2 = S(S+1)$  fixed. In particular we choose the initial state to be fully-magnetized along a specific spatial direction (not necessarily coinciding with the  $z$ -axis), so that the dynamics will be confined on the subspace  $S = N/2$  ( $\mathbf{m}^2 = (S+1)/S$ ). Such sector corresponds to the representation of spin  $N/2$  of the total angular momentum, which is totally symmetric with respect to the permutation symmetry of the LMG model. We will focus on the statistics of the expectation values of the global magnetization  $m_\alpha$ : in this case Eq. (365) takes the form

*Monitored LMG  
stochastic Heisenberg  
equations*

$$\begin{aligned}
d\langle m_x \rangle &= 2h\langle m_y \rangle dt - \frac{\gamma}{2}\langle m_x \rangle dt + \sqrt{\gamma}Sd\xi\langle m_z, m_x \rangle_c, \\
d\langle m_y \rangle &= \langle \{m_x, m_z\} - 2hm_x \rangle dt - \frac{\gamma}{2}\langle m_y \rangle dt \\
&\quad + \sqrt{\gamma}Sd\xi\langle m_z, m_y \rangle_c, \\
d\langle m_z \rangle &= -\langle \{m_x, m_y\} \rangle dt - \frac{\gamma}{2}\langle m_z \rangle dt \\
&\quad + \sqrt{\gamma}Sd\xi\langle m_z, m_z \rangle_c,
\end{aligned} \tag{373}$$

where  $\langle A, B \rangle_c \equiv \langle AB + BA \rangle - 2\langle A \rangle \langle B \rangle$ .

### 7.3 SEMICLASSICAL LIMIT

The unitary LMG model in the thermodynamical limit behaves semiclassically. In particular, collective spin operators in the large- $N$  limit can be seen as classical angular momentum variables. Formally, this is due to the fact that the  $SU(2)$  algebra implies

$$[m_\alpha, m_\beta] = \frac{i}{S}\epsilon_{\alpha\beta\gamma}m_\gamma, \tag{374}$$

so that  $1/S$  plays the role of an effective Planck constant. Therefore, for  $S \gg 1$  there will be states for which the uncertainty over all the components of  $m_\alpha$  is simultaneously small (i.e.  $O(1/S)$ ). On such states one has

$$\langle m_\alpha m_\beta \rangle = \langle m_\alpha \rangle \langle m_\beta \rangle + O(1/S), \tag{375}$$

which is key for the semiclassical description. This is the case for the dynamics in the totally symmetric sector, where  $\langle S_\alpha \rangle = O(N)$  and the uncertainty is of order  $O(1)$ . In this sector, we can approximate the state with a coherent spin state of spin  $S = N/2$ , i.e. the eigenstate of the projection of the spin operators along the direction of  $\langle \mathbf{S} \rangle = (\langle S_x \rangle, \langle S_y \rangle, \langle S_z \rangle)$ . A summary of the properties of coherent spin states is given in 7.6.1. Let us notice that while the mean field approximation works along individual trajectories, as we shall see in Sec. 7.3.2, it is not reliable for the Lindblad dynamics of the mean state. Taking ensemble averages,

$$\langle m_\alpha m_\beta \rangle_\rho = \overline{\langle m_\alpha m_\beta \rangle} \neq \overline{\langle m_\alpha \rangle} \overline{\langle m_\beta \rangle} = \langle m_\alpha \rangle_\rho \langle m_\beta \rangle_\rho.$$

Indeed, while the expectation value  $\langle \cdot \rangle = \text{tr}\{|\psi_\xi\rangle\langle\psi_\xi| \cdot\}$  is performed on a pure state with  $\langle S_\alpha \rangle = O(N)$ , which can be well approximated with a spin coherent state, for the ensemble  $\overline{\langle \cdot \rangle} = \langle \cdot \rangle_\rho = \text{tr}\{\rho \cdot\}$  the quantum expectation value is computed on the highly mixed state  $\rho$ , that has no well-defined mean-field limit. This is apparent for long times, as the Lindblad dynamics will bring  $\rho(t)$  towards the maximally mixed state in the totally symmetric subspace, so that  $\overline{\langle m_\alpha \rangle} = 0$ , while  $\overline{\langle m_\alpha m_\beta \rangle} = (S+1)/S \cdot \delta_{\alpha,\beta}$ . For more details we refer the reader to 7.6.3.

We will now briefly review the consequences of the mean field approximation on the unitary dynamics, before extending the description to the monitored case.

#### 7.3.1 Unitary Evolution

Starting from a maximally magnetized state, the unitary evolution of the magnetization is given by the Eqs. (373) with  $\gamma = 0$ , that become a coupled system of ODEs for  $m_\alpha \equiv \langle m_\alpha \rangle$

$$\dot{\mathbf{m}} = -2(m_x \mathbf{x} + m_z \mathbf{z}) \times \mathbf{m} \tag{376}$$

thanks to the decomposition of Eq. (375). The approximation is consistent if in the large  $S$  limit the state remains coherent, which is true because  $|\mathbf{m}|^2$  is

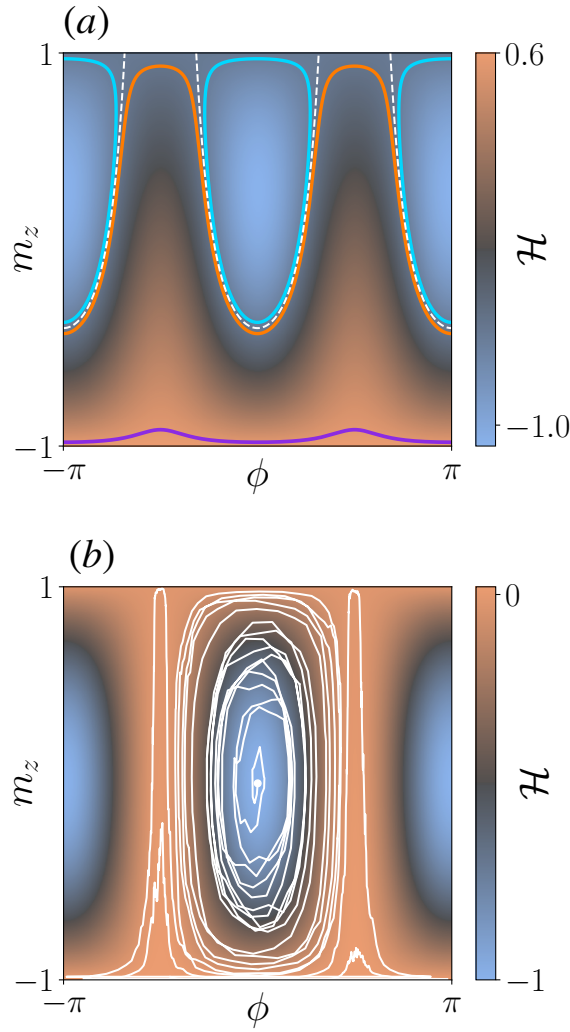


Figure 31: (a) Energy landscape of the unitary dynamics ( $\gamma = 0$ ) for  $h = 0.3$ . As  $h < 1$ , a separatrix  $\mathcal{H}(m_z, \phi) = -2h$  is present (dashed white line). Trajectories with energy  $< -2h$  correspond to librations (light blue curve), otherwise to rotations (orange and purple curves). While in the vicinity of  $m_z = -1$  the Hamiltonian flow remains close to the barrier during the whole dynamics (purple curves), it will eventually drive the system away from  $m_z = 1$ , as the light blue and orange curves are close to the separatrix. (b) Possible realization of a quantum trajectory in the phase space for small  $\gamma = 0.01$  (white solid line), for  $h = 0.02$  and initial conditions  $m_z(0) = \phi(0) = 0$  ( $m_y(0) = 0$ ,  $m_x(0) = 1$ ) superimposed to the Hamiltonian energy landscape of the system, density plot. Parameters  $\gamma = 0.01$ . As the noise is relatively small, on short timescales the evolution of the system remains close to the Hamiltonian flow. In spite of this, as  $\gamma < \gamma_c(h) = 0.28$ , the  $m_z = 1$  barrier is repulsive, and the trajectory converges asymptotically to  $m_z = -1$ .

conserved and the state is fully polarized. To simplify the problem we can introduce cylindrical coordinates

$$m_x = \sqrt{1 - m_z^2} \cos \phi, \quad m_y = \sqrt{1 - m_z^2} \sin \phi \quad (377)$$

with  $m_z \in [-1, 1]$  and  $\phi \in [-\pi, \pi]$ , which are convenient because  $\phi$  is canonically conjugate to the third component of the angular momentum  $m_z$ . This can be checked by noticing that the equations of motion Eqs. 376 become Hamilton equations  $\dot{m}_z = -\partial_\phi \mathcal{H}$ ,  $\dot{\phi} = \partial_{m_z} \mathcal{H}$ , where

$$\mathcal{H}(m_z, \phi) = -(1 - m_z^2) \cos^2 \phi - 2hm_z \quad (378)$$

is the classical Hamiltonian (which corresponds to the classical limit of Eq. (372) expressed in terms the new variables). Quenches of the LMG model undergo a dynamical phase transition. The dynamics will take place on the level curves  $\mathcal{H}(m_z, \phi) = E$  and, as those curves are closed, the dynamics will in general be periodic. However, similarly to the classical pendulum case, we can have two different kind of dynamics. While for  $h > 1$   $\phi$  increases by  $2\pi$  over a period regardless of the initial condition (rotation); if  $h < 1$  for  $E < -2h$ ,  $\phi$  is bounded to oscillate between two extremal values,  $|\phi| < \phi_{\max} \pmod{\pi}$  (libration). In latter case the time average of  $m_x$  on a trajectory is  $\neq 0$  (dynamical ferromagnet). The two classes of trajectories are divided by the separatrix  $\mathcal{H}(m_z, \phi) = -2h$ , i.e.

$$(1 + m_z) \cos^2 \phi = 2h \quad |\cos \phi| > \sqrt{h}, \quad (379)$$

in correspondence of which the period of oscillation diverges. As a consequence, while for  $h > 1$  the Hamiltonian flow remains close to the absorbing barriers  $m_z = \pm 1$  for an infinite amount of time, for  $h < 1$  the dynamics around  $m_z = 1$  takes place in proximity of a separatrix, so that it runs away from the absorbing barrier on a logarithmic timescale (see Fig. 31(a)).

### 7.3.2 Monitored Evolution

In analogous fashion, we can describe the monitored LMG model in the thermodynamic limit by applying the semiclassical approximation to Eqs. (373). Let us notice, however, that the effect of the limit  $S \rightarrow \infty$  here is more subtle due to the presence of the connected correlators  $\langle m_\alpha, m_\beta \rangle_c$  which vanish at the leading order if we factorize the expectation values. We thus need the exact form of the first order correction in  $O(1/S)$  of Eq. (375) on a coherent spin state, which is given by

$$\langle m_\alpha m_\beta \rangle_c = \frac{1}{S} (\delta_{\alpha,\beta} - \langle m_\alpha \rangle \langle m_\beta \rangle) + O(S^{-2}) \quad (380)$$

(see 7.6.1). By introducing once again the shorthand  $m_\alpha = \langle m_\alpha \rangle$ , for  $S \gg 1$  we get another closed system of SDEs, analogous to Eq. (373)

*Semiclassical  
approximation  
stochastic Heisenberg  
equations*

$$dm_x = \left( 2hm_y - \frac{\gamma}{2} m_x \right) dt - \sqrt{\gamma} d\xi m_z m_x \quad (381a)$$

$$dm_y = \left( -2hm_x + 2m_x m_z - \frac{\gamma}{2} m_y \right) dt + \sqrt{\gamma} d\xi m_z m_y \quad (381b)$$

$$dm_z = -2m_x m_y dt + \sqrt{\gamma} d\xi (1 - m_z^2). \quad (381c)$$

The equations imply

$$d\mathbf{m}^2 = \left[ \gamma dt (m_z^2 - 1) - 2m_z \sqrt{\gamma} d\xi \right] (\mathbf{m}^2 - 1), \quad (382)$$

so that if the initial state is chosen in the totally symmetric sector ( $|\mathbf{m}| = 1$ ) the dynamics takes place on the unit sphere and the semiclassical approximation is consistent. This is expected, as in the large  $S$  limit, on the totally symmetric subspace  $\mathbf{m}^2 \sim \langle \mathbf{m}^2 \rangle = (S+1)/S \sim 1$ .

As the dynamics takes place on the surface of the sphere, it is convenient to rewrite Eqs. (381) in terms of  $(m_z, \phi)$  defined in Eq. (377), thus finding

$$\begin{aligned} dm_z &= -2(1 - m_z^2) \sin \phi \cos \phi dt + \sqrt{\gamma} (1 - m_z^2) d\xi, \\ d\phi &= 2(-h + m_z \cos^2 \phi) dt. \end{aligned} \quad (383)$$

Notice that  $m_z = \pm 1$  act now as absorbing barriers, since there  $dm_z = 0$  on each realization. As expected, for  $\gamma = 0$  the evolution reduces to the Hamiltonian dynamics of the unitary case, namely  $dm_z = -\partial_\phi \mathcal{H} dt + \sqrt{\gamma} (1 - m_z^2) d\xi$ ,  $d\phi = \partial_{m_z} \mathcal{H} dt$ , with  $\mathcal{H}(m_z, \phi)$  of Eq. (378). A possible realization of the noisy dynamics in the phase space with small  $\gamma$  is shown in Fig. 31(b).



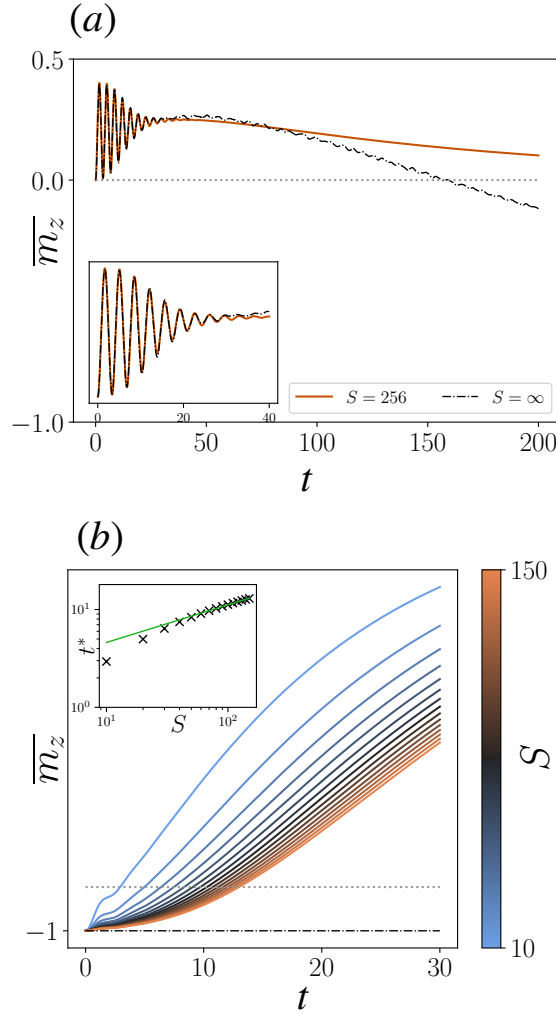


Figure 32: Comparison between  $\overline{m_z}(t)$  for  $N = \infty$ , obtained averaging over the realizations of Eq. (383) (black dash-dotted line), and its finite  $N$  counterpart, obtained by integrating the Lindblad dynamics. While for finite size  $\overline{m_z}(t)$  goes to zero at large times, this is no longer true for  $N = \infty$ . (a)  $S = \infty$  and  $S = N/2 = 256$  dynamics for  $\hbar = 0.2$ ,  $\gamma = 0.01$  and initial conditions  $m_z(0) = m_y(0) = 0$ ,  $m_x(0) = 1$ . (b) Dynamics starting from the  $S = \infty$  absorbing state  $m_x(0) = m_y(0) = 0$ ,  $m_z(0) = -1$ , compared with finite size dynamics  $S = N/2 \in [10, 150]$ , for  $\hbar = 0.3$ ,  $\gamma = 0.25$ . As shown in the inset, the timescale  $t^*$  on which the finite size dynamics differs significantly from the  $S = \infty$  one (formally  $m_z(t^*) = -0.9$ ) grows polynomially in  $S$ .

### 7.3.3 Non-commutativity of the limits

As already mentioned, for any finite  $N$  the Lindblad evolution of a maximally magnetized initial condition will converge towards the infinite-temperature state of the maximal representation  $S = N/2$ . This implies

$$\lim_{N \rightarrow \infty} \lim_{t \rightarrow \infty} \overline{m_\alpha} = 0. \quad (384)$$

On the other hand, the evolution of  $m_\alpha$  in the thermodynamic limit is given by Eq. (381) which, as already noticed, has two absorbing states in correspondence of  $m_z = \pm 1$  (and thus  $m_x = m_y = 0$ ). This means that at large times each realization of the system will end up in one of the two. Depend-

ing on the initial state one of the two boundaries will be reached more easily, implying that

$$\lim_{t \rightarrow \infty} \lim_{N \rightarrow \infty} \overline{m_z} \neq 0, \quad (385)$$

so that the large  $N$  limit will not in general commute with the large time limit.

For finite  $N$ , the Eqs. (383) are valid up to a timescale  $t_{\text{Ehr}}$ , known as Ehrenfest time, after which the approximation (375) is known to break down [254] (see also Fig. 32(a)). As  $t_{\text{Ehr}}$  can be seen as the timescale on which a phase space packet of initial width  $1/S$  acquires a  $O(1)$  spreading, its scaling of  $t_{\text{Ehr}}$  with  $N$  depends strongly on the nature underlying the semiclassical dynamics. While in the chaotic case  $t_{\text{Ehr}} \sim \ln N$ , Eqs. (383) describe an integrable dynamics perturbed by the presence of noise, so that  $t_{\text{Ehr}}$  is expected to grow polynomially  $N$ . This is confirmed by the numerical analysis reported in Fig. 32(b), where the interplay between the large- $N$  limit and the long-time limit is investigated.

#### 7.4 STATIONARY PROBABILITY DISTRIBUTION

In the next section, we will analyze more closely the asymptotic distribution of  $m_z$ . Because of the presence of two absorbing walls, the probability distribution of  $m_z$  will asymptotically have the form

$$P_\infty(m_z) = p_+ \delta(m_z - 1) + p_- \delta(m_z + 1), \quad (386)$$

with  $p_+ + p_- = 1$ . In this case, two different scenarios are possible: either both walls can be reached with finite probability, or one of the two is forbidden by the dynamics. A good order parameter capable of distinguishing the two phases apart is thus  $p_+$ , which can be expressed in terms of the ensemble averages of  $m_z$  as

$$p_+ = \lim_{t \rightarrow \infty} \lim_{N \rightarrow \infty} \frac{1}{2} (1 + \overline{m_z}(t)). \quad (387)$$

The resulting phase diagram as function of  $h$  and  $\gamma$  is plotted in Fig. 33: in the  $h < 1$  region, a finite phase with  $p_+ = 0$  is indeed present for small  $\gamma$ . The boundary of the two phases meets  $\gamma = 0$  at  $h = 0$  and  $h = 1$ . Notice that along the Linblad evolution one would identically have  $p_+ = 1/2$ , as  $p_+$  is linear in the state so that the possibility of using such a quantity as an order parameter is a direct consequence of the non-commutativity of the limits explored in Sec. 7.3.3.

The expected phase diagram is confirmed by an analysis of Eqs. (383). The effect of the noise becomes crucial in the proximity of  $m_z = \pm 1$ , as it can push the dynamics towards the absorbing barriers. Remarkably, as in this regime both the Hamiltonian and the noisy dynamics slow down, we can treat their effects independently. In particular, close to the  $m_z = -1$  barrier, the Hamiltonian dynamics is always a rotation and it remains close to the barrier at any time, so that we can ignore it. Let us denote the distance between  $m_z$  and the barrier as  $\Delta z \equiv 1 + m_z$ . For  $\Delta z \ll 1$  one has

$$d(\Delta z) = 2\sqrt{\gamma}\Delta z d\xi \quad (388)$$

or, by introducing  $\Delta z \equiv e^{-s}$

$$ds = 2\gamma dt + 2\sqrt{\gamma} d\xi. \quad (389)$$

It follows that  $s$  is a Gaussian variable centered around  $2\gamma t$  with a variance  $\sigma^2 = 4\gamma t$ : in this case the presence of the noise effectively pushes the dynamics towards the absorbing barriers at all measurement strengths.

Close to the barrier in  $m_z = 1$  an analogous line of reasoning can be followed for  $h > 1$ . For  $h < 1$ , however, the Hamiltonian dynamics cannot be neglected since in this case the flow runs close to the separatrix (379) (see Fig. 31), which pushes the system away from the barrier. We thus expand the equation for  $dm_z$  in Eqs. (383) for small  $\Delta z \equiv 1 - m_z \ll 1$ , assuming that  $\phi$  and  $m_z$  close to the separatrix that links them as in Eq. (379). At order  $O(\Delta z)$  therefore we find

$$d(\Delta z) = 4\sqrt{h(1-h)}\Delta z dt + 2\sqrt{\gamma}\Delta z d\xi, \quad (390)$$

or. in terms of  $\Delta z \equiv e^{-s}$ ,

$$ds = 2\left(\gamma - 2\sqrt{h(1-h)}\right) dt + 2\sqrt{\gamma} d\xi. \quad (391)$$

It follows that the  $m_z = 1$  barrier is attractive for the dynamics only when  $\gamma > \gamma_c(h) \equiv 2\sqrt{h(1-h)}$ . An alternative argument is given in 7.6.4. For  $\gamma = \gamma_c(h)$  the evolution of  $ds$  becomes a simple Wiener process. This means that a trajectory that starts close to the barrier  $m_z = 1$  has a probability 1/2 to remain close to it for large times. We thus expect  $p_+$  to be finite for  $\gamma = \gamma_c(h)$ , signaling a discontinuous phase transition.

In summary, for  $\gamma > \gamma_c$  both barriers are attractive, so that  $p_+$ ,  $p_-$  will both be finite, while the  $m_z = 1$  barrier becomes repulsive for  $\gamma < \gamma_c(h)$ , so that  $p_+ = 0$  (see also Fig. 31(b)). This explains the numerical phase diagram of Fig. 33 even at the quantitative level, as the transition curve  $\gamma_c(h)$  we foresee is in very good agreement with the numerical results. Notice also that  $\gamma_c(h)$  does not depend on the specific initial condition chosen for our system, while the specific values of  $p_+$  within the  $p_+ \neq 0$  phase will in general depend on it.

In particular, as  $m_z(0) \rightarrow 1$ , one will have  $p_+ = 1/2$ , at  $\gamma = \gamma_c(h)$ ,  $p_+ = 1$  at  $\gamma > \gamma_c(h)$ . In the regime  $\gamma \gg h$  instead, the Hamiltonian dynamics can be neglected on the whole phase space, leading to the single equation for  $m_z$

$$dm_z = \sqrt{\gamma}(1 - m_z^2)d\xi, \quad (392)$$

which preserves the ensemble average of  $m_z$ . We thus conclude that

$$\lim_{N \rightarrow \infty} \lim_{t \rightarrow \infty} \overline{m_z} = m_z(0). \quad (393)$$

As shown in 7.6.5, in this limit also the full counting statistics at any time  $t$  can be computed exactly.

## 7.5 CONCLUSION & OUTLOOK

In this work, we explored the dynamics of the LMG model under continuous weak monitoring. We derived a set of noisy semi-classical SDEs (Eq. (381)) for the expectation values of the magnetization of the system, valid in the thermodynamic limit  $N \rightarrow \infty$ . Our findings highlight a critical distinction, as the large- $N$  limit does not commute with the long-time limit. While for any finite  $N$  the system asymptotically approaches a trivial steady state under noise averaging, in the thermodynamic limit the system exhibits a non-trivial asymptotic behavior, which is already visible at the level of ensemble averages of the expectation values of the magnetization. We discovered that for small enough magnetic fields, such quantities exhibit a MIPT driven by the measurement strength. Our theoretical analysis was able to provide a full quantitative characterization of this transition, which can be explained in terms of a bifurcation of the stationary distribution in the thermodynamic limit, as the system develops two different attractive absorbing states. Our predictions are corroborated by numerical results.

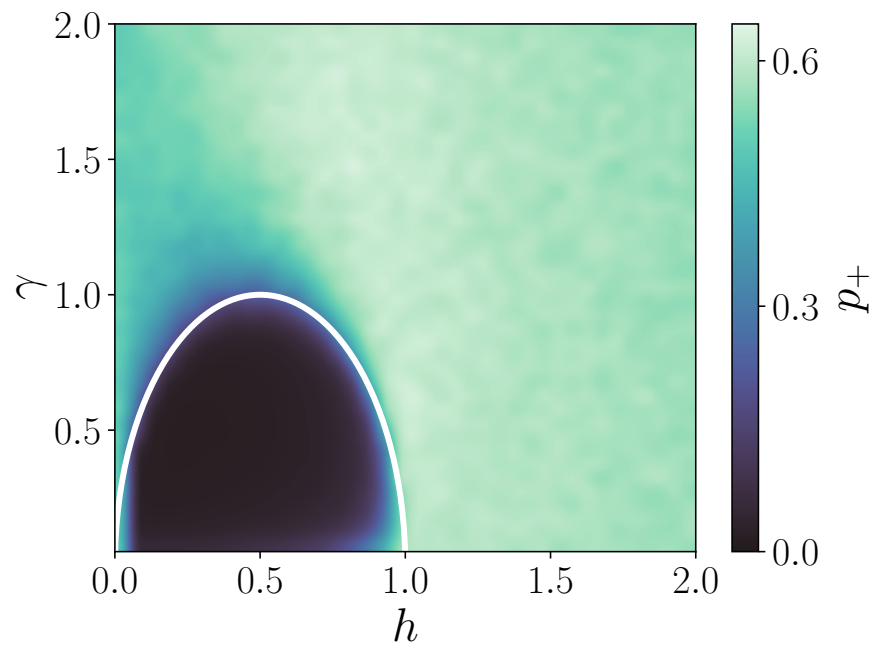


Figure 33: Color plot of  $p_+$  as defined in Eq. (387) with initial conditions  $m_z(0) = \phi(0) = 0$  ( $m_y(0) = 0$ ,  $m_x(0) = 1$ ). The phase  $p_+ = 0$  in which only one absorbing barrier is attractive is clearly visible (black region), and it matches the theoretical estimate  $\gamma < \gamma_c(h) \equiv 2\sqrt{h(1-h)}$  (white line). While the form of such region is independent on the initial conditions, the value of  $p_+$  for  $\gamma > \gamma_c(h)$  will in general depend on them. The possibility of observing a phase transition by looking at observable averages is a direct consequence of the non-commutativity of the limits examined in Sec. 7.3.3.

This study paves the way for further exploration of noise-induced phenomena in other quantum many-body systems and highlights the potential for using noise as a tool for probing and controlling quantum states. In particular, by demonstrating that continuous monitoring can induce non-trivial effect in fully-connected models already at the level of ensemble averages, our findings provide new insights into the interplay between monitoring and quantum dynamics in long-range interacting systems. Although for finite  $N$  this behavior is only visible on an intermediate timescale  $1 \ll t \ll t_{\text{Ehr}}$ , since  $t_{\text{Ehr}}$  grows algebraically in  $N$ , these timescale can become physically accessible. Moreover, as our order parameter  $p_+$  is linear in the quantum state, the possibility of an experimental realization, e.g. in the context of cavity setups, is not hindered by postselection issues.

Further investigations are needed in order to understand whether such behaviors are robust or in presence of short-range couplings, which could be obtained by means of a spin-waves analysis [144, 255]. Analogously, it is worthwhile to investigate whether our theoretical picture still holds if we replace our all-to-all model with slowly-decaying power-law decaying couplings (i.e. strong-long range interactions [262]), as these are known to give rise to a phenomenology which can be similar to the fully-connected case up to thermodynamically large timescales [254, 263–265].

Finally, while our analysis focuses on the monitoring of a collective observable, which preserves the global symmetry of the LMG model, the impact of local measurements on the dynamics of open, fully-connected, quantum systems might reveal an interesting interplay between local and mean-field effects.

## 7.6 APPENDICES

In this section, we provide several appendices related to the chapter.

### 7.6.1 Appendix A: Coherent spin states

The so-called spin, or  $SU(2)$ , coherent states are the generalization of the usual coherent states of the harmonic oscillator to angular momentum states. Like for the harmonic oscillator, they are a complete but not orthogonal set of states and they minimize Heisenberg's uncertainty relations [266–268]. Let us consider a single spin  $s$  (in our case,  $s = N/2$ ). For every spatial direction  $\mathbf{n} = (\sin \theta \cos \phi, \sin \theta \sin \phi, \cos \theta)$  there is an associated coherent spin state defined as

$$|\Omega_{\theta, \phi}\rangle := e^{-i\theta(\mathbf{n} \times \mathbf{z}) \cdot \mathbf{S}} |s\rangle, \quad (394)$$

which is also the maximum eigenstate of  $\mathbf{S} \cdot \mathbf{n}$ . Their expectation values of  $S_\alpha$  have a clear geometric interpretation, as they are equal to the projections

$$\langle S_\alpha \rangle \equiv \langle \Omega_{\theta, \phi} | S_\alpha | \Omega_{\theta, \phi} \rangle = n_\alpha S. \quad (395)$$

Such result can be found by expanding in terms of the eigenbasis of  $S_z$   $|m\rangle$  ( $m = -s, \dots, s$ ) as

$$|\Omega_{\theta, \phi}\rangle = \sum_{m=-s}^s \sqrt{\binom{2s}{m+s}} \left( e^{i\phi} \sin \frac{\theta}{2} \right)^{s-m} \left( \cos \frac{\theta}{2} \right)^{s+m} |m\rangle.$$

An important property they satisfy is  $\langle m_\alpha m_\beta \rangle = \langle m_\alpha \rangle \langle m_\beta \rangle + O(1/S)$ . Below we derive it with the explicit higher-order correction that is necessary for describing quantum trajectories in the semiclassical limit.

## 7.6.2 Appendix B: Derivation of Eq. (380)

We now need to compute  $\langle S_z^q \rangle = \langle \Omega_{\theta\phi} | S_z^q | \Omega_{\theta\phi} \rangle$ . Expanding again over  $|m\rangle$  one finds

$$\begin{aligned} \langle S_x^q \rangle &= \sum_{m=-s}^s m^q \binom{2s}{m+s} \times \\ &\times \left( \frac{1-\cos\theta}{2} \right)^{s-m} \left( \frac{1+\cos\theta}{2} \right)^{s+m} \equiv \langle m^q \rangle_b, \end{aligned} \quad (396)$$

where  $\langle \cdot \rangle_b$  represents the average over a binomial distribution, centered in zero with  $p, q = (1 \pm \cos\theta)/2$ . Thus we have

$$\langle S_z \rangle = \langle m \rangle_b = s(p - q) = s \cos\theta, \quad (397)$$

$$\langle S_z^2 \rangle = \langle m^2 \rangle_b = \langle m \rangle_b^2 + 2spq = \langle S_z \rangle^2 + \frac{s}{2} \sin^2\theta,$$

and analogously  $\langle S_x \rangle = s \sin\theta \cos\phi$ ,  $\langle S_y \rangle = s \sin\theta \sin\phi$ .

Expectation values like  $\langle S_x S_z + S_z S_x \rangle$  can be calculated analogously if we employ

$$\langle m | S_x | n \rangle = \frac{1}{2} \sqrt{s(s+1) - mn} (\delta_{m,n+1} + \delta_{m,n-1}), \quad (398)$$

by expanding in the  $S_z$  basis we get

$$\begin{aligned} \langle S_x S_z + S_z S_x \rangle &= \sum_{m,m'} \sqrt{\binom{2s}{s+m} \binom{2s}{s+m'}} e^{i(m'-m)\phi} \left( \sin \frac{\theta}{2} \right)^{2s-m-m'} \left( \cos \frac{\theta}{2} \right)^{2s+m+m'} \times \\ &\times \frac{1}{2} (m+m') \sqrt{s(s+1) - mm'} (\delta_{m',m+1} + \delta_{m',m-1}) \\ &= \sum_{m=-s}^s \sqrt{\binom{2s}{s+m} \binom{2s}{s+m}} (2m+1) \sqrt{s(s+1) - m(m+1)} \frac{e^{i\phi} + e^{-i\phi}}{2} \times \\ &\times \left( \sin \frac{\theta}{2} \right)^{2(s-m)-1} \left( \cos \frac{\theta}{2} \right)^{2(s+m)+1} \\ &= \cos\phi \cot \frac{\theta}{2} \sum_{m=-s}^s \binom{2s}{s+m} (s-m)(2m+1) \left( \frac{1-\cos\theta}{2} \right)^{s-m} \left( \frac{1+\cos\theta}{2} \right)^{s+m} \\ &= \cos\phi \cot \frac{\theta}{2} (s + (2s-1)\langle m \rangle_b - 2\langle m^2 \rangle_b) \\ &= s(2s-1) \cos\theta \sin\theta \cos\phi + O(1), \end{aligned} \quad (399)$$

where we have used

$$\begin{aligned} \sqrt{s(s+1) - m(m+1)} &= \sqrt{(s-m)(s+m+1)}, \\ \binom{2s}{s+m+1} &= \binom{2s}{s+m} \frac{s-m}{s+m+1}. \end{aligned} \quad (400)$$

In terms of  $\langle S_\alpha \rangle$  we thus get

$$\begin{aligned} \langle S_x S_z + S_z S_x \rangle &= (2 - s^{-1}) \langle S_x \rangle \langle S_z \rangle + O(s^{-2}), \\ \langle S_z^2 \rangle &= \langle S_z \rangle^2 + \frac{s}{2} \left( 1 - \frac{\langle S_z \rangle^2}{s^2} \right), \end{aligned} \quad (401)$$

or equivalently

$$\begin{aligned} \langle m_x, m_z \rangle_c &= -s^{-1} \langle m_x \rangle \langle m_z \rangle + O(s^{-2}), \\ \langle m_z, m_z \rangle_c &= s^{-1} (1 - \langle m_z \rangle^2). \end{aligned} \quad (402)$$

The result for the other pairs of components can be easily obtained by cyclic permutation of the indices, so that Eq. (380) follows.

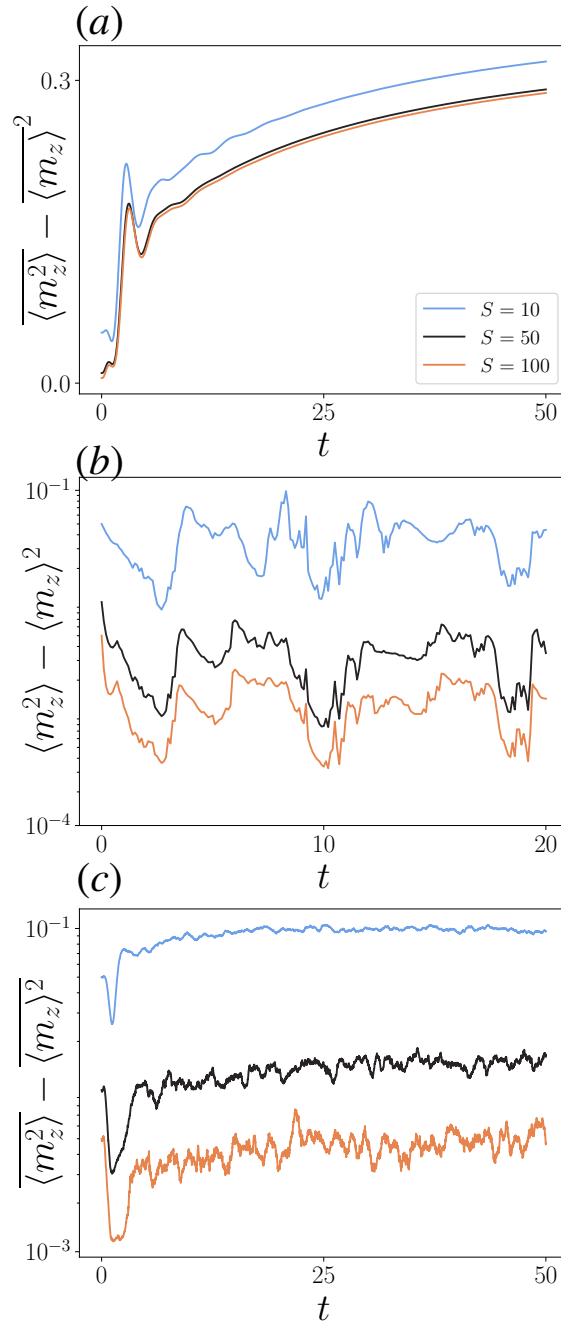


Figure 34: (a) Evolution of  $\overline{\langle m_z^2 \rangle} - \langle m_z \rangle^2$  evaluated over the mean state; both  $\overline{\langle m_z^2 \rangle}$  and  $\langle m_z \rangle$  are linear in the average state. (b) Validation of the semiclassical approximation along individual quantum trajectories. We show that  $\overline{\langle m_z^2 \rangle} - \langle m_z \rangle^2$  for increasing  $S$  tends to zero uniformly in time, as in Eq. (375). The figure refers to the same trajectory, i.e. same realization of the stochastic process  $d\xi_t$ , for different  $S$ . The initial condition is  $m_y(0) = m_z(0) = 0$ ,  $m_x(0) = 1$ , for  $\hbar = 0.5$ ,  $\gamma = 0.1$ . (c) As in panel (b) averaged over the set of quantum trajectories.

### 7.6.3 Appendix C: Semiclassic limit and ensemble averages

Here, we present numerical evidence to support the semiclassical approximation as described in Eq. (375). Specifically, in Fig. 34 we show that

$$\langle m_z^2 \rangle = \langle m_z \rangle^2 + O(1/S) \quad (403)$$

along individual quantum trajectories. This approximation is not valid if the mean is computed on average state. Averaging over quantum trajectories Eq. (403) provides

$$\langle m_z^2 \rangle_\rho = \overline{\langle m_z^2 \rangle} = \overline{\langle m_z \rangle^2} + O(1/S), \quad (404)$$

whereas the decoupling applied to  $\rho$  would give

$$\langle m_z^2 \rangle_\rho \stackrel{?}{=} \langle m_z \rangle_\rho^2 + O(1/S) = \overline{\langle m_z \rangle^2} + O(1/S). \quad (405)$$

As illustrated in Fig. 34,  $\langle m_z^2 \rangle_\rho - \langle m_z \rangle_\rho^2$  does not converge to zero while it does for individual trajectories and their averages. This means that classical correlations among quantum trajectories cannot be neglected as  $\overline{m_z^2} \neq \overline{m_z}^2$ .

### 7.6.4 Appendix D: Hamiltonian dynamics close to the separatrix

We will now give an alternative explanation to our results for the LMG model. First, let us notice that the separatrix corresponds to  $\mathcal{H}(m_z, \phi) = -2\hbar$ . If we thus consider energies  $E = -2\hbar + \epsilon$ , with  $\epsilon$  small, we get

$$m_z(\phi) = \frac{1}{\cos^2 \phi} \left( \hbar - \sqrt{(\hbar - \cos^2 \phi)^2 + \epsilon \cos^2 \phi} \right) \quad (406)$$

from which we see that the closest value to the barrier  $m_z = 1$  is in correspondence of  $\phi = \pi/2$ , namely

$$m_z(\pi/2) = 1 - \frac{\epsilon}{2\hbar}. \quad (407)$$

Let us assume that at  $t = 0$  the system is in  $m_z(\pi/2)$  so that  $\Delta z(t=0) \propto \epsilon$ . For small  $\Delta z$  the typical timescale  $T(\Delta z)$  spent by a trajectory close to the  $m_z = 1$  absorbing wall, can be estimated as the half-period period of the trajectory with energy  $E = -2\hbar + \epsilon$ , i.e.

$$\begin{aligned} T(\Delta z) &= \frac{1}{2} \int_0^\pi \frac{d\phi}{\dot{\phi}} = \frac{1}{4} \int_0^\pi \frac{d\phi}{m_z(\phi) \cos^2 \phi - \hbar} \\ &= \frac{1}{4} \int_0^\pi \frac{d\phi}{\sqrt{(\hbar - \cos^2 \phi)^2 + \epsilon \cos^2 \phi}} \end{aligned}$$

which, through the substitution  $u = \cos^2 \phi$  can be recast as

$$T(\Delta z) = \frac{1}{8} \int_0^1 \frac{du}{\sqrt{u(1-u)}} \frac{1}{\sqrt{(u-\hbar)^2 + \epsilon u}}. \quad (408)$$

For small  $\epsilon$ , only the region close to  $u = \hbar$  is going to contribute. By setting  $u = \hbar + \sqrt{\epsilon} \tilde{u}$  we have

$$\begin{aligned} T(\Delta z) &\approx \frac{1}{8\sqrt{\hbar(1-\hbar)}} \int_{-1/\sqrt{\epsilon}}^{1/\sqrt{\epsilon}} \frac{d\tilde{u}}{\sqrt{\tilde{u}^2 + \hbar}} \\ &\approx \frac{1}{4\sqrt{\hbar(1-\hbar)}} (-\ln \epsilon) \approx \frac{1}{4\sqrt{\hbar(1-\hbar)}} (-\ln \Delta z). \end{aligned} \quad (409)$$



By introducing once again  $\Delta z = e^{-s}$ , one has:

$$\Gamma(e^{-s}) \sim \frac{s}{4\sqrt{h(1-h)}} \quad (410)$$

As the Hamiltonian dynamics in  $m_z$  critically slows down close to  $m_z = 1$ , for  $t < \Gamma(e^{-s})$ . This happens for the trajectories such that

$$s < 4\sqrt{h(1-h)}t. \quad (411)$$

As seen in the main text, however, the noisy dynamics close to the wall is given by

$$ds = 2\gamma dt + 2\sqrt{\gamma}d\xi \quad (412)$$

i.e. a Gaussian distributed around  $2\gamma t$  with a typical width  $\sim \sqrt{t}$ . The probability of having such a trajectory that fulfills the conditions (411) for large times is thus null if  $2\gamma > 4\sqrt{h(1-h)} = 2\gamma_c(h)$ , so that in this range of values the barrier is repulsive.

### 7.6.5 Appendix E: Large $\gamma$ limit

We will now address the limit of large  $\gamma$ . We start from Eq. (392)

$$dm_z = \sqrt{\gamma}(1 - m_z^2)d\xi \quad (413)$$

It is convenient to set  $m_z = \tanh(s)$ ,  $\tau = \gamma t$ , so that

$$ds = \tanh(s)d\tau + d\xi \quad (414)$$

(with  $d\xi^2 = d\tau$ ). This can be rewritten as Fokker-Plank equation for the probability distribution  $P(s, t)$  of the form

$$\partial_\tau P(s, \tau) = \partial_s \left( V'(s) P(s, \tau) + \frac{1}{2} \partial_s P(s, \tau) \right) \quad (415)$$

with  $V = -\ln \cosh(s)$ ,  $P(s, 0) = \delta(s - s_0)$  and  $s_0 = \operatorname{arctanh} z(0)$ . By means of the substitution:

$$\begin{aligned} P(s, \tau) &= e^{-\tau/2} e^{-(V(s)-V(s_0))} \psi(s, \tau) \\ &= e^{-\tau/2} \frac{\cosh(s)}{\cosh(s_0)} \psi(s, \tau) \end{aligned} \quad (416)$$

with  $\psi(s, 0) = \delta(s - s_0)$ , one has

$$\partial_\tau \psi(s, \tau) = \frac{1}{2} \partial_s^2 \psi(s, \tau) \quad (417)$$

from which finally:

$$\psi(s, \tau) = \frac{1}{\sqrt{2\pi\tau}} e^{-(s-s_0)^2/2\tau}. \quad (418)$$

Coming back to  $P(s, \tau)$  we have

$$P(s, \tau) = \frac{1}{2 \cosh s_0} \frac{1}{\sqrt{2\pi\tau}} \left( e^{-s_0} e^{-(s-s_0+\tau)^2/2\tau} + \right. \quad (419)$$

$$\left. + e^{s_0} e^{-(s-s_0-\tau)^2/2\tau} \right), \quad (420)$$

which is the superposition of two Gaussian distributions traveling to the left and the right respectively, with weights that depends on the initial condition.

From this, one can recover  $p_{\pm}$  and the ensemble average of  $m_z$ . For example

$$p_+ = \lim_{\tau \rightarrow \infty} \int_0^{\infty} ds P(s, \tau) = \frac{e^{s_0}}{e^{s_0} + e^{-s_0}} = \frac{1 + z(0)}{2} \quad (421)$$

and analogously for  $p_-$ , so that we recover

$$\lim_{N \rightarrow \infty} \lim_{t \rightarrow \infty} \overline{m_{\alpha}} = p_+ - p_- = z(0) \quad (422)$$





## BIBLIOGRAPHY

---

- [1] Alessandro Santini, Giuseppe E. Santoro, and Mario Collura. «Clean two-dimensional Floquet time crystal.» In: *Phys. Rev. B* 106 (13 Oct. 2022), p. 134301. DOI: [10.1103/PhysRevB.106.134301](https://doi.org/10.1103/PhysRevB.106.134301).
- [2] Antonio Francesco Mello, Alessandro Santini, and Mario Collura. «Hybrid Stabilizer Matrix Product Operator.» In: *Phys. Rev. Lett.* 133 (15 2024), p. 150604. DOI: [10.1103/PhysRevLett.133.150604](https://doi.org/10.1103/PhysRevLett.133.150604).
- [3] Antonio Francesco Mello, Alessandro Santini, Guglielmo Lami, Jacopo De Nardis, and Mario Collura. «Clifford Dressed Time-Dependent Variational Principle.» In: *arXiv* (2024). DOI: <https://arxiv.org/abs/2407.01692>.
- [4] Emanuele Tirrito, Alessandro Santini, Rosario Fazio, and Mario Collura. «Full counting statistics as probe of measurement-induced transitions in the quantum Ising chain.» In: *SciPost Phys.* 15 (2023), p. 096. DOI: [10.21468/SciPostPhys.15.3.096](https://doi.org/10.21468/SciPostPhys.15.3.096).
- [5] Guglielmo Lami, Alessandro Santini, and Mario Collura. «Continuously monitored quantum systems beyond Lindblad dynamics.» In: *New Journal of Physics* 26.2 (Feb. 2024), p. 023041. DOI: [10.1088/1367-2630/ad1f0a](https://doi.org/10.1088/1367-2630/ad1f0a).
- [6] Alessandro Santini, Luca Lumia, Mario Collura, and Guido Giachetti. «Semiclassical Quantum Trajectories in the Monitored Lipkin-Meshkov-Glick Model.» In: *arXiv* (2024). DOI: <https://arxiv.org/abs/2407.20314>.
- [7] Nishan Ranabhat, Alessandro Santini, Emmanuele Tirrito, and Mario Collura. «Dynamical deconfinement transition driven by density of excitations.» In: *arXiv preprint arXiv:2310.02320* (2023). DOI: <https://doi.org/10.48550/arXiv.2310.02320>.
- [8] Alessandro Santini, Andrea Solfanelli, Stefano Gherardini, and Mario Collura. «Work statistics, quantum signatures, and enhanced work extraction in quadratic fermionic models.» In: *Phys. Rev. B* 108 (10 Sept. 2023), p. 104308. DOI: [10.1103/PhysRevB.108.104308](https://doi.org/10.1103/PhysRevB.108.104308).
- [9] Luca Capizzi, Guido Giachetti, Alessandro Santini, and Mario Collura. «Spreading of a local excitation in a quantum hierarchical model.» In: *Phys. Rev. B* 106.13 (13 Oct. 2022), p. 134210. DOI: [10.1103/PhysRevB.106.134210](https://doi.org/10.1103/PhysRevB.106.134210).
- [10] Alessandro Santini and Vittorio Vitale. «Experimental violations of Leggett-Garg inequalities on a quantum computer.» In: *Phys. Rev. A* 105 (3 Mar. 2022), p. 032610. DOI: [10.1103/PhysRevA.105.032610](https://doi.org/10.1103/PhysRevA.105.032610).
- [11] Alessandro Santini, Andrea Solfanelli, Stefano Gherardini, and Guido Giachetti. «Observation of partial and infinite-temperature thermalization induced by repeated measurements on a quantum hardware.» In: *Journal of Physics Communications* 7.6 (2023), p. 065007. DOI: [10.1088/2399-6528/acdd4f](https://doi.org/10.1088/2399-6528/acdd4f).
- [12] Andrea Solfanelli, Alessandro Santini, and Michele Campisi. «Quantum thermodynamic methods to purify a qubit on a quantum processing unit.» In: *AVS Quantum Science* 4.2 (June 2022), p. 026802. ISSN: 2639-0213. DOI: [10.1116/5.0091121](https://doi.org/10.1116/5.0091121).
- [13] Alessandro Santini, Guido Giachetti, and Lapo Casetti. «Violent relaxation in the Hamiltonian mean field model: II. Non-equilibrium phase diagrams.» In: *Journal of Statistical Mechanics: Theory and Experiment* 2022.1 (2022), p. 013210. DOI: [10.1088/1742-5468/ac4516](https://doi.org/10.1088/1742-5468/ac4516).
- [14] Andrea Solfanelli, Alessandro Santini, and Michele Campisi. «Experimental Verification of Fluctuation Relations with a Quantum Computer.» In: *PRX Quantum* 2 (3 Sept. 2021), p. 030353. DOI: [10.1103/PRXQuantum.2.030353](https://doi.org/10.1103/PRXQuantum.2.030353).
- [15] Ulrich Schollwöck. «The density-matrix renormalization group in the age of matrix product states.» In: *Annals of Physics* 326.1 (Jan. 2011). January 2011 Special Issue, pp. 96–192. ISSN: 0003-4916. DOI: <https://doi.org/10.1016/j.aop.2010.09.012>.
- [16] Sebastian Paeckel, Thomas Köhler, Andreas Swoboda, Salvatore R. Manmana, Ulrich Schollwöck, and Claudius Hubig. «Time-evolution methods for matrix-product states.» In: *Annals of Physics* 411 (2019), p. 167998. ISSN: 0003-4916. DOI: <https://doi.org/10.1016/j.aop.2019.167998>.
- [17] Daniel M. Greenberger, Michael A. Horne, and Anton Zeilinger. *Going Beyond Bell's Theorem*. 2007.
- [18] Guifré Vidal. «Efficient Classical Simulation of Slightly Entangled Quantum Computations.» In: *Phys. Rev. Lett.* 91 (14 Oct. 2003), p. 147902. DOI: [10.1103/PhysRevLett.91.147902](https://doi.org/10.1103/PhysRevLett.91.147902).

- [19] Haegeman, Jutho and Cirac, J. Ignacio and Osborne, Tobias J. and Pižorn, Iztok and Verschelde, Henri and Verstraete, Frank. «Time-Dependent Variational Principle for Quantum Lattices.» In: *Phys. Rev. Lett.* 107 (7 Aug. 2011), p. 070601. DOI: [10.1103/PhysRevLett.107.070601](https://doi.org/10.1103/PhysRevLett.107.070601).
- [20] Jutho Haegeman, Christian Lubich, Ivan Oseledets, Bart Vandereycken, and Frank Verstraete. «Unifying time evolution and optimization with matrix product states.» In: *Phys. Rev. B* 94 (16 Oct. 2016), p. 165116. DOI: [10.1103/PhysRevB.94.165116](https://doi.org/10.1103/PhysRevB.94.165116).
- [21] Frank Wilczek. «Quantum Time Crystals.» In: *Phys. Rev. Lett.* 109 (16 Oct. 2012), p. 160401. DOI: [10.1103/PhysRevLett.109.160401](https://doi.org/10.1103/PhysRevLett.109.160401).
- [22] Patrick Bruno. «Impossibility of Spontaneously Rotating Time Crystals: A No-Go Theorem.» In: *Phys. Rev. Lett.* 111 (7 Aug. 2013), p. 070402. DOI: [10.1103/PhysRevLett.111.070402](https://doi.org/10.1103/PhysRevLett.111.070402).
- [23] Haruki Watanabe and Masaki Oshikawa. «Absence of Quantum Time Crystals.» In: *Phys. Rev. Lett.* 114 (25 June 2015), p. 251603. DOI: [10.1103/PhysRevLett.114.251603](https://doi.org/10.1103/PhysRevLett.114.251603).
- [24] Krzysztof Sacha. «Modeling spontaneous breaking of time-translation symmetry.» In: *Phys. Rev. A* 91 (3 Mar. 2015), p. 033617. DOI: [10.1103/PhysRevA.91.033617](https://doi.org/10.1103/PhysRevA.91.033617).
- [25] Dominic V. Else, Bela Bauer, and Chetan Nayak. «Floquet Time Crystals.» In: *Phys. Rev. Lett.* 117 (9 Aug. 2016), p. 090402. DOI: [10.1103/PhysRevLett.117.090402](https://doi.org/10.1103/PhysRevLett.117.090402).
- [26] Vedika Khemani, Achilleas Lazarides, Roderich Moessner, and S. L. Sondhi. «Phase Structure of Driven Quantum Systems.» In: *Phys. Rev. Lett.* 116 (25 June 2016), p. 250401. DOI: [10.1103/PhysRevLett.116.250401](https://doi.org/10.1103/PhysRevLett.116.250401).
- [27] C. W. von Keyserlingk, Vedika Khemani, and S. L. Sondhi. «Absolute stability and spatiotemporal long-range order in Floquet systems.» In: *Phys. Rev. B* 94 (8 Aug. 2016), p. 085112. DOI: [10.1103/PhysRevB.94.085112](https://doi.org/10.1103/PhysRevB.94.085112).
- [28] D.M. Basko, I.L. Aleiner, and B.L. Altshuler. «Metal-insulator transition in a weakly interacting many-electron system with localized single-particle states.» In: *Ann. Phys.* 321.5 (2006), pp. 1126–1205. ISSN: 0003-4916. DOI: <https://doi.org/10.1016/j.aop.2005.11.014>.
- [29] Vadim Oganesyan and David A. Huse. «Localization of interacting fermions at high temperature.» In: *Phys. Rev. B* 75 (15 Apr. 2007), p. 155111. DOI: [10.1103/PhysRevB.75.155111](https://doi.org/10.1103/PhysRevB.75.155111).
- [30] Soonwon Choi, Joonhee Choi, Renate Landig, Georg Kucsko, Hengyun Zhou, Junichi Isoya, Fedor Jelezko, Shinobu Onoda, Hitoshi Sumiya, Vedika Khemani, et al. «Observation of discrete time-crystalline order in a disordered dipolar many-body system.» In: *Nature* 543.7644 (2017), pp. 221–225. DOI: [10.1038/nature21426](https://doi.org/10.1038/nature21426).
- [31] Tian-Sheng Zeng and D. N. Sheng. «Prethermal time crystals in a one-dimensional periodically driven Floquet system.» In: *Phys. Rev. B* 96 (9 Sept. 2017), p. 094202. DOI: [10.1103/PhysRevB.96.094202](https://doi.org/10.1103/PhysRevB.96.094202).
- [32] Dmitry Abanin, Wojciech De Roeck, Wen Wei Ho, and François Huveneers. «A Rigorous Theory of Many-Body Prethermalization for Periodically Driven and Closed Quantum Systems.» In: *Commun. Math. Phys.* 354.3 (Sept. 2017), pp. 809–827. ISSN: 1432-0916. DOI: [10.1007/s00220-017-2930-x](https://doi.org/10.1007/s00220-017-2930-x).
- [33] Dominic V. Else, Bela Bauer, and Chetan Nayak. «Prethermal Phases of Matter Protected by Time-Translation Symmetry.» In: *Phys. Rev. X* 7 (1 Mar. 2017), p. 011026. DOI: [10.1103/PhysRevX.7.011026](https://doi.org/10.1103/PhysRevX.7.011026).
- [34] Antonis Kyprianidis, Francisco Machado, William Morong, Patrick Becker, Kate S Collins, Dominic V Else, Lei Feng, Paul W Hess, Chetan Nayak, Guido Pagano, et al. «Observation of a prethermal discrete time crystal.» In: *Science* 372.6547 (2021), pp. 1192–1196. DOI: [10.1126/science.abg8102](https://doi.org/10.1126/science.abg8102).
- [35] David J. Luitz, Roderich Moessner, S. L. Sondhi, and Vedika Khemani. «Prethermalization without Temperature.» In: *Phys. Rev. X* 10 (2 May 2020), p. 021046. DOI: [10.1103/PhysRevX.10.021046](https://doi.org/10.1103/PhysRevX.10.021046).
- [36] Jared Rovny, Robert L. Blum, and Sean E. Barrett. «Observation of Discrete-Time-Crystal Signatures in an Ordered Dipolar Many-Body System.» In: *Phys. Rev. Lett.* 120 (18 May 2018), p. 180603. DOI: [10.1103/PhysRevLett.120.180603](https://doi.org/10.1103/PhysRevLett.120.180603).
- [37] Francisco Machado, Dominic V. Else, Gregory D. Kahanamoku-Meyer, Chetan Nayak, and Norman Y. Yao. «Long-Range Prethermal Phases of Nonequilibrium Matter.» In: *Phys. Rev. X* 10 (1 Feb. 2020), p. 011043. DOI: [10.1103/PhysRevX.10.011043](https://doi.org/10.1103/PhysRevX.10.011043).
- [38] Kaoru Mizuta, Kazuaki Takasan, Masaya Nakagawa, and Norio Kawakami. «Spatial-Translation-Induced Discrete Time Crystals.» In: *Phys. Rev. Lett.* 121 (9 Aug. 2018), p. 093001. DOI: [10.1103/PhysRevLett.121.093001](https://doi.org/10.1103/PhysRevLett.121.093001).
- [39] Thomas Iadecola and Timothy H. Hsieh. «Floquet Supersymmetry.» In: *Phys. Rev. Lett.* 120 (21 May 2018), p. 210603. DOI: [10.1103/PhysRevLett.120.210603](https://doi.org/10.1103/PhysRevLett.120.210603).

- [40] Angelo Russomanno, Simone Notarnicola, Federica Maria Surace, Rosario Fazio, Marcello Dalmonte, and Markus Heyl. «Homogeneous Floquet time crystal protected by gauge invariance.» In: *Phys. Rev. Research* 2 (1 Jan. 2020), p. 012003. DOI: [10.1103/PhysRevResearch.2.012003](https://doi.org/10.1103/PhysRevResearch.2.012003).
- [41] Christopher J Turner, Alexios A Michailidis, Dmitry A Abanin, Maksym Serbyn, and Zlatko Papić. «Weak ergodicity breaking from quantum many-body scars.» In: *Nat. Phys.* 14.7 (2018), pp. 745–749. DOI: [10.1038/s41567-018-0137-5](https://doi.org/10.1038/s41567-018-0137-5).
- [42] Maksym Serbyn, Dmitry A Abanin, and Zlatko Papić. «Quantum many-body scars and weak breaking of ergodicity.» In: *Nat. Phys.* 17.6 (2021), pp. 675–685. DOI: [10.1038/s41567-021-01230-2](https://doi.org/10.1038/s41567-021-01230-2).
- [43] Dolev Bluvstein, Ahmed Omran, Harry Levine, Alexander Keesling, Giulia Semeghini, Sepehr Ebadi, Tout T Wang, Alexios A Michailidis, Nishad Maskara, Wen Wei Ho, et al. «Controlling quantum many-body dynamics in driven Rydberg atom arrays.» In: *Science* 371.6536 (2021), pp. 1355–1359. DOI: [10.1126/science.abg2530](https://doi.org/10.1126/science.abg2530).
- [44] Mario Collura, Andrea De Luca, Davide Rossini, and Alessio Lerose. «Discrete Time-Crystalline Response Stabilized by Domain-Wall Confinement.» In: *Phys. Rev. X* 12 (3 Sept. 2022), p. 031037. DOI: [10.1103/PhysRevX.12.031037](https://doi.org/10.1103/PhysRevX.12.031037).
- [45] Dmitry A. Abanin, Wojciech De Roeck, Wen Wei Ho, and Fran çois Huveneers. «Effective Hamiltonians, prethermalization, and slow energy absorption in periodically driven many-body systems.» In: *Phys. Rev. B* 95 (1 Jan. 2017), p. 014112. DOI: [10.1103/PhysRevB.95.014112](https://doi.org/10.1103/PhysRevB.95.014112).
- [46] Andrea Pizzi, Andreas Nunnenkamp, and Johannes Knolle. «Classical Prethermal Phases of Matter.» In: *Phys. Rev. Lett.* 127 (14 Sept. 2021), p. 140602. DOI: [10.1103/PhysRevLett.127.140602](https://doi.org/10.1103/PhysRevLett.127.140602).
- [47] Andrea Pizzi, Andreas Nunnenkamp, and Johannes Knolle. «Classical approaches to prethermal discrete time crystals in one, two, and three dimensions.» In: *Phys. Rev. B* 104 (9 Sept. 2021), p. 094308. DOI: [10.1103/PhysRevB.104.094308](https://doi.org/10.1103/PhysRevB.104.094308).
- [48] Pasquale Calabrese, Fabian H L Essler, and Maurizio Fagotti. «Quantum quench in the transverse field Ising chain: I. Time evolution of order parameter correlators.» In: *Journal of Statistical Mechanics: Theory and Experiment* 2012.07 (July 2012), P07016. DOI: [10.1088/1742-5468/2012/07/p07016](https://doi.org/10.1088/1742-5468/2012/07/p07016).
- [49] Awad H. Al-Mohy and Nicholas J. Higham. «Computing the Action of the Matrix Exponential, with an Application to Exponential Integrators.» In: *SIAM J. Sci. Comput* 33(2) (2011), 488–511. DOI: <https://doi.org/10.1137/100788860>.
- [50] Wing Yu, Jirawat Tangpanitanon, Alexander W. Glaetzle, Dieter Jaksch, and Dimitris G. Angelakis. «Discrete time crystal in globally driven interacting quantum systems without disorder.» In: *Phys. Rev. A* 99 (3 2019), p. 033618. DOI: [10.1103/PhysRevA.99.033618](https://doi.org/10.1103/PhysRevA.99.033618).
- [51] Andrea Pizzi, Daniel Malz, Giuseppe De Tomasi, Johannes Knolle, and Andreas Nunnenkamp. «Time crystallinity and finite-size effects in clean Floquet systems.» In: *Phys. Rev. B* 102 (21 Dec. 2020), p. 214207. DOI: [10.1103/PhysRevB.102.214207](https://doi.org/10.1103/PhysRevB.102.214207).
- [52] J. M. Deutsch. «Quantum statistical mechanics in a closed system.» In: *Phys. Rev. A* 43 (4 Feb. 1991), pp. 2046–2049. DOI: [10.1103/PhysRevA.43.2046](https://doi.org/10.1103/PhysRevA.43.2046).
- [53] Mark Srednicki. «Chaos and quantum thermalization.» In: *Phys. Rev. E* 50 (2 Aug. 1994), pp. 888–901. DOI: [10.1103/PhysRevE.50.888](https://doi.org/10.1103/PhysRevE.50.888).
- [54] Joshua M Deutsch. «Eigenstate thermalization hypothesis.» In: *Reports on Progress in Physics* 81.8 (July 2018), p. 082001. DOI: [10.1088/1361-6633/aac9f1](https://doi.org/10.1088/1361-6633/aac9f1).
- [55] Immanuel Bloch, Jean Dalibard, and Wilhelm Zwerger. «Many-body physics with ultracold gases.» In: *Rev. Mod. Phys.* 80 (3 July 2008), pp. 885–964. DOI: [10.1103/RevModPhys.80.885](https://doi.org/10.1103/RevModPhys.80.885).
- [56] Anatoli Polkovnikov, Krishnendu Sengupta, Alessandro Silva, and Mukund Vengalattore. «Colloquium: Nonequilibrium dynamics of closed interacting quantum systems.» In: *Rev. Mod. Phys.* 83 (3 Aug. 2011), pp. 863–883. DOI: [10.1103/RevModPhys.83.863](https://doi.org/10.1103/RevModPhys.83.863).
- [57] Zvi Friedman. «Ising model with a transverse field in two dimensions: Phase diagram and critical properties from a real-space renormalization group.» In: *Phys. Rev. B* 17 (3 Feb. 1978), pp. 1429–1432. DOI: [10.1103/PhysRevB.17.1429](https://doi.org/10.1103/PhysRevB.17.1429).
- [58] R. Peierls. «On Ising’s model of ferromagnetism.» In: *Mathematical Proceedings of the Cambridge Philosophical Society* 32.3 (1936), 477–481. DOI: [10.1017/S0305004100019174](https://doi.org/10.1017/S0305004100019174).
- [59] F. M. Gambetta, F. Carollo, A. Lazarides, I. Lesanovsky, and J. P. Garrahan. «Classical stochastic discrete time crystals.» In: *Phys. Rev. E* 100 (6 Dec. 2019), p. 060105. DOI: [10.1103/PhysRevE.100.060105](https://doi.org/10.1103/PhysRevE.100.060105).
- [60] Jiehang Zhang, PW Hess, A Kyprianidis, P Becker, A Lee, J Smith, G Pagano, I-D Potirniche, Andrew C Potter, A Vishwanath, et al. «Observation of a discrete time crystal.» In: *Nature* 543.7644 (2017), pp. 217–220. DOI: [10.1038/nature21413](https://doi.org/10.1038/nature21413).

- [61] Xiao Mi, Matteo Ippoliti, Chris Quintana, Ami Greene, Zijun Chen, Jonathan Gross, Frank Arute, Kunal Arya, Juan Atalaya, Ryan Babbush, et al. «Time-crystalline eigenstate order on a quantum processor.» In: *Nature* 601.7894 (2022), pp. 531–536. DOI: <https://doi.org/10.1038/s41586-021-04257-w>.
- [62] Youngseok Kim, Christopher J. Wood, Theodore J. Yoder, Seth T. Merkel, Jay M. Gambetta, Kristan Temme, and Abhinav Kandala. «Scalable error mitigation for noisy quantum circuits produces competitive expectation values.» In: *arXiv* (2021). DOI: [10.48550/ARXIV.2108.09197](https://doi.org/10.48550/ARXIV.2108.09197).
- [63] Andrea Solfanelli, Stefano Ruffo, Sauro Succi, and Nicolò Defenu. «Stabilization of discrete time-crystalline response on a superconducting quantum computer by increasing the interaction range.» In: *Phys. Rev. Res.* 6 (1 Mar. 2024), p. 013311. DOI: [10.1103/PhysRevResearch.6.013311](https://doi.org/10.1103/PhysRevResearch.6.013311).
- [64] Scott Aaronson and Daniel Gottesman. «Improved simulation of stabilizer circuits.» In: *Physical Review A* 70.5 (Nov. 2004). DOI: [10.1103/physreva.70.052328](https://doi.org/10.1103/physreva.70.052328).
- [65] Sergey Bravyi, Andrew W Cross, Jay M Gambetta, Dmitri Maslov, Patrick Rall, and Theodore J Yoder. «High-threshold and low-overhead fault-tolerant quantum memory.» In: *Nature* 627.8005 (2024), pp. 778–782. DOI: <https://doi.org/10.1038/s41586-024-07107-7>.
- [66] Bin Cheng, Xiu-Hao Deng, Xiu Gu, Yu He, Guangchong Hu, Peihao Huang, Jun Li, Ben-Chuan Lin, Dawei Lu, Yao Lu, et al. «Noisy intermediate-scale quantum computers.» In: *Frontiers of Physics* 18.2 (2023), p. 21308. DOI: <https://doi.org/10.1007/s11467-022-1249-z>.
- [67] Dolev Bluvstein, Simon J Evered, Alexandra A Geim, Sophie H Li, Hengyun Zhou, Tom Manovitz, Sepehr Ebadi, Madelyn Cain, Marcin Kalinowski, Dominik Hangleiter, et al. «Logical quantum processor based on reconfigurable atom arrays.» In: *Nature* 626.7997 (2024), pp. 58–65. DOI: <https://doi.org/10.1038/s41586-023-06927-3>.
- [68] Guifre Vidal. «Efficient Simulation of One-Dimensional Quantum Many-Body Systems.» In: *Phys. Rev. Lett.* 93 (4 July 2004), p. 040502. DOI: [10.1103/PhysRevLett.93.040502](https://doi.org/10.1103/PhysRevLett.93.040502).
- [69] Pasquale Calabrese and John Cardy. «Evolution of entanglement entropy in one-dimensional systems.» In: *Journal of Statistical Mechanics: Theory and Experiment* 2005.04 (Apr. 2005), P04010. DOI: [10.1088/1742-5468/2005/04/P04010](https://doi.org/10.1088/1742-5468/2005/04/P04010).
- [70] Luigi Amico, Rosario Fazio, Andreas Osterloh, and Vlatko Vedral. «Entanglement in many-body systems.» In: *Rev. Mod. Phys.* 80 (2 May 2008), pp. 517–576. DOI: [10.1103/RevModPhys.80.517](https://doi.org/10.1103/RevModPhys.80.517).
- [71] Andreas M Läuchli and Corinna Kollath. «Spreading of correlations and entanglement after a quench in the one-dimensional Bose–Hubbard model.» In: *Journal of Statistical Mechanics: Theory and Experiment* 2008.05 (May 2008), P05018. DOI: [10.1088/1742-5468/2008/05/P05018](https://doi.org/10.1088/1742-5468/2008/05/P05018).
- [72] M. C. Bañuls, M. B. Hastings, F. Verstraete, and J. I. Cirac. «Matrix Product States for Dynamical Simulation of Infinite Chains.» In: *Phys. Rev. Lett.* 102 (24 June 2009), p. 240603. DOI: [10.1103/PhysRevLett.102.240603](https://doi.org/10.1103/PhysRevLett.102.240603).
- [73] Alexander Müller-Hermes, J Ignacio Cirac, and Mari Carmen Banuls. «Tensor network techniques for the computation of dynamical observables in one-dimensional quantum spin systems.» In: *New Journal of Physics* 14.7 (2012), p. 075003. DOI: [10.1088/1367-2630/14/7/075003](https://doi.org/10.1088/1367-2630/14/7/075003).
- [74] Daniel Gottesman. «Stabilizer Codes and Quantum Error Correction.» In: (1997). DOI: [10.48550/ARXIV.QUANT-PH/9705052](https://doi.org/10.48550/ARXIV.QUANT-PH/9705052).
- [75] Daniel Gottesman. «Theory of fault-tolerant quantum computation.» In: *Phys. Rev. A* 57 (1 Jan. 1998), pp. 127–137. DOI: [10.1103/PhysRevA.57.127](https://doi.org/10.1103/PhysRevA.57.127).
- [76] Daniel Gottesman. «The Heisenberg Representation of Quantum Computers.» In: *arXiv preprint arXiv:9807006* (1998). DOI: [10.48550/ARXIV.QUANT-PH/9807006](https://doi.org/10.48550/ARXIV.QUANT-PH/9807006).
- [77] Jeroen Dehaene and Bart De Moor. «Clifford group, stabilizer states, and linear and quadratic operations over GF(2).» In: *Physical Review A* 68.4 (Oct. 2003). ISSN: 1094-1622. DOI: [10.1103/physreva.68.042318](https://doi.org/10.1103/physreva.68.042318).
- [78] Mark Howard and Earl Campbell. «Application of a Resource Theory for Magic States to Fault-Tolerant Quantum Computing.» In: *Physical Review Letters* 118.9 (Mar. 2017). DOI: [10.1103/physrevlett.118.090501](https://doi.org/10.1103/physrevlett.118.090501).
- [79] Zi-Wen Liu and Andreas Winter. «Many-Body Quantum Magic.» In: *PRX Quantum* 3 (2 May 2022), p. 020333. DOI: [10.1103/PRXQuantum.3.020333](https://doi.org/10.1103/PRXQuantum.3.020333).
- [80] Lorenzo Leone, Salvatore F. E. Oliviero, and Alioscia Hama. «Stabilizer Renyi Entropy.» In: *Phys. Rev. Lett.* 128 (5 Feb. 2022), p. 050402. DOI: [10.1103/PhysRevLett.128.050402](https://doi.org/10.1103/PhysRevLett.128.050402).
- [81] Pradeep Niroula, Christopher David White, Qingfeng Wang, Sonika Johri, Daiwei Zhu, Christopher Monroe, Crystal Noel, and Michael J. Gullans. «Phase transition in magic with random quantum circuits.» In: (2024).



- [82] Guglielmo Lami and Mario Collura. «Quantum Magic via Perfect Pauli Sampling of Matrix Product States.» In: (2023).
- [83] Antonio Francesco Mello, Guglielmo Lami, and Mario Collura. «Retrieving non-stabilizerness with Neural Networks.» In: (2024).
- [84] Poetri Sonya Tarabunga, Emanuele Tirrito, Titas Chanda, and Marcello Dalmonte. «Many-Body Magic Via Pauli-Markov Chains—From Criticality to Gauge Theories.» In: *PRX Quantum* 4 (4 Oct. 2023), p. 040317. DOI: [10.1103/PRXQuantum.4.040317](https://doi.org/10.1103/PRXQuantum.4.040317).
- [85] Guglielmo Lami and Mario Collura. «Nonstabilizerness via Perfect Pauli Sampling of Matrix Product States.» In: *Phys. Rev. Lett.* 131 (18 Oct. 2023), p. 180401. DOI: [10.1103/PhysRevLett.131.180401](https://doi.org/10.1103/PhysRevLett.131.180401).
- [86] Markus Heinrich and David Gross. «Robustness of Magic and Symmetries of the Stabiliser Polytope.» In: *Quantum* 3 (Apr. 2019), p. 132. DOI: [10.22331/q-2019-04-08-132](https://doi.org/10.22331/q-2019-04-08-132).
- [87] Xhek Turkeshi, Marco Schirò, and Piotr Sierant. «Measuring nonstabilizerness via multifractal flatness.» In: *Phys. Rev. A* 108 (4 Oct. 2023), p. 042408. DOI: [10.1103/PhysRevA.108.042408](https://doi.org/10.1103/PhysRevA.108.042408).
- [88] Gerald E. Fux, Emanuele Tirrito, Marcello Dalmonte, and Rosario Fazio. «Entanglement-magic separation in hybrid quantum circuits.» In: (2023).
- [89] Poetri Sonya Tarabunga, Emanuele Tirrito, Mari Carmen Bañuls, and Marcello Dalmonte. «Nonstabilizerness via matrix product states in the Pauli basis.» In: (2024).
- [90] Emanuele Tirrito, Poetri Sonya Tarabunga, Guglielmo Lami, Titas Chanda, Lorenzo Leone, Salvatore F. E. Oliviero, Marcello Dalmonte, Mario Collura, and Alioscia Hamma. «Quantifying nonstabilizerness through entanglement spectrum flatness.» In: *Phys. Rev. A* 109 (4 Apr. 2024), p. L040401. DOI: [10.1103/PhysRevA.109.L040401](https://doi.org/10.1103/PhysRevA.109.L040401).
- [91] Tobias Haug and Lorenzo Piroli. «Stabilizer entropies and nonstabilizerness monotones.» In: *Quantum* 7 (Aug. 2023), p. 1092. ISSN: 2521-327X. DOI: [10.22331/q-2023-08-28-1092](https://doi.org/10.22331/q-2023-08-28-1092).
- [92] M. Frau, P. S. Tarabunga, M. Collura, M. Dalmonte, and E. Tirrito. «Non-stabilizerness versus entanglement in matrix product states.» In: (2024).
- [93] P.Oscar Boykin, Tal Mor, Matthew Pulver, Vwani Roychowdhury, and Farrokh Vatan. «A new universal and fault-tolerant quantum basis.» In: *Information Processing Letters* 75:3 (2000), pp. 101–107. ISSN: 0020-0190. DOI: [https://doi.org/10.1016/S0020-0190\(00\)00084-3](https://doi.org/10.1016/S0020-0190(00)00084-3).
- [94] V.V. Shende, S.S. Bullock, and I.L. Markov. «Synthesis of quantum-logic circuits.» In: *IEEE Transactions on Computer-Aided Design of Integrated Circuits and Systems* 25:6 (2006), pp. 1000–1010. DOI: [10.1109/TCAD.2005.855930](https://doi.org/10.1109/TCAD.2005.855930).
- [95] Byron Drury and Peter Love. «Constructive quantum Shannon decomposition from Cartan involutions.» In: *Journal of Physics A: Mathematical and Theoretical* 41:39 (Sept. 2008), p. 395305. DOI: [10.1088/1751-8113/41/39/395305](https://doi.org/10.1088/1751-8113/41/39/395305).
- [96] Alessio Lerose, Michael Sonner, and Dmitry A. Abanin. «Overcoming the entanglement barrier in quantum many-body dynamics via space-time duality.» In: *Phys. Rev. B* 107 (6 Feb. 2023), p. L060305. DOI: [10.1103/PhysRevB.107.L060305](https://doi.org/10.1103/PhysRevB.107.L060305).
- [97] Michael Sonner, Alessio Lerose, and Dmitry A. Abanin. «Influence functional of many-body systems: Temporal entanglement and matrix-product state representation.» In: *Annals of Physics* 435 (2021). Special issue on Philip W. Anderson, p. 168677. ISSN: 0003-4916. DOI: <https://doi.org/10.1016/j.aop.2021.168677>.
- [98] Stefano Carignano, Carlos Ramos Marimón, and Luca Tagliacozzo. «On temporal entropy and the complexity of computing the expectation value of local operators after a quench.» In: (2023).
- [99] Guido Giachetti, Andrea Solfanelli, Lorenzo Correale, and Nicolò Defenu. «Fractal nature of high-order time crystal phases.» In: *Phys. Rev. B* 108 (14 Oct. 2023), p. L140102. DOI: [10.1103/PhysRevB.108.L140102](https://doi.org/10.1103/PhysRevB.108.L140102).
- [100] Yosuke Mitsuhashi and Nobuyuki Yoshioka. «Clifford Group and Unitary Designs under Symmetry.» In: *PRX Quantum* 4 (4 Nov. 2023), p. 040331. DOI: [10.1103/PRXQuantum.4.040331](https://doi.org/10.1103/PRXQuantum.4.040331).
- [101] Richard P. Feynman. «Simulating physics with computers.» In: *International Journal of Theoretical Physics* 21:6 (1982), pp. 467–488. DOI: [10.1007/BF02650179](https://doi.org/10.1007/BF02650179).
- [102] Andrew J. Daley, Immanuel Bloch, Christian Kokail, Stuart Flannigan, Natalie Pearson, Matthias Troyer, and Peter Zoller. «Practical quantum advantage in quantum simulation.» In: *Nature* 607:7920 (2022), pp. 667–676. DOI: [10.1038/s41586-022-04940-6](https://doi.org/10.1038/s41586-022-04940-6).
- [103] Xiaosi Xu, Simon Benjamin, Jinzhao Sun, Xiao Yuan, and Pan Zhang. «A Herculean task: Classical simulation of quantum computers.» In: (2023).
- [104] Hakop Pashayan, Stephen D. Bartlett, and David Gross. «From estimation of quantum probabilities to simulation of quantum circuits.» In: *Quantum* 4 (Jan. 2020), p. 223. ISSN: 2521-327X. DOI: [10.22331/q-2020-01-13-223](https://doi.org/10.22331/q-2020-01-13-223).

- [105] Anurag Anshu and Srinivasan Arunachalam. «A survey on the complexity of learning quantum states.» In: (2023).
- [106] Pietro Silvi, Ferdinand Tschirsich, Matthias Gerster, Johannes Jünemann, Daniel Jaschke, Matteo Rizzi, and Simone Montangero. «The Tensor Networks Anthology: Simulation techniques for many-body quantum lattice systems.» In: *SciPost Physics Lecture Notes* (Mar. 2019). DOI: [10.21468/scipostphyslectnotes.8](https://doi.org/10.21468/scipostphyslectnotes.8).
- [107] Nishan Ranabhat and Mario Collura. «Thermalization of long range Ising model in different dynamical regimes: a full counting statistics approach.» In: (2022). DOI: [10.48550/ARXIV.2212.00533](https://doi.org/10.48550/ARXIV.2212.00533).
- [108] Bruno Bertini, Mario Collura, Jacopo De Nardis, and Maurizio Fagotti. «Transport in Out-of-Equilibrium XXZ Chains: Exact Profiles of Charges and Currents.» In: *Phys. Rev. Lett.* 117.20 (20 Nov. 2016), p. 207201. ISSN: 1079-7114. DOI: [10.1103/PhysRevLett.117.207201](https://doi.org/10.1103/PhysRevLett.117.207201).
- [109] Vincenzo Alba and Pasquale Calabrese. «Entanglement dynamics after quantum quenches in generic integrable systems.» In: *SciPost Physics* 4.3 (2018), p. 017. DOI: [10.21468/SciPostPhys.4.3.017](https://doi.org/10.21468/SciPostPhys.4.3.017).
- [110] Vincenzo Alba and Pasquale Calabrese. «Entanglement and thermodynamics after a quantum quench in integrable systems.» In: *Proceedings of the National Academy of Sciences* 114 (2016), pp. 7947–7951. DOI: [10.1073/pnas.1703516114](https://doi.org/10.1073/pnas.1703516114).
- [111] Héctor J. García, Igor L. Markov, and Andrew W. Cross. «On the Geometry of Stabilizer States.» In: *arXiv preprint arXiv:1711.07848* (2017). DOI: [10.48550/ARXIV.1711.07848](https://doi.org/10.48550/ARXIV.1711.07848).
- [112] Matthew B. Elliott. «Stabilizer states and local realism.» In: (2008). DOI: [10.48550/ARXIV.0807.2876](https://doi.org/10.48550/ARXIV.0807.2876).
- [113] Guglielmo Lami and Mario Collura. «Unveiling the Stabilizer Group of a Matrix Product State.» In: *Phys. Rev. Lett.* 133 (1 July 2024), p. 010602. DOI: [10.1103/PhysRevLett.133.010602](https://doi.org/10.1103/PhysRevLett.133.010602).
- [114] Sergi Masot-Llima and Artur Garcia-Saez. «Stabilizer Tensor Networks: universal quantum simulator on a basis of stabilizer states.» In: (2024).
- [115] Guglielmo Lami, Tobias Haug, and Jacopo De Nardis. «Quantum State Designs with Clifford Enhanced Matrix Product States.» In: (2024).
- [116] Xiangjian Qian, Jiale Huang, and Mingpu Qin. «Augmenting Density Matrix Renormalization Group with Clifford Circuits.» In: (2024).
- [117] Alessio Paviglianiti, Guglielmo Lami, Mario Collura, and Alessandro Silva. «Estimating Non-Stabilizerness Dynamics Without Simulating It.» In: (2024).
- [118] Sarah True and Alioscia Hamma. «Transitions in Entanglement Complexity in Random Circuits.» In: *Quantum* 6 (Sept. 2022), p. 818. ISSN: 2521-327X. DOI: [10.22331/q-2022-09-22-818](https://doi.org/10.22331/q-2022-09-22-818).
- [119] J. Odavic, G. Torre, N. Mijic, D. Davidovic, F. Franchini, and S. M. Giampaolo. «Random unitaries, Robustness, and Complexity of Entanglement.» In: *Quantum* 7 (Sept. 2023), p. 1115. ISSN: 2521-327X. DOI: [10.22331/q-2023-09-15-1115](https://doi.org/10.22331/q-2023-09-15-1115).
- [120] Claudio Chamon, Alioscia Hamma, and Eduardo R. Mucciolo. «Emergent Irreversibility and Entanglement Spectrum Statistics.» In: *Physical Review Letters* 112.24 (June 2014). ISSN: 1079-7114. DOI: [10.1103/physrevlett.112.240501](https://doi.org/10.1103/physrevlett.112.240501).
- [121] Daniel Shaffer, Claudio Chamon, Alioscia Hamma, and Eduardo R Mucciolo. «Irreversibility and entanglement spectrum statistics in quantum circuits.» In: *Journal of Statistical Mechanics: Theory and Experiment* 2014.12 (Dec. 2014), P12007. ISSN: 1742-5468. DOI: [10.1088/1742-5468/2014/12/p12007](https://doi.org/10.1088/1742-5468/2014/12/p12007).
- [122] Craig Gidney. «Stim: a fast stabilizer circuit simulator.» In: *Quantum* 5 (July 2021), p. 497. ISSN: 2521-327X. DOI: [10.22331/q-2021-07-06-497](https://doi.org/10.22331/q-2021-07-06-497).
- [123] Subir Sachdev. *Quantum phase transitions*. Cambridge University Press, 2011. DOI: <https://doi.org/10.1017/CB09780511973765>.
- [124] Matthias Vojta. «Quantum phase transitions.» In: *Reports on Progress in Physics* 66.12 (2003), p. 2069. DOI: [10.1088/0034-4885/66/12/R01](https://doi.org/10.1088/0034-4885/66/12/R01).
- [125] Heinz-Peter Breuer and Francesco Petruccione. *The Theory of Open Quantum Systems*. Oxford University Press, Jan. 2007. ISBN: 9780199213900. DOI: [10.1093/acprof:oso/9780199213900.001.0001](https://doi.org/10.1093/acprof:oso/9780199213900.001.0001).
- [126] Crispin Gardiner and Peter Zoller. *Quantum Noise: A Handbook of Markovian and Non-Markovian Quantum Stochastic Methods with Applications to Quantum Optics*. 3rd ed. Springer Series in Synergetics. Springer-Verlag Berlin Heidelberg 2004. Springer Berlin, Heidelberg, 2004, pp. XXII, 450. ISBN: 978-3-540-22301-6. DOI: [10.1007/978-3-540-37670-5](https://doi.org/10.1007/978-3-540-37670-5).
- [127] Wojciech Hubert Zurek. «Quantum darwinism.» In: *Nature physics* 5.3 (2009), pp. 181–188.

- [128] Jay Gambetta, Alexandre Blais, M. Boissonneault, A. A. Houck, D. I. Schuster, and S. M. Girvin. «Quantum trajectory approach to circuit QED: Quantum jumps and the Zeno effect.» In: *Phys. Rev. A* 77 (1 Jan. 2008), p. 012112. DOI: [10.1103/PhysRevA.77.012112](https://doi.org/10.1103/PhysRevA.77.012112).
- [129] John Archibald Wheeler and Wojciech Hubert Zurek. *Quantum theory and measurement*. Vol. 53. Princeton University Press, 2014.
- [130] Alexander S Holevo. *Statistical structure of quantum theory*. Vol. 67. Springer Berlin, Heidelberg, 2003. DOI: <https://doi.org/10.1007/3-540-44998-1>.
- [131] Howard M. Wiseman and Gerard J. Milburn. *Quantum Measurement and Control*. Cambridge University Press, 2009. DOI: [10.1017/CB09780511813948](https://doi.org/10.1017/CB09780511813948).
- [132] Angelo Bassi, Kinjalk Lochan, Seema Satin, Tejinder P. Singh, and Hendrik Ulbricht. «Models of wave-function collapse, underlying theories, and experimental tests.» In: *Rev. Mod. Phys.* 85 (2 Apr. 2013), pp. 471–527. DOI: [10.1103/RevModPhys.85.471](https://doi.org/10.1103/RevModPhys.85.471).
- [133] Federico Carollo, Robert L Jack, and Juan P Garrahan. «Unraveling the large deviation statistics of Markovian open quantum systems.» In: *Physical review letters* 122.13 (2019), p. 130605.
- [134] Giulia Piccitto, Angelo Russomanno, and Davide Rossini. «Entanglement transitions in the quantum Ising chain: A comparison between different unravelings of the same Lindbladian.» In: *Phys. Rev. B* 105 (6 Feb. 2022), p. 064305. DOI: [10.1103/PhysRevB.105.064305](https://doi.org/10.1103/PhysRevB.105.064305).
- [135] Giulia Piccitto, Davide Rossini, and Angelo Russomanno. *The impact of different unravelings in a monitored system of free fermions*. 2024.
- [136] Marko Žnidarič. «Large-deviation statistics of a diffusive quantum spin chain and the additivity principle.» In: *Physical Review E* 89.4 (2014), p. 042140.
- [137] Federico Carollo, Juan P Garrahan, Igor Lesanovsky, and Carlos Pérez-Espigares. «Fluctuating hydrodynamics, current fluctuations, and hyperuniformity in boundary-driven open quantum chains.» In: *Physical Review E* 96.5 (2017), p. 052118.
- [138] Clemens Gneiting, A. V. Rozhkov, and Franco Nori. «Jump-time unraveling of Markovian open quantum systems.» In: *Phys. Rev. A* 104 (6 Dec. 2021), p. 062212. DOI: [10.1103/PhysRevA.104.062212](https://doi.org/10.1103/PhysRevA.104.062212).
- [139] Nicolas Gisin and Ian C Percival. «The quantum-state diffusion model applied to open systems.» In: *Journal of Physics A: Mathematical and General* 25.21 (1992), p. 5677. DOI: [10.1088/0305-4470/25/21/023](https://doi.org/10.1088/0305-4470/25/21/023).
- [140] P. Campagne-Ibarcq, P. Six, L. Bretheau, A. Sarlette, M. Mirrahimi, P. Rouchon, and B. Huard. «Observing Quantum State Diffusion by Heterodyne Detection of Fluorescence.» In: *Phys. Rev. X* 6 (1 Jan. 2016), p. 011002. DOI: [10.1103/PhysRevX.6.011002](https://doi.org/10.1103/PhysRevX.6.011002).
- [141] Parveen Kumar, Alessandro Romito, and Kyrylo Snizhko. «Quantum Zeno effect with partial measurement and noisy dynamics.» In: *Phys. Rev. Res.* 2 (4 Dec. 2020), p. 043420. DOI: [10.1103/PhysRevResearch.2.043420](https://doi.org/10.1103/PhysRevResearch.2.043420).
- [142] Dominic Shea and Alessandro Romito. *Stochastic action for the entanglement of a noisy monitored two-qubit system*. 2024.
- [143] Kyrylo Snizhko, Parveen Kumar, and Alessandro Romito. «Quantum Zeno effect appears in stages.» In: *Phys. Rev. Res.* 2 (3 Sept. 2020), p. 033512. DOI: [10.1103/PhysRevResearch.2.033512](https://doi.org/10.1103/PhysRevResearch.2.033512).
- [144] Zejian Li, Anna Delmonte, Xhek Turkeshi, and Rosario Fazio. *Monitored long-range interacting systems: spin-wave theory for quantum trajectories*. 2024.
- [145] Aidan Zabalo, Michael J Gullans, Justin H Wilson, Sarang Gopalakrishnan, David A Huse, and JH Pixley. «Critical properties of the measurement-induced transition in random quantum circuits.» In: *Physical Review B* 101.6 (2020), p. 060301. DOI: <https://doi.org/10.1103/PhysRevB.101.060301>.
- [146] Dorit Aharonov. «Quantum to classical phase transition in noisy quantum computers.» In: *Physical Review A* 62.6 (2000), p. 062311. DOI: <https://doi.org/10.1103/PhysRevA.62.062311>.
- [147] Yaodong Li, Xiao Chen, and Matthew PA Fisher. «Quantum Zeno effect and the many-body entanglement transition.» In: *Physical Review B* 98.20 (2018), p. 205136. DOI: <https://doi.org/10.1103/PhysRevB.98.205136>.
- [148] Brian Skinner, Jonathan Ruhman, and Adam Nahum. «Measurement-induced phase transitions in the dynamics of entanglement.» In: *Physical Review X* 9.3 (2019), p. 031009. DOI: <https://doi.org/10.1103/PhysRevX.9.031009>.
- [149] Oles Shtanko, Yaroslav A Kharkov, Luis Pedro García-Pintos, and Alexey V Gorshkov. «Classical models of entanglement in monitored random circuits.» In: *arXiv preprint arXiv:2004.06736* (2020). DOI: <https://doi.org/10.48550/arXiv.2004.06736>.

- [150] Chao-Ming Jian, Bela Bauer, Anna Keselman, and Andreas WW Ludwig. «Criticality and entanglement in non-unitary quantum circuits and tensor networks of non-interacting fermions.» In: *Physical Review B* 106.13 (2020), p. 134206. DOI: <https://doi.org/10.1103/PhysRevB.106.134206>.
- [151] Amos Chan, Rahul M Nandkishore, Michael Pretko, and Graeme Smith. «Unitary-projective entanglement dynamics.» In: *Physical Review B* 99.22 (22 June 2019), p. 224307. DOI: <https://doi.org/10.1103/PhysRevB.99.224307>.
- [152] Yaodong Li, Xiao Chen, and Matthew PA Fisher. «Measurement-driven entanglement transition in hybrid quantum circuits.» In: *Physical Review B* 100.13 (2019), p. 134306. DOI: <https://doi.org/10.1103/PhysRevB.100.134306>.
- [153] Xiangyu Cao, Antoine Tilloy, and Andrea De Luca. «Entanglement in a fermion chain under continuous monitoring.» In: *SciPost Phys.* 7 (2 2019), p. 024. DOI: [10.21468/SciPostPhys.7.2.024](https://doi.org/10.21468/SciPostPhys.7.2.024).
- [154] Yohei Fuji and Yuto Ashida. «Measurement-induced quantum criticality under continuous monitoring.» In: *Physical Review B* 102.5 (2020), p. 054302. DOI: <https://doi.org/10.1103/PhysRevB.102.054302>.
- [155] T. Boorman, M. Szyniszewski, H. Schomerus, and A. Romito. «Diagnostics of entanglement dynamics in noisy and disordered spin chains via the measurement-induced steady-state entanglement transition.» In: *Phys. Rev. B* 105 (14 Apr. 2022), p. 144202. DOI: [10.1103/PhysRevB.105.144202](https://doi.org/10.1103/PhysRevB.105.144202).
- [156] Ori Alberton, Michael Buchhold, and Sebastian Diehl. «Entanglement Transition in a Monitored Free-Fermion Chain: From Extended Criticality to Area Law.» In: *Physical Review Letters* 126.17 (2021), p. 170602. DOI: <https://doi.org/10.1103/PhysRevLett.126.170602>.
- [157] Thomas Müller, Sebastian Diehl, and Michael Buchhold. «Measurement-induced dark state phase transitions in long-ranged fermion systems.» In: *Physical Review Letters* 128.1 (2022), p. 010605. DOI: <https://doi.org/10.1103/PhysRevLett.128.010605>.
- [158] Shimpei Goto and Ippei Danshita. «Measurement-induced transitions of the entanglement scaling law in ultracold gases with controllable dissipation.» In: *Physical Review A* 102.3 (2020), p. 033316. DOI: <https://doi.org/10.1103/PhysRevA.102.033316>.
- [159] M Buchhold, Y Minoguchi, A Altland, and S Diehl. «Effective theory for the measurement-induced phase transition of Dirac fermions.» In: *Physical Review X* 11.4 (2021), p. 041004. DOI: <https://doi.org/10.1103/PhysRevX.11.041004>.
- [160] Takaaki Minato, Koudai Sugimoto, Tomotaka Kuwahara, and Keiji Saito. «Fate of measurement-induced phase transition in long-range interactions.» In: *Physical review letters* 128.1 (2022), p. 010603. DOI: <https://doi.org/10.1103/PhysRevLett.128.010603>.
- [161] Thibaud Maimbourg, Denis M. Basko, Markus Holzmann, and Alberto Rosso. «Bath-Induced Zeno Localization in Driven Many-Body Quantum Systems.» In: *Phys. Rev. Lett.* 126 (12 Mar. 2021), p. 120603. DOI: [10.1103/PhysRevLett.126.120603](https://doi.org/10.1103/PhysRevLett.126.120603).
- [162] Alessio Paviglianiti and Alessandro Silva. «Multipartite entanglement in the measurement-induced phase transition of the quantum Ising chain.» In: *Phys. Rev. B* 108 (18 Nov. 2023), p. 184302. DOI: [10.1103/PhysRevB.108.184302](https://doi.org/10.1103/PhysRevB.108.184302).
- [163] Graham Kells, Dganit Meidan, and Alessandro Romito. «Topological transitions in weakly monitored free fermions.» In: *SciPost Phys.* 14 (2023), p. 031. DOI: [10.21468/SciPostPhys.14.3.031](https://doi.org/10.21468/SciPostPhys.14.3.031).
- [164] Michele Coppola, Emanuele Tirrito, Dragi Karevski, and Mario Collura. «Growth of entanglement entropy under local projective measurements.» In: *Physical Review B* 105.9 (2022), p. 094303. DOI: <https://doi.org/10.1103/PhysRevB.105.094303>.
- [165] Mikheil Tsitsishvili, Dario Poletti, Marcello Dalmonte, and Giuliano Chiriacò. «Measurement induced transitions in non-Markovian free fermion ladders.» In: *SciPost Phys. Core* 7 (2024), p. 011. DOI: [10.21468/SciPostPhysCore.7.1.011](https://doi.org/10.21468/SciPostPhysCore.7.1.011).
- [166] Luca Lumia, Emanuele Tirrito, Rosario Fazio, and Mario Collura. «Measurement-induced transitions beyond Gaussianity: A single particle description.» In: *Phys. Rev. Res.* 6 (2 May 2024), p. 023176. DOI: [10.1103/PhysRevResearch.6.023176](https://doi.org/10.1103/PhysRevResearch.6.023176).
- [167] Federico Gerbino, Pierre Le Doussal, Guido Giachetti, and Andrea De Luca. «A Dyson Brownian Motion Model for Weak Measurements in Chaotic Quantum Systems.» In: *Quantum Reports* 6.2 (2024), pp. 200–230. ISSN: 2624-960X. DOI: [10.3390/quantum6020016](https://doi.org/10.3390/quantum6020016).
- [168] Shradha Sharma, Xhek Turkeshi, Rosario Fazio, and Marcello Dalmonte. «Measurement-induced criticality in extended and long-range unitary circuits.» In: *SciPost Physics Core* 5.2 (2022), p. 023.
- [169] Xhek Turkeshi, Marcello Dalmonte, Rosario Fazio, and Marco Schirò. «Entanglement transitions from stochastic resetting of non-Hermitian quasiparticles.» In: *Physical Review B* 105.24 (2022), p. L241114.

- [170] Guillaume Cecile, Hugo Lóio, and Jacopo De Nardis. *Measurement-induced phase transitions by matrix product states scaling*. 2024.
- [171] Igor Poboiko, Paul Pöpperl, Igor V. Gornyi, and Alexander D. Mirlin. «Theory of Free Fermions under Random Projective Measurements.» In: *Phys. Rev. X* 13 (4 Dec. 2023), p. 041046. DOI: [10.1103/PhysRevX.13.041046](https://doi.org/10.1103/PhysRevX.13.041046).
- [172] Igor Poboiko, Igor V. Gornyi, and Alexander D. Mirlin. «Measurement-Induced Phase Transition for Free Fermions above One Dimension.» In: *Phys. Rev. Lett.* 132 (11 Mar. 2024), p. 110403. DOI: [10.1103/PhysRevLett.132.110403](https://doi.org/10.1103/PhysRevLett.132.110403).
- [173] Soonwon Choi, Yimu Bao, Xiao-Liang Qi, and Ehud Altman. «Quantum Error Correction in Scrambling Dynamics and Measurement-Induced Phase Transition.» In: *Phys. Rev. Lett.* 125 (3 July 2020), p. 030505. DOI: [10.1103/PhysRevLett.125.030505](https://doi.org/10.1103/PhysRevLett.125.030505).
- [174] Michael J. Gullans and David A. Huse. «Dynamical Purification Phase Transition Induced by Quantum Measurements.» In: *Phys. Rev. X* 10 (4 Oct. 2020), p. 041020. DOI: [10.1103/PhysRevX.10.041020](https://doi.org/10.1103/PhysRevX.10.041020).
- [175] Sarang Gopalakrishnan and Michael J. Gullans. «Entanglement and Purification Transitions in Non-Hermitian Quantum Mechanics.» In: *Physical Review Letters* 126.17 (Apr. 2021). ISSN: 1079-7114. DOI: [10.1103/physrevlett.126.170503](https://doi.org/10.1103/physrevlett.126.170503).
- [176] Hugo Lóio, Andrea De Luca, Jacopo De Nardis, and Xhek Turkeshi. «Purification timescales in monitored fermions.» In: *Phys. Rev. B* 108 (2 July 2023), p. L020306. DOI: [10.1103/PhysRevB.108.L020306](https://doi.org/10.1103/PhysRevB.108.L020306).
- [177] Guido Giachetti and Andrea De Luca. *Elusive phase transition in the replica limit of monitored systems*. 2023.
- [178] Yaodong Li, Xiao Chen, Andreas WW Ludwig, and Matthew Fisher. «Conformal invariance and quantum non-locality in hybrid quantum circuits.» In: *Physical Review B* 104.104305 (2021). DOI: <https://doi.org/10.1103/PhysRevB.104.104305>.
- [179] Marcin Szyniszewski, Alessandro Romito, and Henning Schomerus. «Universality of entanglement transitions from stroboscopic to continuous measurements.» In: *Physical review letters* 125.21 (2020), p. 210602. DOI: <https://doi.org/10.1103/PhysRevLett.125.210602>.
- [180] Lei Zhang, Justin A Reyes, Stefanos Kourtis, Claudio Chamon, Eduardo R Mucciolo, and Andrei E Ruckenstein. «Nonuniversal entanglement level statistics in projection-driven quantum circuits.» In: *Physical Review B* 101.23 (2020), p. 235104. DOI: <https://doi.org/10.1103/PhysRevB.101.235104>.
- [181] Adam Nahum, Jonathan Ruhman, Sagar Vijay, and Jeongwan Haah. «Quantum entanglement growth under random unitary dynamics.» In: *Physical Review X* 7.3 (2017), p. 031016. DOI: <https://doi.org/10.1103/PhysRevX.7.031016>.
- [182] Marcin Szyniszewski, Alessandro Romito, and Henning Schomerus. «Entanglement transition from variable-strength weak measurements.» In: *Physical Review B* 100.6 (2019), p. 064204. DOI: <https://doi.org/10.1103/PhysRevB.100.064204>.
- [183] Alessandro Santini, Andrea Solfanelli, Stefano Gherardini, and Guido Giachetti. *Observation of partial and infinite-temperature thermalization induced by continuous monitoring on a quantum hardware*. 2022. DOI: [10.48550/ARXIV.2211.07444](https://doi.org/10.48550/ARXIV.2211.07444).
- [184] Ali Lavasani, Yahya Alavirad, and Maissam Barkeshli. «Topological order and criticality in  $(2+1)$  D monitored random quantum circuits.» In: *Physical Review Letters* 127.23 (2021), p. 235701. DOI: <https://doi.org/10.1103/PhysRevLett.127.235701>.
- [185] Ali Lavasani, Yahya Alavirad, and Maissam Barkeshli. «Measurement-induced topological entanglement transitions in symmetric random quantum circuits.» In: *Nature Physics* 17.3 (2021), pp. 342–347. DOI: <https://doi.org/10.5281/zenodo.4031884>.
- [186] Maxwell Block, Yimu Bao, Soonwon Choi, Ehud Altman, and Norman Y Yao. «Measurement-induced transition in long-range interacting quantum circuits.» In: *Physical Review Letters* 128.1 (2022), p. 010604. DOI: <https://doi.org/10.1103/PhysRevLett.128.010604>.
- [187] Shengqi Sang and Timothy H Hsieh. «Measurement-protected quantum phases.» In: *Physical Review Research* 3.2 (2021), p. 023200. DOI: <https://doi.org/10.1103/PhysRevResearch.3.023200>.
- [188] Bowen Shi, Xin Dai, and Yuan-Ming Lu. «Entanglement negativity at the critical point of measurement-driven transition.» In: *arXiv preprint arXiv:2012.00040* (2020). DOI: <https://doi.org/10.48550/arXiv.2012.00040>.
- [189] Oliver Lunt and Arijeet Pal. «Measurement-induced entanglement transitions in many-body localized systems.» In: *Physical Review Research* 2.4 (2020), p. 043072. DOI: <https://doi.org/10.1103/PhysRevResearch.2.043072>.
- [190] Xhek Turkeshi, Marcello Dalmonte, Rosario Fazio, and Marco Schirò. «Entanglement transitions from stochastic resetting of non-Hermitian quasiparticles.» In: *Phys. Rev. B* 105 (24 2022), p. L241114. DOI: [10.1103/PhysRevB.105.L241114](https://doi.org/10.1103/PhysRevB.105.L241114).



- [191] Xhek Turkeshi, Alberto Biella, Rosario Fazio, Marcello Dalmonte, and Marco Schiró. «Measurement-induced entanglement transitions in the quantum Ising chain: From infinite to zero clicks.» In: *Phys. Rev. B* 103 (22 2021), p. 224210. DOI: [10.1103/PhysRevB.103.224210](https://doi.org/10.1103/PhysRevB.103.224210).
- [192] Shrabanti Dhar and Subinay Dasgupta. «Measurement-induced phase transition in a quantum spin system.» In: *Physical Review A* 93.5 (2016), p. 050103. DOI: <https://doi.org/10.1103/PhysRevA.93.050103>.
- [193] Xhek Turkeshi, Rosario Fazio, and Marcello Dalmonte. «Measurement-induced criticality in  $(2+1)$ -dimensional hybrid quantum circuits.» In: *Physical Review B* 102.1 (2020), p. 014315. DOI: <https://doi.org/10.1103/PhysRevB.102.014315>.
- [194] Nicolai Lang and Hans Peter Büchler. «Entanglement transition in the projective transverse field Ising model.» In: *Physical Review B* 102.9 (2020), p. 094204. DOI: <https://doi.org/10.1103/PhysRevB.102.094204>.
- [195] Davide Rossini and Ettore Vicari. «Measurement-induced dynamics of many-body systems at quantum criticality.» In: *Physical Review B* 102.3 (2020), p. 035119. DOI: <https://doi.org/10.1103/PhysRevB.102.035119>.
- [196] Xhek Turkeshi, Alberto Biella, Rosario Fazio, Marcello Dalmonte, and Marco Schiró. «Measurement-induced entanglement transitions in the quantum Ising chain: From infinite to zero clicks.» In: *Physical Review B* 103.22 (2021), p. 224210. DOI: <https://doi.org/10.1103/PhysRevB.103.224210>.
- [197] Thomas Botzung, Sebastian Diehl, and Markus Müller. «Engineered dissipation induced entanglement transition in quantum spin chains: from logarithmic growth to area law.» In: *Physical Review B* 104.18 (2021), p. 184422. DOI: <https://doi.org/10.1103/PhysRevB.104.184422>.
- [198] T Boorman, M Szyniszewski, H Schomerus, and A Romito. «Diagnostics of entanglement dynamics in noisy and disordered spin chains via the measurement-induced steady-state entanglement transition.» In: *Physical Review B* 105.14 (2022), p. 144202. DOI: <https://doi.org/10.1103/PhysRevB.105.144202>.
- [199] Matteo Ippoliti and Vedika Khemani. «Postselection-free entanglement dynamics via spacetime duality.» In: *Physical Review Letters* 126.6 (2021), p. 060501. DOI: <https://doi.org/10.1103/PhysRevLett.126.060501>.
- [200] Xhek Turkeshi. «Measurement-induced criticality as a data-structure transition.» In: *Physical Review B* 106.14 (2022), p. 144313. DOI: <https://doi.org/10.1103/PhysRevB.106.144313>.
- [201] Piotr Sierant and Xhek Turkeshi. «Universal behavior beyond multifractality of wave functions at measurement-induced phase transitions.» In: *Physical Review Letters* 128.13 (2022), p. 130605. DOI: <https://doi.org/10.1103/PhysRevLett.128.130605>.
- [202] Thomas J Elliott, Wojciech Kozłowski, SF Caballero-Benitez, and Igor B Mekhov. «Multipartite entangled spatial modes of ultracold atoms generated and controlled by quantum measurement.» In: *Physical review letters* 114.11 (2015), p. 113604. DOI: <https://doi.org/10.1103/PhysRevLett.114.113604>.
- [203] Stefanie Czischek, Giacomo Torlai, Sayonee Ray, Rajibul Islam, and Roger G Melko. «Simulating a measurement-induced phase transition for trapped-ion circuits.» In: *Physical Review A* 104.6 (2021), p. 062405. DOI: <https://doi.org/10.1103/PhysRevA.104.062405>.
- [204] Crystal Noel, Pradeep Niroula, Daiwei Zhu, Andrew Risinger, Laird Egan, Debopriyo Biswas, Marko Cetina, Alexey V Gorshkov, Michael J Gullans, David A Huse, et al. «Measurement-induced quantum phases realized in a trapped-ion quantum computer.» In: *Nature Physics* (2022), pp. 1–5. DOI: <https://doi.org/10.1038/s41567-022-01619-7>.
- [205] Piotr Sierant, Giuliano Chiriacò, Federica M Surace, Shraddha Sharma, Xhek Turkeshi, Marcello Dalmonte, Rosario Fazio, and Guido Pagano. «Dissipative Floquet dynamics: from steady state to measurement induced criticality in trapped-ion chains.» In: *Quantum* 6 (Feb. 2022), p. 638. ISSN: 2521-327X. DOI: <https://doi.org/10.22331/q-2022-02-02-638>.
- [206] Vincenzo Alba and Pasquale Calabrese. «Entanglement and thermodynamics after a quantum quench in integrable systems.» In: *Proceedings of the National Academy of Sciences* 114.30 (2017), pp. 7947–7951.
- [207] Vincenzo Alba. «Entanglement and quantum transport in integrable systems.» In: *Physical Review B* 97.24 (2018), p. 245135.
- [208] Marcos Rigol, Vanja Dunjko, and Maxim Olshanii. «Thermalization and its mechanism for generic isolated quantum systems.» In: *Nature* 452.7189 (2008), pp. 854–858.
- [209] Rahul Nandkishore and David A Huse. «Many-body localization and thermalization in quantum statistical mechanics.» In: *Annu. Rev. Condens. Matter Phys.* 6.1 (2015), pp. 15–38.

- [210] Dmitry A Abanin, Ehud Altman, Immanuel Bloch, and Maksym Serbyn. «Colloquium: Many-body localization, thermalization, and entanglement.» In: *Reviews of Modern Physics* 91.2 (2019), p. 021001.
- [211] A Degasperis, L Fonda, and GC Ghirardi. «Does the lifetime of an unstable system depend on the measuring apparatus?» In: *Il Nuovo Cimento A (1965-1970)* 21.3 (1974), pp. 471–484.
- [212] Baidyanath Misra and EC George Sudarshan. «The Zeno’s paradox in quantum theory.» In: *Journal of Mathematical Physics* 18.4 (1977), pp. 756–763. DOI: <https://doi.org/10.1063/1.523304>.
- [213] Asher Peres. «Zeno paradox in quantum theory.» In: *American Journal of Physics* 48.11 (1980), pp. 931–932. DOI: <https://doi.org/10.1119/1.12204>.
- [214] Kyrylo Snizhko, Parveen Kumar, and Alessandro Romito. «Quantum Zeno effect appears in stages.» In: *Physical Review Research* 2.3 (2020), p. 033512. DOI: <https://doi.org/10.1103/PhysRevResearch.2.033512>.
- [215] Alberto Biella and Marco Schiró. «Many-body quantum Zeno effect and measurement-induced subradiance transition.» In: *Quantum* 5 (2021), p. 528. DOI: <https://doi.org/10.22331/q-2021-08-19-528>.
- [216] Xiao Chen, Yaodong Li, Matthew PA Fisher, and Andrew Lucas. «Emergent conformal symmetry in nonunitary random dynamics of free fermions.» In: *Physical Review Research* 2.3 (2020), p. 033017. DOI: <https://doi.org/10.1103/PhysRevResearch.2.033017>.
- [217] Qicheng Tang, Xiao Chen, and W Zhu. «Quantum criticality in the nonunitary dynamics of  $(2+1)$ -dimensional free fermions.» In: *Physical Review B* 103.17 (2021), p. 174303. DOI: <https://doi.org/10.1103/PhysRevB.103.174303>.
- [218] Yimu Bao, Soonwon Choi, and Ehud Altman. «Symmetry enriched phases of quantum circuits.» In: *Annals of Physics* 435 (2021), p. 168618.
- [219] Oliver Lunt, Marcin Szyniszewski, and Arijeet Pal. «Measurement-induced criticality and entanglement clusters: A study of one-dimensional and two-dimensional Clifford circuits.» In: *Physical Review B* 104.15 (2021), p. 155111. DOI: <https://doi.org/10.1103/PhysRevB.104.155111>.
- [220] Kurt Jacobs and Daniel A. Steck. «A straightforward introduction to continuous quantum measurement.» In: *Contemporary Physics* 47.5 (Sept. 2006), 279–303. ISSN: 1366-5812. DOI: [10.1080/00107510601101934](https://doi.org/10.1080/00107510601101934).
- [221] Michael A. Nielsen and Isaac L. Chuang. *Quantum Computation and Quantum Information: 10th Anniversary Edition*. Cambridge University Press, 2010. DOI: [10.1017/CB09780511976667](https://doi.org/10.1017/CB09780511976667).
- [222] J. S. Bell. «On the Einstein Podolsky Rosen paradox.» In: *Physics Physique Fizika* 1 (3 1964), pp. 195–200. DOI: [10.1103/PhysicsPhysiqueFizika.1.195](https://doi.org/10.1103/PhysicsPhysiqueFizika.1.195).
- [223] Giulia Piccitto, Angelo Russomanno, and Davide Rossini. «Entanglement transitions in the quantum Ising chain: A comparison between different unravelings of the same Lindbladian.» In: *Physical Review B* 105.6 (2022), p. 064305.
- [224] Todd A Brun. «A simple model of quantum trajectories.» In: *American Journal of Physics* 70.7 (2002), pp. 719–737. DOI: <https://doi.org/10.1119/1.1475328>.
- [225] Martin B Plenio and Peter L Knight. «The quantum-jump approach to dissipative dynamics in quantum optics.» In: *Reviews of Modern Physics* 70.1 (1998), p. 101. DOI: <https://doi.org/10.1103/RevModPhys.70.101>.
- [226] Mario Collura. «Relaxation of the order-parameter statistics in the Ising quantum chain.» In: *SciPost Phys.* 7 (6 2019), p. 72. DOI: [10.21468/SciPostPhys.7.6.072](https://doi.org/10.21468/SciPostPhys.7.6.072).
- [227] Ingemar Bengtsson. *The Importance of Being Unistochastic*. 2004.
- [228] Karol Zyczkowski, Marek Kus, Wojciech Słomczyński, and Hans-Jürgen Sommers. «Random unistochastic matrices.» In: *Journal of Physics A: Mathematical and General* 36.12 (Mar. 2003), p. 3425. DOI: [10.1088/0305-4470/36/12/333](https://doi.org/10.1088/0305-4470/36/12/333).
- [229] Crispin Gardiner. *Stochastic methods*. Vol. 4. Springer Berlin, Heidelberg, 2009.
- [230] David Morin. *Introduction to Classical Mechanics: With Problems and Solutions*. Cambridge University Press, 2008. DOI: [10.1017/CB09780511808951](https://doi.org/10.1017/CB09780511808951).
- [231] P. W. Anderson. «Absence of Diffusion in Certain Random Lattices.» In: *Phys. Rev.* 109 (5 Mar. 1958), pp. 1492–1505. DOI: [10.1103/PhysRev.109.1492](https://doi.org/10.1103/PhysRev.109.1492).
- [232] Antonello Scardicchio and Thimothée Thiery. *Perturbation theory approaches to Anderson and Many-Body Localization: some lecture notes*. 2017.
- [233] Kiran E. Khosla, Ardan Armin, and M. S. Kim. «Quantum trajectories, interference, and state localisation in dephasing assisted quantum transport.» In: (2021). DOI: <https://doi.org/10.48550/arXiv.2111.02986>.

- [234] Debraj Das and Shamik Gupta. «Quantum random walk and tight-binding model subject to projective measurements at random times.» In: *Journal of Statistical Mechanics: Theory and Experiment* 2022.3 (Mar. 2022), p. 033212. DOI: [10.1088/1742-5468/ac5dc0](https://doi.org/10.1088/1742-5468/ac5dc0).
- [235] B. Mukherjee, K. Sengupta, and Satya N. Majumdar. «Quantum dynamics with stochastic reset.» In: *Phys. Rev. B* 98 (10 Sept. 2018), p. 104309. DOI: [10.1103/PhysRevB.98.104309](https://doi.org/10.1103/PhysRevB.98.104309).
- [236] Zi Cai and Thomas Barthel. «Algebraic versus Exponential Decoherence in Dissipative Many-Particle Systems.» In: *Phys. Rev. Lett.* 111 (15 Oct. 2013), p. 150403. DOI: [10.1103/PhysRevLett.111.150403](https://doi.org/10.1103/PhysRevLett.111.150403).
- [237] Nicolò Defenu, Tobias Donner, Tommaso Macrì, Guido Pagano, Stefano Ruffo, and Andrea Trombettoni. «Long-range interacting quantum systems.» In: *Rev. Mod. Phys.* 95 (3 Aug. 2023), p. 035002. DOI: [10.1103/RevModPhys.95.035002](https://doi.org/10.1103/RevModPhys.95.035002).
- [238] José I. Latorre, Román Orús, Enrique Rico, and Julien Vidal. «Entanglement entropy in the Lipkin-Meshkov-Glick model.» In: *Phys. Rev. A* 71 (6 June 2005), p. 064101. DOI: [10.1103/PhysRevA.71.064101](https://doi.org/10.1103/PhysRevA.71.064101).
- [239] M. D. Lukin, M. Fleischhauer, R. Cote, L. M. Duan, D. Jaksch, J. I. Cirac, and P. Zoller. «Dipole Blockade and Quantum Information Processing in Mesoscopic Atomic Ensembles.» In: *Phys. Rev. Lett.* 87 (3 June 2001), p. 037901. DOI: [10.1103/PhysRevLett.87.037901](https://doi.org/10.1103/PhysRevLett.87.037901).
- [240] M. Saffman, T. G. Walker, and K. Mølmer. «Quantum information with Rydberg atoms.» In: *Rev. Mod. Phys.* 82 (3 Aug. 2010), pp. 2313–2363. DOI: [10.1103/RevModPhys.82.2313](https://doi.org/10.1103/RevModPhys.82.2313).
- [241] Antoine Browaeys and Thierry Lahaye. «Many-body physics with individually controlled Rydberg atoms.» In: *Nature Physics* 16.2 (Jan. 2020), 132–142. ISSN: 1745-2481. DOI: [10.1038/s41567-019-0733-z](https://doi.org/10.1038/s41567-019-0733-z).
- [242] C. Monroe et al. «Programmable quantum simulations of spin systems with trapped ions.» In: *Rev. Mod. Phys.* 93 (2 Apr. 2021), p. 025001. DOI: [10.1103/RevModPhys.93.025001](https://doi.org/10.1103/RevModPhys.93.025001).
- [243] J. I. Cirac and P. Zoller. «Quantum Computations with Cold Trapped Ions.» In: *Phys. Rev. Lett.* 74 (20 May 1995), pp. 4091–4094. DOI: [10.1103/PhysRevLett.74.4091](https://doi.org/10.1103/PhysRevLett.74.4091).
- [244] Renate Landig, Lorenz Hruby, Nishant Dogra, Manuele Landini, Rafael Mottl, Tobias Donner, and Tilman Esslinger. «Quantum phases from competing short-and long-range interactions in an optical lattice.» In: *Nature* 532.7600 (2016), pp. 476–479.
- [245] Farokh Mivehvar, Francesco Piazza, Tobias Donner, and Helmut Ritsch. «Cavity QED with quantum gases: new paradigms in many-body physics.» In: *Adv. Phys.* 70.1 (Jan. 2021), 1–153. ISSN: 1460-6976. DOI: [10.1080/00018732.2021.1969727](https://doi.org/10.1080/00018732.2021.1969727).
- [246] Harry J Lipkin, N Meshkov, and AJ Glick. «Validity of many-body approximation methods for a solvable model:(I). Exact solutions and perturbation theory.» In: *Nuclear Physics* 62.2 (1965), pp. 188–198. ISSN: 0029-5582. DOI: [https://doi.org/10.1016/0029-5582\(65\)90862-X](https://doi.org/10.1016/0029-5582(65)90862-X).
- [247] Tommaso Caneva, Rosario Fazio, and Giuseppe E. Santoro. «Adiabatic quantum dynamics of the Lipkin-Meshkov-Glick model.» In: *Phys. Rev. B* 78 (10 Sept. 2008), p. 104426. DOI: [10.1103/PhysRevB.78.104426](https://doi.org/10.1103/PhysRevB.78.104426).
- [248] Pedro Ribeiro, Julien Vidal, and Rémy Mosseri. «Exact spectrum of the Lipkin-Meshkov-Glick model in the thermodynamic limit and finite-size corrections.» In: *Phys. Rev. E* 78 (2 Aug. 2008), p. 021106. DOI: [10.1103/PhysRevE.78.021106](https://doi.org/10.1103/PhysRevE.78.021106).
- [249] Steve Campbell. «Criticality revealed through quench dynamics in the Lipkin-Meshkov-Glick model.» In: *Phys. Rev. B* 94 (18 Nov. 2016), p. 184403. DOI: [10.1103/PhysRevB.94.184403](https://doi.org/10.1103/PhysRevB.94.184403).
- [250] Angelo Russomanno, Fernando Iemini, Marcello Dalmonte, and Rosario Fazio. «Floquet time crystal in the Lipkin-Meshkov-Glick model.» In: *Phys. Rev. B* 95 (21 June 2017), p. 214307. DOI: [10.1103/PhysRevB.95.214307](https://doi.org/10.1103/PhysRevB.95.214307).
- [251] Andrea Pizzi, Johannes Knolle, and Andreas Nunnenkamp. «Higher-order and fractional discrete time crystals in clean long-range interacting systems.» In: *Nature Communications* 12.1 (Apr. 2021), p. 2341. ISSN: 2041-1723. DOI: [10.1038/s41467-021-22583-5](https://doi.org/10.1038/s41467-021-22583-5).
- [252] Manuel H. Muñoz Arias, Karthik Chinni, and Pablo M. Poggi. «Floquet time crystals in driven spin systems with all-to-all p-body interactions.» In: *Phys. Rev. Res.* 4 (2 Apr. 2022), p. 023018. DOI: [10.1103/PhysRevResearch.4.023018](https://doi.org/10.1103/PhysRevResearch.4.023018).
- [253] Federica Maria Surace, Angelo Russomanno, Marcello Dalmonte, Alessandro Silva, Rosario Fazio, and Fernando Iemini. «Floquet time crystals in clock models.» In: *Phys. Rev. B* 99 (10 Mar. 2019), p. 104303. DOI: [10.1103/PhysRevB.99.104303](https://doi.org/10.1103/PhysRevB.99.104303).
- [254] Pappalardi, Silvia and Russomanno, Angelo and Žunkovič, Bojan and Iemini, Fernando and Silva, Alessandro and Fazio, Rosario. «Scrambling and entanglement spreading in long-range spin chains.» In: *Phys. Rev. B* 98 (13 Oct. 2018), p. 134303. DOI: [10.1103/PhysRevB.98.134303](https://doi.org/10.1103/PhysRevB.98.134303).



- [255] Alessio Lerose, Jamir Marino, Bojan Žunkovič, Andrea Gambassi, and Alessandro Silva. «Chaotic dynamical ferromagnetic phase induced by nonequilibrium quantum fluctuations.» In: *Physical review letters* 120.13 (2018), p. 130603.
- [256] Maxwell Block, Yimu Bao, Soonwon Choi, Ehud Altman, and Norman Y. Yao. «Measurement-Induced Transition in Long-Range Interacting Quantum Circuits.» In: *Phys. Rev. Lett.* 128 (1 Jan. 2022), p. 010604. DOI: [10.1103/PhysRevLett.128.010604](https://doi.org/10.1103/PhysRevLett.128.010604).
- [257] T. Müller, S. Diehl, and M. Buchhold. «Measurement-Induced Dark State Phase Transitions in Long-Ranged Fermion Systems.» In: *Phys. Rev. Lett.* 128 (1 Jan. 2022), p. 010605. DOI: [10.1103/PhysRevLett.128.010605](https://doi.org/10.1103/PhysRevLett.128.010605).
- [258] Gianluca Passarelli, Xhek Turkeshi, Angelo Russomanno, Procolo Lucignano, Marco Schirò, and Rosario Fazio. «Many-Body Dynamics in Monitored Atomic Gases without Postselection Barrier.» In: *Phys. Rev. Lett.* 132 (16 Apr. 2024), p. 163401. DOI: [10.1103/PhysRevLett.132.163401](https://doi.org/10.1103/PhysRevLett.132.163401).
- [259] Angelo Russomanno, Giulia Piccitto, and Davide Rossini. «Entanglement transitions and quantum bifurcations under continuous long-range monitoring.» In: *Phys. Rev. B* 108 (10 Sept. 2023), p. 104313. DOI: [10.1103/PhysRevB.108.104313](https://doi.org/10.1103/PhysRevB.108.104313).
- [260] Xhek Turkeshi, Lorenzo Piroli, and Marco Schirò. *Density and current statistics in boundary-driven monitored fermionic chains*. 2024.
- [261] M. Kac, G. E. Uhlenbeck, and P. C. Hemmer. «On the van der Waals Theory of the Vapor-Liquid Equilibrium. I. Discussion of a One-Dimensional Model.» In: *Journal of Mathematical Physics* 4.2 (Feb. 1963), pp. 216–228. DOI: [10.1063/1.1703946](https://doi.org/10.1063/1.1703946).
- [262] Nicolò Defenu, Alessio Lerose, and Silvia Pappalardi. «Out-of-equilibrium dynamics of quantum many-body systems with long-range interactions.» In: *Physics Reports* 1074 (2024). Out-of-equilibrium dynamics of quantum many-body systems with long-range interactions, pp. 1–92. ISSN: 0370-1573. DOI: <https://doi.org/10.1016/j.physrep.2024.04.005>.
- [263] Nicolò Defenu. «Metastability and discrete spectrum of long-range systems.» In: *Proceedings of the National Academy of Sciences* 118.30 (2021), e2101785118. ISSN: 0027-8424. DOI: [10.1073/pnas.2101785118](https://doi.org/10.1073/pnas.2101785118).
- [264] Guido Giachetti and Nicolò Defenu. «Entanglement propagation and dynamics in non-additive quantum systems.» In: *Scientific Reports* 13 (1 2023). DOI: [10.1038/s41598-023-37984-3](https://doi.org/10.1038/s41598-023-37984-3).
- [265] Michael Kastner. «Diverging equilibration times in long-range quantum spin models.» In: *Physical Review Letters* 106.13 (2011), p. 130601.
- [266] J M Radcliffe. «Some properties of coherent spin states.» In: *Journal of Physics A: General Physics* 4.3 (May 1971), p. 313. DOI: [10.1088/0305-4470/4/3/009](https://doi.org/10.1088/0305-4470/4/3/009).
- [267] F. T. Arecchi, Eric Courtens, Robert Gilmore, and Harry Thomas. «Atomic Coherent States in Quantum Optics.» In: *Phys. Rev. A* 6 (6 Dec. 1972), pp. 2211–2237. DOI: [10.1103/PhysRevA.6.2211](https://doi.org/10.1103/PhysRevA.6.2211).
- [268] A M Perelomov. «Generalized coherent states and some of their applications.» In: *Soviet Physics Uspekhi* 20.9 (Sept. 1977), p. 703. DOI: [10.1070/PU1977v020n09ABEH005459](https://doi.org/10.1070/PU1977v020n09ABEH005459).